TECHNISCHE UNIVERSITÄT MÜNCHEN

Fakultät für Chemie

Lehrstuhl für Theoretische Chemie

DISSERTATION

First-Principles Modeling in Poisson-Boltzmann Electrolytes

Stefan Ringe

Garching b. München, April 2017

All work presented in this dissertation was performed between June 2013 – April 2017 at the Chair of Theoretical Chemistry of the Technische Universität München under the supervision of Prof. Dr. Karsten Reuter.

TECHNISCHE UNIVERSITÄT MÜNCHEN

Fakultät für Chemie

Lehrstuhl für Theoretische Chemie

First-Principles Modeling in Poisson-Boltzmann Electrolytes

Stefan Ringe

Vollständiger Abdruck der von der Fakultät für Chemie der Technischen Universität München zur Erlangung des akademischen Grades eines

Doktors der Naturwissenschaften (Dr. rer. nat.)

genehmigten Dissertation.

Vorsitzende: Prof. Dr. Kathrin Lang

Prüfer der Dissertation: 1. Prof. Dr. Karsten Reuter
2. Prof. Dr. Ville Kaila

Die Dissertation wurde am 11.04.2017 bei der Technischen Universität München eingereicht und durch die Fakultät für Chemie am 27.04.2017 angenommen.

Für Jinyoung.

„Auch aus Steinen,
die einem in den Weg gelegt werden,
kann man Schönes bauen."

Johann Wolfgang von Goethe

Abstract

First-principles modeling of chemical reactions in electrolytic environments is at the center of modern computational chemistry. Continuum implicit solvation methods have thereby become a standard means for computationally efficient descriptions of solvated systems. Poisson-Boltzmann (PB) techniques on the other hand have been successful in the modeling of ionic charge distributions. In this thesis, we develop a combined implicit solvation-PB approach which notably also accounts for non-electrostatic ion-specific effects by introducing a finite size and Stern layer modified PB (SMPB) method. We implemented the full methodology into the highly parallelizable numerically tabulated atom-centered orbitals (NAO)-based all-electron density functional theory (DFT) package `FHI-aims`.[1] Thereby, the key obstacle is the solution of a non-linear partial differential equation (PDE): The SMPB equation (SMPBE) relates the total charge density to the mean-field electrostatic potential. Commonly, such PDEs are solved via grid- or function-space-based numerical solution schemes like the finite difference method (FDM) or finite element method (FEM).[2–4] However, the all-electron framework of `FHI-aims` utilizing an irregular integration grid structure to optimally resolve the Coulomb singularity and wave-function cusps close to the nuclei renders such approaches in practice numerically inefficient. Therefore, we develop here a novel function-space-based approach utilizing multi-center multipole representations of the electrostatic potential. Such a multipole basis is particularly well suited for the solution of non-local Green's function integrals. We use this property by employing the Newton method to linearize the SMPBE and a multipole expansion relaxation method (MERM) to solve the resulting linearized PDE by iterative Green's function integrations of a screened Poisson equation (SPE). By this, we make optimal use of the already present multi-center multipole framework in `FHI-aims` which we show to give fast convergence of energies and forces with the order of the expansion.

As a coarse-grained effective model, the developed SMPB-density functional theory (DFT) scheme relies on a number of parameters defining the solute's interactions with the electrolyte. Solvent-specific parameters determing among others the dielectric function have been obtained already in previous studies for the case of molecular solutes in aqueous solutions by fitting to experimental hydration energies.[5,6] In this thesis, we focus on the ionic parameters for which coherent parametrization strategies are lacking so far. A so far rarely considered but valuable route to such parameters are experimentally measurable properties related to the ion effect on the solvation energy as mean activity[7] or Setschenow coefficients.[8] We use these quantities to assess the SMPB parameter space in the here considered case of monovalent aqueous salt solutions and detect the Stern layer thickness expressed in units of the solute's electron density as the crucial parameter to explain experimentally observed ion-specific effects. The efficiency of our Stern layer model is studied at the example of neutral molecules by optimizing the Stern layer thickness parameter to reproduce tabulated experimentally measured Setschenow coefficients. The resulting low root mean square errors as well as a physically meaningful scaling of the optimized Stern layer thicknesses with ionic hydration numbers[9] demonstrates the high

transferability of the parametrization strategy and motivates future studies on more complex electrolytic systems.

Zusammenfassung

Die *first-principles* Modellierung von chemischen Reaktionen in elektrolytischen Umgebungen stellt eine der zentralsten Herausforderungen der modernen Computerchemie dar. Von besonderer Bedeutung sind in diesem Zusammenhang implizite Kontinuum-Solvatationsmethoden, die heutzutage standardmäßig für rechnerisch effiziente Simulationen von solvatisierten Systemen eingesetzt werden. Ionische Ladungsverteilungen können des Weiteren oft akkurat durch sogenannte Poisson-Boltzmann (PB) Methoden beschrieben werden. In dieser Doktorarbeit wurde ein implizites Lösungsmittelmodell mit einem PB Ansatz kombiniert, der zusätzlich zu *mean-field* elektrostatischen auch nicht-elektrostatische ionen-spezifische Effekte berücksichtigt. Letzteres wird erreicht durch die Einführung einer finiten Ionengröße und eines ionen-freien Stern-Schicht Modells (SMPB Modell). Die komplette Methodik wurde in das hoch-parallelisierbare Allelektronen-Dichtefunktionaltheorie (DFT) Programmpaket `FHI-aims` implementiert, welches numerische atom-zentrierte (NAO) Orbitalbasisfunktionen verwendet.[1] Eine zentrale Hürde stellt dabei die Lösung der nicht-linearen partiellen Differentialgleichung (PDE), der SMPB Gleichung dar, welche die totale Ladungsdichte mit dem elektrostatischen *mean-field* Potential verknüpft. Üblicherweise werden solche PDEs über gitter- oder funktionenraumbasierte numerische Algorithmen wie Finite Differenzen oder Finite Elemente Methoden gelöst.[2–4] Für all-Elektronen-DFT Programme wie `FHI-aims` werden solche Methoden allerdings in der Anwendung ineffizient, da Erstere eine für Letztere ungeeignete irreguläre Integrationsgitterstruktur benutzen um die Coulomb Singularität und Wellenfunktionsspitze nahe der Atomkerne optimal aufzulösen. Aus diesem Grund entwickeln wir hier einen neuartigen Ansatz im Funktionenraum, der auf Multizentren-Multipol-Repräsentationen des elektrostatischen Potentials basiert. Die Benutzung einer solchen Basis ist speziell geeignet um nicht-lokale Green's Funktionenintegrale zu lösen. Unsere Methode benutzt diese Eigenschaft, indem sie erst die SMPB Gleichung linearisiert und anschließend die resultierende linearisierte PDE mit einer Multipol-Expansions-Relaxationsmethode (MERM) löst. Die MERM vollführt dabei iterative Integrationen über die Green's Funktion der gescreenten Poisson Gleichung. Dieser Ansatz ermöglicht eine optimale Nutzung der schon vorhandenen Multizentren-Multipol Infrastruktur in `FHI-aims`, für welche wir schnelle Konvergenz von Energien und Kräften mit der Ordnung der Expansion zeigen.

Wie jedes effektive Modell, welches sich aus einem *coarse-graining* physikalischer Wechselwirkungen herleitet, hängt auch die entwickelte SMPB-DFT Methode von einer Reihe an Parametern ab. Lösungsmittel-spezifische Parameter, die z.B. die dielektrische Funktion festlegen, wurden bereits im Voraus im Rahmen anderer Arbeiten für den Fall von Molekülen in wässrigen Lösungen durch einen Fit an experimentelle Hydratationsenergien bestimmt.[5,6] In dieser Doktorarbeit liegt deshalb ein spezifischer Fokus auf den übrigen ionischen Parametern, für die es bisher keine kohärenten Parametrisierungsstrategien gibt. Für eine Analyse des Parameterraumes nutzen wir den experimentell messbaren Ioneneffekt auf die Solvatisierungsenergie, der in der Literatur oft als mittlerer Aktivitätskoeffizient[7] oder Setschenow Koeffizient[8] tabelliert ist. Für den hier betrachteten Fall von monovalenten

wässrigen Salzlösungen können wir schließlich so den Parameterraum auf einen einzigen Stern-Schichtdicke Parameter einengen, der in Einheiten der Elektronendichte des gelösten Stoffes gemessen wird und die experimentell beobachteten ionen-spezifischen Effekte eindeutig erkärt. Die Effizienz eines solchen Ansatzes wird in dieser Arbeit am Beispiel von gelösten neutralen Molekülen untersucht, wobei der Stern-Schichtdicke Parameter optimiert wird, um experimentell gemessene Setschenow Koeffizienten zu reproduzieren. Die resultierenden niedrigen mittleren quadratischen Fehler zusammen mit der physikalisch sinnvollen Skalierung der optimierten Stern-Schichtdicken mit Hydratationszahlen der entsprechenden Ionen (*hydration numbers* [9]) unterstreichen die hohe Transferabilität der Parametrisierungsstrategie und motivieren zukünftige Studien an komplexeren elektroly-tischen Systemen.

Contents

Introduction

<div style="text-align: right; font-size: 3em;">**1**</div>

Most of the known chemical and biological processes in nature happen in electrolytic environments. Although the presence of solvent molecules and ions is known to often substantially alter thermodynamic stabilities and reaction rates, particularly ion effects remain largely elusive to quantitative understanding. Notwithstanding the technical and methodological advance in experimental and computer technologies over the last decades, the investigation of such systems remains a huge challenge and has still not succeeded to overcome the large prevailing knowledge gap.

From the theoretical modeling point of view, the largest difficulty arises thereby from the huge phase space inherent to liquid media. Even small solutes require a large number of solvent molecules to accurately describe their solvation environment. Being in the liquid phase each of the solvent molecules possesses a large degree of freedom to explore phase space. The resulting huge number of solvent configurations requires elaborate thermodynamic sampling to converge macroscopic properties of interest. In cases where more accurate theoretical methods like quantum-chemical electronic structure calculations are needed to describe the chemical system, this renders corresponding simulations computationally intractable. This becomes even more problematic when dissolved ions have to be accounted as well, as their low concentrations – generally at least one order of magnitude lower than the solvent molecules – require even longer simulations. A possible way to overcome this hurdle is the use of embedding techniques. These partition the system into a chemically active region treated with a high methodological accuracy e.g. by applying quantum mechanics (QM) techniques and a remaining background regime treated on a more coarse-grained level e.g. by the use of molecular mechanics (MM). Although such QM/MM techniques have been successfully applied in various contexts, [10–12] the appearing QM-MM interface often gives rise to conceptual or numerical problems. These comprise e.g. the definition of interactions or forces across the interface or the penetration of solvent molecules into the QM region. [10,11] Furthermore, even such elegant approaches do in general not provide a convergence of essential bulk properties like e.g. the dielectric solvent response which in the case of aqueous solutions often dominates the overall solvation effect. [5]

These major drawbacks of QM/MM approaches led to the rebirth of implicit solvation techniques approximating the solvent as a mere dielectric continuum. Such a rather harsh coarse-graining of the liquid phase requires a careful modeling of the dielectric function which uniquely defines the electrostatic solvation energy. Early studies of Born on the

dielectric embedding of ions thereby assumed a simple dielectric step function adopting the value of the isotropic, low-frequency limit bulk dielectric permittiviy in the solvent and the vacuum value of one inside the so called solvation cavity around the solute.[13] Nowadays, corresponding solvation cavities are commonly defined on the basis of structural information of the solute as obtained from e.g. density functional theory (DFT) or force field program packages.[5,14–18] Additionally, the inclusion of further parametrized non-mean-field correction terms has been shown to be crucial in order to account for e.g. cavity creation energies or dispersive solute-solvent interactions. Although implicit solvation schemes are by construction limited in the modeling of dynamic interactions, such as hydrogen bonds,[18] they have shown to often provide reasonably accurate estimates of the thermodynamic solvation effect while at the same time requiring low computational resources.[18,19] The additional recent advance of corresponding parametrization schemes has further made them become a standard tool for the modeling of chemical reactions in solvents, in particular in biology[20–22] and electrochemistry[23,24]

In contrast to the reasonably well studied nature of solute-solvent interactions, little is known so far about the influence of finite ionic strengths. Chemically, ions are often assumed to merely play the role of spectators. This view is supported by the fact that ion effects are in general around one order of magnitude smaller than e.g. hydration effects. In spite of this, the presence of ions was shown to crucially impact for example biological systems (cf. Fig. 1.1), leading to substantial modifications of chemical stabilities and thermodynamic equilibria[25] like e.g. acid dissociation[26] or protein denaturation.[27] Corresponding empirical observations already date back to the studies of Hofmeister who started to systematically order ions in the famous *Hofmeister series* according to their ability to induce certain ion-specific effects.[28] Although the Hofmeister series was intensively studied over the years, a general physical understanding is to a large extent still missing and it remains object of current research.[25] From a computational modeling perspective, difficulties arise mainly from the large computational expense of entirely explicit simulations, as biomolecules already typically consist of thousands of atoms.

Fortunately, the dominating ion effects can in many cases be traced back to a simple electrostatic screening of solute charges. This allows to also coarse-grain the ionic charge distributions and the related interactions with the solute. Systematic investigations in this direction were already performed over a century ago in the context of electrochemistry (cf. Fig. 1.1) where ions were found to form the electric double layer. The sum of diffusive ions and rigid ions in the double layer efficiently screens electrode charges and establishes a constant electrochemical potential at the electrode surface. Related early studies led to the development of diffusive ion models such as the Poisson-Boltzmann (PB) (or Debye-Hückel (DH)/Gouy-Chapman (GC)[32–35]) theory approximating the ions as ideal point charges interacting only via a mean-field electrostatic potential. Despite its conceptual and mathematical simplicity, PB theory has experienced a long history of success[36–39,39–47] and has until today been applied in various areas of science such as chemistry,[48] (electro)catalysis,[49–51] electrochemistry,[52–54] electrokinetics[55,56] and biology.[36,37,45,47,57–63] Notwithstanding this enormous success, the intensive application of PB theory also revealed substantial limitations of the original approach in particular in cases of high ionic charge densities as emerging close to large electrostatic potentials,[60,64–72] higher-valent ions[73] or large ion sizes. In order to extend the validity to these particular
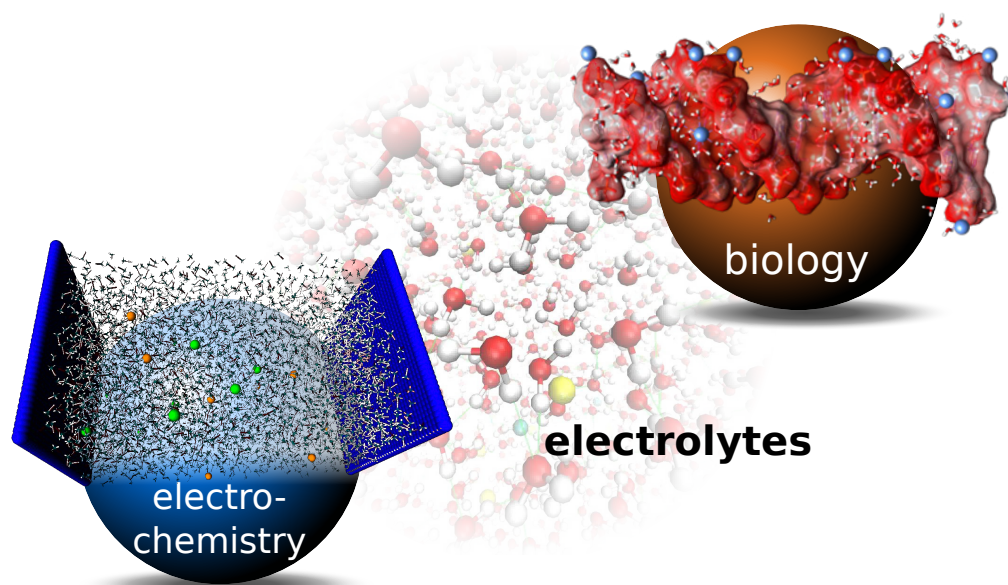
Figure 1.1.: Schematic representations for two of the most important research areas in which electrolytes play a major role: In biology, the presence of ions and solvents critically influences e.g. protein conformer stabilities, protein denaturation abilities or enzyme activities. Shown in the inset is DNA and some surrounding ions and water molecules.[29] In electrochemistry and -catalysis ions are not only supplying charge transfer between the electrodes, but the electric double layer also determines the electrode potential.[30] The image in the center shows a molecular dynamics snapshot from a NaCl aquous solution.[31]

situations, a number of modifications were proposed such as the inclusion of a Stern layer,[74] ion-correlation effects[73,75–77] or finite ionic size corrections.[60,64–71] In the scope of this thesis, we will be exclusively concerned with monovalent ions for which ion-correlation effects at moderate ionic strenghts can commonly be safely ignored.[73] Besides the already mentioned finite-size modification of the ions the treatment of such salt solutions furthermore requires the consideration of a Stern layer which is typically viewed as an ion-free region consisting of the solute's solvation layer and the rigid solvation shells of the ions. Considering both these modifications leads to the finite size and Stern layer modified PB (SMPB) theory which has been recently applied in different contexts.[23,24,60,72,78]

The wide success of implicit solvation and PB methods in various areas of science motivates to combine both approaches in a methodological framework for a full modeling of electrolyte effects. Although corresponding implementations have recently been reported in DFT[23,24,79–83] or force field (FF)[58,60,63,84,85] program packages, an important bottleneck remains the parametrization of the underlying coarse-grained physical interactions. While the parametrization of ion-free implicit solvation models is already a complex issue of current research, there exist to date no comparable strategies for the ionic part of such methods. Moreover, the assumption of a complete decoupling of ionic and solvent parametrizations might not be valid in cases where the solvent structure is substantially influenced by the

presence of the ions. In this thesis, we will, however, show that there exists also a wide range of systems where both effects at least partly decouple, thus allowing the development of separate transferable parametrization schemes for solvent and ion induced interactions.
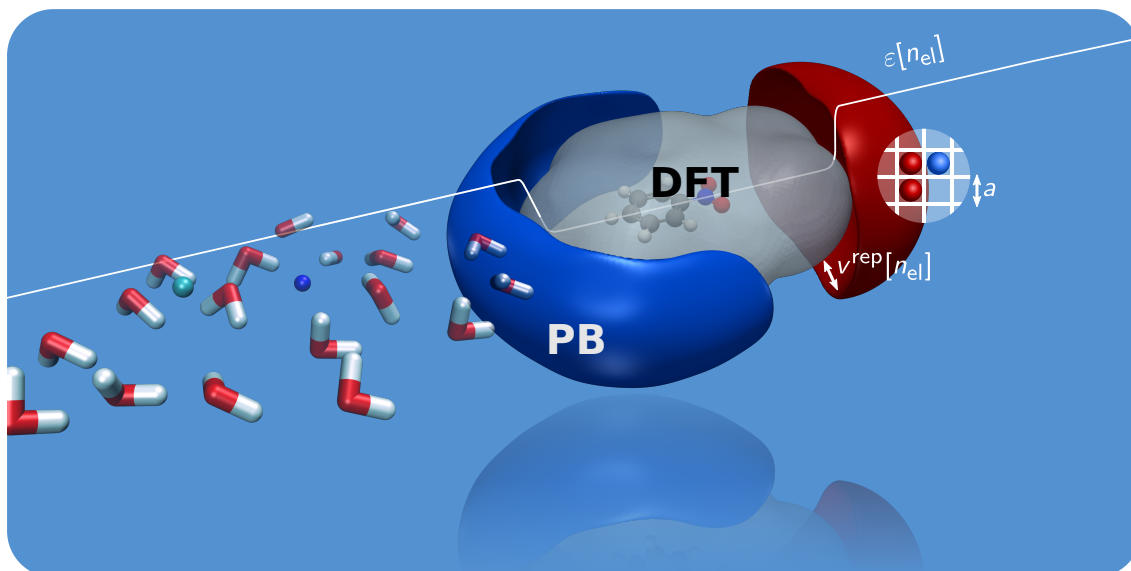
Figure 1.2.: Our SMPB-DFT scheme coarse-grains the electrolyte by replacing the solvent with a dielectric continuum as well as the ions with continuous charge distributions (illustrated by the arbitrarily chosen blue and red contour planes). The solute of choice (here nitrobenzene) is thereby embedded into a solvation cavity which is defined by the transition of a dielectric function from its solvent bulk value to one (shown schematically as white line) parametrized in terms of the solute's electron density n_{el}. Ions are on the other hand modeled by introducing a statistical lattice model leading to the appearance of an ionic size parameter a. Solute and ions furthermore interact via a repulsive potential v^{rep} which is also expressed in terms of n_{el}. Reproduced in part with permission from ref. [86]. © 2016 American Chemical Society.

Combinations with DFT program packages are especially useful in the context of electrocatalytical applications[23,24] where a quantum-mechanical treatment of electrons is generally unavoidable. In the context of electrochemistry, the modeling of electrodes and catalysts often requires the modeling of extended surface slabs. This is normally done using solid-state specialized DFT program packages, such as `VASP`[87–90] or `CASTEP`[91] which utilize plane-wave basis sets to expand the Kohn-Sham (KS) orbitals and replace the explicit core electron density by effective pseudo-potentials.[92–95] Necessary integrations are commonly carried out on regular integration grids which are optimally suited to resolve the smooth periodic functions. Such a grid architecture also simplifies the solution of partial differential equations (PDEs) like the Poisson equation by applying advanced finite difference method (FDM) schemes. Similar strategies can be utilized to solve the PB equation (PBE) which yields the electrostatic potential of the combined solute-electrolyte system. Unfortunately, such combined PB-DFT schemes are to date not publicly available and there has been furthermore no attempt to implement such schemes into potentially more accurate all-electron localized basis functions DFT program packages like `FHI-aims` (Fritz Haber Institute *ab-initio* molecular simulations).[1,96] One reason for that is the

commonly irregular integration grid structure inherent to such programs which optimally resolves the wave-function cusp and Coulomb singularity at the atomic centers but complicates the direct application of grid-based solution schemes for the PB-equation. On the other hand, the usage of `FHI-aims` is particularly appealing, since it not only provides an explicit description of core electrons but also a wide range of advanced methodological features like explicitly-correlated exchange-correlation (xc)-functionals and excited states related implementations (Møller-Plesset perturbation theory of 2nd order (MP2), random phase approximation (RPA), GW, ...),[96] many-body dispersion (MBD)[97,98] and van der Waals corrections,[99] density functional perturbation theory (DFPT)[100] or a solid-state QM/MM embedding infrastructure.[101] This extended functionality has proven to be particularly suited for the modeling of catalytic materials,[12,102–104] while the full-potential character and excellent scalability with system size and number of central processing units (CPUs)[1] favors the application to larger biological systems.[105–108] The wide applicability of `FHI-aims` on the same footing for both biological as electrochemical applications motivated us to implement a PB implicit solvation scheme in order to arrive at a powerful framework for the modeling of chemical reactions in electrolytes (cf. Fig. 1.2).

This thesis is structured as follows. In Chapter 2 we first shortly introduce into the basics of electrostatics as pertaining to the foundations of implicit solvation models, followed by a concise summary of the principles of quantum chemistry and DFT. Subsequently we present a full derivation of the SMPB implicit solvation theory utilizing statistical thermodynamics and path integral formulations.

Following this merely theoretical preface, Chapter 3 then focuses on methodological issues and begins by deriving the necessary modifications of standard DFT needed for the implementation of the SMPB scheme. After having derived the full SMPB-DFT formalism, we then give an introduction into the peculiarities of `FHI-aims` as an all-electron DFT program package. The following central part of this chapter then deals with the solution of the SMPB-equation in `FHI-aims`, for which we developed an efficient function-space oriented Newton scheme coupled with a self-consistent solver of the resulting linearized PDE utilizing a multipole expansion relaxation method (MERM). Finally, we derive modified atomic force expressions to enable dynamic modeling within the SMPB-DFT approach.

As already mentioned before, deriving transferable parameters is essential for the application of effective methods like implicit solvation or PB schemes. Chapter 4 therefore expands on this issue by first adopting the parametrization of the implicit solvation model for water as a solvent as performed by Andreussi *et al.*[5] in order to validate the numerical efficiency of the implementation. In the second part, we then explicitly study the ionic part of the parameters and perform an extensive analysis and assessment of the PB parameter space by comparing to experimental observables like activity[7] and Setschenow coefficients.[8,109] By fitting to experimental training sets, we then arrive at transferable parametrizations for the particular case of neutral molecules in monovalent salt solutions.

2

Theoretical Background

2.1. Charge Distributions in Dielectric Media: Implicit Solvation

2.1.1. Polarization

If a static electric field $\boldsymbol{E}$ acts on a polarizable dielectric medium, a corresponding displacement field $\boldsymbol{D}$ will be created in the dielectric acting contrary to the perturbation:

$$\boldsymbol{D} = \boldsymbol{E} + \boldsymbol{P} - \frac{1}{2}\nabla \boldsymbol{Q} + ... \quad . \tag{2.1}$$

Here, $\boldsymbol{P}$ is the polarization or dipole moment density and $\boldsymbol{Q}$ the tensor of the quadrupole moment density (cf. ref. [110]) of the dielectric medium. Throughout this thesis atomic units will be used if not mentioned otherwise. Commonly, the expansion in Eq. (2.1) is truncated already after the second term.[110] The polarization density $\boldsymbol{P}$ can be expressed as the sum over all microscopic dipole moments $\boldsymbol{p}_j$ per volume unit V of the dielectric material

$$\boldsymbol{P} = \frac{\sum\limits_{j} \boldsymbol{p}_j}{V} \quad . \tag{2.2}$$

In order to circumvent an explicit calculation of the microscopic dipole moments, the polarization density can be Taylor expanded in the electric field:

$$P_\alpha = \sum_\beta \chi^{(1)}_{\alpha\beta} E_\beta + \sum_{\beta\gamma} \chi^{(2)}_{\alpha\beta\gamma} E_\beta E_\gamma + \sum_{\beta\gamma\delta} \chi^{(3)}_{\alpha\beta\gamma\delta} E_\beta E_\gamma E_\delta + ... \quad , \tag{2.3}$$

with the expansion coefficients being the n-th order susceptibilities tensors $\chi^{(n)}$ which are a measure of the polarization of a material in response to the electric field. In isotropic materials, these tensors can be diagonalized with the respective eigenvalues being degenerate. The polarization density is consequently parallel to the electric field simplifying the equation to:

$$\boldsymbol{P} = \chi^{(1)}\boldsymbol{E} + \chi^{(2)}\boldsymbol{E}^2 + \chi^{(3)}\boldsymbol{E}^3 + ... \tag{2.4}$$

In the case of a linear response of the dielectric medium, Eq. (2.4) can be truncated after the first term to yield

$$\boldsymbol{P} = \chi^{(1)}\boldsymbol{E} = (\varepsilon - 1)\,\boldsymbol{E} \quad , \tag{2.5}$$

and therefore also

$$D = E + P = \varepsilon E \quad , \tag{2.6}$$

where we replaced the susceptibilities with the more frequently used dielectric permittivity ε. Correspondingly, also the microscopic dipole moments are in the linear response regime linearly related to the electric field by the static dipole polarizability tensor $\boldsymbol{\alpha}_{0,j}$

$$\boldsymbol{p}_j = \boldsymbol{\alpha}_{0,j} \boldsymbol{E} \quad . \tag{2.7}$$

Further, for isotropic materials, one can then as before replace the tensor $\boldsymbol{\alpha}_{0,j}$ with a scalar, the static isotropic dipole polarizability $\alpha_{0,j}^{\text{iso}}$.

Eqs. (2.5) to (2.7) are valid for linear, isotropic dielectric media under the assumption of static electric fields. In the case of time-dependent perturbations, one instead has to consider the complex frequency dependent dielectric permittivity $\varepsilon(\omega)$ which yields the static permittivity in the low-frequency limit $\varepsilon = \lim_{\omega \to 0} \varepsilon(\omega)$. The real part is shown exemplarily in Fig. 2.1 for water indicating that at low electric field frequencies the molecular dipole polarization of water is dominating the overall dielectric response. Changes of the temperature can further influence the clustering of molecular dipoles and therefore lead to changes of the dielectric permittivity.
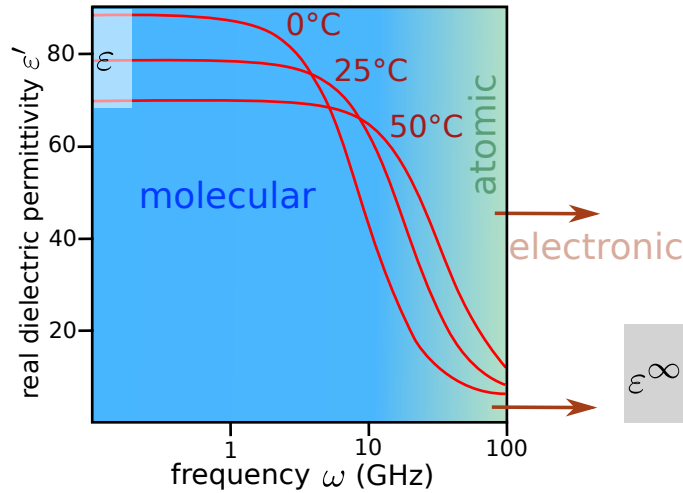
Figure 2.1.: Measured real part of the dielectric permittivity spectrum of water at different temperatures. The figure was modified from Fig. 3 in ref. [111] by schematically indicating the different dominating dielectric response regimes, i.e. molecular, atomic and electronic.

2.1.2. Electric Field

We consider now a charge distribution n_{sol} as source of the above considered electric perturbation field which is then defined according to the first Maxwell equation (Gauss's law) as

$$\nabla E(r) = 4\pi n_{\text{sol}}(r) \quad . \tag{2.8}$$

In terms of implicit solvation methods, $n_{\text{sol}}(r)$ denotes the solute's charge density which is attempted to be embedded into a liquid. In order to coarse-grain such system, one can

formally integrate out the solvent degrees of freedom. This naturally leads to a separation of space into regions, one with explicitly treated solute charges ($\varepsilon = 1$) and another with continuum dielectric response ($\varepsilon = \varepsilon^{\mathrm{s,bulk}}$), as illustrated in Fig. 2.2. $\varepsilon^{\mathrm{s,bulk}}$ is thereby in most implicit solvation methods taken as the low-frequency limit, isotropic dielectric permittiviy of the bulk solvent assuming that the dielectric tensor can be diagonalized with all eigenvalues being roughly the same.[18] The dielectric transition region is called the solvation cavity and sensitively defines the overall solvation effect. The parametrization of the now spatially dependent dielectric function $\varepsilon(\boldsymbol{r})$ by utilizing known solute properties is at the heart of implicit solvation techniques. We here postpone a detailed discussion to Section 3.2.2 where we present a functional form utilizing the solute's electron density as descriptor.
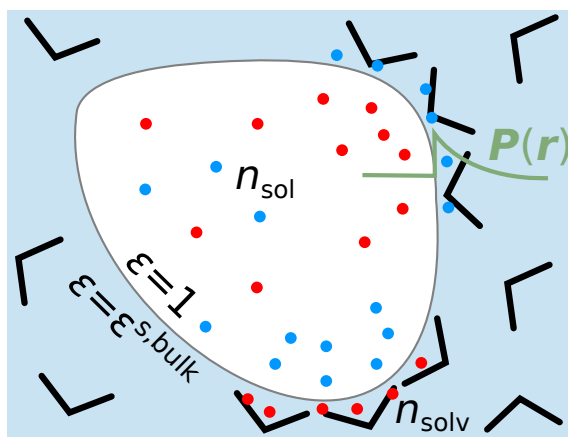
Figure 2.2.: Schematic representation of the implicit solvation model approach. A charge distribution n_{sol} is embedded into a dielectric continuum with a certain static dielectric permittivity $\varepsilon^{\mathrm{s,bulk}}$. The solvent molecules (in this case water) react to the electric field created by the fixed charge distribution by orienting around highly charged regions. This creates a divergence in the polarization density which can be related to an effective charge density n_{solv}. The sum of the two charge densities creates a new electric field according to Gauss's law (cf. Eq. (2.10)).

Solvent molecules are often polar molecules which orient according to the electric field of the solute and thereby screen the solute's charges. The increased density of oriented molecules closer to the charge distribution induces a divergence in the polarization density (cf. Fig. 2.2) which can by using Gauss's law be associated to a charge density n_{solv}:

$$\nabla \boldsymbol{P}(\boldsymbol{r}) = -4\pi n_{\mathrm{solv}}(\boldsymbol{r}) \quad . \tag{2.9}$$

The overall charge density that enters the right hand side of Eq. (2.8) is therefore now the sum of the solute charge density and the effective charge density of the solvent, giving

$$\nabla \boldsymbol{E}(\boldsymbol{r}) = 4\pi n_{\mathrm{sol}}(\boldsymbol{r}) + \underbrace{4\pi n_{\mathrm{solv}}(\boldsymbol{r})}_{-\nabla \boldsymbol{P}(\boldsymbol{r})}$$

$$\Leftrightarrow \quad \nabla \boldsymbol{D}(\boldsymbol{r}) = \nabla \left[\varepsilon(\boldsymbol{r}) \boldsymbol{E}(\boldsymbol{r}) \right] = 4\pi n_{\mathrm{sol}}(\boldsymbol{r}) \quad , \tag{2.10}$$

where we used Eq. (2.6) to introduce the displacement field and the spatially dependent dielectric function $\varepsilon(\boldsymbol{r})$. We now introduce the electrostatic potential v by using $\boldsymbol{E} = -\nabla v$

and obtain a partial differential equation (PDE), the generalized Poisson equation (GPE) for a charge distribution in a dielectric medium

$$\nabla \cdot [\varepsilon(\boldsymbol{r})\nabla v] = -4\pi n_{\text{sol}} \quad . \tag{2.11}$$

From here onwards we drop the $\boldsymbol{r}$-dependencies of all but the dielectric function, for an increased legibility.

2.1.3. Electrostatic Energy

In the last section, we have derived the generalized Poisson equation which defines the electrostatic potential of a charge distribution n_{sol} as embedded into a dielectric medium. Of more interest in the application of implicit solvent methods are, however, integrated properties like free energies which can be more easily compared to experimental measurements. The assembly of a charge distribution n_{sol} in the dielectric medium gives for instance rise to an electrostatic energy cost which is defined by both the charge density and the electrostatic potential. To derive a corresponding expression, we start by searching for an energy functional of v which is constructed in such a way that the electrostatic potential at its minimum v_{o} fulfills exactly the generalized Poisson equation Eq. (2.11). Such a functional can be then in principle also used in variational functional minimization techniques to determine the electrostatic potential instead of directly solving the generalized Poisson equation.

We start by writing down the self-energy of an electric field $\boldsymbol{E} = -\nabla v$ in a dielectric medium described by the dielectric function $\varepsilon(\boldsymbol{r})$:

$$E^{\text{elstat}}[v] = \frac{1}{8\pi} \int \mathrm{d}\boldsymbol{r}\varepsilon(\boldsymbol{r})|\nabla v|^2 \quad . \tag{2.12}$$

We aim to minimize this functional with respect to v, i.e. find the roots of the functional derivative with respect to v. In general, for functionals of the form

$$\mathcal{F}[\rho] = \int \mathrm{d}\boldsymbol{r}g\left(\boldsymbol{r}, \rho(\boldsymbol{r}), \nabla\rho(\boldsymbol{r})\right) \tag{2.13}$$

the functional derivative with respect to a function ρ is given by

$$\frac{\delta \mathcal{F}}{\delta \rho} = \frac{\delta}{\delta \rho}\left[\int \mathrm{d}\boldsymbol{r}g[\rho, \nabla\rho]\right] = \left[\frac{\partial g}{\partial \rho} - \nabla \cdot \frac{\partial g}{\partial(\nabla\rho)}\right] \quad . \tag{2.14}$$

In the case of Eq. (2.12) we can then associate ρ with v and obtain

$$\frac{\delta E^{\text{elstat}}}{\delta v} = -\frac{1}{4\pi}\nabla\left[\varepsilon(\boldsymbol{r})\nabla v\right] = 0 \quad , \tag{2.15}$$

which is the homogeneous generalized Poisson equation or generalized Laplace equation. In order to also account for the presence of a finite solute's charge density to arrive instead

at Eq. (2.11), we can modify this functional by adding the generalized Poisson equation as a constraint using a Lagrange multiplier function λ:

$$
\begin{aligned}
E^{\text{elstat}}[v] &= \frac{1}{8\pi} \int \mathrm{d}\boldsymbol{r} \left\{ \varepsilon(\boldsymbol{r})|\nabla v|^2 + \lambda \left(\frac{1}{4\pi} \nabla \cdot [\varepsilon(\boldsymbol{r})\nabla v] + n_{\text{sol}} \right) \right\} \\
&= \frac{1}{8\pi} \int \mathrm{d}\boldsymbol{r}\varepsilon(\boldsymbol{r}) \left(|\nabla v|^2 - 2(\nabla v)(\nabla \lambda) \right) + \frac{1}{4\pi} \oint \mathrm{d}A \left[\varepsilon(\boldsymbol{r})\nabla v \right] \lambda + \int \mathrm{d}\boldsymbol{r}n_{\text{sol}}\lambda \quad,
\end{aligned}
$$
$$(2.16)$$

where we in the second step used the product rule and furthermore $\int \mathrm{d}\boldsymbol{r}\nabla f(\boldsymbol{r}) = \oint \mathrm{d}Af(\boldsymbol{r})$ where $\oint$ denotes an integral over the boundary surface. By comparing Eq. (2.16) to Eq. (2.12), we can easily see that choosing the Lagrange multiplier as $\lambda = v$ leads to a functional

$$
E^{\text{elstat}}[v] = \int \mathrm{d}\boldsymbol{r} \left\{ -\frac{1}{8\pi}\varepsilon(\boldsymbol{r})|\nabla v|^2 + n_{\text{sol}}v \right\} \quad,
$$
$$(2.17)$$

which minimizes as desired to the generalized Poisson equation. The surface integral in Eq. (2.16) thereby vanishes for the here considered Dirichlet boundary condition $v \to 0$ for $|\boldsymbol{r}| \to \infty$ which we will consistently apply throughout the thesis.

With Eq. (2.17), we have arrived at a proper energy functional which at its minimum equals the electrostatic energy of charge distributions embedded into dielectric media. Inserting the generalized Poisson equation Eq. (2.11) into Eq. (2.17), then finally yields the well-known expression for the electrostatic energy

$$
E^{\text{elstat}}_{\circ} = \frac{1}{2} \int \mathrm{d}\boldsymbol{r}n_{\text{sol}}v_{\circ} \quad,
$$
$$(2.18)$$

where we introduced the subscript "$\circ$" to indicate that this expression resembles the minimum of a functional.

2.2. Quantum Chemistry

So far, we have derived all necessary equations to describe classical charge distributions embedded into dielectric media. To calculate the energy of such a system via Eq. (2.18) one, however, requires knowledge about the actual charge distribution which then defines the electrostatic potential v via the generalized Poisson equation. In this thesis, we are interested in the modeling of chemical systems for which a wide range of computational techniques provide different levels of approximations to the corresponding charge densities. Such approaches range from highly coarse-grained bead-models in biology in which functional groups are considered as single particles up to highly accurate quantum-mechanical theories catching most of the correlated interactions between the charge assembly of atomic nuclei and electrons. In this thesis, we concentrate on density functional theory (density functional theory (DFT)) because it offers for most chemical systems of interest a good compromise between accuracy and computational speed. As in all electronic structure theories, the solute charge density is thereby expressed as a sum of electronic n_{el} and nuclear contributions n_{nuc}

$$
n_{\text{sol}} = n_{\text{el}} - \sum_{\text{at}}^{N_{\text{at}}} Z_{\text{at}}\delta(\boldsymbol{r} - \boldsymbol{R}_{\text{at}}) = n_{\text{el}} + n_{\text{nuc}}(\boldsymbol{r} - \boldsymbol{R}_{\text{at}}) \quad,
$$
$$(2.19)$$

where Z_{at}, $\boldsymbol{R}_{at}$ and N_{at} are the nuclear charges, positions and the total number, respectively. Note that in agreement with the common convention in DFT, we will adapt the positive sign convention for the electronic charge density.

2.2.1. Schrödinger Equation

A system consisting of electrons and nuclei is generally described by the Hamiltonian $\hat{H}$ given as

$$\hat{H} = \hat{H}_{el}(\{\boldsymbol{r}\}, \{\boldsymbol{R}\}) + \hat{T}_n(\{\boldsymbol{R}\})$$
$$\hat{H}_{el} = \hat{T}_{el} + \hat{V}_{ee} + \hat{V}_{en} + \hat{V}_{nn} \quad , \tag{2.20}$$

where $\hat{H}_{el}$ is the electronic Hamiltonian and $\hat{T}_{el}$ and $\hat{T}_n$ denote the kinetic energies of the electrons and nuclei, respectively. The potential energy operators $\hat{V}_{ee}$, $\hat{V}_{en}$ and $\hat{V}_{nn}$ cover the electron-electron, electron-nuclei and nuclei-nuclei interactions, respectively. The electron coordinates are thereby given as $\{\boldsymbol{r}\} = \{\boldsymbol{r_1}, ..., \boldsymbol{r_i}, ..., \boldsymbol{r_{N_e}}\}$, with the total number of electrons N_e, while the nuclear coordinates are expressed as $\{\boldsymbol{R}\} = \{\boldsymbol{R}_1, ..., \boldsymbol{R}_{at}, ..., \boldsymbol{R}_{N_{at}}\}$.

The Hamiltonian in Eq. (2.20) can be utilized in a fully quantum mechanical treatment of protons and electrons described by the time-dependent many-particle wave function Φ and the system state then evolves according to the time-dependent Schrödinger equation (TD-SE)

$$i\hbar\frac{\partial\Phi(\{\boldsymbol{r}\}, \{\boldsymbol{R}\}, t)}{\partial t} = \hat{H}(\{\boldsymbol{r}\}, \{\boldsymbol{R}\})\Phi(\{\boldsymbol{r}\}, \{\boldsymbol{R}\}, t) \quad . \tag{2.21}$$

2.2.2. Born-Oppenheimer Approximation

The solution of the Schrödinger equation (SE) can in many cases be simplified by separating the fast electronic motion from the much slower nuclear motion. Electrons are thereby assumed to adjust instantaneously to the motion of the nuclei and can for each nuclear arrangement be found in an electronic state $E_i(\{\boldsymbol{R}\})$ (Born-Oppenheimer approximation (BOA)). The BOA is one of the most important approximations in quantum chemistry because it allows the simulation of a broad range of complex systems. Exceptions are so called nonadiabatic processes which can be observed e.g. in the dynamics of molecules at metal surfaces.

The electronic states $E_i(\{\boldsymbol{R}\})$ define an energy landscape in the space of nuclear coordinates commonly referred to as potential energy surface (PES). The often also called Born-Oppenheimer (BO) or adiabatic states $E_i(\{\boldsymbol{R}\})$ are defined as eigenvalues of the electronic Hamiltonian with the corresponding time-independent electronic SE given by

$$\hat{H}_{el}(\{\boldsymbol{r}\}, \{\boldsymbol{R}\})\Psi_i(\{\boldsymbol{r}\}, \{\boldsymbol{R}\}) = E_i(\{\boldsymbol{R}\})\Psi_i(\{\boldsymbol{r}\}, \{\boldsymbol{R}\}) \quad , \tag{2.22}$$

We can expand the wave function $\Phi(\{\boldsymbol{r}\}, \{\boldsymbol{R}\}, t)$ in terms of these states with the expansion coefficients $\Xi_i(\{\boldsymbol{R}\}, t)$ then depending on the nuclear coordinates and the time (due to the kinetic energy operator of the nuclei):

$$\Phi(\{\boldsymbol{r}\}, \{\boldsymbol{R}\}, t) = \sum_i \Xi_i(\{\boldsymbol{R}\}, t)\Psi_i(\{\boldsymbol{r}\}, \{\boldsymbol{R}\}) \tag{2.23}$$

If the coupling between nuclear and electronic motion is large, $\Phi(\{\boldsymbol{r}\}, \{\boldsymbol{R}\}, t)$ is given at each time by a combination of several BO wave functions $\Psi_i(\{\boldsymbol{r}\}, \{\boldsymbol{R}\})$ (nonadiabatic regime) and one has to perform computationally expensive quantum dynamics or combined quantum-classical techniques (surface hopping, Ehrenfest dynamics,...) to evolve the system's coordinates. On the other hand, if the coupling is small, the nuclear motion evolves on a PES built up by a single BO wave function $\Psi_i(\{\boldsymbol{r}\}, \{\boldsymbol{R}\})$ or adiabatic state (adiabatic dynamics or standard molecular dynamics). In this case the time-independent SE Eq. (2.22) is enough to describe the system at a specific nuclear arrangement and the time evolution in the nuclear coordinates can be performed classically. Fortunately, for most chemical systems as also in this thesis, one generally finds nuclear motion to evolve classically on the ground state PES $E_\circ(\{\boldsymbol{R}\})$.

2.2.3. Density Functional Theory

2.2.3.1. Hohenberg-Kohn Theorem

Although the BOA allows for many systems to decouple electronic and nuclear motion and therefore to solve the SE only for a specific nuclear arrangement (we will therefore from now on drop the dependency of Ψ on the nuclear positions for better readability), the many-particle wave function

$$\Psi(\{\boldsymbol{r}_1, \ldots, \boldsymbol{r}_{N_\mathrm{e}}\}, \{\sigma_1, \ldots, \sigma_{N_\mathrm{e}}\}) \tag{2.24}$$

is still of a high dimensionality of $3N_\mathrm{e}$ spatial and N_e spin coordinates $\{\sigma_i = \pm\frac{1}{2}\}$. The strength of DFT now arises from the *Hohenberg-Kohn* theorem which states that the three-dimensional electron density

$$n_\mathrm{el}(\boldsymbol{r}) = N_\mathrm{e} \sum_{\sigma_1} \cdots \sum_{\sigma_{N_\mathrm{e}}} \int \mathrm{d}\boldsymbol{r}_2 \int \mathrm{d}\boldsymbol{r}_3 \cdots \int \mathrm{d}\boldsymbol{r}_{N_\mathrm{e}} |\Psi|^2 \tag{2.25}$$

already contains all necessary information required for an exact ground state theory. More precisely, one can show, that the electron density n_el uniquely defines the nuclear positions and in consequence also the nuclear potential V_en, more generally denoted as external potential V^ext. For a fixed number of electrons, this potential, however, resembles the only system-dependent contribution to the electronic Hamiltonian in Eq. (2.20), while all other parts can be readily written as unique functionals of n_el. In consequence, one can then with the knowledge of V^ext define a SE which unique solution is given by the ground state wave function Ψ. In sum, there exists therefore a unique map from n_el to $\Psi[n_\mathrm{el}]$, i.e. $\Psi[n_\mathrm{el}]$ is a unique functional of the electron density. This also implies that we can write the energy expectation value as a functional of the electron density:

$$
\begin{aligned}
E[n_\mathrm{el}] &= \langle \Psi[n_\mathrm{el}] | \hat{H}_\mathrm{el} | \Psi[n_\mathrm{el}] \rangle \\
&= \langle \Psi[n_\mathrm{el}] | \hat{T}_\mathrm{el} + \hat{V}_\mathrm{ee} | \Psi[n_\mathrm{el}] \rangle + \underbrace{\int \mathrm{d}\boldsymbol{r}\, \hat{V}^\mathrm{ext} n_\mathrm{el} + V_\mathrm{nn}}_{V^\mathrm{ext}[n_\mathrm{el}]} \quad .
\end{aligned} \tag{2.26}
$$

The Hohenberg-Kohn theorem also states that for any specific external potential V^ext the ground state is a global minimum of this functional minimized by the ground state electron

density $n_{\mathrm{el,o}}$. Thus, the ground state energy is obtained by functional minimization with respect to n_{el}:

$$E_{\mathrm{o}} = \min_{n_{\mathrm{el}}} E[n_{\mathrm{el}}] \quad . \tag{2.27}$$

This variational principle provides the basis of using energy minimization techniques to determine the ground state in DFT calculations based on Eq. (2.26).

2.2.3.2. Kohn-Sham Equation

Although the Hohenberg-Kohn theorem states the existence of a unique map of the electron density to the many-body wave function $\Psi[n_{\mathrm{el}}]$, the exact analytical expression performing this map is unknown. This necessitates to approximate this relation e.g. by turning off all inter-electronic interactions. For such a reference system of non-interacting electrons, we then write the Hamiltonian of the system as $\hat{H} = \hat{T}^{\mathrm{S}} + \hat{V}^{\mathrm{S}}$, where $\hat{T}^{\mathrm{S}}$ is the kinetic energy and $\hat{V}^{\mathrm{S}}$ an effective potential. Since the potential $\hat{V}^{\mathrm{S}}$ uniquely determines the electronic ground state, we can also choose it in such a way that the ground state electron density of the system of non-interacting electrons coincides with that of the many-body system. The goal has therefore switched from finding a map between Ψ and n_{el} to the determination of an effective potential contributing to the operator $\hat{V}^{\mathrm{S}}$ which gives us the same ground state as in the many-body system.

Starting from Eq. (2.26), the energy functional of the system can then be written as:

$$E^{\mathrm{KS}}[v, n_{\mathrm{el}}] = T^{\mathrm{S}}[n_{\mathrm{el}}] + V^{\mathrm{S}}[v, n_{\mathrm{el}}] \quad , \tag{2.28}$$

where we introduced a dependency on the still to be determined electrostatic potential $v = v_{\mathrm{es}} + v_{\mathrm{nuc}}$ with the electronic Hartree potential v_{es} and the known nuclear potential $v_{\mathrm{nuc}} = -\sum_{\mathrm{at}} \frac{Z_{\mathrm{at}}}{|\boldsymbol{r} - \boldsymbol{R}_{\mathrm{at}}|}$. The electron density is given by a simple sum over single-electron orbitals ψ_l

$$n_{\mathrm{el}} = \sum_{l=1}^{N_{\mathrm{states}}} |\psi_l|^2 \quad , \tag{2.29}$$

with the ψ_l being the single-electron wave-function and N_{states} the corresponding total number of such states . Eq. (2.29) results from the fact that the many-electron wave-function in the case of non-interacting electrons is given by a Slater determinant of single-electron wave-functions ψ_l. The kinetic energy functional in Eq. (2.28) is therefore given by

$$T^{\mathrm{S}}[n_{\mathrm{el}}] = \langle \Psi[n_{\mathrm{el}}] | \hat{T}^{\mathrm{S}} | \Psi[n_{\mathrm{el}}] \rangle = \sum_{l=1}^{N_{\mathrm{states}}} \langle \psi_l | \hat{t}^{\mathrm{S}} | \psi_l \rangle \quad . \tag{2.30}$$

The effective potential energy functional is expressed in terms of the electrostatic energy functional as given in Eq. (2.17) (with $\varepsilon = 1$):

$$V^{\mathrm{S}}[v, n_{\mathrm{el}}] = E^{\mathrm{elstat}}[v, n_{\mathrm{el}}] + E^{\mathrm{xc}}[n_{\mathrm{el}}] = \int \mathrm{d}\boldsymbol{r} \left\{ -\frac{1}{8\pi} |\nabla v|^2 + n_{\mathrm{el}} v + n_{\mathrm{nuc}} v \right\} + E^{\mathrm{xc}}[n_{\mathrm{el}}] \quad , \tag{2.31}$$

where the exchange-correlation (xc) energy E^{xc} contains all non-mean-field electron-electron interactions as well as kinetic energy corrections.

Minimization of the Kohn-Sham (KS) functional Eq. (2.28) with respect to the electrostatic potential v leads to the Poisson equation in vacuum (cf. Section 2.1.3). In order to also find the minimum in the direction of the electron density, we additionally ensure the orthonormalization of the single-electron wave functions by constructing a Lagrangian functional

$$\mathcal{L}[v, n_{\mathrm{el}}] = E^{\mathrm{KS}}[v, n_{\mathrm{el}}] + \sum_{l=1}^{N_{\mathrm{states}}} \sum_{k=1}^{N_{\mathrm{states}}} \lambda_{lk} \left[\int \mathrm{d}\boldsymbol{r}\, \psi_l^* \psi_k - \delta_{lk} \right] \quad , \tag{2.32}$$

with δ_{lk} being the Kronecker delta. We then minimize this functional with respect to the single-electron orbitals

$$\frac{\delta \mathcal{L}[n_{\mathrm{el}}, v]}{\delta \psi_l^*} = 0 \; \forall l, \tag{2.33}$$

and by again applying Eq. (2.14) to evaluate the functional derivatives, we get:

$$\sum_k \lambda_{lk} \psi_k = \frac{\delta \mathcal{L}}{\delta \psi_l^*} = \underbrace{\frac{\delta T^{\mathrm{S}}[n_{\mathrm{el}}]}{\delta \psi_l^*}}_{\hat{t}^{\mathrm{s}} = -\frac{1}{2}\nabla^2 \psi_l} + \underbrace{\frac{\delta V^{\mathrm{S}}[v, n_{\mathrm{el}}]}{\delta n_{\mathrm{el}}}}_{v^{\mathrm{s}}} \underbrace{\frac{\mathrm{d}n_{\mathrm{el}}}{\mathrm{d}\psi_l^*}}_{\psi_l} = \hat{h}^{\mathrm{KS}} \psi_l \quad , \tag{2.34}$$

where we introduced the KS operator $\hat{h}^{\mathrm{KS}} = \hat{t}^{\mathrm{s}} + v^{\mathrm{s}}$ with $v^{\mathrm{s}} = v + v^{\mathrm{xc}}$ and

$$v^{\mathrm{xc}} = \frac{\delta E^{\mathrm{xc}}}{\delta n_{\mathrm{el}}} \quad . \tag{2.35}$$

Applying a unitary conformation, these equations can be recast into the KS equations

$$\hat{h}^{\mathrm{KS}} \psi_l = \epsilon_l \psi_l \quad , \tag{2.36}$$

where we have replaced the Lagrange multipliers λ_l with the single-electron states ϵ_l. Solving the KS equations yields the single-electron wave functions defining the ground state electron density. However, since v^{s} depends on the electron density itself, fixed point iteration techniques have to be applied. In most DFT program packages simple self-consistent field (SCF) cycles are used in combination with mixing schemes to increase the overall convergence.

Finally, we point out that all derivations in this section as in the whole thesis are performed for the case of a spin-less electron density for simplicity, although it is straightforward to generalize the method to include spin. Indeed, the results as presented in Chapter 4 were performed using spin-polarized DFT calculations.

2.2.3.3. Total Energy Expression

The Poisson and KS equations can be inserted into the KS functional in order to arrive at the ground state or minimum energy expression. Inserting the optimal electron density

$n_{\mathrm{el,o}}$ and electrostatic potential v_{o} into Eq. (2.31) and using the validity of the Poisson equation we then get for the effective potential

$$V^{\mathrm{S}}[n_{\mathrm{el,o}}] = V^{\mathrm{S}}[v_{\mathrm{o}}, n_{\mathrm{el,o}}] = E_{\mathrm{es}}[v_{\mathrm{es,o}}, n_{\mathrm{el,o}}] + E_{\mathrm{en}}[n_{\mathrm{el,o}}] + E_{\mathrm{nn}} + E^{\mathrm{xc}}[n_{\mathrm{el,o}}] \quad , \qquad (2.37)$$

where $v_{\mathrm{es,o}}$ is the solution to the Poisson equation with the electronic charge density $n_{\mathrm{el,o}}$. E_{es} is the Coulomb integral or Hartree energy representing mean-field electron-electron interactions (cf. Eq. (2.18)):

$$E_{\mathrm{es}}[v_{\mathrm{es,o}}, n_{\mathrm{el,o}}] = \frac{1}{2} \int \mathrm{d}\boldsymbol{r} \, n_{\mathrm{el,o}} v_{\mathrm{es,o}} \quad . \qquad (2.38)$$

Correspondingly, E_{en} denotes the electron-nuclei interaction energy and E_{nn} the nuclei-nuclei interaction energy. The minimum free energy is then given by

$$E_{\mathrm{o}} = \min_{n_{\mathrm{el}},v} E^{\mathrm{KS}}[v, n_{\mathrm{el}}] = T^{\mathrm{S}}[n_{\mathrm{el,o}}] + E_{\mathrm{es}}[v_{\mathrm{es,o}}, n_{\mathrm{el,o}}] + E_{\mathrm{en}}[n_{\mathrm{el,o}}] + E_{\mathrm{nn}} + E^{\mathrm{xc}}[n_{\mathrm{el,o}}] \quad . \qquad (2.39)$$

In many cases, it can be useful to express the total energy in terms of the single-electron states $\epsilon_{l,\mathrm{o}}$. To achieve this, we can expand the electron density in the single-electron orbitals according to Eq. (2.29), replace the operators with the KS operator and finally insert the KS equation to obtain:

$$E_{\mathrm{o}} = E^{\mathrm{KS}}[v_{\mathrm{o}}, n_{\mathrm{el,o}}] = \sum_{l=1}^{N_{\mathrm{states}}} \epsilon_{l,\mathrm{o}} - \int \mathrm{d}\boldsymbol{r} \, n_{\mathrm{el,o}} v^{\mathrm{xc}} + E^{\mathrm{xc}}[n_{\mathrm{el,o}}] \underbrace{- \frac{1}{2} \int \mathrm{d}\boldsymbol{r} \, n_{\mathrm{el,o}} v_{\mathrm{es,o}}}_{E_{\mathrm{double}}} + E_{\mathrm{nn}} \quad , \qquad (2.40)$$

where E_{double} denotes the so called double-counting correction.

2.2.3.4. Exchange-Correlation Functionals

Exchange-correlation energy contributions are comprised of the Pauli-repulsion or exchange correction and the electron-electron correlation energy. Although DFT itself is an exact theory, the lacking knowledge about the correct analytical form of the xc-functional renders it an approximation. More precisely, corresponding analytical expressions are only available for specific systems as e.g. the homogeneous electron gas (HEG). The local density approximation (LDA) makes use of this limiting case by expressing the xc-energy in terms of the local electron density and the corresponding HEG xc energy density $\epsilon_{\mathrm{xc,LDA}}$:

$$E^{\mathrm{xc,LDA}}[n_{\mathrm{el}}] = \int \mathrm{d}\boldsymbol{r} \, n_{\mathrm{el}} \epsilon^{\mathrm{xc,LDA}}(n_{\mathrm{el}}) \quad . \qquad (2.41)$$

Although the LDA is useful in the case of highly delocalized electrons and a smooth electron density as one usually finds in metalic systems, more localized systems such as molecules are often represented with an insufficient accuracy. To correct on this bottleneck, more advanced generalized gradient approximation (GGA) xc-functionals explicitely consider

also the local gradient of the electron density as a parameter for the xc-energy. Through this the accuracy can be drastically increased in particular in situations where the electron density changes rapidly. In this thesis, we will exclusively rely on the Perdew-Burke-Ernzerhof-generalized gradient approximation (PBE-GGA) variant[112,113] for which the xc-functional is parameterized as

$$E^{\mathrm{xc,PBE}}[n_{\mathrm{el}}] = \int \mathrm{d}\boldsymbol{r}\, n_{\mathrm{el}} \epsilon^{\mathrm{xc,PBE}}\left(r_{\mathrm{s}}(\boldsymbol{r}), s(\boldsymbol{r})\right) \tag{2.42}$$

with $s = \frac{|\nabla n_{\mathrm{el}}|}{2k_{\mathrm{F}} n_{\mathrm{el}}}$ denoting the reduced density gradient ($k_{\mathrm{F}} = (3\pi^2 n_{\mathrm{el}})^{1/3}$) and $r_{\mathrm{s}} = (4\pi n_{\mathrm{el}})^{-1/3}$ the Wigner-Seitz radius. Since the Poisson-Boltzmann (PB) equation (PBE)-functional reduces to the LDA version in the case of small electron density gradients, it in practice not only performs well for molecules[113] but importantly and in contrast to many other GGAs also reproduces accurately metallic properties like the bulk modulus or the cohesive energy.[114,115] It therefore offers in many cases a good compromise between computational speed and accuracy and represents a widely used standard xc-functional. For that purpose, we use PBE-GGA throughout the whole thesis. We, however, found that properties of interest as solvation energies show only a slight dependence on the choice of the xc-functional. This is somehow expected since solvation cavities that determine such effects are located far away from the nuclei where electron densities are commonly small.

2.2.4. Atomic Forces

So far, we introduced DFT as an efficient method for solving the electronic SE and obtaining the electronic ground state for a fixed nuclear configuration. Often, one is additionally interested in the dynamics of the system, which in the BOA arises on a single PES. The gradient of this multi-dimensional object along the direction of a particular nuclear coordinate then resembles the force acting on the respective atom. Starting from the energy expectation value Eq. (2.26), we can calculate the atomic force by performing the total derivative with respect to the position of the respective atom:

$$\boldsymbol{F}_{\mathrm{at}} = -\frac{\mathrm{d}E[n_{\mathrm{el,o}}]}{\mathrm{d}\boldsymbol{R}_{\mathrm{at}}} = -\underbrace{\left\langle \Psi \left| \frac{\mathrm{d}\hat{H}_{\mathrm{el}}}{\mathrm{d}\boldsymbol{R}_{\mathrm{at}}} \right| \Psi \right\rangle}_{\boldsymbol{F}_{\mathrm{at}}^{\mathrm{HF}}} \underbrace{-2\left\langle \frac{\mathrm{d}\Psi}{\mathrm{d}\boldsymbol{R}_{\mathrm{at}}} \left| \hat{H}_{\mathrm{el}} \right| \Psi \right\rangle}_{\boldsymbol{F}_{\mathrm{at}}^{\mathrm{Pulay}}} \quad, \tag{2.43}$$

where we used the hermiticity of the Hamiltonian. The first term is called Hellmann-Feynman (HF) forces and arises from the position dependence of the electronic Hamiltonian:

$$\boldsymbol{F}_{\mathrm{at}}^{\mathrm{HF}} = -\left\langle \Psi \left| \frac{\mathrm{d}\hat{V}_{\mathrm{en}} + \hat{V}_{\mathrm{nn}}}{\mathrm{d}\boldsymbol{R}_{\mathrm{at}}} \right| \Psi \right\rangle \quad. \tag{2.44}$$

The second part in Eq. (2.43) is called Pulay forces. If Ψ is an exact solution of the electronic SE, this term vanishes (HF theorem):

$$\boldsymbol{F}_{\mathrm{at}}^{\mathrm{Pulay}} = 2E_{\circ}\left\langle \frac{\mathrm{d}\Psi}{\mathrm{d}\boldsymbol{R}_{\mathrm{at}}} \middle| \Psi \right\rangle = 2E_{\circ}\frac{\mathrm{d}}{\mathrm{d}\boldsymbol{R}_{\mathrm{at}}}\underbrace{\left\langle \Psi | \Psi \right\rangle}_{=1} = 0 \quad. \tag{2.45}$$

In general, however, the exact solution Ψ is not known and one approximates it by a finite expansion in basis functions which is why one can not simply replace $\hat{H}_{\mathrm{el}}\Psi$ with $E_{\mathrm{o}}\Psi$. If the basis functions are plane-waves, the Pulay forces still vanish since the approximated Ψ does then not depend on the atomic positions and therefore $\frac{\mathrm{d}\Psi}{\mathrm{d}\boldsymbol{R}_{\mathrm{at}}} = 0$. In the case of atom-centered basis functions, the representation of Ψ in a truncated basis set leads, however, to non-vanishing derivatives and therefore necessitates the explicit calculation of Pulay forces.

2.3. Modeling Finite Ionic Strengths: Poisson-Boltzmann Theory

In Section 2.1, we introduced the basics of implicit solvation methods by deriving the generalized Poisson equation and the corresponding electrostatic energy expression describing charge distributions in dielectric media. This section now deals with modifications of this theory necessary to account also for the presence of dissolved ions leading to the well-known PB theory.

2.3.1. PB Theory

The modeling of electrolytes is a long-standing scientific challenge with its roots reaching back to the very beginnings of electrochemistry. Since the early studies of Helmholtz over 150 years ago, [116] the solid-electrolyte interface has been of continuous interest and motivated the development of a wide range of different theoretical models. Figure 2.3 illustrates the current view of the structural composition of this interface (cf. ref. [117]). Close to the charged electrode surface the accumulation of ions leads to the creation of a double layer, i.e. a capacitor like arrangement of counter-ions which effectively screen the charges causing a linear drop in the total electrostatic potential. At the outer Helmholtz plane, the double layer descends into the diffuse ion layer which can be in general well described by the famous Gouy-Chapman (GC) or PB theory. Thereby, diffusive ions are approximated as point charges distributed according to the mean-field electrostatic potential. [32–35,117] Considering again the generalized Poisson equation Eq. (2.11), the previously introduced solute charge density is here simply given by the electrode charge and the inclusion of ions requires merely the addition of the ionic charge density distribution $n_{\mathrm{ion}}^{\mathrm{PB}}$ on top of the total charge density resulting in the PBE:

$$\nabla \cdot [\varepsilon(\boldsymbol{r})\nabla v(\boldsymbol{r})] = -4\pi n_{\mathrm{sol}}(\boldsymbol{r}) - 4\pi n_{\mathrm{ion}}^{\mathrm{PB}}(\boldsymbol{r}) \quad . \tag{2.46}$$

v here denotes the total electrostatic potential as created by both ionic and solute charge densities. The ionic charge densities can be expressed in terms of the ion concentrations via

$$n_{\mathrm{ion}}^{\mathrm{PB}}(\boldsymbol{r}) = z\left[c_+^{\mathrm{s}}(\boldsymbol{r}) - c_-^{\mathrm{s}}(\boldsymbol{r})\right] \quad , \tag{2.47}$$

which implies that the electrolyte consists of cations and anions with the same charge z. The focus in this thesis on such so called z:z electrolytes is mainly motivated from the fact that a larger amount of experimental reference data is available which is in general needed

to benchmark and parameterize PB models (cf. Section 4.2). Yet, equivalent relations for other salts can be derived analogously[64] and the methodology developed here should be in principle also applicable for those cases.

The ion concentrations introduced in Eq. (2.47) can be expressed as a function of the potential of mean force (PMF) $w_\pm$:[118]

$$c_\pm^{\mathrm{s}}(\boldsymbol{r}) = c^{\mathrm{s,bulk}} \mathrm{e}^{\mp \beta w_\pm(\boldsymbol{r})} \quad , \tag{2.48}$$

where $c^{\mathrm{s,bulk}}$ denotes the ionic bulk concentration and $\beta = 1/(k_{\mathrm{B}}T)$ with the temperature T and the Boltzmann constant k_{B}. The PMF $w_\pm$ equals the average work that has to be done to bring the ion of charge $\pm$ to the position $\boldsymbol{r}$ with the fixed local charge density n_{sol}. In order to obtain $w_\pm$ one has to therefore perform explicit simulations of the electrolyte and average out all interactions of the depicted ion yielding the averaged interaction energy. Fortunately, such an elaborate effort can in many cases be avoided by approximating the PMF with the mean-field electrostatic potential v which is the main assumption behind PB theory. As an example, in the original formulation of PB theory the ion concentrations are then simply given by:[118]

$$c_\pm^{\mathrm{s}}(\boldsymbol{r}) = c^{\mathrm{s,bulk}} \mathrm{e}^{\mp \beta v(\boldsymbol{r})} \quad . \tag{2.49}$$

2.3.2. Debye-Hückel Theory

In most PB variants, the ionic charge density is a nonlinear function of the potential v which complicates the numerical solution of the corresponding PBE Eq. (2.46). In the limit of low electrostatic potentials ($|v| \ll 25\,\mathrm{mV}$ for monovalent ions at room temperature[35,65,119]) the PBE can, however, be drastically simplified by Taylor expanding the ionic charge density $n_{\mathrm{ion}}^{\mathrm{PB}}$ around $v = 0$ up to 1st order in v

$$n_{\mathrm{ion}}^{\mathrm{LPB}} = \underbrace{n_{\mathrm{ion}}^{\mathrm{PB}}\Big|_{v=0}}_{-\frac{1}{4\pi}\bar{\kappa}_0^2} + \underbrace{\frac{\partial n_{\mathrm{ion}}^{\mathrm{PB}}}{\partial v}\Big|_{v=0}}_{-\frac{1}{4\pi}\bar{\kappa}^2} v \quad , \tag{2.50}$$

where $\bar{\kappa}_0$ is an often zero offset and $\bar{\kappa}$ the modified Debye-Hückel (DH) coefficient. Applying this formalism to standard PB theory with the ion concentrations given in Eq. (2.49), then yields the DH theory with $\bar{\kappa}_0 = 0$ and $\bar{\kappa}^2 = \kappa^2 \varepsilon^{\mathrm{s,bulk}}$ and κ denoting the standard DH coefficient given as

$$\kappa = \sqrt{\frac{8\pi c^{\mathrm{s,bulk}} z^2 \beta}{\varepsilon^{\mathrm{s,bulk}}}} \quad . \tag{2.51}$$

In this limit, the main ionic effect in dilute solutions is the screening of the Coulomb interactions characterized by the DH screening length κ^{-1} (cf. Fig. 2.3). In aqueous electrolytes κ^{-1} is in the order of nanometers and therefore much smaller than any macroscopic length, thus the bulk solution containing diffusing ions stays quasineutral.
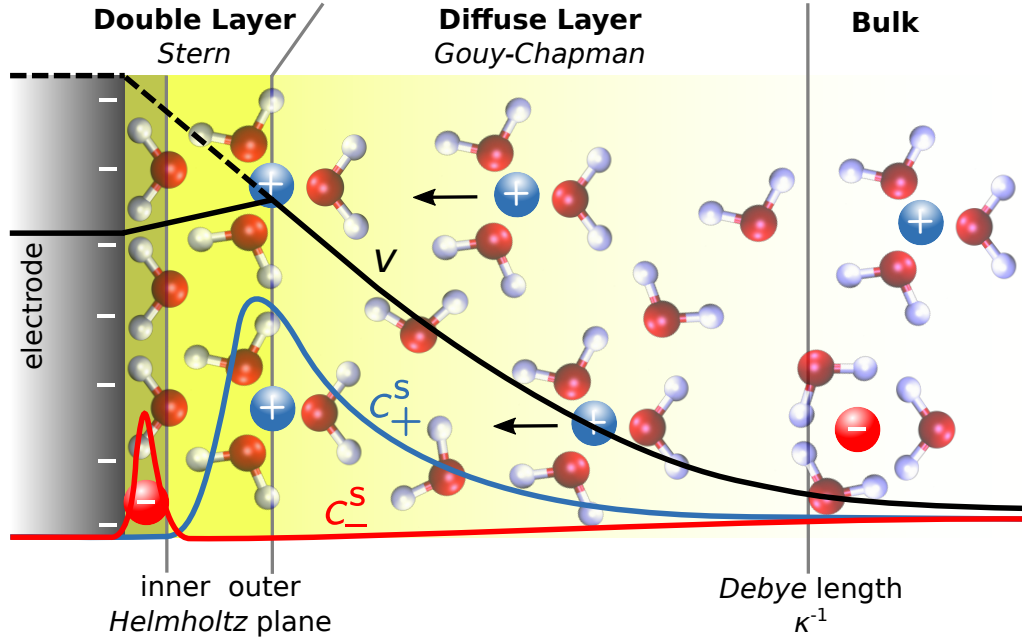
Figure 2.3.: Schematic representation of the electrolytic aqueous environment of a negatively charged electrode. Shown is the electrostatic potential v in black, the concentration of the cations c_+^s in blue and the anions c_-^s in red. In the here considered case we explicitly account for possibly present specifically adsorbed co-ions at the electrode surface. Without such ions, there is no sign inversion of the electrostatic field at the outer Helmholtz plane indicated by the dashed black line. Close to the negatively charged surface one finds high concentrations of hydrated cations balancing out the negative surface charge leading to the creation of an electric double layer. The separation layer between ions and surface built up by solvent molecules is called the Stern layer. Outside the outer Helmholtz plane, in the diffusive ion regime, the ion concentrations decay exponentially according to GC/PB theory. The Debye length κ^{-1} is commonly considered as the beginning of bulk-like behaviour of the electrolyte.

Inserting the approximated ionic charge density into the PBE then gives the linearized PB (LPB) equation (LPBE):

$$(\nabla \cdot [\varepsilon(\boldsymbol{r})\nabla]\, v = -4\pi n_{\text{sol}} - 4\pi n_{\text{ion}}^{\text{LPB}}$$
$$\Updownarrow$$
$$(\nabla \cdot [\varepsilon(\boldsymbol{r})\nabla] - \bar{\kappa}^2(\boldsymbol{r}))v = \hat{L}_0 v = -4\pi n_{\text{sol}} + \bar{\kappa}_0^2 \quad ,\tag{2.52}$$

with the linear operator $\hat{L}_0$.

2.3.3. Improvements on PB Theory

As appealing as the conceptual simplicity of the original PB or DH theory is, such approaches have proven insufficient for the modeling of e.g. highly charged solutes, enzyme active sites, [63,120] or charged surfaces like Langmuir monolayers. [64] The failure of standard PB theory in these particular cases can be thereby attributed to the point-like description of the ions leading to an overestimation of ionic charge densities close to high electrostatic

potentials.[60,64–72] Two most prominent avenues to improve on this limitation are the finite size modified PB (MPB) and Stern layer modified PB (SPB) (or GC-Stern model) approaches. MPB theory accounts for solvated ion-ion short-range repulsions by introducing finite ion sizes via a statistical lattice model in which the lattice cells are only allowed to be occupied by one ion at a time.[60,64,65,68,69,71,72] This creates an upper bound for local ionic charge accretion and thereby avoids an overshooting of ion concentrations e.g. close to high electrostatic potentials. The Stern layer concept[74] on the other hand accounts for the existence of a finite layer of solvent molecules or specifically adsorbed ions separating the solute (or electrode) from the diffusive ionic charge distribution (cf. Fig. 2.3). In SPB theory the Stern layer is accounted for by simply introducing an ion-free (ion-exclusion) region between the solvation cavity and the diffusive ionic solution. As discussed in detail in Section 4.2 the ion-exclusion Stern layer may thereby partly arise from the solvation shells around the ions, which also prevent the latter from further approaching the solute.[121–123]

Although MPB and SPB theory both correct for the overestimation of ionic charge densities with the PB method, they do in principle adress completely different physical shortcomings of PB theory. While the MPB model introduces solvated ion-ion repulsions and thereby introduces a volume-based ion exclusion, the Stern layer in the finite size and Stern layer modified PB (SMPB) model is mainly caused by repulsive solute-ion interactions. This fact led to the combination of both strands into the SMPB theory.[23,24,60,72,78] In the following section, we will derive a corresponding SMPB free energy functional for our system of interest, i.e. a charge distribution embedded into a dielectric continuum containing now also an ionic charge distribution. At its minimum with respect to the electrostatic potential v this functional then recovers the corresponding SMPB equation (SMPBE) which provides an improved description of ionic charge distributions compared to Eq. (2.49).

2.3.4. Finite Size and Stern layer Modified PB Model

We will start the derivation of SMPB theory by first constructing a model Hamiltonian for the system which then defines the partition function. This lets us then derive all thermodynamic properties of interest such as ion distributions or a corresponding free energy functional which minimizes to the SMPBE. The procedure is thereby partly guided by the discussions of refs. [64] and [124], but to our knowledge there exists so far no published full derivation taking into account both finite ion sizes and the existence of a Stern layer, as well as a fixed solute charge distribution.

2.3.4.1. Hamiltonian

We start by again considering a system consisting of a solvation cavity inside of which $\varepsilon = 1$ and a surrounding region where $\varepsilon = \varepsilon^{\mathrm{s,bulk}}$ (solvent) as illustrated in Fig. 2.4 and introduced in the previous sections. To this we then add an ensemble of $N = N_+ + N_- + N_0$ particles, with N_+ cations, N_- anions and N_0 solvent molecules. The interactions between all ions are defined by the electrostatic potential v_{ion} which is the solution of the generalized Poisson equation Eq. (2.11), given here as:

$$\nabla[\varepsilon(\boldsymbol{r})\nabla v_{\mathrm{ion}}] = -4\pi n_{\mathrm{ion}} \tag{2.53}$$

with

$$n_{\mathrm{ion}} = \sum_j^N s_j z \delta(\boldsymbol{r} - \boldsymbol{r}_j) \qquad (2.54)$$

with $\boldsymbol{r}_j$ being the positions of the ions and solvent molecules and s_j the sign of the particle's charge adopting the value of ± 1 for the ions and 0 for solvent molecules. v_{ion} can be expressed in terms of the ionic charge density by the help of the corresponding Green's function $G(\boldsymbol{r}, \boldsymbol{r}')$ which is the solution of the PDE

$$\nabla \left[\varepsilon(\boldsymbol{r}) \nabla G(\boldsymbol{r}, \boldsymbol{r}') \right] = -\delta(\boldsymbol{r} - \boldsymbol{r}') \quad . \qquad (2.55)$$

The electrostatic potential created by the ions v_{ion} can then (neglecting all surface integrals) be written as

$$
\begin{aligned}
v_{\mathrm{ion}} &= \int \mathrm{d}\boldsymbol{r}' \delta(\boldsymbol{r} - \boldsymbol{r}') v_{\mathrm{ion}}(\boldsymbol{r}') = - \int \mathrm{d}\boldsymbol{r}' \nabla \left[\varepsilon(\boldsymbol{r}) \nabla G(\boldsymbol{r}, \boldsymbol{r}') \right] v_{\mathrm{ion}}(\boldsymbol{r}') \\
&= - \int \mathrm{d}\boldsymbol{r}' G(\boldsymbol{r}, \boldsymbol{r}') \nabla \left[\varepsilon(\boldsymbol{r}) \nabla v(\boldsymbol{r}') \right] = 4\pi \int \mathrm{d}\boldsymbol{r}' G(\boldsymbol{r}, \boldsymbol{r}') \sum_j^N s_j z \delta(\boldsymbol{r}' - \boldsymbol{r}_j) \\
&= 4\pi \sum_j^N s_j z G(\boldsymbol{r}, \boldsymbol{r}_j) \quad .
\end{aligned}
\qquad (2.56)
$$

Following Eq. (2.18), the potential energy of the electrolyte becomes [64,71]

$$
\begin{aligned}
\mathcal{V}_{\mathrm{elt}} &= \frac{1}{2} \int \mathrm{d}\boldsymbol{r} n_{\mathrm{ion}} v_{\mathrm{ion}} + \sum_j^N \sum_{j' \neq j}^N v^{\mathrm{elt,rep}}(\boldsymbol{r}_j, \boldsymbol{r}_{j'}) \\
&= \frac{4\pi}{2} \sum_j^N \sum_{j'}^N s_j s_{j'} z^2 G(\boldsymbol{r}_j, \boldsymbol{r}_{j'}) + \sum_j^N \sum_{j' \neq j}^N v^{\mathrm{elt,rep}}(\boldsymbol{r}_j, \boldsymbol{r}_{j'}) \quad .
\end{aligned}
\qquad (2.57)
$$

We thereby added a hard-sphere repulsion potential $v^{\mathrm{elt,rep}}$ which becomes infinite for $|\boldsymbol{r}_j - \boldsymbol{r}_{j'}| \leq a$ and zero elsewise. Ions and solvent molecules are therefore equally approximated as hard spheres with a sphere radius of a. Such a modification avoids unphysically high local ion concentrations arising within the original PB formulation considering only point-like particles.
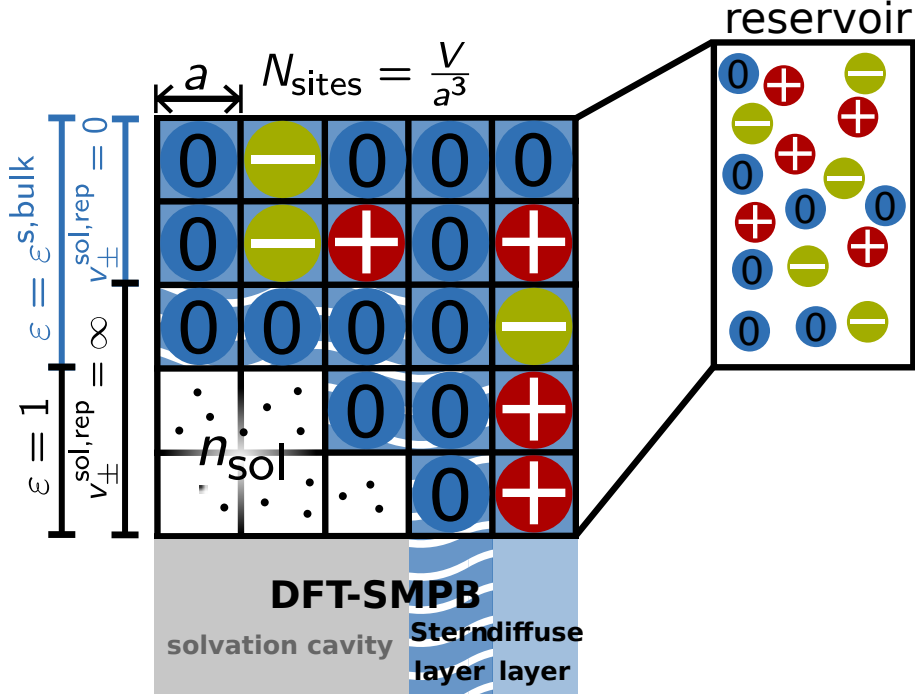
Figure 2.4.: Schematic representation of the SMPB-DFT model. DFT is used to describe the continuous solute charge density n_{sol} with the main part residing in a vacuum-like region in which $\varepsilon = 1$. This charge density is embedded into a solvent represented by the bulk dielectric permittivity $\varepsilon^{\mathrm{s,bulk}}$. Solvent molecules (symbol "0") and dissolved ions (symbols "+" and "-") are introduced by discretizing the whole space into $N_{\mathrm{sites}} = \frac{V}{a^3}$ lattice cells of site length a which is then filled and coupled to a corresponding reservoir. Ions can interact via repulsive interactions $v_{\pm}^{\mathrm{sol,rep}}$ with the solute charge density which prevents them from approaching the solute closer than a certain distance, creating an ion-free layer around the solvation cavity, the Stern layer.

Next, we introduce a fixed charge distribution consisting of electrons and nuclei located at positions $\boldsymbol{r}_i$ and $\boldsymbol{R}_{\mathrm{at}}$ in space and the potential energy then becomes

$$
\mathcal{V}^{(0)} = \mathcal{V}_{\mathrm{elt}} - 4\pi \underbrace{\sum_j^N \int \mathrm{d}\boldsymbol{r}\, s_j z n_{\mathrm{el}} G(\boldsymbol{r}_j, \boldsymbol{r})}_{\mathrm{e}\leftrightarrow\pm} + 4\pi \underbrace{\sum_j^N \sum_{\mathrm{at}}^{N_{\mathrm{at}}} s_j z Z_{\mathrm{at}} G(\boldsymbol{r}_j, \boldsymbol{R}_{\mathrm{at}})}_{\mathrm{n}\leftrightarrow\pm}
$$

$$
+ \frac{4\pi}{2} \underbrace{\int \mathrm{d}\boldsymbol{r}\mathrm{d}\boldsymbol{r}'\, n_{\mathrm{el}}(\boldsymbol{r}) n_{\mathrm{el}}(\boldsymbol{r}') G(\boldsymbol{r}, \boldsymbol{r}')}_{\mathrm{e}\leftrightarrow\mathrm{e}} - 4\pi \underbrace{\sum_{\mathrm{at}}^{N_{\mathrm{at}}} \int \mathrm{d}\boldsymbol{r}\, Z_{\mathrm{at}} n_{\mathrm{el}} G(\boldsymbol{r}, \boldsymbol{R}_{\mathrm{at}})}_{\mathrm{e}\leftrightarrow\mathrm{n}}
$$

$$
+ \frac{4\pi}{2} \underbrace{\sum_{\mathrm{at}}^{N_{\mathrm{at}}} \sum_{\mathrm{at}'}^{N_{\mathrm{at}'}} Z_{\mathrm{at}} Z_{\mathrm{at}'} G(\boldsymbol{R}_{\mathrm{at}}, \boldsymbol{R}_{\mathrm{at}'})}_{\mathrm{n}\leftrightarrow\mathrm{n}} \quad, \tag{2.58}
$$

where the respective interactions between electrons ("e"), nuclei ("n") and ions ("±") have been indicated. This can be written in a much more condensed form by introducing the total charge density

$$n = n_{\text{ion}} + n_{\text{sol}} \tag{2.59}$$

and the total electrostatic potential

$$v = 4\pi \int \mathrm{d}\boldsymbol{r}' G(\boldsymbol{r}, \boldsymbol{r}') n(\boldsymbol{r}') \quad . \tag{2.60}$$

If we then insert Eq. (2.60) into the electrostatic energy as given by Eq. (2.18) however using the charge density n instead of just n_{sol} we obtain

$$\mathcal{V}^{(0)} = \frac{4\pi}{2} \int \mathrm{d}\boldsymbol{r}\mathrm{d}\boldsymbol{r}' n(\boldsymbol{r}) G(\boldsymbol{r}, \boldsymbol{r}') n(\boldsymbol{r}') + E^{\text{SIC}}[n] + \sum_j^N \sum_{j' \neq j}^N v^{\text{elt,rep}}(\boldsymbol{r}_j, \boldsymbol{r}_{j'}) \quad . \tag{2.61}$$

where we now also added a term E^{SIC} which corrects for the self-interaction of all particles which are incorrectly included in the first integral.

So far, we have assumed that the ions interact with the solute merely on the basis of electrostatic interactions. The finite size of the ions, however, leads to additional repulsive forces which we account for by introducing a solute-ion repulsion potential $v_{s_j}^{\text{sol,rep}}$. This leads to an additional potential energy contribution given by

$$\mathcal{V}' = \sum_j^N v_{s_j}^{\text{sol,rep}}(\boldsymbol{r}_j) \quad . \tag{2.62}$$

As seen from Eq. (2.62), we thereby account for different repulsion potentials of cations, anions and solvent molecules. Solute-solvent repulsive interactions are already partly included by the chosen form of the dielectric function which defines the minimal distance between solvent molecules and solute. Indeed, we will later show that non-electrostatic solute-solvent interactions can be reliably expressed in terms of the dielectric function. A corresponding effective free energy correction term (later called $\Omega_\varepsilon^{\text{non-mf}}$) can then also be directly added to the final free energy expression derived in this section. This removes the necessity to include such interactions here in the Hamiltonian, which is why we simply set $v_0^{\text{sol,rep}} = 0$. Since in most cases the ions will be further apart from the solute than the solvent (cf. Section 4.2), we will in the scope of this thesis discuss the modification in Eq. (2.62) as *Stern layer correction*.

2.3.4.2. Grand Partition Function

Combining the total potential energy $\mathcal{V} = \mathcal{V}^{(0)} + \mathcal{V}'$ with the kinetic energy $\mathcal{T} = \sum_j^N \frac{p_j}{2m_j}$ of all solvent molecules and ions (the solute charge density is assumed to be fixed), we arrive at the full Hamiltonian of the system

$$
\mathcal{H} = \sum_j^N \frac{p_j}{2m_j} + \frac{4\pi}{2} \int \mathrm{d}r \mathrm{d}r' n(r) G(r, r') n(r') + E^{\mathrm{SIC}}[n] + \sum_j^N \sum_{j' \neq j}^N v^{\mathrm{elt,rep}}(r_j, r_{j'})
$$
$$
+ \sum_j^N v_{s_j}^{\mathrm{sol,rep}}(r_j) \quad . \tag{2.63}
$$

Since the number of solvent molecules and ions is always much larger than the number of solute particles, we further introduce a reservoir of ions and solvent molecules which keeps the respective chemical potentials $\{\mu_\pm, \mu_0\}$ of ions and solvent molecules constant. The grand-partition function of the system is thus given by

$$
Z_{\mathrm{G}}(\mu_0, \mu_+, \mu_-, V, T) = \sum_{N_0=0}^\infty \sum_{N_+=0}^\infty \sum_{N_-=0}^\infty \mathrm{e}^{\sum_j^N \beta \mu_j} Z(\{N_0, N_+, N_-\}, V, T) \quad , \tag{2.64}
$$

with V the volume and Z the canonical partition function of the system given as

$$
Z(\{N_0, N_+, N_-\}, V, T) = \frac{1}{N_0! N_+! N_-! h^{3N}} \int \mathrm{d}\{r\} \mathrm{d}\{p\} \mathrm{e}^{-\beta \mathcal{H}(\{r\}, \{p\})}
$$
$$
= \frac{1}{N_0! N_+! N_-! \Lambda_0^{3N_0} \Lambda_+^{3N_+} \Lambda_-^{3N_-}} \int \mathrm{d}\{r\} \mathrm{e}^{-\beta \mathcal{V}(\{r\})} \quad , \tag{2.65}
$$

where $\{p\}$ and $\{r\}$ denote the phase spaces of all ions and solvent molecules and $\Lambda_{\pm/0} = \frac{h}{\sqrt{2\pi m_{\pm/0}\beta}}$ is the thermodynamic de Broglie wave length. Thereby, we applied the ideal gas approximation for the kinetic energies of solvent molecules and ions to enable the analytic solution of the integral over momentum space.

Eq. (2.65) is the fundamental equation from which different PB theories can be derived. In the original PB theory of Gouy and Chapman, one assumes that $a = 0$ and the multidimensional integral of position space in Eq. (2.65) then separates into a product over single-particle integrals. Such a product of integrals can be straightforwardly solved[124] leading to a free energy expression which minimizes to the original PBE as given by Eqs. (2.46), (2.47) and (2.49). In the general case of $a \neq 0$ the solution of this integral is, however, far from trivial and requires the use of approximations. One possible approach is the introduction of a lattice model in which all lattice cells are occupied by either solvent molecules or ions (cf. Fig. 2.4). In the grand-partition function, one then has to sum over all possible partitionings of the total number of lattice sites (which are equal to the number of particles) N into numbers of cations, anions and solvent molecules:

$$
Z_{\mathrm{G}}(\mu_0, \mu_+, \mu_-, V, T) = \sum_i^{N_{\mathrm{part}}} \mathrm{e}^{\beta \sum_j^N \mu_{j,i}} Z(\{N_{0,i}, N_{+,i}, N_{-,i}\}, V, T) \tag{2.66}
$$

where $\mu_{j,i}$ denotes the chemical potential of particle j and $\{N_{0,i}, N_{+,i}, N_{-,i}\}$ the number of solvent molecules, cations and anions in the current partitioning i. In total there are $N_{\mathrm{part}} = \frac{1}{2}\left((N+1)^2 + (N+1)\right)$ of such ways to partition N into the three numbers.

The corresponding canonical partition function becomes a discrete sum over all possible configurations $N_{\mathrm{conf},i} = \binom{N}{N_{+,i}}\binom{N-N_{+,i}}{N_{-,i}}$ of the particles $\{N_{0,i}, N_{+,i}, N_{-,i}\}$ on the lattice sites, hence:

$$Z(\{N_{0,i}, N_{+,i}, N_{-,i}\}, V, T) = \sum_{k}^{N_{\mathrm{conf},i}} \mathrm{e}^{-\beta\mathcal{V}(\{\boldsymbol{r}_{j,ik}\})}$$

$$= \sum_{k}^{N_{\mathrm{conf},i}} \exp\left(-\beta\frac{4\pi}{2}\int \mathrm{d}\boldsymbol{r}\mathrm{d}\boldsymbol{r}' n_{ik}(\boldsymbol{r})G(\boldsymbol{r},\boldsymbol{r}')n_{ik}(\boldsymbol{r}') + \sum_{j}^{N} v_{s_{j,i}}^{\mathrm{sol,rep}}(\boldsymbol{r}_{j,ik})\right) \qquad (2.67)$$

where $\{\boldsymbol{r}_{j,ik}\}$ and $\{s_{j,i}\}$ denote the positions and spin-like variables of all particles, respectively, and n_{ik} the total charge density in the current partitioning i and lattice configuration k. The hard-sphere repulsion operator $v^{\mathrm{elt,rep}}$ can thereby be neglected since the considered lattice configurations do not allow particles to come closer than a. In accordance with the literature, we thereby additionally neglected the self-interaction contributions E^{SIC},[64,124] but note that electronic self-interaction is later accounted for by means of the xc-functional (cf. Section 3.2.1). We further ignored the kinetic energies of ions and solvent molecules as these are usually not accounted for in lattice-based PB models.[64]

In order to simplify Eq. (2.67), we first consider the two-center integral in the argument of the exponent which represents the correlated charge interactions. It can be simplified with the help of common Gaussian integrals, a procedure also known as *Hubbard-Stratonovitch transformation*.[64] To this end, we consider the well known relation[125,126]

$$\mathrm{e}^{\frac{1}{2}\boldsymbol{J}^{\mathsf{T}}\boldsymbol{A}^{-1}\boldsymbol{J}} = \sqrt{\frac{\det(\boldsymbol{A})}{(2\pi)^{3M}}}\int \mathrm{d}x_1\ldots\mathrm{d}x_{3M}\mathrm{e}^{-\frac{1}{2}\boldsymbol{x}^{\mathsf{T}}\boldsymbol{A}\boldsymbol{x}+\boldsymbol{J}^{\mathsf{T}}\boldsymbol{x}} \quad , \qquad (2.68)$$

where $\boldsymbol{J}$ and $\boldsymbol{x}$ are vectors of dimension $3M$ and $\boldsymbol{A}$ a square matrix of dimensions $3M \times 3M$. The elements of the vectors $\boldsymbol{J}$ and $\boldsymbol{x}$ can be associated with the values of respective functions $J(\boldsymbol{r})$ and $x(\boldsymbol{r})$ at a number of $3M$ discrete grid points. Analogously, the elements of the matrix $\boldsymbol{A}$ can be seen as values of a two-centered function $A(\boldsymbol{r},\boldsymbol{r}')$ on a number of $3M \times 2$ grid points. For $M \to \infty$ and by making the increments of the vectors infinitely small, we can therefore replace the dot products by integrals[124,126] yielding

$$\mathrm{e}^{\frac{1}{2}\int \mathrm{d}\boldsymbol{r}\mathrm{d}\boldsymbol{r}' J(\boldsymbol{r})A^{-1}(\boldsymbol{r},\boldsymbol{r}')J(\boldsymbol{r}')} = \sqrt{\det(\boldsymbol{A})}\int \mathcal{D}x(\boldsymbol{r})\mathrm{e}^{-\frac{1}{2}\int \mathrm{d}\boldsymbol{r}\mathrm{d}\boldsymbol{r}' x(\boldsymbol{r})A(\boldsymbol{r},\boldsymbol{r}')x(\boldsymbol{r}') + \int \mathrm{d}\boldsymbol{r}Jx} \quad , \qquad (2.69)$$

where we introduced the path integral measure

$$\mathcal{D}x(\boldsymbol{r}) = \lim_{\xi \to 0, 3M \to \infty}\left(2\pi/\xi^3\right)^{-(3M)/2}\mathrm{d}x_1\ldots\mathrm{d}x_{3M} \quad , \qquad (2.70)$$

with the spatial increment ξ. We use this expression to simplify Eq. (2.67) by substituting $J = -in_{ik}$, $A = (4\pi\beta\boldsymbol{G})^{-1}$ and $x = \Psi$ where Ψ then takes the role of the auxiliary function to get:

$$\exp\left(-\beta\frac{4\pi}{2}\int \mathrm{d}\boldsymbol{r}\mathrm{d}\boldsymbol{r}'n_{ik}(\boldsymbol{r})G(\boldsymbol{r},\boldsymbol{r}')n_{ik}(\boldsymbol{r}')\right)$$

$$\frac{1}{\sqrt{\det(4\pi\boldsymbol{G})}}\int \mathcal{D}\Psi(\boldsymbol{r})\exp\left(-\left[\frac{1}{2\beta}\int \mathrm{d}\boldsymbol{r}\mathrm{d}\boldsymbol{r}'\Psi(\boldsymbol{r})(4\pi G)^{-1}(\boldsymbol{r},\boldsymbol{r}')\Psi(\boldsymbol{r}') + i\int \mathrm{d}\boldsymbol{r}n_{ik}\Psi\right]\right)$$

$$= \frac{1}{\sqrt{\det(4\pi\boldsymbol{G})}}\int \mathcal{D}\Psi(\boldsymbol{r})\exp\left(-\beta K_{ik}[\Psi]\right)\quad, \tag{2.71}$$

with the modified path integral measure $\mathcal{D}\Psi(\boldsymbol{r}) = \lim\limits_{\xi\to 0, 3M\to\infty}(2\pi\beta/\xi^3)^{-(3M)/2}\,\mathrm{d}\Psi_1\ldots\mathrm{d}\Psi_{3M}$ and the functional $K_{ik}[\Psi]$. If $K[\Psi] >> k_\mathrm{B}T$ and $K_{ik}[\Psi]$ has a stationary phase point at $\Psi = \bar{\Psi}$, i.e. $\left.\frac{\delta K_{ik}[\Psi]}{\delta\Psi(\boldsymbol{r})}\right|_{\Psi=\bar{\Psi}} = 0$, this can be expected to dominate the value for the whole functional integral due to the exponential function (*stationary phase approximation* or *saddle point approximation*).[127] We can then expand the functional $K_{ik}[\Psi]$ in a Taylor series around the stationary point $\bar{\Psi}$:

$$K_{ik}[\Psi] \approx K_{ik}[\bar{\Psi}] + \frac{1}{2}\int \mathrm{d}\boldsymbol{r}\mathrm{d}\boldsymbol{r}'\Psi(\boldsymbol{r})\underbrace{\left.\frac{\delta^2 K_{ik}[\Psi]}{\delta\Psi(\boldsymbol{r})\delta\Psi(\boldsymbol{r}')}\right|_{\Psi=\bar{\Psi}}}_{\frac{1}{4\pi\beta}G^{-1}(\boldsymbol{r},\boldsymbol{r}')}\Psi(\boldsymbol{r}')\quad, \tag{2.72}$$

where we used $\boldsymbol{G} = \boldsymbol{G}^\mathsf{T}$. The linear term thereby vanishes since the expansion is done around a stationary point. The second integral in Eq. (2.72) can again be rewritten by the help of Eq. (2.69) with $J = 0$, $x = \Psi$ and $A = \frac{1}{4\pi\beta}G^{-1}$ yielding:

$$\int \mathcal{D}\Psi(\boldsymbol{r})\exp\left(-\frac{1}{2}\int \mathrm{d}\boldsymbol{r}\mathrm{d}\boldsymbol{r}'\Psi(\boldsymbol{r})\frac{1}{4\pi\beta}G^{-1}(\boldsymbol{r},\boldsymbol{r}')\Psi(\boldsymbol{r}')\right) = \sqrt{\det(4\pi\boldsymbol{G})}\quad. \tag{2.73}$$

Finally, we arrive at

$$\mathrm{e}^{-\beta\frac{4\pi}{2}\int \mathrm{d}\boldsymbol{r}\mathrm{d}\boldsymbol{r}'n_{ik}(\boldsymbol{r})G(\boldsymbol{r},\boldsymbol{r}')n_{ik}(\boldsymbol{r}')} = \mathrm{e}^{-\beta K_{ik}[\bar{\Psi}]}$$

$$= \exp\left(-\left[\frac{1}{2\beta}\int \mathrm{d}\boldsymbol{r}\mathrm{d}\boldsymbol{r}'\bar{\Psi}(\boldsymbol{r})(4\pi G)^{-1}(\boldsymbol{r},\boldsymbol{r}')\bar{\Psi}(\boldsymbol{r}') + i\int \mathrm{d}\boldsymbol{r}n_{ik}\bar{\Psi}\right]\right)\quad. \tag{2.74}$$

This method of replacing the fluctuating field Ψ by its value $\bar{\Psi}$ at the stationary point is often also called mean-field approximation.[124]

The grand-canonical partition function is now given as

$$Z_\mathrm{G}(\{\mu_0, \mu_+, \mu_-\}, V, T)$$

$$= \exp\left(-\left[\frac{1}{2\beta}\int \mathrm{d}\boldsymbol{r}\mathrm{d}\boldsymbol{r}'\bar{\Psi}(\boldsymbol{r})(4\pi G)^{-1}(\boldsymbol{r},\boldsymbol{r}')\bar{\Psi}(\boldsymbol{r}') + i\int \mathrm{d}\boldsymbol{r}n_\mathrm{sol}\bar{\Psi}\right]\right)$$

$$\times \sum_i^{N_\mathrm{part}}\sum_k^{N_{\mathrm{conf},i}}\left[\exp\left(-\beta\sum_j^N\left[-\mu_{j,i} + \frac{i}{\beta}s_{j,i}z\bar{\Psi}(\boldsymbol{r}_{j,ik}) + v_{s_{j,i}}^{\mathrm{sol,rep}}(\boldsymbol{r}_{j,ik})\right]\right)\right]\quad, \tag{2.75}$$

where we separated the charge density into solute and ionic contributions where only the latter depends on the configuration and partitioning of the lattice.

The sums over all partitions and configurations give in total $N_{\text{totconf}} = \sum\limits_{i}^{N_{\text{part}}} N_{\text{conf},i} = 3^N$ terms, since each of the N lattice sites is occupied by one of three different species (solvent molecule, cation or anion). Considering this, we can simplify Eq. (2.75) by changing from a sum in the exponential over all particles to a sum over all lattice sites located at $\boldsymbol{r}_m$ (cf. also ref. [64]):

$$
\begin{aligned}
Z_{\text{G}}(\{&\mu_0, \mu_+, \mu_-\}, V, T) \\
&= \exp\left(-\left[\frac{1}{2\beta}\int \mathrm{d}\boldsymbol{r}\mathrm{d}\boldsymbol{r}'\bar{\Psi}(\boldsymbol{r})\,(4\pi G)^{-1}(\boldsymbol{r},\boldsymbol{r}')\bar{\Psi}(\boldsymbol{r}') + i\int \mathrm{d}\boldsymbol{r}\,n_{\text{sol}}\bar{\Psi}\right]\right) \\
&\quad\times \sum_{l}^{N_{\text{totconf}}}\left[\exp\left(-\beta\sum_{m}^{N}\underbrace{\left[-\mu_{m,l} + \frac{i}{\beta}s_{m,l}z\bar{\Psi}(\boldsymbol{r}_m) + v_{s_{m,l}}^{\text{sol,rep}}(\boldsymbol{r}_m)\right]}_{h_{s_{m,l}}(\boldsymbol{r}_m)}\right)\right] \quad , \qquad (2.76)
\end{aligned}
$$

where we introduced the auxiliary function $h_{s_{m,l}}$. Compared to Eq. (2.75), the arising position vectors do now not anymore depend on the configurational sum which enables us to further rewrite this as

$$
\begin{aligned}
\sum_{l}^{N_{\text{totconf}}}&\left[\exp\left(-\beta\sum_{m}^{N}h_{s_{m,l}}(\boldsymbol{r}_m)\right)\right] = \\
&\left.\begin{aligned}
&\mathrm{e}^{-\beta\left[\sum\limits_{m}^{N}h_0(\boldsymbol{r}_m)\right]} + \mathrm{e}^{-\beta\left[\sum\limits_{m}^{N-1}h_0(\boldsymbol{r}_m)+h_+(\boldsymbol{r}_N)\right]} + \cdots + \mathrm{e}^{-\beta\left[\sum\limits_{m}^{N-1}h_+(\boldsymbol{r}_m)+h_0(\boldsymbol{r}_N)\right]} \\
&+ \cdots + \mathrm{e}^{-\beta\left[\sum\limits_{m}^{N}h_-(\boldsymbol{r}_m)\right]}
\end{aligned}\right\} 3^N \text{ terms} \\
&= \prod_{m}^{N}\left(\mathrm{e}^{-\beta h_0(\boldsymbol{r}_m)} + \mathrm{e}^{-\beta h_+(\boldsymbol{r}_m)} + \mathrm{e}^{-\beta h_-(\boldsymbol{r}_m)}\right) \\
&= \exp\left(\sum_{m}^{N}\ln\left[\mathrm{e}^{-\beta h_0(\boldsymbol{r}_m)} + \mathrm{e}^{-\beta h_+(\boldsymbol{r}_m)} + \mathrm{e}^{-\beta h_-(\boldsymbol{r}_m)}\right]\right) \\
&\approx \exp\left(\frac{1}{a^3}\int \mathrm{d}\boldsymbol{r}\ln\left[\mathrm{e}^{-\beta h_0(\boldsymbol{r})} + \mathrm{e}^{-\beta h_+(\boldsymbol{r})} + \mathrm{e}^{-\beta h_-(\boldsymbol{r})}\right]\right) \quad , \qquad (2.77)
\end{aligned}
$$

where in the last step we replaced the sum again with an integral. This is justified, because the size of a single lattice cell is small compared to macroscopic volumes. We now further recast the partly infinite and therefore numerically not tractable solute-ion repulsive potentials $v_{\pm}^{\text{sol,rep}}$ into equivalent ionic exclusion functions by defining $v_{\pm}^{\text{sol,rep}} = -\frac{1}{\beta}\ln\left(\alpha_{\text{ion}}^{\pm}\right)$. The exclusion functions are correspondingly zero close to the solute (highly repulsive solute-ion potential) and one in the bulk electrolyte (zero repulsive solute-ion

potential). Furthermore, the chemical potential reference state for salt solutions is the ion-free solution which enables us to set $\mu_0 = 0$ [64] and we get:

$$\text{Eq. (2.77)} = \exp\left(\frac{1}{a^3}\int d\boldsymbol{r}\ln\left[1 + \alpha_{\text{ion}}^+ e^{-\beta\left(\frac{i}{\beta}z\bar{\Psi}-\mu_+\right)} + \alpha_{\text{ion}}^- e^{-\beta\left(-\frac{i}{\beta}z\bar{\Psi}-\mu_-\right)}\right]\right) \quad . \quad (2.78)$$

The grand-canonical partition function then becomes

$$Z_{\text{G}}(\{\mu_+,\mu_-\},V,T) = \exp\left(-\beta\left(\frac{1}{2\beta^2}\int d\boldsymbol{r}d\boldsymbol{r}'\bar{\Psi}(\boldsymbol{r})(4\pi G)^{-1}(\boldsymbol{r},\boldsymbol{r}')\bar{\Psi}(\boldsymbol{r}') + \frac{i}{\beta}\int d\boldsymbol{r}n_{\text{sol}}\bar{\Psi}\right.\right.$$

$$\left.\left. -\frac{1}{a^3\beta}\int d\boldsymbol{r}\ln\left[1 + \alpha_{\text{ion}}^+ e^{-\beta\left(\frac{i}{\beta}z\bar{\Psi}-\mu_+\right)} + \alpha_{\text{ion}}^- e^{-\beta\left(-\frac{i}{\beta}z\bar{\Psi}-\mu_-\right)}\right]\right)\right) \quad .$$

$$(2.79)$$

In principle the auxiliary function can be chosen freely. However, as we show below, choosing a different auxiliary function $v = \frac{i}{\beta}\bar{\Psi}$ gives a physically meaningful result. We therefore first switch to v as an auxiliary function and get

$$Z_{\text{G}}(\{\mu_+,\mu_-\},V,T) = \exp\left(-\beta\left(-\frac{1}{2}\int d\boldsymbol{r}d\boldsymbol{r}'v(\boldsymbol{r})(4\pi G)^{-1}(\boldsymbol{r},\boldsymbol{r}')v(\boldsymbol{r}') + \int d\boldsymbol{r}n_{\text{sol}}v\right.\right.$$

$$\left.\left. -\frac{1}{a^3\beta}\int d\boldsymbol{r}\ln\left[1 + \alpha_{\text{ion}}^+ e^{-\beta(zv-\mu_+)} + \alpha_{\text{ion}}^- e^{-\beta(-zv-\mu_-)}\right]\right)\right) \quad . \quad (2.80)$$

The first two-center integral in the argument of the exponential can be further simplified into a single integral by making use of the Green's function definition in Eq. (2.55):

$$\int d\boldsymbol{r}d\boldsymbol{r}'v(\boldsymbol{r})(4\pi G)^{-1}(\boldsymbol{r},\boldsymbol{r}')v(\boldsymbol{r}') = \frac{1}{4\pi}\int d\boldsymbol{r}d\boldsymbol{r}'v(\boldsymbol{r})v(\boldsymbol{r}')\int d\boldsymbol{r}''\delta(\boldsymbol{r}'-\boldsymbol{r}'')G^{-1}(\boldsymbol{r},\boldsymbol{r}'')$$

$$= -\frac{1}{4\pi}\int d\boldsymbol{r}d\boldsymbol{r}'v(\boldsymbol{r})v(\boldsymbol{r}')\int d\boldsymbol{r}''\nabla'\cdot\left[\varepsilon(\boldsymbol{r}')\nabla'G(\boldsymbol{r}',\boldsymbol{r}'')\right]G^{-1}(\boldsymbol{r},\boldsymbol{r}'')$$

$$= -\frac{1}{4\pi}\int d\boldsymbol{r}d\boldsymbol{r}'v(\boldsymbol{r})\nabla'\cdot\left[\varepsilon(\boldsymbol{r}')\nabla'v(\boldsymbol{r}')\right]\int d\boldsymbol{r}''G(\boldsymbol{r}',\boldsymbol{r}'')G^{-1}(\boldsymbol{r},\boldsymbol{r}'')$$

$$= -\frac{1}{4\pi}\int d\boldsymbol{r}d\boldsymbol{r}'v(\boldsymbol{r})\nabla'\cdot\left[\varepsilon(\boldsymbol{r}')\nabla'v(\boldsymbol{r}')\right]\delta(\boldsymbol{r}'-\boldsymbol{r})$$

$$= -\frac{1}{4\pi}\int d\boldsymbol{r}v(\boldsymbol{r})\nabla\cdot\left[\varepsilon(\boldsymbol{r})\nabla v(\boldsymbol{r})\right]$$

$$= \frac{1}{4\pi}\int d\boldsymbol{r}\varepsilon(\boldsymbol{r})|\nabla v(\boldsymbol{r})|^2 \quad , \quad (2.81)$$

with $\nabla' = \nabla_{r'}$ and we neglected the surface integrals (again using the boundary condition $v \to 0$ for $|r| \to \infty$). Inserting this expression into the grand partition function, gives:

$$
Z_{\mathrm{G}}(\{\mu_+, \mu_-\}, V, T) = \exp\left(-\beta \left(\int \mathrm{d}r \left\{ -\frac{1}{8\pi} \varepsilon(r) |\nabla v(r)|^2 + n_{\mathrm{sol}} v \right\} \right. \right.
$$

$$
\left. \left. -\frac{1}{\beta a^3} \int \mathrm{d}r \ln\left[1 + \alpha_{\mathrm{ion}}^+ \mathrm{e}^{-\beta(zv - \mu_+)} + \alpha_{\mathrm{ion}}^- \mathrm{e}^{-\beta(-zv - \mu_-)} \right] \right) \right) \quad . \quad (2.82)
$$

The first line represents electrostatic energy contributions as one can immediately see by comparing to Eq. (2.17) which we derived for the ion-free case. The auxiliary potential v has therefore been chosen wisely in the sense that v can be associated with the electrostatic mean-field potential of the considered system and the resulting functional minimizes to an ionic strength modified generalized Poisson equation.

2.3.4.3. Ionic Concentrations, Chemical Potentials and Grand Potential

The grand partition function in Eq. (2.82) can be used to calculate the average number of ionic particles in the system:

$$
\langle N_\pm \rangle = \int \mathrm{d}r c_\pm^{\mathrm{s}}(r) = \frac{\partial 1/\beta \ln(Z_{\mathrm{G}})}{\partial \mu_\pm}
$$

$$
= \int \mathrm{d}r \alpha_{\mathrm{ion}}^\pm(r) \frac{\mathrm{e}^{\beta\mu_\pm \mp \beta zv}}{1 + \alpha_{\mathrm{ion}}^+(r)\mathrm{e}^{-\beta(zv - \mu_+)} + \alpha_{\mathrm{ion}}^-(r)\mathrm{e}^{-\beta(-zv - \mu_-)}} \quad , \quad (2.83)
$$

where we introduced the spatially dependent ion concentrations $c_\pm^{\mathrm{s}}$

$$
c_\pm^{\mathrm{s}}(r) = \alpha_{\mathrm{ion}}^\pm(r) \frac{\mathrm{e}^{\beta\mu_\pm \mp \beta zv}}{1 + \alpha_{\mathrm{ion}}^+(r)\mathrm{e}^{-\beta(zv - \mu_+)} + \alpha_{\mathrm{ion}}^-(r)\mathrm{e}^{-\beta(-zv - \mu_-)}} \quad , \quad (2.84)
$$

In the bulk electrolyte we have $v \to 0$ and $\alpha_{\mathrm{ion}}^\pm(r) \to 1$, giving the electrolyte bulk concentrations:

$$
c_\pm^{\mathrm{s,bulk}} = \lim_{v \to 0} c_\pm(r) = \frac{\mathrm{e}^{\beta\mu_\pm}}{1 + \mathrm{e}^{\beta\mu_+} + \mathrm{e}^{\beta\mu_-}} \quad . \quad (2.85)
$$

Furthermore, in the bulk solvent there exists no net charge, so $c_+^{\mathrm{s,bulk}} = c_-^{\mathrm{s,bulk}}$ and therefore

$$
\mathrm{e}^{\beta\mu_+} = \mathrm{e}^{\beta\mu_-} \quad . \quad (2.86)
$$

Eq. (2.86) can be inserted into Eq. (2.85) and then solved for the chemical potentials:

$$
\mathrm{e}^{\beta\mu_\pm} = \frac{1}{2} \frac{\phi_0}{1 - \phi_0} \quad , \quad (2.87)
$$

where we introduced the volume fraction of ion occupied sites $\phi_0 = 2c^{\text{s,bulk}}a^3$. This expression can now be inserted into Eq. (2.84) to get a simplified expression for the ion concentrations:

$$c_{\pm}^{\text{s}} = c^{\text{s,bulk}}\alpha_{\text{ion}}^{\pm}(\boldsymbol{r})\frac{\text{e}^{\mp\beta zv}}{1 - \phi_0 + \frac{1}{2}\phi_0\left[\alpha_{\text{ion}}^{+}(\boldsymbol{r})\text{e}^{-\beta zv} + \alpha_{\text{ion}}^{-}(\boldsymbol{r})\text{e}^{\beta zv}\right]} \quad . \tag{2.88}$$

Inserting these into Eq. (2.47) makes the PBE Eq. (2.46) the finite ion size and Stern layer modified PBE (SMPBE)

$$\nabla \cdot [\varepsilon(\boldsymbol{r})\nabla v(\boldsymbol{r})] = -4\pi n_{\text{sol}}(\boldsymbol{r}) - 4\pi n_{\text{ion}}^{\text{SMPB}}(\boldsymbol{r}) \quad , \tag{2.89}$$

with the ionic charge density given as

$$n_{\text{ion}}^{\text{SMPB}} = zc^{\text{s,bulk}}\frac{\alpha_{\text{ion}}^{+}(\boldsymbol{r})\text{e}^{-\beta zv} - \alpha_{\text{ion}}^{-}(\boldsymbol{r})\text{e}^{\beta zv}}{1 - \phi_0 + \frac{1}{2}\phi_0\left[\alpha_{\text{ion}}^{+}(\boldsymbol{r})\text{e}^{-\beta zv} + \alpha_{\text{ion}}^{-}(\boldsymbol{r})\text{e}^{\beta zv}\right]} \quad . \tag{2.90}$$

Inserting the chemical potentials into the energy functional in Eq. (2.82), finally yields the SMPB grand potential of the system

$$\begin{aligned}
\Omega_{\varepsilon,\alpha_{\text{ion}}^{\pm}}^{\text{mf}} (\{\mu_+, \mu_-\}, V, T)[v, n_{\text{el}}] &= -1/\beta \ln (Z_{\text{G}}) = \\
&\int \text{d}\boldsymbol{r}\Bigg\{ -\frac{1}{8\pi}\varepsilon(\boldsymbol{r})|\nabla v(\boldsymbol{r})|^2 + n_{\text{sol}}v \\
&- \frac{1}{\beta a^3}\ln\left(1 + \frac{1}{2}\frac{\phi_0}{1 - \phi_0}\left[\alpha_{\text{ion}}^{+}(\boldsymbol{r})\text{e}^{-\beta zv} + \alpha_{\text{ion}}^{-}(\boldsymbol{r})\text{e}^{\beta zv}\right]\right)\Bigg\} \quad ,
\end{aligned} \tag{2.91}$$

where the superscript "mf" was introduced to indicate that the functional was derived from a mean-field model.

<div style="text-align: right; font-size: 4em; font-weight: bold; color: gray;">3</div>

Methods*

In the last chapter, we derived a complete theory for the modeling of electrolytes by means of a SMPB implicit solvation approach. We also briefly discussed the principles of DFT which has become a wide-spread standard tool in various fields of chemistry. In this chapter, we now combine the two methodologies and derive all necessary equations needed for the implementation of a corresponding SMPB-DFT framework. After this, we describe the technical details related to the implementation of the SMPB-DFT scheme in the `FHI-aims`[1] all-electron DFT program package. There, a special focus lies on the particularly challenging numerical solution of the SMPBE which results from minimizing the grand potential function Eq. (2.91) with respect to the electrostatic potential. For this purpose, we develop here a function-space-based approach utilizing multipole representations of the electrostatic potential. Since a detailed discussion of the SMPB-DFT implementation was already published by us recently, this chapter closely follows and includes parts of the corresponding work [86].

3.1. Physical Observables of Interest

A main observable of interest in an implicit solvation scheme is the solvation (or electrolyzation) free energy ΔG_{sol} which resembles the free energy change induced by the combination of previously separated solute and solvent. It is defined for a particular ionic strength as

$$\Delta G_{\mathrm{sol}} = \Omega_{\circ}(\varepsilon^{\mathrm{s,bulk}}, c^{\mathrm{s,bulk}}, n_{\mathrm{sol}}(\boldsymbol{r}))$$
$$- \Omega_{\circ}(\varepsilon^{\mathrm{s,bulk}} = 1, c^{\mathrm{s,bulk}} = 0, n_{\mathrm{sol}}(\boldsymbol{r})) - \Omega_{\circ}(\varepsilon^{\mathrm{s,bulk}}, c^{\mathrm{s,bulk}}, n_{\mathrm{sol}}(\boldsymbol{r}) = 0) \quad , \quad (3.1)$$

where $\Omega_{\circ}(\varepsilon^{\mathrm{s,bulk}}, c^{\mathrm{s,bulk}}, n_{\mathrm{sol}}(\boldsymbol{r}))$ is the free energy of the solute embedded into a solvent connected to a reservoir of solvent molecules and ions, $\Omega_{\circ}(\varepsilon^{\mathrm{s,bulk}} = 1, c^{\mathrm{s,bulk}} = 0, n_{\mathrm{sol}}(\boldsymbol{r}))$ the free energy of the solute in vacuum, and $\Omega_{\circ}(\varepsilon^{\mathrm{s,bulk}}, c^{\mathrm{s,bulk}}, n_{\mathrm{sol}}(\boldsymbol{r}) = 0)$ the free energy of the pure electrolyte.

If one is interested in the specific effect of ions, another well-investigated quantity is the ion effect on the solvation free energy, given by the difference of solvation energies induced by a finite ionic strength:

$$\Delta\Delta G_{\mathrm{ion}} = \Delta G_{\mathrm{sol}}(c^{\mathrm{s,bulk}}) - \Delta G_{\mathrm{sol}}(c^{\mathrm{s,bulk}} = 0) \quad . \tag{3.2}$$

Solvation energies and ion effects on solvation energies are experimentally accessible for a wide range of different solutes, opening up the possibility to also utilize these e.g. for the parametrization of continuum models. As an effective model, our SMPB scheme gives rise to a number of parameters defining among others the dielectric or ion exclusion functions which we discuss in detail in Section 3.2.2. These *a priori* unknown variables can be determined by utilizing experimentally measured quantities like those presented here. In Chapter 4 we show that this leads to transferable parameter sets describing both solute-solvent as solute-ion interactions.

3.2. Combining Modified PB Theory and DFT

3.2.1. Modified Kohn-Sham Free Energy Functional

In Section 2.3, we introduced a statistical lattice model providing a mean-field theoretical ansatz for the desription of finite-sized ion distributions around a fixed charge distribution embedded into a dielectric continuum. The resulting SMPB approach led to the derivation of a free energy functional as given in Eq. (2.91) depending on both the electrostatic potential v and the (fixed) solute charge density n_{sol}. However, since this derivation was based on a mean-field approximation for the electrostatic potential, correlated interactions are by construction not included. While ionic correlation effects can be safely ignored at least for the case of monovalent ions, [73] dynamic interactions between electrons are often critical for chemical reactions. To account for this, we introduced in Section 2.2.3 the xc functional correcting both for Pauli repulsions as for correlated interactions between the electrons. In the spirit of DFT, the free energy energy functional of Eq. (2.91) can be rewritten as modified KS functional (cf. Eq. (2.28))

$$\Omega_{\varepsilon,\alpha_{\mathrm{ion}}^{\pm}}[v, n_{\mathrm{el}}] = T^{\mathrm{S}}[n_{\mathrm{el}}] + E^{\mathrm{xc}}[n_{\mathrm{el}}] + \Omega_{\varepsilon,\alpha_{\mathrm{ion}}^{\pm}}^{\mathrm{mf}}[v, n_{\mathrm{el}}] + \Omega_{\varepsilon}^{\mathrm{non-mf}}[n_{\mathrm{el}}] \quad . \tag{3.3}$$

Eq. (3.3) also considers the kinetic energy of the electrons, while at the same time neglecting finite temperature corrections for the nuclear motion. Such contributions, while in principle accessible from e.g. *ab initio* atomistic thermodynamics, [128] are often assumed to be not largely effected by the presence of an electrolytic environment. [5,14,16] In consequence these cancel out in the evaluation of energy differences like solvation energies or ion effects on solvation energies which are the only properties of interest in the scope of this thesis (cf. Section 3.1). We will therefore throughout this work neglect finite temperature effects of the nuclei.

While the derived SMPB model explicitly accounts for solute-ion repulsions, we did so far not consider the presence of non-mean-field non-electrostatic solute-solvent interactions. As briefly mentioned in the introductory chapter, we correct for this by adding a further

term in the KS functional which is denoted as $\Omega_\varepsilon^{\mathrm{non-mf}}$ in Eq. (3.3). While in principle far from trivial, such a functional can to a good degree of accuracy be modeled as a linear function of volume and surface of the cavity formed around the solute.[16] This seemingly crude approximation was shown by Andreussi *et al.*[5] to be reasonably accurate for the evaluation of macroscopic properties like solvation energies, as in detail discussed in Section 4.1. As further described in the following section, both cavity surface and volume can thereby be written as integrals over the electron density, which is why we consider here only a dependence on n_{el} for this term.

3.2.2. Modeling Functions for Solute-Electrolyte Interactions

The most sensitive part in effective implicit solvation schemes is the functional form of the dielectric function which determines the predicted electrostatic solvation energies. In case of our developed SMPB scheme, additional models have to be defined for the non-mean-field solute-solvent interactions and ion exclusion functions. Since effective solvation schemes model only the solute explicitly, corresponding functional forms have to be constructed solely on the basis of properties of the solute. When choosing descriptors and functions wisely, this enables to derive transferable parameters which can be applied without re-optimization to a wide range of different solutes. As later shown in Chapter 4 the electron density of the solute resembles such an efficient descriptor which is easily accessible from DFT and enables a predictive modeling of solvation and ion effects.

3.2.2.1. Dielectric Function

As discussed in Section 2.1.1, the solvent's dielectric function is generally a highly complicated, frequency-dependent tensorial quantity. It can in principle be obtained from explicit solvent simulations as recently achieved for the anisotropic dielectric spectrum of water at the level of force-field molecular dynamics (MD) simulations.[129] Although such studies are important to reveal the physical nature of the dielectric response, an explicit treatment of solvent molecules is generally not tractable on the level of DFT calculations. Fortunately, the dielectric function can be, however, often efficiently approximated as a simple step function varying from the isotropic, low-frequency limit dielectric permittivity of the solvent to the vacuum permittivity at the solvation cavity (cf. Section 2.1.2). This fact eventually led to the rise and wide success of implicit solvation methods differing mainly in the definition of the solvation cavity or dielectric transition region.[18,19] The transition region uniquely defines the electrostatic solvation energy (cf. Eq. (2.17)) making it a crucial factor for the performance of such effective approaches. Recently, such cavities have been successfully defined in terms of an isosurface of the solute's electron density yielding highly transferable parametrizations.[5,14,18,23] Assuming a sharp step function for the dielectric transition further simplifies the solution of the generalized Poisson equation and enables a separate treatment of the solvent and solute regions. The two resulting linear Poisson equations are then coupled by the respective boundary conditions on the solvation cavity.[18]

Although such sharp-cavity approaches were shown to often be sufficient for reasonably accurate solvation energies, a physically more realistic treatment is to further introduce

a parameter describing the smoothness of the dielectric transition.[5,14,16] Such an approach also provides a numerically stable definition of all physical properties on the full computational domain and simplifies a systematic assessment and improvement of the methodological setup. In this thesis, we therefore also utilize a smooth parametrization of the dielectric function and adopt a form as suggested by Andreussi *et al.*,[5] given as

$$\varepsilon_{n_{\min},n_{\max}}[n_{\mathrm{el}}] = \begin{cases} 1 & n_{\mathrm{el}} > n_{\max}, \\ \exp\left(t_{n_{\min},n_{\max}}\left(\ln(n_{\mathrm{el}})\right)\right) & n_{\min} < n_{\mathrm{el}} < n_{\max} \\ \varepsilon^{\mathrm{s,bulk}} & n_{\mathrm{el}} < n_{\min} \end{cases} , \qquad (3.4)$$

with

$$t_{n_{\min},n_{\max}}\left(\ln(n_{\mathrm{el}})\right) = \frac{\ln(\varepsilon^{\mathrm{s,bulk}})}{2\pi}\left[2\pi\frac{\ln(n_{\max}) - \ln(n_{\mathrm{el}})}{\ln(n_{\max}) - \ln(n_{\min})} - \sin\left(2\pi\frac{\ln(n_{\max}) - \ln(n_{\mathrm{el}})}{\ln(n_{\max}) - \ln(n_{\min})}\right)\right] . \tag{3.5}$$

This function goes to one for large n_{el} close to the nuclei and switches smoothly to $\varepsilon^{\mathrm{s,bulk}}$ for low n_{el} far away. The transition region – i.e. its position and width with respect to the electron density – is controlled by the two parameters $n_{\min}$ and $n_{\max}$. There are two main benefits to this particular functional form. First, that its gradients are exactly zero outside of the transition region. Second, that also $\nabla \ln(\varepsilon[n_{\mathrm{el}}])$, which appears in the function-space-based solution scheme developed here (cf. Eqs. (3.74) and (3.76) in Section 3.4.1.1 below), is a smooth function[5] increasing both numerical stability and convergence. Fig. 3.1 exemplarily depicts such a dielectric function for a nitrobenzene molecule embedded in implicit water.

Finally, the choice of the electron density used in the definition of the dielectric transition deserves further mention. In principle, the evaluation could either be based on the true electron density n_{el} in each SCF step of the KS equation solver, or it could be based on a rigid electron density obtained e.g. by mere superposition of free atom densities. In contrast to other authors[24] we hitherto found only a negligible impact of a fully self-consistent cavity on the SCF convergence as long as the cavity lies within reasonable distances to the charge distribution, cf. Fig. 3.7 below. All calculations in this thesis are correspondingly performed using the self-consistent density, through which we are able to model the mutual influence of the dielectric function and the electron density.

3.2.2.2. Non-Mean-Field Solute-Solvent Interactions

In general, the solvation cavity defined through the transition functions also governs the non-mean-field part of the free energy functional $\Omega^{\mathrm{non-mf}}[n_{\mathrm{el}}]$. Non-mean-field free energy contributions mainly result from the exclusion of solvent molecules from the cavity and non-bonded short-range, as well as dispersion interactions

$$\Omega_\varepsilon^{\mathrm{non-mf}}[n_{\mathrm{el}}] = \Omega_\varepsilon^{\mathrm{cav}}[n_{\mathrm{el}}] + \Omega_\varepsilon^{\mathrm{rep}}[n_{\mathrm{el}}] + \Omega_\varepsilon^{\mathrm{dis}}[n_{\mathrm{el}}] \quad , \tag{3.6}$$

respectively. In this work we employ the effective parametrization for these terms suggested by Andreussi *et al.*,[5] which provide these terms as mere functions of the "quantum surface" S and the "quantum volume" V of the solvation cavity

$$\Omega_\varepsilon^{\mathrm{non-mf}}[n_{\mathrm{el}}] = (\alpha + \gamma)\, S[n_{\mathrm{el}}] + \beta V[n_{\mathrm{el}}] \quad , \tag{3.7}$$
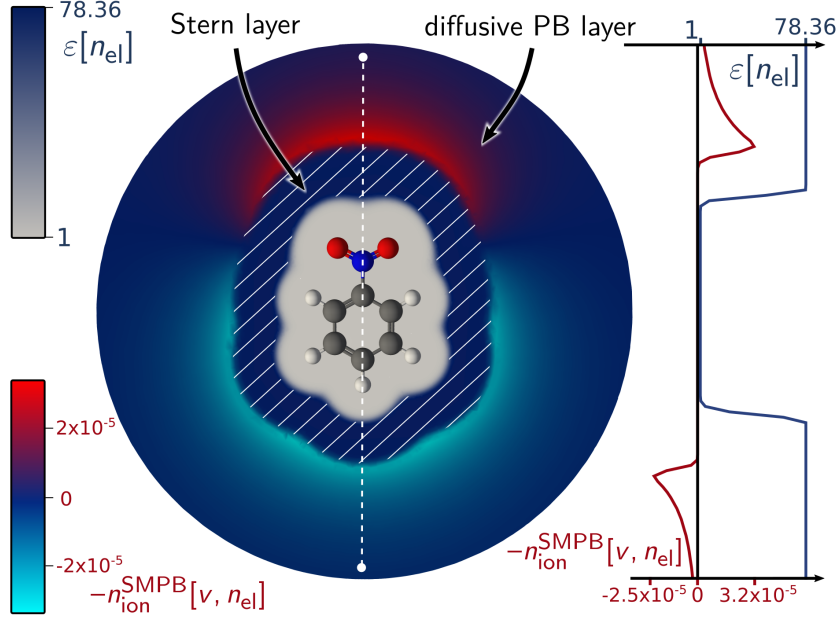
Figure 3.1.: Schematic visualization of nitrobenzene dissolved in water containing a 1 M 1:1 electrolyte as described at the level of SMPB theory with additional ion exclusion (Stern) layer. The gray innermost part around the molecule denotes the solvation cavity, in which $\varepsilon[n_{\mathrm{el}}] = 1$, the remaining area denotes the solvent region, in which $\varepsilon[n_{\mathrm{el}}] = \varepsilon^{\mathrm{s,bulk}}$. A contour plot of the ionic charge density $n_{\mathrm{ion}}^{\mathrm{SMPB}}[v, n_{\mathrm{el}}]$ is overlaid (using the intuitive sign convention), where the striped region depicts the ion-free Stern layer. On the right $\varepsilon[n_{\mathrm{el}}]$ and $n_{\mathrm{ion}}^{\mathrm{SMPB}}[v, n_{\mathrm{el}}]$ are shown as 1D cut along the dashed line through the center of the molecule. Reproduced with permission from ref. [86]. © 2016 American Chemical Society.

with γ the surface tension of the solvent. α and β constitute additional free parameters of the model. V and S are hereby defined as

$$V = \int \mathrm{d}\boldsymbol{r}\,\vartheta[n_{\mathrm{el}}] \tag{3.8}$$

and

$$S = \int \mathrm{d}\boldsymbol{r}\left\{\left(\vartheta\left[n_{\mathrm{el}} + \frac{\Delta}{2}\right] - \vartheta\left[n_{\mathrm{el}} - \frac{\Delta}{2}\right]\right) \times \frac{|\nabla n_{\mathrm{el}}|}{\Delta}\right\} \quad, \tag{3.9}$$

with the switching function ϑ defined in terms of the chosen dielectric function

$$\vartheta\left[n_{\mathrm{el}}\right] = \frac{\varepsilon^{\mathrm{s,bulk}} - \varepsilon[n_{\mathrm{el}}]}{\varepsilon^{\mathrm{s,bulk}} - 1} \quad. \tag{3.10}$$

The integrand of Eq. (3.9) is a numerical derivative of the switching function evaluated through finite differences with a parameter Δ. In the present work this parameter is set to a low value of 10^{-8}, with negligible effect of variations around this value on reported solvation free energies.

The free parameters $\{(\alpha + \gamma), \beta, n_{\min}, n_{\max}\}$ determining the solvation cavity and the non-mean-field free energy contribution of solute-solvent interactions were optimized by

Andreussi *et al.* in order to reproduce experimental hydration energies for a large test set of neutral molecules. [5] In Section 4.1, we present these results and show the generally good accuracy achieved with the their parametrization. Throughout this thesis we therefore use the parameter set of Andreussi and co-workers without further optimization.

3.2.2.3. Ionic Exclusion Function

From a physical point of view, solvated ions are expected to interact with the solute not only via the mean-field electrostatic potential but also via repulsive interactions. In this thesis, we assume that such repulsions can – in analogy to the solute-solvent interactions – also be parametrized as a function of the solute's electron density. In Section 4.2 we show that this approach indeed leads to transferable parameter sets for the case of monovalent salt solutions. Utilizing the same functional form as for the dielectric function, the ion exclusion functions are given by

$$
\alpha^\pm_{\mathrm{ion},n^{\alpha,\pm}_{\min},n^{\alpha,\pm}_{\max}}[n_{\mathrm{el}}] = \begin{cases} 0 & n_{\mathrm{el}} > n^{\alpha,\pm}_{\max} \\ \frac{1}{\varepsilon^{\mathrm{s,bulk}}-1}\left(\exp\left(t_{n^{\alpha,\pm}_{\min},n^{\alpha,\pm}_{\max}}(\ln(n_{\mathrm{el}}))\right)-1\right) & n^{\alpha,\pm}_{\min} < n_{\mathrm{el}} < n^{\alpha,\pm}_{\max} \\ 1 & n_{\mathrm{el}} < n^{\alpha,\pm}_{\min} \end{cases},
$$

$$(3.11)$$

where the ion-dependent parameters $\{n^{\alpha,\pm}_{\min}, n^{\alpha,\pm}_{\max}\}$ define the concentration transition for cations and anions and

$$
t_{n^{\alpha,\pm}_{\min},n^{\alpha,\pm}_{\max}}(\ln(n_{\mathrm{el}})) = \frac{\ln(\varepsilon^{\mathrm{s,bulk}})}{2\pi}\left[2\pi\frac{\ln(n^{\alpha,\pm}_{\max})-\ln(n_{\mathrm{el}})}{\ln(n^{\alpha,\pm}_{\max})-\ln(n^{\alpha,\pm}_{\min})}-\sin\left(2\pi\frac{\ln(n^{\alpha,\pm}_{\max})-\ln(n_{\mathrm{el}})}{\ln(n^{\alpha,\pm}_{\max})-\ln(n^{\alpha,\pm}_{\min})}\right)\right].
$$

$$(3.12)$$

Physically, both dielectric and ion exclusion function transitions are related to each other since both depend on the effective size of the solute as described here by isosurfaces of the solute's electron density. We therefore substitute the ion parameters with a shift $d^\pm_{\alpha_{\mathrm{ion}}}$ and a scaling parameter $\xi^\pm_{\alpha_{\mathrm{ion}}}$ defined with respect to the parameters of the dielectric transition

$$
n^{\alpha,\pm}_{\min/\max} = \exp\left(a^\pm_{\min/\max} \pm (a^\pm_{\max}-a^\pm_{\min})\frac{1-\xi^\pm_{\alpha_{\mathrm{ion}}}}{2}\right) \tag{3.13}
$$

with

$$
a^\pm_{\min/\max} = \ln(n_{\min/\max}) + (\ln(n_{\min})-\ln(n_{\max}))\,d^\pm_{\alpha_{\mathrm{ion}}}. \tag{3.14}
$$

$d^\pm_{\alpha_{\mathrm{ion}}} > 0$ then corresponds to the inclusion of a Stern layer or non-diffusive ion region around the solvation cavity and an increase (decrease) of $\xi^\pm_{\alpha_{\mathrm{ion}}}$ to a smoothening (sharpening) of the Stern layer transition. In the case of aqueous solutions the inclusion of an ion-free Stern layer physically accounts for both the more or less rigid hydration shells of the ions and the hydration layer of the solute (cf. Section 4.2). Figure 3.1 shows exemplarily for nitrobenzene the ionic charge density as resulting from the above presented parametrization strategy.

3.2.3. Modified Kohn-Sham Equations

In Section 3.2.1, we introduced the modified KS free energy functional $\Omega_{\varepsilon,\alpha^\pm_{\text{ion}}}[v, n_{\text{el}}]$ given in Eq. (3.3), which provides the basis of the combined SMPB-DFT formalism. In order to calculate physically relevant properties of systems, one has to find the minimum of this functional with respect to both n_{el} and v. Analogously to standard DFT (cf. Section 2.2.3.2), the minimization with respect to the electron density yields KS equations which define the optimal electron density $n_{\text{el,o}}$. Similarly, the dependency on the electrostatic potential can be removed by minimization, leading to a Poisson-like equation, in our case the SMPBE.

We start by constructing, analogously to Section 2.2.3.2, a Lagrangian functional which constrains the orthonormality of the orbitals:

$$\mathcal{L}[v, n_{\text{el}}] = \Omega_{\varepsilon,\alpha^\pm_{\text{ion}}}[v, n_{\text{el}}] + \sum_{l=1}^{N_{\text{states}}} \sum_{k=1}^{N_{\text{states}}} \lambda_{lk} \left[\int \mathrm{d}\boldsymbol{r}\, \psi_l^* \psi_k - \delta_{lk} \right] \quad . \tag{3.15}$$

This functional can be utilized for a variational minimization with respect to the single-electron wave-functions ψ_l

$$\frac{\delta \mathcal{L}[v, n_{\text{el}}]}{\delta \psi_l^*} = 0 \ \forall l \quad , \tag{3.16}$$

which then yields the modified KS equations

$$\sum_{k=1}^{N_{\text{states}}} \lambda_{lk}\psi_k = \frac{\delta T^{\text{S}}[n_{\text{el}}]}{\delta \psi_l^*} + \left[\frac{\delta E^{\text{xc}}[n_{\text{el}}]}{\delta n_{\text{el}}} + \frac{\delta \Omega^{\text{mf}}_{\varepsilon,\alpha^\pm_{\text{ion}}}[v, n_{\text{el}}]}{\delta n_{\text{el}}} + \frac{\delta \Omega^{\text{non-mf}}_\varepsilon[n_{\text{el}}]}{\delta n_{\text{el}}} \right] \frac{\mathrm{d}n_{\text{el}}}{\mathrm{d}\psi_l^*}$$

$$= \frac{1}{2}\nabla^2 \psi_l + \left[v^{\text{xc}} + \frac{\delta \Omega^{\text{mf}}_{\varepsilon,\alpha^\pm_{\text{ion}}}[v, n_{\text{el}}]}{\delta n_{\text{el}}} + \frac{\delta \Omega^{\text{non-mf}}_\varepsilon[n_{\text{el}}]}{\delta n_{\text{el}}} \right] \psi_l \quad . \tag{3.17}$$

Applying Eq. (2.14) to evaluate the functional derivative of the mean-field part then gives

$$\frac{\delta \Omega^{\text{mf}}_{\varepsilon,\alpha^\pm_{\text{ion}}}[v, n_{\text{el}}]}{\delta n_{\text{el}}}$$

$$= v - \frac{1}{8\pi} \frac{\partial \varepsilon[n_{\text{el}}]}{\partial n_{\text{el}}} |\nabla v|^2 - \frac{1}{2} \frac{\phi_0}{\beta a^3} \frac{\frac{\partial \alpha^+_{\text{ion}}[n_{\text{el}}]}{\partial n_{\text{el}}} \mathrm{e}^{-\beta z v} + \frac{\partial \alpha^-_{\text{ion}}[n_{\text{el}}]}{\partial n_{\text{el}}} \mathrm{e}^{\beta z v}}{1 - \phi_0 + \frac{1}{2}\phi_0 \left[\alpha^+_{\text{ion}}[n_{\text{el}}]\mathrm{e}^{-\beta z v} + \alpha^-_{\text{ion}}[n_{\text{el}}]\mathrm{e}^{\beta z v} \right]} \quad , \tag{3.18}$$

while the non-mean-field part separates into two parts

$$\frac{\delta \Omega^{\text{non-mf}}_\varepsilon[n_{\text{el}}]}{\delta n_{\text{el}}} = (\alpha + \gamma)\frac{\delta S[n_{\text{el}}]}{\delta n_{\text{el}}} + \beta \frac{\partial \vartheta[n_{\text{el}}]}{\partial n_{\text{el}}} \quad . \tag{3.19}$$

The first term of the last equation can be further recast into

$$(\alpha + \gamma)\frac{\delta S[n_{\text{el}}]}{\delta n_{\text{el}}} = (\alpha + \gamma)\left[\frac{\partial s[n_{\text{el}}]}{\partial n_{\text{el}}} + \nabla \frac{\partial s[n_{\text{el}}]}{\partial \nabla n_{\text{el}}} \right] \tag{3.20}$$

3. Methods

with

$$\frac{\partial s[n_{\text{el}}]}{\partial n_{\text{el}}} = \left(\frac{\partial \vartheta \left[n_{\text{el}} + \frac{\Delta}{2} \right]}{\partial n_{\text{el}}} - \frac{\partial \vartheta \left[n_{\text{el}} - \frac{\Delta}{2} \right]}{\partial n_{\text{el}}} \right) \times \frac{|\nabla n_{\text{el}}|}{\Delta} \tag{3.21}$$

and

$$\nabla \frac{\partial s[n_{\text{el}}]}{\partial \nabla n_{\text{el}}} = \nabla \left\{ \left(\vartheta \left[n_{\text{el}} + \frac{\Delta}{2} \right] - \vartheta \left[n_{\text{el}} - \frac{\Delta}{2} \right] \right) \frac{1}{\Delta} \frac{\nabla n_{\text{el}}}{|\nabla n_{\text{el}}|} \right\} \quad . \tag{3.22}$$

While the first partial derivative can be easily evaluated, the second requires the calculation of computationally expensive Hessian matrix elements of the basis functions φ_i (for the definition cf. Eqs. (3.34) and (3.35) below). In static DFT calculations, one, however, only needs to evaluate KS operator matrix elements, for which the ∇-operator can be transfered to the basis functions similarly to the procedure commonly used for the GGA-xc-operator[1] and which gets rid of this bottleneck:

$$- \int \mathrm{d}\boldsymbol{r} \varphi_i \varphi_j \left(\nabla \frac{\partial s[n_{\text{el}}]}{\partial \nabla n_{\text{el}}} \right) = \int \mathrm{d}\boldsymbol{r} \nabla \left[\varphi_i \varphi_j \right] \frac{\partial s[n_{\text{el}}]}{\partial \nabla n_{\text{el}}} \quad . \tag{3.23}$$

While the implemented SMPB-DFT methodology supports a fully self-consistent minimization of the KS functional, it can often be useful to treat the non-mean-field part $\Omega_\varepsilon^{\text{non}-\text{mf}}$ as a non-self-consistent post-correction of the free energy, thereby assuming that $\frac{\delta \Omega_\varepsilon^{\text{non}-\text{mf}}[n_{\text{el}}]}{\delta n_{\text{el}}} \approx 0$. The results of Section 4.1 show that such an approximation yields only negligible errors, while simultaneously allowing to avoid the demanding computation of the second derivatives of the free energy functional as well as to circumvent numerical instabilities that were observed before.[130]

After determining all necessary derivatives, we can then again perform a unitary transformation on Eq. (3.17) to arrive at the modified KS equations (cf. Eq. (2.34)) with the modified KS operator

$$\hat{h}^{\text{KS}} = \hat{t}_{\text{s}} + v_{\text{xc}} + v$$
$$\left. \begin{array}{l} -\frac{1}{8\pi} \frac{\partial \varepsilon[n_{\text{el}}]}{\partial n_{\text{el}}} |\nabla v|^2 - \frac{1}{2} \frac{\phi_0}{\beta a^3} \frac{\frac{\partial \alpha_{\text{ion}}^+[n_{\text{el}}]}{\partial n_{\text{el}}} \mathrm{e}^{-\beta z v} + \frac{\partial \alpha_{\text{ion}}^-[n_{\text{el}}]}{\partial n_{\text{el}}} \mathrm{e}^{\beta z v}}{1 - \phi_0 + \frac{1}{2} \phi_0 \left[\alpha_{\text{ion}}^+[n_{\text{el}}] \mathrm{e}^{-\beta z v} + \alpha_{\text{ion}}^-[n_{\text{el}}] \mathrm{e}^{\beta z v} \right]} \\ + (\alpha + \gamma) \left[\frac{\partial s[n_{\text{el}}]}{\partial n_{\text{el}}} + \nabla \frac{\partial s[n_{\text{el}}]}{\partial \nabla n_{\text{el}}} \right] + \beta \frac{\partial \vartheta}{\partial n_{\text{el}}} \end{array} \right\} \delta v_{\varepsilon, \alpha_{\text{ion}}}^{\text{KS,SMPB}}[v, n_{\text{el}}] \quad . \tag{3.24}$$

Here we introduced $\delta v_{\varepsilon, \alpha_{\text{ion}}}^{\text{KS,SMPB}}$ representing the perturbation on the KS Hamiltonian induced by the embedding into the electrolytic environment.

3.2.4. SMPB Equation

The modified KS equations derived above allows us to evaluate the self-consistent electron density $n_{\text{el,o}}$ of the solute as embedded into the electrolytic environment. Similarly, the electrostatic potential v_{o} of the system has to be determined from the modified KS functional

(Eq. (3.3)) by functional minimization with respect to v, again using Eq. (2.14). This leads to the SMPBE, Eq. (2.89)

$$\nabla \cdot [\varepsilon[n_{\mathrm{el}}]\nabla v] = -4\pi n_{\mathrm{sol}} - 4\pi n_{\mathrm{ion}}^{\mathrm{SMPB}}[v, n_{\mathrm{el}}] \quad , \tag{3.25}$$

but with the ionic charge densities given by (cf. Eq. (2.90))

$$n_{\mathrm{ion}}^{\mathrm{SMPB}}[v, n_{\mathrm{el}}] = zc^{\mathrm{s,bulk}} \frac{\alpha_{\mathrm{ion}}^{+}[n_{\mathrm{el}}]\mathrm{e}^{-\beta zv} - \alpha_{\mathrm{ion}}^{-}[n_{\mathrm{el}}]\mathrm{e}^{\beta zv}}{1 - \phi_0 + \frac{1}{2}\phi_0 \left[\alpha_{\mathrm{ion}}^{+}[n_{\mathrm{el}}]\mathrm{e}^{-\beta zv} + \alpha_{\mathrm{ion}}^{-}[n_{\mathrm{el}}]\mathrm{e}^{\beta zv}\right]} \quad . \tag{3.26}$$

3.2.5. Minimum Free Energy Expression

The modified KS and SMPB equations can now be inserted into Eq. (3.3) analogously to the procedure in Section 2.2.3.3 in order to obtain the minimum free energy expression in the SMPB-DFT model:

$$\Omega_{\circ}(\varepsilon^{\mathrm{s,bulk}}, c^{\mathrm{s,bulk}}, n_{\mathrm{sol},\circ})$$

$$= \sum_{l=1}^{N_{\mathrm{states}}} \epsilon_{l,\circ} - \int \mathrm{d}\boldsymbol{r}\, n_{\mathrm{el},\circ}v_{\circ}^{\mathrm{xc}} + E^{\mathrm{xc}}[n_{\mathrm{el},\circ}] - \frac{1}{2}\int \mathrm{d}\boldsymbol{r}\, n_{\mathrm{el},\circ}v_{\circ} + \frac{1}{2}\int \mathrm{d}\boldsymbol{r}\, n_{\mathrm{nuc}}v_{\circ}$$

$$- \int \mathrm{d}\boldsymbol{r}\, n_{\mathrm{el},\circ}\delta v_{\varepsilon,\alpha_{\mathrm{ion}},\circ}^{\mathrm{KS,SMPB}} +$$

$$\left.\begin{array}{l} \int \mathrm{d}\boldsymbol{r}\left\{-\frac{1}{2}n_{\mathrm{ion}}^{\mathrm{SMPB}}[v_{\circ}, n_{\mathrm{el},\circ}]v_{\circ}\right. \\[2mm] \left. -\frac{1}{\beta a^3}\ln\left(1 + \frac{1}{2}\frac{\phi_0}{1-\phi_0}\left[\alpha_{\mathrm{ion}}^{+}[n_{\mathrm{el},\circ}]\mathrm{e}^{-\beta zv_{\circ}} + \alpha_{\mathrm{ion}}^{-}[n_{\mathrm{el},\circ}]\mathrm{e}^{\beta zv_{\circ}}\right)\right]\right\} \end{array}\right\} \Omega_{\alpha_{\mathrm{ion}}^{\pm}}^{\mathrm{ion}}[v_{\circ}, n_{\mathrm{el},\circ}]$$

$$+ \Omega_{\varepsilon}^{\mathrm{non-mf}}[n_{\mathrm{el},\circ}] \quad . \tag{3.27}$$

In this equation, the part highlighted in blue is equivalent to the expression in standard DFT (cf. Eq. (2.40)) and comprises the sum over all eigenstates, xc and electrostatic energy correction terms. The latter correspond to the sum of double-counting correction and nuclei-nuclei interaction energies in standard DFT. The red part denotes the KS Hamiltonian correction terms which arise due to the electron density dependence of the dielectric and ion exclusion functions. Finally, highlighted in dark green are ionic correction terms to the standard DFT expression $\Omega_{\alpha_{\mathrm{ion}}^{\pm}}^{\mathrm{ion}}$ and in lighter green the non-mean-field solute-solvent interaction energy.

For the later derivations in this chapter, a different notation for $\Omega_{\circ}$ in terms of electrostatic and nonelectrostatic contributions will be useful. For that, we again consider the KS functional as given in Eq. (3.3):

$$\Omega_{\circ}(\varepsilon^{\mathrm{s,bulk}}, c^{\mathrm{s,bulk}}, n_{\mathrm{sol},\circ}) = T^{\mathrm{S}}[n_{\mathrm{el},\circ}] + E^{\mathrm{xc}}[n_{\mathrm{el},\circ}]$$

$$+ \underbrace{\Omega^{\mathrm{elstat}}[n_{\mathrm{el},\circ}, v_{\circ}] + \Omega_{\alpha_{\mathrm{ion}}^{\pm}}^{\mathrm{nonel}}[n_{\mathrm{el},\circ}, v_{\circ}]}_{\Omega_{\varepsilon,\alpha_{\mathrm{ion}}^{\pm}}^{\mathrm{mf}}[v_{\circ}, n_{\mathrm{el},\circ}]} + \Omega_{\varepsilon}^{\mathrm{non-mf}}[n_{\mathrm{el},\circ}] \quad , \tag{3.28}$$

41

where we rewrote the functional $\Omega^{\mathrm{mf}}_{\varepsilon,\alpha^{\pm}_{\mathrm{ion}}}$ in terms of its electrostatic and nonelectrostatic contributions, given as

$$\Omega^{\mathrm{elstat}}[n_{\mathrm{el,o}}, v_{\mathrm{o}}] = \frac{1}{2}\int \mathrm{d}\boldsymbol{r}\, n_{\mathrm{tot,o}} v_{\mathrm{o}}$$

$$\Omega^{\mathrm{nonel}}_{\alpha^{\pm}_{\mathrm{ion}}}[n_{\mathrm{el,o}}, v_{\mathrm{o}}] = \Omega^{\mathrm{ion}}_{\alpha^{\pm}_{\mathrm{ion}}}[n_{\mathrm{el,o}}, v_{\mathrm{o}}] - \frac{1}{2}\int \mathrm{d}\boldsymbol{r}\, n^{\mathrm{SMPB}}_{\mathrm{ion}}[n_{\mathrm{el,o}}, v_{\mathrm{o}}] v_{\mathrm{o}} \quad , \tag{3.29}$$

with the total charge density $n_{\mathrm{tot}} = n_{\mathrm{sol}} + n^{\mathrm{SMPB}}_{\mathrm{ion}}$.

3.2.6. Modified Debye-Hückel Theory

The complicated non-linear ionic charge density expression given in Eq. (3.26) can in many cases be simplified by expansion into a Taylor series up to 1st order around $v = 0$, analogously to the procedure in standard DH theory (cf. Section 2.3.2). This yields the charge density of the LPBE

$$n^{\mathrm{LPB}}_{\mathrm{ion}}[v, n_{\mathrm{el}}] = -\frac{\kappa^2 \varepsilon^{\mathrm{s,bulk}}}{4\pi}\left\{ -\frac{1}{2\beta z}\frac{\alpha^+_{\mathrm{ion}}[n_{\mathrm{el}}] - \alpha^-_{\mathrm{ion}}[n_{\mathrm{el}}]}{1 - \phi_0 + \frac{1}{2}\phi_0\left[\alpha^+_{\mathrm{ion}}[n_{\mathrm{el}}] + \alpha^-_{\mathrm{ion}}[n_{\mathrm{el}}]\right]} \right.$$

$$\left. + \frac{\phi_0\alpha^+_{\mathrm{ion}}[n_{\mathrm{el}}]\alpha^-_{\mathrm{ion}}[n_{\mathrm{el}}] - \frac{1}{2}(\phi_0 - 1)\left[\alpha^+_{\mathrm{ion}}[n_{\mathrm{el}}] + \alpha^-_{\mathrm{ion}}[n_{\mathrm{el}}]\right]}{\left(1 - \phi_0 + \frac{1}{2}\phi_0\left[\alpha^+_{\mathrm{ion}}[n_{\mathrm{el}}] + \alpha^-_{\mathrm{ion}}[n_{\mathrm{el}}]\right]\right)^2}v \right\}$$

$$= \bar{\kappa}^2_0[n_{\mathrm{el}}] + \bar{\kappa}^2[n_{\mathrm{el}}]v \quad , \tag{3.30}$$

which becomes the well-known DH expression $n^{\mathrm{LPB}}_{\mathrm{ion}} = -\frac{1}{4\pi}\varepsilon^{\mathrm{s,bulk}}\kappa^2 v$ in the case of $\alpha^{\pm}_{\mathrm{ion}} = 1$ and $a = 0$. Although Eq. (3.30) is still a relatively complicated function of the electron density, it depends linearly on the electrostatic potential which drastically simplifies the numerical solution of the resulting linearized PDE, the LPBE, as given in Eq. (2.52).

Similarly to the ionic charge density, one can also obtain a corresponding simplified KS functional by expanding the logarithmic function in Eq. (2.91) as a Taylor series around $v = 0$ up to 2nd order and the mean-field functional then becomes

$$\Omega^{\mathrm{mf,LPB}}_{\varepsilon,\alpha^{\pm}_{\mathrm{ion}}}[v, n_{\mathrm{el}}] = \int \mathrm{d}\boldsymbol{r}\left\{ -\frac{\varepsilon[n_{\mathrm{el}}]}{8\pi}|\nabla v|^2 + n_{\mathrm{sol}}v \right.$$

$$\left. -\frac{1}{\beta a^3}\ln\left(1 + \frac{1}{2}\frac{\phi_0}{1 - \phi_0}\left[\alpha^+_{\mathrm{ion}}[n_{\mathrm{el}}] + \alpha^-_{\mathrm{ion}}[n_{\mathrm{el}}]\right]\right) + \frac{1}{2}n^{\mathrm{LPB}}_{\mathrm{ion}}[v, n_{\mathrm{el}}]v \right\} \quad . \tag{3.31}$$

Setting the functional derivative of $\Omega^{\mathrm{mf,LPB}}_{\varepsilon,\alpha^{\pm}_{\mathrm{ion}}}[v, n_{\mathrm{el}}]$ with respect to v to zero then yields the LPBE as defined above. Note again that in the case $\alpha^{\pm}_{\mathrm{ion}} = 1$ and $a = 0$ we recover a free energy expression which minimizes to the original DH-LPBE with a minimum free energy expression being just the electrostatic energy as given in Eq. (2.18) (plus a constant non-relevant factor), since all non-electrostatic interactions and entropy terms are removed.

Setting the functional derivative with respect to n_{el} equal to zero leads to the corresponding modified KS equations with the additional operator (defined analogously to $\delta v_{\text{KS}}^{\text{SMPB}}$ in Eq. (3.24))

$$
\begin{aligned}
\delta v_{\text{KS}}^{\text{LPB}}[v, n_{\text{el}}] = & -\frac{1}{8\pi} \frac{\partial \varepsilon[n_{\text{el}}]}{\partial n_{\text{el}}} |\nabla v|^2 + \frac{1}{2} \frac{\partial n_{\text{ion}}^{\text{LPB}}[v, n_{\text{el}}]}{\partial n_{\text{el}}} v^2 \\
& - \frac{1}{2\beta a^3} \left(1 + \frac{1}{2} \frac{\phi_0}{1 - \phi_0} \left[\alpha_{\text{ion}}^+[n_{\text{el}}] + \alpha_{\text{ion}}^-[n_{\text{el}}] \right] \right)^{-1} \\
& \times \frac{\phi_0}{1 - \phi_0} \left(\frac{\partial \alpha_{\text{ion}}^+[n_{\text{el}}]}{\partial n_{\text{el}}} + \frac{\partial \alpha_{\text{ion}}^-[n_{\text{el}}]}{\partial n_{\text{el}}} \right) \quad ,
\end{aligned}
\tag{3.32}
$$

with the remaining partial derivative $\frac{\partial n_{\text{ion}}^{\text{LPB}}}{\partial n_{\text{el}}}$ given explicitly in Appendix A.1.

Inserting both modified KS equation and LPBE into the modified KS functional in Eq. (3.31) gives the minimum free energy expression in the LPB approximation

$$
\begin{aligned}
& \Omega_\circ^{\text{LPB}}(\varepsilon^{\text{s,bulk}}, c^{\text{s,bulk}}, n_{\text{sol},\circ}) \\
& = \sum_{l=1}^{N_{\text{states}}} \epsilon_{l,\circ} - \int \mathrm{d}\boldsymbol{r} n_{\text{el},\circ} v_\circ^{\text{xc}} + E^{\text{xc}}[n_{\text{el},\circ}] - \frac{1}{2} \int \mathrm{d}\boldsymbol{r} n_{\text{el},\circ} v_\circ + \frac{1}{2} \int \mathrm{d}\boldsymbol{r} n_{\text{nuc}} v_\circ \\
& - \int \mathrm{d}\boldsymbol{r} n_{\text{el},\circ} \delta v_{\varepsilon,\alpha_{\text{ion}},\circ}^{\text{KS,LPB}} - \frac{1}{\beta a^3} \int \mathrm{d}\boldsymbol{r} \left\{ \ln \left(1 + \frac{1}{2} \frac{\phi_0}{1 - \phi_0} \left[\alpha_{\text{ion}}^+[n_{\text{el},\circ}] + \alpha_{\text{ion}}^-[n_{\text{el},\circ}] \right] \right) \right\} \\
& + \Omega^{\text{non-mf}}[n_{\text{el},\circ}] \quad .
\end{aligned}
\tag{3.33}
$$

Replacing the SMPB electrostatic potential with the one obtained from solving the LPBE is justified in cases where $\beta z v \ll 1$ which has often been found to be the case e.g. in biomolecular simulations.[118] Unfortunately, however, differences are generally more critical in the actual free energies $\Omega_\circ^{\text{SPB/LPB}}$ and simply inserting the LPB potential in the SMPB free energy expression will most often not work.[118] In this thesis, we restrict this discussion to the theoretical derivations presented in this section and leave it to future work to investigate limits and means of such an approximation.

3.3. All-Electron DFT with NAO Basis Sets: `FHI-aims`

In this section we introduce `FHI-aims` as example for an all-electron DFT program package. We thereby particularly focus on technical peculiarities which are relevant for the implementation of the derived SMPB-DFT scheme. We remark that most of the information given here has been taken from the respective `FHI-aims` publication ref. [1].

3.3.1. General Infrastructure

In `FHI-aims`, the single-electron wave-functions ψ_l are expanded into a number N_{basis} of numerically tabulated atom-centered orbitalss (NAOs) φ_i:

$$
\psi_l = \sum_{li}^{N_{\text{basis}}} c_{li} \varphi_i \quad ,
\tag{3.34}
$$
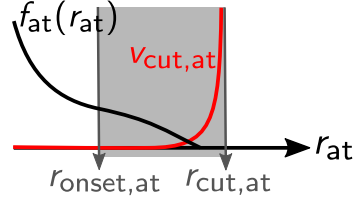
Figure 3.2.: Sketch of the confinement potential and the radii defining the region of confinement. The confinement potential leads to a localization of radial atom-centered functions f_{at} as e.g. the radial basis functions u_i or the free atom electron density $n_{\mathrm{el,at}}^{\mathrm{free}}$.

with the expansion coefficients c_{li} and the basis functions

$$\varphi_i = \frac{u_i(r_{\mathrm{at}})}{r} Y_{lm}(\Omega_{\mathrm{at}}) \quad . \tag{3.35}$$

Here, Y_{lm} denote the real-valued spherical harmonics functions, and r_{at} and $\Omega_{\mathrm{at}} = \{\theta_{\mathrm{at}}, \phi_{\mathrm{at}}\}$ spherical coordinates with respect to the atom center the basis function φ_i is assigned to. The radial functions $u_i(r)$ are directly obtained from the numerical solution of Schrödinger-like radial equations

$$\left[-\frac{1}{2} \frac{\mathrm{d}^2}{\mathrm{d}r_{\mathrm{at}}^2} + \frac{l(l+1)}{r_{\mathrm{at}}^2} + v_i(r_{\mathrm{at}}) + v_{\mathrm{cut,at}}(r_{\mathrm{at}}) \right] u_i(r_{\mathrm{at}}) = \epsilon_i u_i(r_{\mathrm{at}}) \tag{3.36}$$

providing an accurate description of all electrons and optimally resolving the Coulomb singularity. v_i thereby defines the character of the basis functions and is for a minimal basis set simply set to the free atoms potential $v_{\mathrm{at}}^{\mathrm{free}}$ introduced in the next section. To achieve fast convergence of all calculated properties, the Hamiltonian in the Schrödinger-like equation is furthermore extended by a radial confinement potential $v_{\mathrm{at,cut}}$ which locally confines all basis functions $\{\varphi_i\}$ to atomic radii $r_{\mathrm{at}} = |\boldsymbol{r} - \boldsymbol{R}_{\mathrm{at}}| < r_{\mathrm{cut,at}}$ as illustrated in Fig. 3.2. The radial Schrödinger equation is solved on a dense 1D logarithmic grid $r_{\mathrm{at}}(i) = r_{\mathrm{at,0}} \mathrm{e}^{(i-1)\alpha}$ with $i = \{1, \ldots, N_{\mathrm{log}}\}$ with α_{log}, $r_{\mathrm{at,0}}$ and the total number of grid points N_{log} being adjustable numerical parameters.

All variables in `FHI-aims` depending on three spatial coordinates are discretized and all corresponding integrals solved on an integration grid which is located on atom-centered spherical shells. The radial shells are placed at logarithmic distances from the atom centers:

$$r_{\mathrm{at}}(i) = r_{\mathrm{outer,at}} \frac{\ln\left(1 - [i/(N_{\mathrm{r}}+1)]^2\right)}{\ln\left(1 - [N_{\mathrm{r}}/(N_{\mathrm{r}}+1)]^2\right)} \quad , \tag{3.37}$$

with the outer shell radius $r_{\mathrm{outer,at}}$ and the total number of radial shells N_{r} being adjustable numerical parameters. As seen from Fig. 3.3 this so defined integration grid is particularly dense at the nuclei and thus enables to optimally resolve the sometimes strong variations of calculated properties at the atomic centers while reducing the computation costs in regions where the respective functions are sufficiently smooth. Starting from this initial grid, the user can then simply increase the radial grid accuracy by raising a parameter called the `radial_multiplier` which places additional shells at integer fractions of the original grid.

A `radial_multiplier` = 2 for example places a single additional grid shell between all shells and in- and outside of the previous grid.

The placing of angular grid points is done by a predefined *Lebedev* procedure which enables an exact integration of all angular momentum functions up to a certain order and is in detail described in the `FHI-aims` publication.[1] These settings have been shown to provide system-independent accurate energy and force calculations, although the `FHI-aims` input file also in principle enables the user to manually adjust the number of grid points between specific radii.
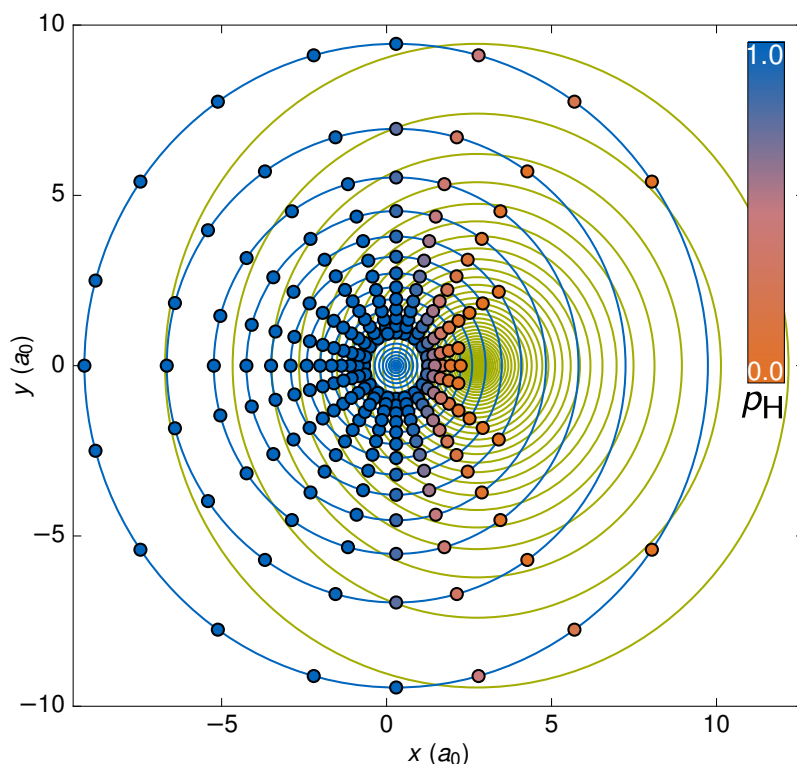
Figure 3.3.: `FHI-aims` *light* integration grid in the bonding plane of an HCl molecule. Circles indicate the radial grid shells of both H-atom (left grid center) and Cl-atom (right grid center). For the H-atom, all grid points except for the ones close to the nuclei and the ones where the H-atom partition function p_H is exactly zero are explicitly shown and colored by the value of p_H.

For an efficient CPU parallelization of the implemented integration schemes all numerical integrals are partitioned into blocks of grid points. This is achieved in `FHI-aims` by an atom-centered partition of unity scheme using the partition functions

$$p_{\text{at}}(\boldsymbol{r}) = \frac{g_{\text{at}}(\boldsymbol{r})}{\sum\limits_{\text{at}'} g_{\text{at}'}(\boldsymbol{r})} \quad . \tag{3.38}$$

`FHI-aims` provides several options for the function g_{at}, for example by making use of the superposition of free atom electron densities $n_{\text{el,at}}^{\text{free}}$ as introduced in the next section

$$g_{\text{at}}(\boldsymbol{r}) = \frac{n_{\text{el,at}}^{\text{free}}{}^2(r_{\text{at}})}{2r_{\text{at}}} \quad . \tag{3.39}$$

In this thesis, we apply the more advanced Stratmann-approach[131] for g_{at} which is the default setting in `FHI-aims` and is depicted exemplarily in Fig. 3.3. For a more detailed account, we refer the reader to the corresponding ref. [131].

3.3.2. Electrostatic Potential

3.3.2.1. Regularization

In order evaluate the Hartree energy E_{es} in Eq. (2.38) every DFT program package needs to solve the Poisson equation to obtain the electrostatic potential v_{o} created by the electron density n_{el}. In an all-electron framework the explicit consideration of core electrons leads to the well-known cusps of the electron density at the atomic centers as well as singularities in the electrostatic potential complicating the numerical solution of the Poisson equation. In order to solve this issue, `FHI-aims` regularizes the electron density with the superposition of free atom electron densities $n_{\text{el}}^{\text{free}}$

$$n_{\text{el}} = \sum_{\text{at}} n_{\text{el,at}}^{\text{free}}(|\boldsymbol{r} - \boldsymbol{R}_{\text{at}}|) + \delta n_{\text{el}} = n_{\text{el}}^{\text{free}} + \delta n_{\text{el}} \quad . \tag{3.40}$$

Here, the electron density for a particular atom $n_{\text{el,at}}^{\text{free}}$ is obtained from the solution of a radial Schrödinger equation, analogously to the procedure for the radial basis functions, but including the same xc functional as in the subsequent SCF cycle. Thereby, one uses by default the same confinement potential as for the radial basis functions. Similarly, the full electrostatic potential of electrons and nuclei is also expressed in terms of the sum of the corresponding free atom potentials

$$v = \sum_{\text{at}} v_{\text{at}}^{\text{free}}(|\boldsymbol{r} - \boldsymbol{R}_{\text{at}}|) + \delta v = v^{\text{free}} + \delta v \quad . \tag{3.41}$$

Both $n_{\text{el}}^{\text{free}}$ and v^{free} are accurately stored as 1D cubic spline interpolations on dense radial logarithmic grids. The remaining difference functions δn_{el} and δv are both smooth and free of singularities and can therefore efficiently be expressed in terms of other smooth functions such as e.g. spherical harmonics (see next section).

In practice, `FHI-aims` further uses the fact that the electrostatic potential of the nuclei is well known. The free atom potential can thus be expressed as

$$v_{\text{at}}^{\text{free}} = v_{\text{es}}^{\text{free}} - \sum_{\text{at}} \frac{Z_{\text{at}}}{|\boldsymbol{r} - \boldsymbol{R}_{\text{at}}|} \quad , \tag{3.42}$$

where $v_{\text{es}}^{\text{free}}$ is the electronic part of the free atom potential. The electronic part of the full electrostatic potential is then given as

$$v_{\text{es}} = v_{\text{es}}^{\text{free}} + \delta v \tag{3.43}$$

3.3.2.2. Multi-Center Multipole Expansion

In order to solve the Poisson equation and obtain the electrostatic potential δv from the electron density δn_{el}, it is useful to express δn_{el} first as a sum over its atomic contributions $p_{\mathrm{at}}\delta n_{\mathrm{el}}$ which are expanded into a basis of spherical harmonics

$$\delta n_{\mathrm{el}} = \sum_{\mathrm{at}} p_{\mathrm{at}}\delta n_{\mathrm{el}} = \sum_{\mathrm{at}} \sum_{l} \sum_{-m}^{m} n_{\mathrm{el,at},lm}(r_{\mathrm{at}})Y_{lm}(\Omega_{\mathrm{at}}) \quad . \tag{3.44}$$

$n_{\mathrm{el,at},lm}$ are the multipolar components of δn_{el} which are given by the projection of the atom-centered functions $p_{\mathrm{at}}\delta n_{\mathrm{el}}$ onto the space of spherical harmonics

$$n_{\mathrm{el,at},lm} = \int_{r_{\mathrm{at}}} \mathrm{d}^2\Omega_{\mathrm{at}} Y_{lm}(\Omega_{\mathrm{at}})p_{\mathrm{at}}\delta n_{\mathrm{el}} \quad , \tag{3.45}$$

with $\mathrm{d}^2\Omega_{\mathrm{at}} = \mathrm{d}\theta_{\mathrm{at}}\mathrm{d}\phi_{\mathrm{at}}\sin(\theta_{\mathrm{at}})$. These radial functions can also be utilized to express the electrostatic potential δv via (cf. Eq. (2.56))

$$\delta v = 4\pi \int \mathrm{d}\boldsymbol{r}' \delta n_{\mathrm{el}}(\boldsymbol{r}')G_0(|\boldsymbol{r}-\boldsymbol{r}'|)$$

$$= 4\pi \sum_{\mathrm{at}} \sum_{l} \sum_{-m}^{m} \int \mathrm{d}\boldsymbol{r}' \delta n_{\mathrm{el,at},lm}(r'_{\mathrm{at}})Y_{lm}(\Omega'_{\mathrm{at}})G_0(|\boldsymbol{r}-\boldsymbol{r}'|) \tag{3.46}$$

with the Green's function $G_0(|\boldsymbol{r}-\boldsymbol{r}'|) = \frac{1}{4\pi|\boldsymbol{r}-\boldsymbol{r}'|}$ being the solution of the PDE

$$\Delta G_0(|\boldsymbol{r}-\boldsymbol{r}'|) = -\delta(\boldsymbol{r}-\boldsymbol{r}') \quad . \tag{3.47}$$

The integrations in Eq. (3.46) can be also carried out in a coordinate system centered at the respective atoms. Shifting the center of integrations to the respective atoms, i.e. $\boldsymbol{r}' \to \boldsymbol{r}'_{\mathrm{at}} = \boldsymbol{r}' - \boldsymbol{R}_{\mathrm{at}}$, Eq. (3.46) then becomes

$$\delta v = 4\pi \sum_{\mathrm{at}} \sum_{l} \sum_{-m}^{m} \int \mathrm{d}\boldsymbol{r}'_{\mathrm{at}}\delta n_{\mathrm{el,at},lm}(r'_{\mathrm{at}})Y_{lm}(\Omega'_{\mathrm{at}})G_0(|\boldsymbol{r}_{\mathrm{at}}-\boldsymbol{r}'_{\mathrm{at}}|) \quad . \tag{3.48}$$

The now atom-centered Green's function can be expressed in terms of spherical harmonics by making use of the *Laplace expansion* (for a full derivation cf. Appendix A.2)

$$G_0(|\boldsymbol{r}_{\mathrm{at}}-\boldsymbol{r}'_{\mathrm{at}}|) = \sum_{\mathrm{at}} \sum_{l} \sum_{-m}^{m} \frac{1}{2l+1}Y_{lm}(\Omega_{\mathrm{at}})Y_{lm}^*(\Omega'_{\mathrm{at}}) \cdot \begin{cases} \frac{r'^l_{\mathrm{at}}}{r^{l+1}_{\mathrm{at}}} = g_l(r'_{\mathrm{at}}, r_{\mathrm{at}}) & \text{for } r_{\mathrm{at}} > r'_{\mathrm{at}} \\ \frac{r^l_{\mathrm{at}}}{r'^{l+1}_{\mathrm{at}}} = g_l(r_{\mathrm{at}}, r'_{\mathrm{at}}) & \text{for } r'_{\mathrm{at}} > r_{\mathrm{at}} \end{cases} \quad . \tag{3.49}$$

Insertion into Eq. (3.48), splitting of the radial integral (cf. Appendix A.2) and recasting then yields

$$
\begin{aligned}
\delta v(\boldsymbol{r}) &= \sum_{\text{at}} \sum_l \sum_{-m}^m \sum_{l'} \sum_{-m'}^{m'} \frac{1}{2l+1} \Bigg[\int_0^{r_{\text{at}}} \mathrm{d}r'_{\text{at}} \delta n_{\text{el,at},lm}(r'_{\text{at}}) g_{l'}(r_{\text{at}}, r'_{\text{at}}) \\
&\quad + \int_{r_{\text{at}}}^\infty \mathrm{d}r'_{\text{at}} \delta n_{\text{el,at},lm}(r'_{\text{at}}) g_{l'}(r'_{\text{at}}, r_{\text{at}}) \Bigg] \times \underbrace{\left[\int \mathrm{d}^2\Omega'_{\text{at}} Y_{lm}(\Omega'_{\text{at}}) Y^*_{l'm'}(\Omega'_{\text{at}}) \right]}_{\delta_{ll'}\delta_{mm'}} Y_{l'm'}(\Omega_{\text{at}}) \\
&= \sum_{\text{at}} \sum_l \sum_{-m}^m \underbrace{\left[\frac{1}{2l+1} \left[\begin{array}{l} \int_0^{r_{\text{at}}} \mathrm{d}r'_{\text{at}} \delta n_{\text{el,at},lm}(r'_{\text{at}}) g_l(r_{\text{at}}, r'_{\text{at}}) \\ + \int_{r_{\text{at}}}^\infty \mathrm{d}r'_{\text{at}} \delta n_{\text{el,at},lm}(r'_{\text{at}}) g_l(r'_{\text{at}}, r_{\text{at}}) \end{array} \right] \right]}_{\delta v_{\text{at},lm}(r_{\text{at}})} Y_{lm}(\Omega_{\text{at}}) \\
&= \sum_{\text{at}} \sum_l \sum_{-m}^m \delta v_{\text{at},lm}(r_{\text{at}}) Y_{lm}(\Omega_{\text{at}}) \quad ,
\end{aligned}
\tag{3.50}
$$

where the first part of $\delta v_{\text{at},lm}$ denotes the interior ($r_{\text{at}} < r'_{\text{at}}$) and the second the exterior ($r_{\text{at}} > r'_{\text{at}}$) multipole components. The radial integrals are evaluated on the dense 1D logarithmic grid which is also used for the solution of the radial Schrödinger equation (cf. Section 3.3.1). In practise, the multipole expansion in Eq. (3.50) has to be truncated at a particular angular momentum $l_{\text{hartree,at}}$ leading to an error in the Hartree energy E_{es} (cf. Section 3.3.5). For standard `FHI-aims` calculations, a value of $l_{\text{hartree,at}} = 6$ was shown to be sufficient for most systems providing meV-converged energy differences. [1]

3.3.3. Default Settings

So far, we have introduced several numerical parameters in `FHI-aims` which are sometimes critically influencing the outcome of calculations. By modifying the `FHI-aims` input file, they can be tuned either individually or in groups by changing the default settings as listed in Tab. 3.1. An increase in the order *light, tight* up to *really tight* settings leads to higher accuracy in the integration grid, a larger set of basis functions, larger confinement radii and higher orders in the multipole expansion of the electrostatic potential. The angular grid is in the case of very high $l_{\text{hartree,at}}$ – if differing from the default settings – automatically adjusted by `FHI-aims` to give numerically stable spherical harmonics representations. Finally, 1D integrations on the logarithmic grid are no computational bottleneck and the corresponding grid can be therefore always chosen fine enough for all possible systems using $\alpha_{\text{log}} = \ln(1.0123)$, $r_{\text{at},0} = 0.0001/Z_{\text{at}}$ and $r_{\text{at}}(N_{\text{log}}) = 100$ for all default settings corresponding for an H-atom to $N_{\text{log}} = \lfloor \frac{1}{\alpha} \ln\left(\frac{r_{\text{at}}(N_{\text{log}})}{r_{\text{at},0}} \right) + 1 \rfloor = 1131$ grid points.

		light	*tight*	*really tight/ safe*
grid	$r_{\text{outer,at}}$ (Å)	5	7	7
	N_{r}	24	24	24
	`radial_multiplier`	1	2	2
	N_{grid}	302	434	590
$v_{\text{cut,at}}$	$r_{\text{onset,at}}$ (Å)	3.5	4.0	4.0
	$r_{\text{cut,at}}$ (Å)	5.0	6.0	6.0
basis	$l_{\text{hartree,at}}$	4	6	8
	N_{basis}	5	15	15

Table 3.1.: Default settings in `FHI-aims` at the example of an H-atom. The first block represents settings of the 3D integration grid with N_{grid} being the total number of grid points. Further, the second block refers to parameters adjusting the confinement potential and the last one comprises basis specific settings adjusting the multipole or NAO basis expansion.

3.3.4. Total Energy Expression

Starting from Eq. (2.40), the total energy is in `FHI-aims` evaluated via:

$$E_{\text{tot}} = \sum_{l=1}^{N_{\text{states}}} \epsilon_{l,\circ} - \int \mathrm{d}\boldsymbol{r} n_{\text{el},\circ} v^{\text{xc}} + E^{\text{xc}}[n_{\text{el},\circ}]$$
$$+ (E_{\text{double}}^{\text{free}} + E_{\text{en}}^{\text{free}}) + (\delta E_{\text{double}} + \delta E_{\text{en}}) + (E_{\text{nn}} - E_{\text{en}}^{\text{free}}) - \delta E_{\text{en}} \quad . \tag{3.51}$$

In the last line, the electron-nuclei interaction energy E_{en} was added and subtracted. This leads to charge neutral electrostatic terms which increase the numerical stability of the energy expression.[1] Moreover, we separated both E_{en} as E_{double} into a free atom contribution and a δ-term defined as:

$$E_{\text{double}}^{\text{free}} = -\frac{1}{2} \int \mathrm{d}\boldsymbol{r} n_{\text{el}}^{\text{free}} v_{\text{es}}^{\text{free}}$$
$$\delta E_{\text{double}} = E_{\text{double}} - E_{\text{double}}^{\text{free}} = -\frac{1}{2} \int \mathrm{d}\boldsymbol{r} \left[\delta n_{\text{el},\circ} v_{\text{es}}^{\text{free}} + n_{\text{el},\circ} \delta v_{\circ} \right]$$
$$E_{\text{en}}^{\text{free}} = -\frac{1}{2} \int \mathrm{d}\boldsymbol{r} n_{\text{el}}^{\text{free}} v_{\text{nuc}}$$
$$\delta E_{\text{en}} = E_{\text{en}} - E_{\text{en}}^{\text{free}} = -\frac{1}{2} \int \mathrm{d}\boldsymbol{r} \delta n_{\text{el},\circ} v_{\text{nuc}} = -\frac{1}{2} \sum_{\text{at}} Z_{\text{at}} \left[\lim_{\boldsymbol{r} \to \boldsymbol{R}_{\text{at}}} \delta v_{\circ}(\boldsymbol{r}) \right] \quad . \tag{3.52}$$

The arising energy terms in Eq. (3.51) are then evaluated in practice via

$$E_{\text{double}}^{\text{free}} + E_{\text{en}}^{\text{free}} = -\frac{1}{2} \int \mathrm{d}\boldsymbol{r}\, n_{\text{el}}^{\text{free}} v^{\text{free}}$$

$$\delta E_{\text{double}} + \delta E_{\text{en}} = -\frac{1}{2} \int \mathrm{d}\boldsymbol{r} \left[n_{\text{el},\circ} v_{\circ} - n_{\text{el}}^{\text{free}} v^{\text{free}} \right]$$

$$E_{\text{nn}} - E_{\text{en}}^{\text{free}} = -\frac{1}{2} \sum_{\text{at}} Z_{\text{at}} \left[\sum_{\text{at}' \neq \text{at}} \frac{Z_{\text{at}'}}{|\boldsymbol{R}_{\text{at}} - \boldsymbol{R}_{\text{at}'}|} + v_{\text{es}}^{\text{free}}(\boldsymbol{R}_{\text{at}}) \right] \quad . \tag{3.53}$$

3.3.5. Multipole Correction

In Section 3.3.2 we introduced the multi-center multipole expansion approach as an efficient method for solving the Poisson equation. In practice, the unavoidable truncation of this expansion, however, leads to an error in the electrostatic potential and therefore the total energy which vanishes with increasing maximum angular momentum $l_{\text{hartree,at}}$. Considering the KS functional given in Eq. (2.39) the only part that depends on the error-carrying electrostatic potential δv is the Hartree energy (cf. Eq. (2.38))

$$E_{\text{es}} = \frac{1}{2} \int \mathrm{d}\boldsymbol{r}\, n_{\text{el},\circ} v_{\text{es},\circ} = \frac{1}{2} \int \mathrm{d}\boldsymbol{r}\, n_{\text{el},\circ} v_{\text{es},\circ}^{\text{mp}} + \underbrace{\frac{1}{2} \int \mathrm{d}\boldsymbol{r}\, n_{\text{el},\circ} v_{\text{es},\circ}^{\text{res}}}_{\Delta E_{\text{es}}^{\text{mp}}} \quad , \tag{3.54}$$

with $v_{\text{es},\circ}^{\text{res}} = v_{\text{es},\circ} - v_{\text{es},\circ}^{\text{mp}}$ and $v_{\text{es},\circ}^{\text{mp}}$ being the multipole expansion approximated electrostatic potential. The term $\Delta E_{\text{es}}^{\text{mp}}$ denotes the error in the total energy that comes from the approximation of $v_{\text{es},\circ}$ by $v_{\text{es},\circ}^{\text{mp}}$ in the evaluation of the Hartree energy. By introducing the multipole approximated electron density $n_{\text{el},\circ}^{\text{mp}}$ and the corresponding error $n_{\text{el},\circ}^{\text{res}}$, we can rewrite this expression as (for a full derivation cf. Appendix A.3) [132]

$$E_{\text{es}} = \underbrace{\int \mathrm{d}\boldsymbol{r}\, n_{\text{el},\circ} v_{\text{es},\circ}^{\text{mp}} - \frac{1}{2} \int \mathrm{d}\boldsymbol{r}\, n_{\text{el},\circ}^{\text{mp}} v_{\text{es},\circ}^{\text{mp}}}_{\tilde{E}_{\text{es}}} + \frac{1}{2} \int \mathrm{d}\boldsymbol{r}\, n_{\text{el},\circ}^{\text{res}} v_{\text{es},\circ}^{\text{res}} \quad . \tag{3.55}$$

The last term can be rewritten using the Green's function G_0 as

$$\frac{1}{2} \int \mathrm{d}\boldsymbol{r}\, n_{\text{el},\circ}^{\text{res}} v_{\text{es},\circ}^{\text{res}} = 2\pi \int \mathrm{d}\boldsymbol{r}\mathrm{d}\boldsymbol{r}'\, n_{\text{el},\circ}^{\text{res}}(\boldsymbol{r}) n_{\text{el},\circ}^{\text{res}}(\boldsymbol{r}') G_0(|\boldsymbol{r} - \boldsymbol{r}'|) \quad . \tag{3.56}$$

Comparing the two residual terms $\Delta E_{\text{es}}^{\text{mp}}$ and Eq. (3.56), one immediately sees that the convergence with respect to the multipole error in the electron density increases from linear to quadratic when neglecting Eq. (3.56) instead of $\Delta E_{\text{es}}^{\text{mp}}$ in the evaluation of the Hartree energy. In `FHI-aims` the Hartree energy is therefore evaluated as

$$\tilde{E}_{\text{es}} = \underbrace{\int \mathrm{d}\boldsymbol{r}\, n_{\text{el},\circ} v_{\text{es},\circ}^{\text{mp}}}_{\text{included in } \sum_{l}^{N_{\text{states}}} \epsilon_{l,\circ}} \underbrace{- \frac{1}{2} \int \mathrm{d}\boldsymbol{r}\, n_{\text{el},\circ}^{\text{mp}} v_{\text{es},\circ}^{\text{mp}}}_{\tilde{E}_{\text{double}}} \quad , \tag{3.57}$$

where the respective parts of the Hartree energy in the total energy expression Eq. (3.51) have been indicated. Compared to the expressions given in Eq. (3.53) this induces the following changes of the energy term evaluations

$$E_{\mathrm{en}} \to \tilde{E}_{\mathrm{en}} = -\frac{1}{2} \int \mathrm{d}\boldsymbol{r}\, n_{\mathrm{el,\circ}}^{\mathrm{mp}} v_{\mathrm{nuc}}$$

$$\delta E_{\mathrm{double}} + \delta E_{\mathrm{en}} \to \delta \tilde{E}_{\mathrm{double}} + \delta \tilde{E}_{\mathrm{en}} = -\frac{1}{2} \int \mathrm{d}\boldsymbol{r} \left[n_{\mathrm{el,\circ}}^{\mathrm{mp}} v_{\circ}^{\mathrm{mp}} - n_{\mathrm{el}}^{\mathrm{free}} v^{\mathrm{free}} \right]$$

$$(3.58)$$

where the electron-nuclei interaction energy is now also evaluated with the multipole expanded electron density.

3.3.6. Atomic Forces in `FHI-aims`

3.3.6.1. Hellmann-Feynman and Pulay Forces

In Section 2.2.4, we already derived atomic forces as arising from the atomic position dependence of the Hamiltonian (HF forces) and the basis functions (Pulay forces). To derive corresponding expressions in `FHI-aims`, we start by writing down the derivative of the total energy expression E_{tot} with respect to the atomic positions:

$$\boldsymbol{F}_{\mathrm{at}} = -\frac{\mathrm{d}E_{\mathrm{tot}}}{\mathrm{d}\boldsymbol{R}_{\mathrm{at}}} \quad . \tag{3.59}$$

Instead of now writing the total energy as an expectation value as in Section 2.2.4, we here aim for a different formulation which can be directly utilized also for the derivation of forces in the SMPB-DFT method (cf. Section 3.4.4). It is then useful to consider again the definition of the Lagrangian energy functional in Eq. (2.32) in its unitary transformed form:

$$\mathcal{L}[v, n_{\mathrm{el}}] = E^{\mathrm{KS}}[v, n_{\mathrm{el}}] + \sum_{l=1}^{N_{\mathrm{states}}} \epsilon_l \left[\int \mathrm{d}\boldsymbol{r}\, \psi_l \psi_l^* - 1 \right] \quad , \tag{3.60}$$

and express the total energy in terms of this functional

$$E_{\mathrm{tot}} = \min(\mathcal{L}[v, n_{\mathrm{el}}]) = \mathcal{L}[v_{\circ}, n_{\mathrm{el,\circ}}] = \int \mathrm{d}\boldsymbol{r}\, \ell[v_{\circ}, n_{\mathrm{el,\circ}}] \quad , \tag{3.61}$$

where we introduced the Lagrangian energy functional density ℓ. The Lagrangian $\mathcal{L}$ depends directly on the nuclear positions via the nuclear charge density and implicitly via the electrostatic potential $v_{\circ}$ and its gradient $\nabla v_{\circ}$. Moreover, since the atom-centered basis set moves with the nuclei, also the orbitals and its gradients variations have to be taken into account. Although generally the basis expansion coefficients $\{c_{li,\circ}\}$ depend on the

nuclear positions as well, the respective partial derivative $\frac{\partial E_{\text{tot}}}{\partial c_{li,\circ}}$ vanishes at self-consistency, since E_{tot} is variational with respect to the $\{c_{li,\circ}\}$. One can then calculate the forces as

$$
\begin{aligned}
\boldsymbol{F}_{\text{at}} &= -\int \mathrm{d}\boldsymbol{r} \frac{\mathrm{d}\ell[v_{\circ}, \{\psi_{l,\circ}\}, \{\boldsymbol{R}_{\text{at}}\}]}{\mathrm{d}\boldsymbol{R}_{\text{at}}} \\
&= -\sum_{l=1}^{N_{\text{states}}} \left\{ \int \mathrm{d}\boldsymbol{r} \frac{\partial \ell}{\partial \psi_{l,\circ}} \nabla_{\text{at}} \psi_{l,\circ} + \frac{\partial \ell}{\partial \nabla \psi_{l,\circ}} \nabla_{\text{at}} [\nabla \psi_{l,\circ}] \right\} + c.c. \\
&\quad - \int \mathrm{d}\boldsymbol{r} \left\{ \frac{\partial \ell}{\partial v_{\circ}} \nabla_{\text{at}} v_{\circ} + \frac{\partial \ell}{\partial \nabla v_{\circ}} \nabla_{\text{at}} [\nabla v_{\circ}] \right\} - \int \mathrm{d}\boldsymbol{r} \frac{\partial \ell}{\partial n_{\text{nuc}}} \nabla_{\text{at}} n_{\text{nuc}} \quad , \qquad (3.62)
\end{aligned}
$$

where we introduced the gradient with respect to $\boldsymbol{R}_{\text{at}}$ as ∇_{at}. We thereby made use of the fact that $\frac{\mathrm{d}f(\boldsymbol{R}_{\text{at}})}{\mathrm{d}\boldsymbol{R}_{\text{at}}} = \nabla_{\text{at}} f(\boldsymbol{R}_{\text{at}})$ with $f(\boldsymbol{R}_{\text{at}}) = \{\psi_{l,\circ}, \nabla_{\text{at}} \psi_{l,\circ}, v_{\circ}, \nabla_{\text{at}} v_{\circ}, n_{\text{nuc}}\}$.

We can now move the ∇-operator from the terms $\nabla_{\text{at}} [\nabla \psi_{l,\circ}]$ and $\nabla_{\text{at}} [\nabla v_{\circ}]$ onto the respective prefactor derivatives by integrating by parts and omitting the surface terms. Using again Eq. (2.14), we can then rewrite the expression using functional derivatives

$$
\begin{aligned}
\boldsymbol{F}_{\text{at}} &= -2 \sum_{l=1}^{N_{\text{states}}} \int \mathrm{d}\boldsymbol{r} \left\{ \underbrace{\frac{\delta \mathcal{L}}{\delta \psi_{l,\circ}}}_{(\hat{h}_{\circ}^{\text{KS}} - \epsilon_{l,\circ}) \psi_{l,\circ}^{*}} \nabla_{\text{at}} \psi_{l,\circ} \right\} - \int \mathrm{d}\boldsymbol{r} \left\{ \underbrace{\frac{\delta \mathcal{L}}{\delta n_{\text{nuc}}}}_{v_{\circ}} \nabla_{\text{at}} n_{\text{nuc}} \right\} - \int \mathrm{d}\boldsymbol{r} \left\{ \underbrace{\frac{\delta \mathcal{L}}{\delta v_{\circ}}}_{=0} \nabla_{\text{at}} v_{\circ} \right\} \\
&= \underbrace{-2 \sum_{l=1}^{N_{\text{states}}} \int \mathrm{d}\boldsymbol{r} \nabla_{\text{at}} \psi_{l,\circ} \left(\hat{h}_{\circ}^{\text{KS}} - \epsilon_{l,\circ} \right) \psi_{l,\circ}^{*}}_{\boldsymbol{F}_{\text{at}}^{\text{Pulay}}} \underbrace{- \int \mathrm{d}\boldsymbol{r} \left\{ v_{\circ} \nabla_{\text{at}} n_{\text{nuc}} \right\}}_{\boldsymbol{F}_{\text{at}}^{\text{HF}}} \quad , \qquad (3.63)
\end{aligned}
$$

where we made use of both KS and Poisson equations, valid at self-consistency. The resulting expression separates into HF $\boldsymbol{F}_{\text{at}}^{\text{HF}}$ and Pulay force terms $\boldsymbol{F}_{\text{at}}^{\text{Pulay}}$ (cf. Section 2.2.4). The HF forces can be further rewritten as

$$
\begin{aligned}
\boldsymbol{F}_{\text{at}}^{\text{HF}} &= -\int \mathrm{d}\boldsymbol{r} \left\{ v_{\circ} \nabla_{\text{at}} n_{\text{nuc}} \right\} = -\int \mathrm{d}\boldsymbol{r} \left\{ v_{\text{nuc}} \nabla_{\text{at}} n_{\text{nuc}} \right\} - \int \mathrm{d}\boldsymbol{r} \left\{ v_{\text{es},\circ} \nabla_{\text{at}} n_{\text{nuc}} \right\} \\
&= -4\pi \int \mathrm{d}\boldsymbol{r} \mathrm{d}\boldsymbol{r}' \left\{ n_{\text{nuc}} \nabla_{\text{at}} \left(G_0(|\boldsymbol{r} - \boldsymbol{r}'|) n_{\text{nuc}} \right) \right\} - 4\pi \int \mathrm{d}\boldsymbol{r} \mathrm{d}\boldsymbol{r}' \left\{ n_{\text{el},\circ} \nabla_{\text{at}} \left(G_0(|\boldsymbol{r} - \boldsymbol{r}'|) n_{\text{nuc}} \right) \right\} \\
&= -\int \mathrm{d}\boldsymbol{r} \left\{ n_{\text{nuc}} \nabla_{\text{at}} v_{\text{nuc}} \right\} - \int \mathrm{d}\boldsymbol{r} \left\{ n_{\text{el},\circ} \nabla_{\text{at}} v_{\text{nuc}} \right\} \\
&= \sum_{\text{at},\text{at}' \neq \text{at}} \frac{Z_{\text{at}} Z_{\text{at}'}}{|\boldsymbol{R}_{\text{at}} - \boldsymbol{R}_{\text{at}'}|^3} (\boldsymbol{R}_{\text{at}} - \boldsymbol{R}_{\text{at}'}) - \int \mathrm{d}\boldsymbol{r} n_{\text{el},\circ} \sum_{\text{at}} \frac{Z_{\text{at}}}{|\boldsymbol{r} - \boldsymbol{R}_{\text{at}}|^3} (\boldsymbol{r} - \boldsymbol{R}_{\text{at}}) \quad , \quad (3.64)
\end{aligned}
$$

where we utilized the independence of the Green's function G_0 of the atomic positions.

3.3.6.2. Multipole Correction Force

The truncation of the multipole expansion in the evaluation of the Hartree potential v_{es} leads to an error in the total energy. However, by evaluating the Hartree energy via Eq. (3.57), we showed that this error vanishes quadratically with the order of the multipole expansion. The corresponding necessary modification of the energy expression leads to

modified force terms which we will derive in this section. We start by writing down the multipole corrected energy expression by making use of Eq. (2.39):

$$
\begin{aligned}
\tilde{E}_{\text{tot}} &= \min(\mathcal{L}[v, n_{\text{el}}]) = \mathcal{L}[v_{\text{o}}^{\text{mp}}, n_{\text{el,o}}] \\
&= T^{\text{S}}[n_{\text{el,o}}] + \tilde{E}_{\text{es}}[v_{\text{es,o}}^{\text{mp}}, n_{\text{el,o}}, n_{\text{el,o}}^{\text{mp}}] + E_{\text{en}}[n_{\text{el,o}}, v_{\text{nuc}}] + E_{\text{nn}}[n_{\text{nuc}}, v_{\text{nuc}}] \\
&\quad + E^{\text{xc}}[n_{\text{el,o}}] + \sum_{l=1}^{N_{\text{states}}} \epsilon_{l,\text{o}} \left[\int \mathrm{d}\boldsymbol{r}\, \psi_{l,\text{o}} \psi_{l,\text{o}}^* - 1 \right] \quad,
\end{aligned}
\tag{3.65}
$$

where all dependencies on the atomic position dependent functions $\{n_{\text{el,o}}(\{\psi_l\}), n_{\text{nuc}}, v_{\text{nuc}}, n_{\text{el,o}}^{\text{mp}}, v_{\text{es,o}}^{\text{mp}}\}$ are explicitly given in brackets. In comparison to the previous section, we therefore additionally have to consider the multipole approximated variables as separate test functions. Analogously to before, we can then again utilize functional derivatives to derive a corresponding atomic force expression:

$$
\boldsymbol{F}_{\text{at}} = -\frac{\mathrm{d}}{\mathrm{d}\boldsymbol{R}_{\text{at}}}\tilde{E}_{\text{tot}} = -2 \underbrace{\sum_{l=1}^{N_{\text{states}}} \int \mathrm{d}\boldsymbol{r}\left\{ \underbrace{\frac{\delta\mathcal{L}}{\delta\psi_{l,\text{o}}}}_{(\hat{h}_{\text{o}}^{\text{KS}}-\epsilon_{l,\text{o}})\psi_{l,\text{o}}^*} \nabla_{\text{at}}\psi_{l,\text{o}} \right\}}_{\boldsymbol{F}_{\text{at}}^{\text{Pulay}}} - \int \mathrm{d}\boldsymbol{r}\left\{ \frac{\delta\mathcal{L}}{\delta n_{\text{nuc}}} \nabla_{\text{at}}n_{\text{nuc}} \right\}
$$

$$
- \int \mathrm{d}\boldsymbol{r}\left\{ \frac{\delta\mathcal{L}}{\delta v_{\text{nuc}}} \nabla_{\text{at}}v_{\text{nuc}} \right\} - \int \mathrm{d}\boldsymbol{r}\left\{ \frac{\delta\mathcal{L}}{\delta n_{\text{el,o}}^{\text{mp}}} \nabla_{\text{at}}n_{\text{el,o}}^{\text{mp}} \right\} - \int \mathrm{d}\boldsymbol{r}\left\{ \frac{\delta\mathcal{L}}{\delta v_{\text{es,o}}^{\text{mp}}} \nabla_{\text{at}}v_{\text{es,o}}^{\text{mp}} \right\} \quad.
\tag{3.66}
$$

The derivative with respect to the KS orbitals gives again the Pulay force defined by the same equation as in the previous section, only now evaluated with the multipole approximated $v_{\text{es,o}}^{\text{mp}}$. The remaining terms can be further recast to:

$$
\boldsymbol{F}_{\text{at}} = \boldsymbol{F}_{\text{at}}^{\text{Pulay}} - \underbrace{\int \mathrm{d}\boldsymbol{r}\left\{ \underbrace{\frac{\delta E_{\text{nn}}}{\delta n_{\text{nuc}}}}_{\frac{1}{2}v_{\text{nuc}}} \nabla_{\text{at}}n_{\text{nuc}} + \underbrace{\frac{\delta\left(E_{\text{en}} + E_{\text{nn}}\right)}{\delta v_{\text{nuc}}}}_{n_{\text{el,o}}+\frac{1}{2}n_{\text{nuc}}} \nabla_{\text{at}}v_{\text{nuc}} \right\}}_{\substack{\underbrace{}_{v_{\text{o}}\nabla_{\text{at}}n_{\text{nuc}}} \\ \boldsymbol{F}_{\text{at}}^{\text{HF}}}}
$$

$$
- \underbrace{\int \mathrm{d}\boldsymbol{r}\left\{ \frac{\delta\tilde{E}_{\text{es}}}{\delta n_{\text{el,o}}^{\text{mp}}} \nabla_{\text{at}}n_{\text{el,o}}^{\text{mp}} + \frac{\delta\tilde{E}_{\text{es}}}{\delta v_{\text{es,o}}^{\text{mp}}} \nabla_{\text{at}}v_{\text{es,o}}^{\text{mp}} \right\}}_{\boldsymbol{F}_{\text{at}}^{\text{mp}}} \quad,
\tag{3.67}
$$

where we utilized again the independence of the Green's function G_0 of atomic positions to rewrite the first line. Compared to Eq. (3.63), we find the same expression for the HF force. The only new force term is the last term which we denote as multipole correction force $\boldsymbol{F}_{\text{at}}^{\text{mp}}$. It results from the additional functional dependence of the Hartree energy on the multipole approximated properties. Performing the respective functional derivatives and reordering leads to

$$
\boldsymbol{F}_{\text{at}}^{\text{mp}} = \int \mathrm{d}\boldsymbol{r}\left\{ \frac{1}{2}\left(v_{\text{es,o}}^{\text{mp}} \nabla_{\text{at}}n_{\text{el,o}}^{\text{mp}} + n_{\text{el,o}}^{\text{mp}} \nabla_{\text{at}}v_{\text{es,o}}^{\text{mp}} \right) - n_{\text{el,o}} \nabla_{\text{at}}v_{\text{es,o}}^{\text{mp}} \right\} \quad.
\tag{3.68}
$$

We can now express the potential as a Green's function integral over the electron density (cf. Eq. (2.56)) and again utilize the independence of the Green's function $G_0(|\boldsymbol{r} - \boldsymbol{r}'|)$ on the atomic positions to rewrite this as

$$\boldsymbol{F}_{\text{at}}^{\text{mp}} = \int \mathrm{d}\boldsymbol{r} \left(n_{\text{el},\circ}^{\text{mp}} - n_{\text{el},\circ} \right) \nabla_{\text{at}} v_{\text{es},\circ}^{\text{mp}} \quad . \tag{3.69}$$

3.4. PB in `FHI-aims`

As discussed in the last section, employing an all-electron DFT program package like `FHI-aims` gives rise to a range of technical peculiarities which have to be taken into account when integrating the SMPB-DFT scheme. This section now deals with the specific implementation of the SMPB-DFT scheme in `FHI-aims`. Of particular importance is thereby the numerical solution of the SMPBE defined in Eqs. (3.25) and (3.26) for which we developed a function-space-based scheme optimally making use of the multipole expansion infrastructure of `FHI-aims`. Following this, we then derive the minimum free energy expression as evaluated in `FHI-aims` including a modified multipole correction term. We then present technical details of the coupling of SCF cycle and SMPBE solution scheme and investigate the overall numerical convergence and accuracy. Finally, we then derive atomic forces for the SMPB-DFT scheme in `FHI-aims` as needed for e.g. molecular structure relaxations or dynamics.

3.4.1. Solving the Modified PB Equation

We start in the following by first developing a function-space-based solution scheme of the SMPBE, Eqs. (3.25) and (3.26), that is adapted to the peculiarities of a full-potential DFT program package like `FHI-aims`. The non-rectangular integration grids of `FHI-aims` thereby severely hamper solving the SMPBE using standard methods such as multi-grid finite difference method (FDM) or finite element method (FEM) schemes[23,24] due to the high costs of interpolation onto regular meshes. Additionally, the singularities and cusps present in an all-electron treatment can contribute to higher computational cost of the common methods. Regular meshes here would require very small step sizes and a correspondingly large number of nodes, in order to resolve the regions close to the nuclei. Unstructured meshes instead require an *a priori* grid generation step, which, for large problems, can easily become the bottleneck. This is further complicated through the rapid variation of the ion exclusion function and the dielectric function close to the cavity's boundary, which itself changes during the SCF-cycle. As discussed in Section 3.3.2, `FHI-aims` achieves an efficient solution of the plain Poisson equation through a regularization of the electrostatic potential v by subtraction of a superposition of free-atom electrostatic potentials v^{free} and by utilizing the analytic Laplace expansion of the unscreened Green's function $G_0(|\boldsymbol{r} - \boldsymbol{r}'|) = \frac{1}{4\pi|\boldsymbol{r}-\boldsymbol{r}'|}$ in order to solve the two-center integrals (cf. Section 3.3.2). Our own function-space-based solution scheme for the SMPBE follows a similar strategy by utilizing multipole representations specifically designed for radial integration grids. We thereby automatically resolve the rapid variation close to the nuclei and also avoid interpolating between two

very different grids. Furthermore, we can exploit the efficient machinery for operating on multipole representations built-in into `FHI-aims`.

3.4.1.1. Newton Method

The formulation of PDEs like the SMPBE in a function-space oriented solution approach is nowadays quite common.[3] This is mainly due to the availability of highly efficient solution schemes, like Newton methods, offering fast quadratical convergence.[133] In our implementation we employ such a Newton solver, albeit not based on commonly used FEM,[3] but rather using a multipole basis expansion. This lets us exploit the highly parallel and efficient machinery of `FHI-aims` without the overhead for mesh generation or uniform grids and any additional interpolation steps.

As a first step we thus reformulate the SMPBE, Eqs. (3.25) and (3.26), as a functional root-finding problem with respect to v

$$\mathcal{F}[v] = \nabla \cdot [\varepsilon \nabla v] + 4\pi (n_{\text{sol}} + n_{\text{ion}}^{\text{SMPB}}[v]) = 0 \quad . \tag{3.70}$$

Here and in the remainder of this section we thereby drop the explicit n_{el}-dependence of $\varepsilon[n_{\text{el}}]$ and $\alpha_{\text{ion}}^{\pm}[n_{\text{el}}]$ in the equations for clarity, recognizing that for the SMPBE solver only the v-dependence matters. Regularizing v as in Eq. (3.41) the root with respect to the difference potential δv can then be obtained through an iterative Newton method

$$\mathcal{F}'[v_n](\delta v_{n+1} - \delta v_n) = -\mathcal{F}[v_n] \quad , \tag{3.71}$$

where $\mathcal{F}'$ is the Fréchet derivative of $\mathcal{F}$, the existence of which is proven in Appendix A.4. Inserting $\mathcal{F}$ and $\mathcal{F}'$ yields a LPB-type equation, i.e. a linear PDE in the updated difference potential $\delta v_{\text{n}+1}$ (for the full derivation see Appendix A.4)

$$\left(\nabla \cdot [\varepsilon \nabla] - h^2[v_n] \right) \delta v_{n+1} = -4\pi \varepsilon q[v_n] \tag{3.72}$$

with

$$h^2[v_n] = \frac{\phi_0 \alpha_{\text{ion}}^+ \alpha_{\text{ion}}^- - \frac{1}{2}(\phi_0 - 1) \left[\alpha_{\text{ion}}^+[n_{\text{el}}] e^{-\beta z v} + \alpha_{\text{ion}}^-[n_{\text{el}}] e^{\beta z v} \right]}{\left(1 - \phi_0 + \frac{1}{2}\phi_0 \left[\alpha_{\text{ion}}^+[n_{\text{el}}] e^{-\beta z v} + \alpha_{\text{ion}}^-[n_{\text{el}}] e^{\beta z v} \right] \right)^2} \varepsilon^{\text{s,bulk}} \kappa^2 \tag{3.73}$$

and a modified source term

$$-4\pi \varepsilon q[v_n] = -4\pi \left(n_{\text{el}} + n_{\text{ion}}^{\text{SMPB}}[v_n] - \varepsilon n^{\text{free}} \right) - \varepsilon (\nabla \ln(\varepsilon)) \cdot (\nabla v^{\text{free}}) - h^2[v_n] \delta v_n \quad . \tag{3.74}$$

Straightforward solution of this LPB-type equation can be achieved by rewriting it in form of a screened Poisson equation (SPE)

$$\left(\Delta - \kappa^2 \right) \delta v_{n+1} = -4\pi q[v_n] + \hat{L}_1[v_n] \delta v_{n+1} \tag{3.75}$$

with the response operator

$$\hat{L}_1[v_n] = -(\nabla \ln(\varepsilon)) \cdot \nabla - \left(\kappa^2 - \frac{h^2[v_n]}{\varepsilon} \right) \quad . \tag{3.76}$$

3. Methods

The equations (3.72) or (3.75) could in principle be discretized using one of the standard techniques, such as FDM or FEM. The resulting linear algebraic system then needs to be solved numerically, usually employing an iterative solver. A common prerequisite is a suitable preconditioner for the linear system, which reduces the number of iteration steps. Here, we instead follow a different strategy and perform the preconditioning directly on the function space level.

In principle, a preconditioner can be regarded as an approximation to the inverse of the operator defining our linear problem. In Eq. (3.75) the latter is $(\Delta - \kappa^2 - \hat{L}_1[v_n])$, and for $(\Delta - \kappa^2)$ we know the inverse, which is determined by the screened Green's function $G_1(|\boldsymbol{r} - \boldsymbol{r}'|) = \frac{1}{4\pi|\boldsymbol{r}-\boldsymbol{r}'|}\mathrm{e}^{-\kappa|r-r'|}$. Using the Green's function for preconditioning, we multiply Eq. (3.75) with $G_1(|\boldsymbol{r} - \boldsymbol{r}'|)$ and integrate over space to arrive at

$$\delta v_{n+1}(\boldsymbol{r}) = -\int \mathrm{d}\boldsymbol{r}' G_1(|\boldsymbol{r} - \boldsymbol{r}'|)\left(-4\pi q[v_n(\boldsymbol{r}')] + \hat{L}_1[v_n(\boldsymbol{r}')]\delta v_{n+1}(\boldsymbol{r}')\right) \quad , \qquad (3.77)$$

with surface terms vanishing due to the boundary conditions applied on the potential ($v \to 0$ for $|\boldsymbol{r}| \to \infty$). For the special case $\hat{L}_1[v_n] = 0$ a single evaluation of the right hand side of Eq. (3.77) would yield δv_{n+1} for the next Newton step from the given v_n of the current Newton step. The integration is performed by expanding δv_{n+1} in multi-center multipoles as further described in the next subsection. Newton steps are then repeated until convergence in δv is reached. In contrast, in the general case $\hat{L}_1[v_n] \neq 0$, the right hand side of Eq. (3.77) also depends on δv_{n+1}, requiring this equation to be solved self-consistently. For that purpose we perform iterative integrations applying our developed multipole expansion relaxation method (MERM). In this method we apply a simple linear mixing scheme with a mixing parameter η to the source term $-4\pi q[v_n] + \hat{L}_1[v_n]\delta v_{n+1}$. Thereby, at each Newton step we iteratively solve Eq. (3.77) for fixed $q[v_n]$ and $\hat{L}_1[v_n]$ until δv_{n+1} is converged. This converged δv_{n+1} is subsequently used to update $q[v_{n+1}]$ and $\hat{L}_1[v_{n+1}]$ for the next Newton step defining a new SPE to be solved by the relaxation method. As in the special case, Newton steps are then repeated until convergence of δv is reached.

The multi-center multipole expansion for the integrations in Eq. (3.77) is not a prerequisite, but other approaches can also be employed, in particular any solver for SPEs with fixed right hand sides. Which solver to use can be decided depending on the available infrastructure of the DFT program package at hand. Also the iterative linear solver could be replaced by more sophisticated schemes such as Conjugate Gradient.[79] However, we find that the above approach converges sufficiently fast in all our tests and therefore do not expect the extra amount of CPU load per iteration of higher-level methods to pay off (cf. Section 3.4.3.2).

As a side note, Andreussi *et al.* developed a similar iterative scheme to solve the generalized Poisson equation for a solvent without ions, Eq. (2.11), by their self-consistent continuum solvation method (SCCS) scheme.[5] When used with fast Fourier transforms to solve the SPE instead of multipole expansions, our approach formally reduces to the SCCS method for ion-free solvents with $c^{\mathrm{s,bulk}} = 0$. While the SCCS makes use of the Poisson equation using the unscreened G_0 as preconditioner, the SMPB method utilizes the SPE and the screened G_1. We find our approach favored when solving the PBE or SMPBE, as the SPE then describes exactly the bulk limit for $|\boldsymbol{r}| \to \infty$, i.e. $n_{\mathrm{ion}}^{\mathrm{SMPB}} \to -\frac{1}{4\pi}\epsilon^{\mathrm{s,bulk}}\kappa^2 v$. This

has a beneficial effect on the numerics of the relaxation method as will be addressed in detail in the following section.

### 3.4.1.2. Multipole Expansion Relaxation Method
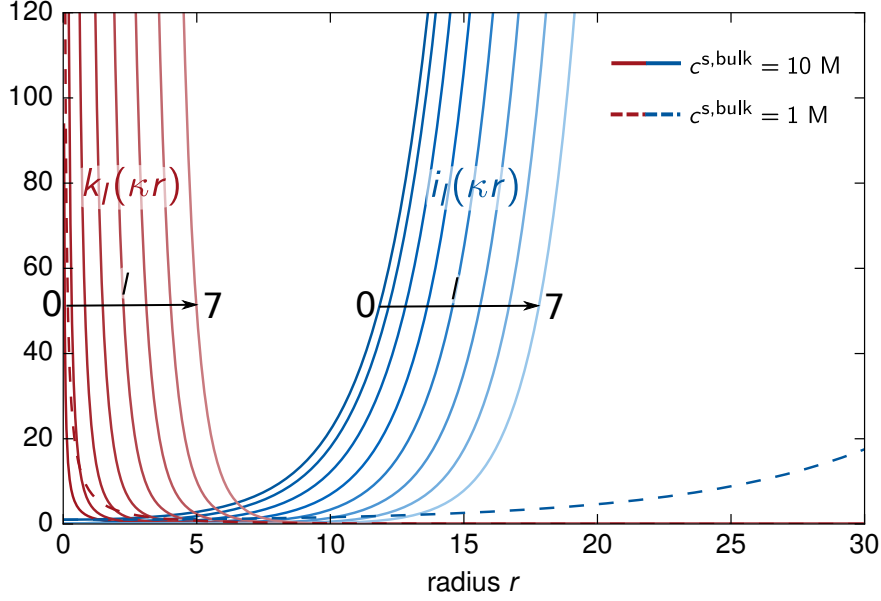
Figure 3.4.: Modified spherical Bessel functions of the first i_l and second k_l kind shown here exemplarily for orders $l = 0$ to $l = 7$ (along increasing brightness) and two ion concentrations $c^{\mathrm{s,bulk}} = 10\,\mathrm{M}$ and $c^{\mathrm{s,bulk}} = 1\,\mathrm{M}$ ($T = 300\,\mathrm{K}$, $\varepsilon^{\mathrm{s,bulk}} = 78.36, z = 1$).

The main numerical effort of the derived SMPB Newton solver lies in solving the SPE by numerical integration of the right hand side of Eq. (3.75) via Eq. (3.77). The developed Newton-MERM scheme is generally applicable and computationally efficient approaches to this integration task will depend on the particular program environment into which the scheme is incorporated. A basic solver for SPEs is in fact often already present in diverse DFT program packages [1,134,135] in the form of Kerker preconditioners [136] for the electron density. In case of the Kerker preconditioner utilized by the NAO-based DFT program package `FHI-aims`, [1] the screened atom-centered Green's function is first expanded into spherical harmonics similar to the Laplace expansion of the unscreened Green's function (cf. Eq. (3.49)) by applying Gegenbauer's addition theorem [137–139] (for a derivation utilizing the more common plane-wave or *Rayleigh* expansion cf. ref. [140])

$$G_1(|\boldsymbol{r}_{\mathrm{at}} - \boldsymbol{r}'_{\mathrm{at}}|) = \frac{8\kappa}{4\pi} \sum_l \sum_{-m}^{m} Y_{lm}(\Omega_{\mathrm{at}}) Y_{lm}^*(\Omega'_{\mathrm{at}}) \begin{cases} k_l(\kappa r_{\mathrm{at}}) i_l(\kappa r'_{\mathrm{at}}) & \text{for } r'_{\mathrm{at}} < r_{\mathrm{at}} \\ k_l(\kappa r'_{\mathrm{at}}) i_l(\kappa r_{\mathrm{at}}) & \text{for } r_{\mathrm{at}} < r'_{\mathrm{at}} \end{cases} , \quad (3.78)$$

where i_l and k_l are the modified spherical Bessel functions of first and second kind, respectively. These functions illustrated in Fig. 3.4 are given as[141]

$$i_n(z) = \sqrt{\frac{\pi}{2z}} I_{n+1/2}(z) = z^n \left(\frac{d}{z dz}\right)^n \frac{\sinh(z)}{z}$$

$$k_n(z) = \sqrt{\frac{\pi}{2z}} K_{n+1/2}(z) = (-1)^n \frac{\pi}{2} z^n \left(\frac{d}{z dz}\right)^n \frac{e^{-z}}{z} \quad , \tag{3.79}$$

where $I_{n+1/2}$ and $K_{n+1/2}$ are the modified Bessel functions of first and second kind, respectively, which can be evaluated by applying common recursion rules.[142] Inserting Eq. (3.78) into Eq. (3.77) yields a multi-center multipole expansion of δv_{n+1} analogous to Eq. (3.50)

$$\delta v_{n+1} = \sum_{\text{at}} \sum_{l=0}^{l_{\text{max,at}}} \sum_{m=-l}^{l} \delta v_{\text{at},lm,n+1}(r_{\text{at}}) Y_{lm}(\Omega_{\text{at}}) \quad , \tag{3.80}$$

with the atom-specific maximum order of the multipole expansion $l_{\text{max,at}}$ and the corresponding multipole moments $\delta v_{\text{at},lm,n+1}$ given by radial integrals

$$\delta v_{\text{at},lm,n+1}(r_{\text{at}}) =$$

$$- \frac{8\kappa}{4\pi} \left[-4\pi k_l(\kappa r_{\text{at}}) \int_0^{r_{\text{at}}} dr'_{\text{at}} \left\{ i_l(\kappa r'_{\text{at}}) q_{\text{at},lm}(r'_{\text{at}}) \right\} \right.$$

$$+ k_l(\kappa r_{\text{at}}) \int_0^{r_{\text{at}}} dr'_{\text{at}} \left\{ i_l(\kappa r'_{\text{at}}) \left\{ \hat{L}_1 \delta v_{n+1} \right\}_{\text{at},lm}(r'_{\text{at}}) \right\}$$

$$- 4\pi i_l(\kappa r_{\text{at}}) \int_{r_{\text{at}}}^{\infty} dr'_{\text{at}} \left\{ k_l(\kappa r'_{\text{at}}) q_{\text{at},lm}(r'_{\text{at}}) \right\}$$

$$\left. + i_l(\kappa r_{\text{at}}) \int_{r_{\text{at}}}^{\infty} dr'_{\text{at}} \left\{ k_l(\kappa r'_{\text{at}}) \left\{ \hat{L}_1 \delta v_{n+1} \right\}_{\text{at},lm}(r'_{\text{at}}) \right\} \right] \quad , \tag{3.81}$$

where $q_{\text{at},lm}$ and $\left\{ \hat{L}_1 \delta v_{n+1} \right\}_{\text{at},lm}$ are the SPE source term multipole moments obtained by angular integration over the source term itself

$$- 4\pi q_{\text{at},lm}(r_{\text{at}}) = -4\pi \int_{r_{\text{at}}} d^2\Omega_{\text{at}} \left\{ p_{\text{at}} q[v_n] Y_{lm}(\Omega_{\text{at}}) \right\} \tag{3.82}$$

and

$$\left\{ \hat{L}_1 \delta v_{n+1} \right\}_{\text{at},lm}(r_{\text{at}}) = \int_{r_{\text{at}}} d^2\Omega_{\text{at}} \left\{ p_{\text{at}}(\boldsymbol{r}) \left(\hat{L}_1[v_n] \delta v_{n+1}(\boldsymbol{r}) \right) Y_{lm}(\Omega_{\text{at}}) \right\} \quad . \tag{3.83}$$

Numerical evaluation of the radial integral of Eq. (3.81) can then efficiently exploit the internal `FHI-aims` integration grids. Specifically, we interpolate the radial functions on the extra-fine 1D logarithmic grid also used by `FHI-aims` for the solution of the radial

Schrödinger equation (cf. Section 3.3.1) and then employ a multistep Adams-Moulton integrator.[143] This allows to optimally resolve the strong variations of δv in the vicinity of the nuclei, but involves only a numerically undemanding 1D cubic spline interpolation that is not performance critical compared to the summation of the multipole moments.

As already discussed in Section 3.3.1 the extent of the radial basis functions is limited in `FHI-aims` by an atom-specific confinement potential $v_{\mathrm{cut,at}}$. Due to this and the multiplication with the atom-centered partition function p_{at} in Eq. (3.82), many contributions to the multipole moments $q_{\mathrm{at},lm}(r_{\mathrm{at}})$ arising from electron density dependencies in $q[v_n]$ are also automatically confined. Confined-source multipole moments are beneficial for computational scaling with system size and speed.[1] In our approach we therefore also aim to spatially confine all parts of $q_{\mathrm{at},lm}(r_{\mathrm{at}})$ and $\left\{\hat{L}_1\delta v_{n+1}\right\}_{\mathrm{at},lm}(r_{\mathrm{at}})$ arising from other terms in Eqs. (3.74) and (3.76). For instance, by choosing a dielectric function of the form of Eq. (3.4) that has a zero gradient outside the transition region many terms in $q_{\mathrm{at},lm}(r_{\mathrm{at}})$ and $\left\{\hat{L}_1\delta v_{n+1}\right\}_{\mathrm{at},lm}(r_{\mathrm{at}})$ associated with $\nabla\varepsilon$ terms in Eqs. (3.74) and (3.76) vanish already after the dielectric transition region, which is usually much closer to the nuclei than $r_{\mathrm{onset,at}}$. The remaining terms coming from the functions $\kappa^2 - \frac{h^2[v_n]}{\varepsilon}$ and $\frac{n_{\mathrm{ion}}^{\mathrm{SMPB}}[v_n]}{\varepsilon}$ yield multipole moments which become negligibly small already before $r_{\mathrm{onset,at}}$ for all test cases considered here. Yet, this detailed convergence with cutoff radius must, of course, be checked for every individual problem, cf. Section 3.4.3.2. The fast decay of the function $\kappa^2 - \frac{h^2[v_n]}{\varepsilon}$ is thereby also the main reason why we recast the Newton method into a SPE instead of a Poisson equation as e.g. done by Andreussi *et al.*[5] Using a Poisson equation as resolvent would instead give rise to a term $\frac{h^2[v_n]}{\varepsilon}$ in $\hat{L}_1[v_n]$. This term would take a constant value of κ^2 in the bulk solvent, leading to overall unconfined $\left\{\hat{L}_1\delta v_{n+1}\right\}_{\mathrm{at},lm}(r_{\mathrm{at}})$ multipole moments. A similar argumentation motivated us not to regularize v with the vacuum potential (cf. Eq. (3.41)) as obtained from a solvent-free calculation in `FHI-aims` as this also leads to unconfined source multipole moments.

Due to the spatially-confined multipole moments $q_{\mathrm{at},lm}(r_{\mathrm{at}})$ and $\left\{\hat{L}_1\delta v_{n+1}\right\}_{\mathrm{at},lm}(r_{\mathrm{at}})$, the explicit radial integration in Eq. (3.81) is in principle bounded by the cutoff radius. For grid points $r_{\mathrm{at}} < r_{\mathrm{cut,at}}$, this means that the integration of the third and fourth term in Eq. (3.81) only needs to be carried out up to $r_{\mathrm{cut,at}}$. At grid points $r_{\mathrm{at}} > r_{\mathrm{cut,at}}$ in the far field, the numerical gain is even more pronounced. For such points Eq. (3.81) reduces to

$$\delta v_{\mathrm{at},lm,n+1}^{\mathrm{ff}}(r_{\mathrm{at}}) = -\frac{8\kappa}{4\pi}\left[-4\pi k_l(\kappa r_{\mathrm{at}})\int_0^{r_{\mathrm{at}}^{\mathrm{cut}}}\mathrm{d}r_{\mathrm{at}}'i_l(\kappa r_{\mathrm{at}}')q_{\mathrm{at},lm}(r_{\mathrm{at}}')\right.$$

$$\left. + k_l(\kappa r_{\mathrm{at}})\int_0^{r_{\mathrm{at}}^{\mathrm{cut}}}\mathrm{d}r_{\mathrm{at}}'i_l(\kappa r_{\mathrm{at}}')\left(\hat{L}_1\delta v_{n+1}\right)_{\mathrm{at},lm}(r_{\mathrm{at}}')\right]\quad. \tag{3.84}$$

To evaluate $\delta v_{\mathrm{at},lm,n+1}^{\mathrm{ff}}$, we thus need no additional integration steps in the Adams-Moulton integrator, since the radial integral is independent of r_{at} and therefore fixed for all $r_{\mathrm{at}} > r_{\mathrm{cut,at}}$. Apart from the obvious numerical gain compared to having to run the Adams-Moulton integrator over a much larger number of grid points, this also implies that

the solution of the SPE and therefore also of the SMPBE is free of finite integration errors or surface integral terms, since due to the spatially-confined integrand all integrations are formally carried out over the whole space.

Next to these optimized integration routines, the computational efficiency of the iterative multipole-expansion scheme can additionally be improved by exploiting the rapid decay of high-l multipole moments in the far field. Similar to the regular multipole-based solution of the Poisson equation,[1] significant speed-ups and a greatly improved scaling of the SMPBE solver can in particular be obtained for large systems by restricting the actual calculation to low-l multipole moments in the far field. Our implementation of the iterative solver furthermore evaluates the angular and radial integrals associated with $q[v_n]$ only once at the beginning of each Newton step. At each iterative step in the MERM then only integrals associated to $\hat{L}_1[v_n]\delta v_{n+1}$ have to be carried out. Due to the spatial confinement of $\hat{L}_1[v_n]\delta v_{n+1}$ this update is, however, not necessary on the whole integration grid, but instead only on the points where $\hat{L}_1[v_n]\delta v_{n+1} \neq 0$. A full update of δv_{n+1} according to Eq. (3.80) on the entire integration grid is correspondingly only done after the last iterative MERM step. While generally increasing the computational efficiency, this update strategy is particularly effective for solvent calculations without ions. In this case δv_{n+1} has to be updated during the MERM only on the integration grid points of the dielectric transition region and the majority of the integration points close to the nuclei are only considered in the final update. The presented alternative solution strategy can be switched on in the `FHI-aims` input file by setting the flag `MERM_in_SPE_solver = .True.` (cf. Appendix B).

3.4.1.3. Solution scheme for the Linearized PB Equation

The developed MERM is generally suited to solve any LPB-type equations since these can, in principle, be rewritten in the form of a SPE. It may therefore also be applied to solve the LPBE that arises from the Taylor expansion of the non-linear ionic charge density, given in Eqs. (2.52) and (3.30). As discussed in Section 3.2.6 a solution could not only be of interest for comparison with other PB software, but also offers a faster alternative to the coupled Newton-MERM solution of the SMPBE for cases where the LPBE is a good approximation.

The recasting of the LPBE of Eqs. (2.52) and (3.30) into a SPE of the form of Eq. (3.75) is analogous to the procedure described in Section 3.4.1.1 and leads to an LPB modified source term

$$-4\pi\varepsilon q^{\mathrm{LPB}} = -4\pi\left(n_{\mathrm{el}} - \varepsilon n_{\mathrm{el}}^{\mathrm{free}}\right) - \varepsilon\left(\nabla\ln\left(\varepsilon\right)\right)\cdot\left(\nabla v^{\mathrm{free}}\right) + \bar{\kappa}_0^2 + \bar{\kappa}^2 v^{\mathrm{free}} \tag{3.85}$$

with the modified DH coefficient as given by Eq. (3.30) and the LPB response operator

$$\hat{L}_1^{\mathrm{LPB}} = -\left(\nabla\ln\left(\varepsilon\right)\right)\cdot\nabla + \left(\frac{\bar{\kappa}^2}{\varepsilon} - \kappa^2\right) \quad . \tag{3.86}$$

Furthermore, q^{LPB} and $\hat{L}_1^{\mathrm{LPB}}$ are exactly zero beyond the cutoff radius as long as both ionic and dielectric transitions lie inside the confinement region. This avoids any numerical instabilities in the update procedure of the electrostatic potential which could appear in the SMPB case using $q[v_n]$ and $\hat{L}_1[v_n]$.

3.4.2. Total Energy and Multipole Correction

The fact that we approximate the potential $\delta v_\circ$ by a multipole expansion gives rise to errors in the evaluated total energy. In contrast to the vacuum case presented in Section 3.3.5 the multipole-expanded potential $\delta v_\circ$ contains, however, now also contributions from the nuclear and ionic charges (cf. Appendix A.4). Furthermore, the truncation of the multipole expansion induces not only an error in the Hartree or electrostatic energy Ω^{elstat}, but in principle on all energy terms in the modified KS functional given in Eq. (3.3) that depend on $\delta v_\circ$. In contrast to the vacuum case, the multipole expanded potential $\delta v_\circ^{\text{mp}}$ is now generated by the source term $q_{\text{iter,}\circ}^{\text{mp}} = q_\circ^{\text{mp}} - \frac{1}{4\pi} \hat{L}_1 \delta v_\circ^{\text{mp}}$ instead of $\delta n_{\text{el,}\circ}^{\text{mp}}$ (cf. Eq. (3.77)). The by far largest contribution to the multipole expansion truncation error comes thereby from the electrostatic energy $\frac{1}{2} \int \mathrm{d}\boldsymbol{r} n_{\text{sol,}\circ} v_\circ$. Ionic contributions resulting from the evaluation of $\Omega^{\text{ion}}_{\substack{\pm \\ \alpha_{\text{ion}}}}$ with $\delta v_\circ^{\text{mp}}$ are commonly small as discussed in more detail in Appendix A.3. Introducing the source term multipole error $q_{\text{iter,}\circ}^{\text{res}} = q_{\text{iter,}\circ}^{\text{mp}} - q_{\text{iter,}\circ}$, we can then employ an analogous approach to Section 3.3.5 to write this as (for a full derivation cf. Appendix A.5):

$$\frac{1}{2} \int \mathrm{d}\boldsymbol{r} n_{\text{sol,}\circ} v_\circ = \int \mathrm{d}\boldsymbol{r} n_{\text{sol,}\circ} v_\circ^{\text{mp}} - \frac{1}{2} \int \mathrm{d}\boldsymbol{r} \left(n_{\text{sol,}\circ} - q_{\text{iter,}\circ}^{\text{res}} \right) v_\circ^{\text{mp}} + \frac{1}{2} \int \mathrm{d}\boldsymbol{r} q_{\text{iter,}\circ}^{\text{res}} v_\circ^{\text{res}} \quad . \tag{3.87}$$

Expressing the residues of the electrostatic potential $v_\circ^{\text{res}}$ in terms of the source term $q_{\text{iter,}\circ}$ and the Green's function $G_1(|\boldsymbol{r} - \boldsymbol{r}'|)$, we can rewrite the last term as

$$\frac{1}{2} \int \mathrm{d}\boldsymbol{r} q_{\text{iter,}\circ}^{\text{res}} v_\circ^{\text{res}} = 2\pi \int \mathrm{d}\boldsymbol{r} \mathrm{d}\boldsymbol{r}' q_{\text{iter,}\circ}^{\text{res}}(\boldsymbol{r}) q_{\text{iter,}\circ}^{\text{res}}(\boldsymbol{r}') G_1(|\boldsymbol{r} - \boldsymbol{r}'|) \quad . \tag{3.88}$$

The final expression thus vanishes quadratically with the source term multipole error. Further recasting the remaining integrals in Eq. (3.87) we can associate the energy terms again with the double counting correction, electron-nuclei and nuclei-nuclei interactions (cf. Eq. (3.51)):

$$\frac{1}{2} \int \mathrm{d}\boldsymbol{r} n_{\text{sol,}\circ} v_\circ \approx \underbrace{\int \mathrm{d}\boldsymbol{r} n_{\text{el,}\circ} v_\circ^{\text{mp}}}_{\substack{\text{included in} \sum\limits_{l}^{N_{\text{states}}} \epsilon_l}} + \underbrace{\frac{1}{2} \int \mathrm{d}\boldsymbol{r} n_{\text{nuc}} v_\circ^{\text{mp}}}_{\tilde{E}_{\text{nn}} - \tilde{E}_{\text{en,1}}} - \underbrace{\frac{1}{2} \int \mathrm{d}\boldsymbol{r} (n_{\text{el,}\circ} - q_{\text{iter,}\circ}^{\text{res}}) v_\circ^{\text{mp}}}_{\tilde{E}_{\text{double}} + \tilde{E}_{\text{en,2}}} \quad . \tag{3.89}$$

Compared to Eq. (3.27), the first term reappears in the sum of eigenstates while the remaining parts comprise multipole corrected nuclei-nuclei and double counting energy terms. As appealing as the mathematical simplicity of the final expression is, it has to be taken with caution. Regarding for example the terms labeled as electron-nuclei interactions

$$\tilde{E}_{\text{en,1}} = -\frac{1}{2} \int \mathrm{d}\boldsymbol{r} n_{\text{nuc}} v_{\text{es,}\circ}^{\text{mp}} \tag{3.90}$$

and

$$\tilde{E}_{\text{en,2}} = -\frac{1}{2} \int \mathrm{d}\boldsymbol{r} \left(n_{\text{el,}\circ} - q_{\text{iter,}\circ}^{\text{res}} \right) v_{\text{nuc}}^{\text{mp}} \quad , \tag{3.91}$$

we realize that these are not equivalent. Due to the non-linearity of the SMPBE, there exists no Green's function, and electronic and nuclear contributions to the electrostatic potential can thus not easily be separated. We, nevertheless, keep this notation, since it simplifies the comparison with the original `FHI-aims` implementation. The energy differences introduced in Eq. (3.89) are then calculated in `FHI-aims` by again separating them into free-atom contributions and δ-correction terms:

$$\tilde{E}_{\mathrm{nn}} - \tilde{E}_{\mathrm{en},1} = \left(E_{\mathrm{nn}}^{\mathrm{free}} - E_{\mathrm{en}}^{\mathrm{free}} \right) + \left(\delta\tilde{E}_{\mathrm{nn}} - \delta\tilde{E}_{\mathrm{en},1} \right) \quad , \tag{3.92}$$

with

$$\delta\tilde{E}_{\mathrm{nn}} - \delta\tilde{E}_{\mathrm{en},1} = \sum_{\mathrm{at}} \left[Z_{\mathrm{at}} \delta v_{\mathrm{at},\circ}^{\mathrm{mp}}(0) + \sum_{\mathrm{at}'} \delta v_{\mathrm{at}',\circ}^{\mathrm{mp}}(\boldsymbol{R}_{\mathrm{at}} - \boldsymbol{R}_{\mathrm{at}'}) \right] \quad , \tag{3.93}$$

where $\delta v_{\mathrm{at},\circ}$ denotes the contribution of the atom "at" to $\delta v_{\circ}$

$$\delta v_{\mathrm{at},\circ}^{\mathrm{mp}} = \sum_{l=0}^{l_{\mathrm{max,at}}} \sum_{m=-l}^{l} \delta v_{\mathrm{at},lm,\circ}(r_{\mathrm{at}}) Y_{lm}(\Omega_{\mathrm{at}}) \quad . \tag{3.94}$$

Furthermore, we get

$$\tilde{E}_{\mathrm{double}} + \tilde{E}_{\mathrm{en},2} = \left(E_{\mathrm{double}}^{\mathrm{free}} + E_{\mathrm{en}}^{\mathrm{free}} \right) + \left(\delta\tilde{E}_{\mathrm{double}} + \delta\tilde{E}_{\mathrm{en},2} \right) \quad , \tag{3.95}$$

with

$$\delta\tilde{E}_{\mathrm{double}} + \delta\tilde{E}_{\mathrm{en},2} = -\frac{1}{2} \int \mathrm{d}\boldsymbol{r} \left[\left(n_{\mathrm{el},\circ} - q_{\mathrm{iter},\circ}^{\mathrm{res}} \right) v_{\circ}^{\mathrm{mp}} - n_{\mathrm{el},\circ}^{\mathrm{free}} v_{\circ}^{\mathrm{free}} \right] \quad , \tag{3.96}$$

where the free atoms parts of both expressions are again defined as in Eq. (3.53). We can now rewrite the minimum free energy expression given in Eq. (3.27) as evaluated in `FHI-aims` as:

$$\Omega_{\circ}(\varepsilon^{\mathrm{s,bulk}}, c^{\mathrm{s,bulk}}, n_{\mathrm{sol},\circ})$$
$$= \sum_{l=1}^{N_{\mathrm{states}}} \epsilon_{l,\circ} - \int \mathrm{d}\boldsymbol{r} n_{\mathrm{el},\circ} v_{\circ}^{\mathrm{xc}} + E^{\mathrm{xc}}[n_{\mathrm{el},\circ}] - \int \mathrm{d}\boldsymbol{r} n_{\mathrm{el},\circ} \delta v_{\varepsilon,\alpha_{\mathrm{ion}},\circ}^{\mathrm{KS,SMPB}}$$
$$+ \int \mathrm{d}\boldsymbol{r} \left\{ -\frac{1}{2} n_{\mathrm{ion}}^{\mathrm{SMPB}}[v_{\circ}^{\mathrm{mp}}, n_{\mathrm{el},\circ}] v_{\circ}^{\mathrm{mp}} - \frac{1}{\beta a^3} \ln \left(1 + \frac{1}{2} \frac{\phi_0}{1-\phi_0} \left[\alpha_{\mathrm{ion}}^{+} \mathrm{e}^{-\beta z v_{\circ}^{\mathrm{mp}}} + \alpha_{\mathrm{ion}}^{-} \mathrm{e}^{\beta z v_{\circ}^{\mathrm{mp}}} \right) \right] \right\}$$
$$+ \Omega_{\varepsilon}^{\mathrm{non-mf}}[n_{\mathrm{el},\circ}]$$
$$+ (E_{\mathrm{double}}^{\mathrm{free}} + E_{\mathrm{en}}^{\mathrm{free}}) + (\delta\tilde{E}_{\mathrm{double}} + \delta\tilde{E}_{\mathrm{en}}) + (E_{\mathrm{nn}}^{\mathrm{free}} - E_{\mathrm{en}}^{\mathrm{free}}) + \left(\delta\tilde{E}_{\mathrm{nn}} - \delta\tilde{E}_{\mathrm{en}} \right) \quad . \tag{3.97}$$

3.4.3. Coupling Modified PB and Kohn-Sham Equations

3.4.3.1. Iterative Functional Minimization

So far, we have focused on the theoretical derivation of the Newton-MERM scheme and the resulting necessary modifications of the energy expression. This section now deals

with the actual implementation of the methodology into `FHI-aims` with the basic workflow illustrated in Fig. 3.6. The workflow for the also implemented MERM-based LPBE solver is analogous and shown in Fig. 3.5. `FHI-aims` solves the modified KS equations containing the additional term $\delta v_{\varepsilon,\alpha_{\text{ion}}}^{\text{KS,SMPB}}$ of Eq. (3.24) through an SCF cycle. At each corresponding SCF step, i.e. for the then given n_{el}, the SMPBE of Eqs. (3.25) and (3.26) are solved with the Newton-MERM scheme. For this, the iterative Newton scheme to optimize δv is initiated, with each Newton step involving the self-consistent solution of the SPE of Eq. (3.75) through the MERM. Once the SCF cycle is converged, the resulting ground-state electron density and electrostatic potential are used to evaluate the free energy of the solute Ω_0 in the presence of solvent and ions through Eq. (3.97).

The SCF cycle is initialized with the superposition of free-atom electron densities $n_{\text{el}}^{\text{free}}$ and the superposition of free-atom potentials v^{free}. In principle, it could be beneficial to start solving the SMPBE only after a certain number of SCF steps, i.e. avoid the additional cost of solving the SMPBE in the first SCF steps when the electron density still changes rapidly. However, in practice we obtained a faster SCF convergence in fewer steps when including the SMPBE solver directly from the second SCF step onwards. To initiate the SMPBE solver, $\varepsilon[n_{\text{el}}]$ and $\alpha_{\text{ion}}[n_{\text{el}}]$ are first evaluated from the n_{el} of the given SCF step. At the very first time the SMPBE solver is executed, δv is initialized with the solution of the corresponding LPBE, cf. Section 3.4.1.3, with $\delta v = 0$ in the case of the SMPBE scheme, whereas for LPB calculations, cf. Section 3.4.1.3, we simply set $\delta v = 0$. At all later SCF steps, δv is initialized with the self-consistent δv of the preceding SCF step. The initialized quantities are used to evaluate the SPE source functions $-4\pi q[v_n]$ and $\hat{L}_1[v_n]\delta v_{n+1}$ (SMPBE) or $-4\pi q^{\text{LPB}}$ and $\hat{L}_1^{\text{LPB}}\delta v$ (LPBE), and the resulting SPE is solved via the MERM until self-consistency in δv_{n+1} (SMPBE) or δv (LPBE) is reached. In case of the SMPBE solver, the updated δv_{n+1} is then used to update the SPE source functions, $n \to n+1$, and restart the MERM until overall convergence of δv is reached. With this converged δv, the KS Hamiltonian $\hat{h}^{\text{KS}}$ is updated and the eigenvalue problem is solved in the next SCF step.

`FHI-aims` measures the numerical convergence of the electron density by evaluating the integrated root mean square change of n_{el} from one SCF step to the next[1]

$$\tau_{\text{SCF}} = \sqrt{\int d\boldsymbol{r} \left\{ (\delta n_{\text{el,new}}(\mathbf{r}) - \delta n_{\text{el,old}}(\mathbf{r}))^2 \right\}} \quad . \tag{3.98}$$

In analogy, the convergence of the Newton method and the MERM is measured through convergence criteria τ_{Newton} and τ_{MERM}, respectively, which calculate the corresponding change in the iteratively optimized potential

$$\tau_{\text{Newton/MERM}} = \sqrt{\int d\boldsymbol{r} \left\{ (\delta v_{\text{new}}(\mathbf{r}) - \delta v_{\text{old}}(\mathbf{r}))^2 \right\}} \quad . \tag{3.99}$$

3.4.3.2. Numerical convergence

We assess the numerical convergence of the implemented SMPB-DFT scheme by calculating a test set of 13 differently functionalized neutral, organic molecules dissolved in water ($\varepsilon^{\text{s,bulk}} = 78.36$ at room temperature,[14] cf. Fig. 2.1) containing a 1 M electrolyte with

3. Methods
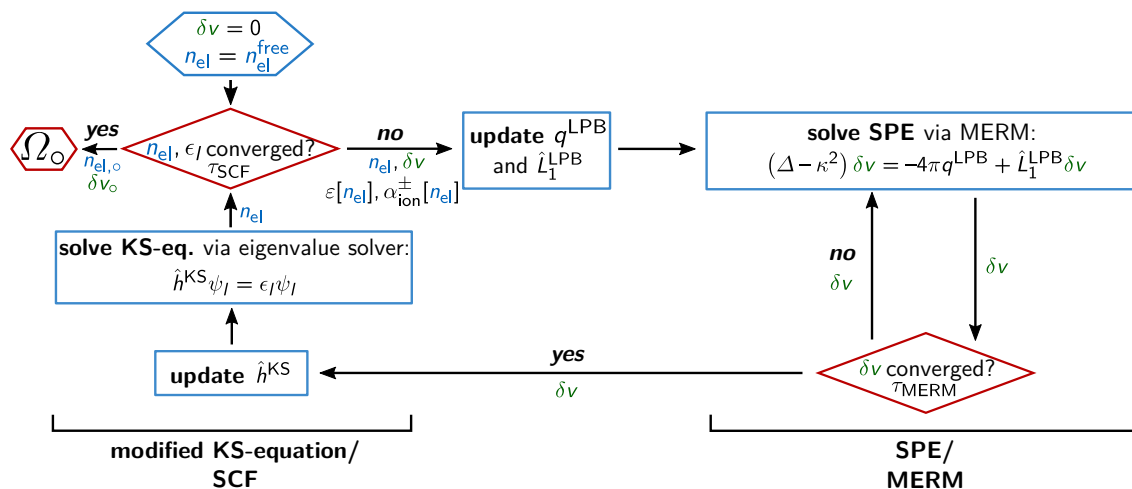
Figure 3.5.: Workflow of the MERM-based LPB solver inside `FHI-aims`. Always one SCF step is performed in approaching the minimum of n_{el} and then δv is converged as solution of the LPBE by the MERM. The converged v is used to update the KS operator, the KS equation is solved and the electron density updated. The process is repeated until overall self-consistency in energy, electron density and eigenvalues has been reached. Reproduced with permission from ref. [86]. © 2016 American Chemical Society.
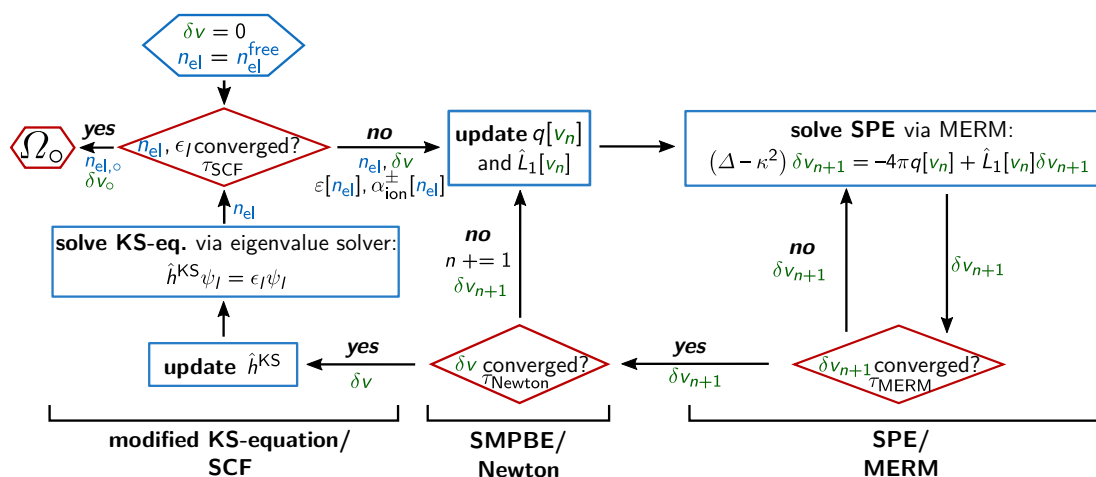
Figure 3.6.: Workflow of the Newton-MERM-based SMPB solver inside `FHI-aims`. At each electronic SCF step of `FHI-aims` the iterative Newton scheme to optimize δv is initiated. Each Newton step then involves the self-consistent solution of the SPE of Eq. (3.75) through the MERM. Reproduced with permission from ref. [86]. © 2016 American Chemical Society.

ionic charges $z = 1$. This set constitutes a sub-set of the test set introduced by Shivakumar *et al.* [144] and is given in Tab. 3.2. For all calculations we employ the parametrization of Andreussi *et al.* for the dielectric function (n_{min} and n_{max}) and for the non-mean-field solvent-solute interaction part of the solvation energy $\Omega_\varepsilon^{non-mf}$ (($\alpha + \gamma$) and β) as obtained by their best fit to experimental solvation energies ("fitg03+β") (cf. Section 4.1). [5] For the ion-specific SMPBE parameters representative values $a = 5\,\text{Å}$, $d_{\alpha_{ion}}^\pm = d_{\alpha_{ion}} = 0.5$,

$\xi_{\alpha_{\mathrm{ion}}}^{\pm} = \xi_{\alpha_{\mathrm{ion}}} = 1$ and $T = 300\,\mathrm{K}$ are used, cf. Section 4.2. As mentioned in the introduction, PBE-GGA[112] is used as DFT xc functional for all calculations in this thesis.

index	name	index	name	index	name
13	piperazine	90	morpholine	163	tert-butyl methyl ether
16	trimethylamine	117	propanoic acid	200	propiononitrile
36	butyraldehyde	140	cyclopropane	206	nitrobenzene
69	4-methyl-1H-imidazole	142	diethyl disulfide		
79	biphenyl	160	1,3-dioxolane		

Table 3.2.: Test set of neutral molecules used for the convergence tests. The index numbers refer to the number in the large test set from Shivakumar *et al.*,[144] from which these molecules were drawn.

For this test set, using conservative default convergence criteria of $\tau_{\mathrm{Newton/MERM}} < 1 \cdot 10^{-10}$ is found to be more than enough to obtain highly converged electrostatic potentials and solvation free energies. Fastest convergence of the MERM is observed for a linear mixing parameter $\eta = 0.5$. For this η the self-consistent solution of the SPE converged below the convergence criterion for τ_{MERM} is similarly quickly achieved for all tested molecules – independent of their size and polarity. The number of corresponding MERM steps is initially typically around 60 and then decreases quickly to about five in subsequent Newton and SCF steps (cf. the case of nitrobenzene in Fig. 3.8 as an example), which proves the efficiency of the employed preconditioner. The maximum number of Newton steps required to reach the $\tau_{\mathrm{Newton}} < 1 \cdot 10^{-10}$ convergence criterion is three. As illustrated in Fig. 3.7, at these settings the incorporation of the SMPBE solver has only an insignificant effect on the SCF convergence, i.e. the total number of SCF steps required to reach the predefined τ_{SCF} convergence criterion is about the same with or without the additional solvent calculations. This finding also extends to the case, where the rigid superposition of free atom densities $n_{\mathrm{el}}^{\mathrm{free}}$ is employed in the evaluation of the dielectric and ion exclusion function, cf. Section 3.2.2.1.

In general, the computational overhead due to the solvation calculation is therefore mostly determined by the SPE solving step. Therein, the multipole summation is the most expensive computational transformation scaling $\mathrm{O}(N^2)$ with system size.[1] This is, however, drastically improved for larger systems where the confinement of the source multipole moments due to the neglect of all fast-dying far field multipole moments $\delta v_{\mathrm{at},lm,n+1}^{\mathrm{ff}}(r_{\mathrm{at}})$ with $l_{\mathrm{max,at}} > 0$ crucially reduces the computational time of the multipole summation. For smaller systems of the size of those of the molecular test set, this saving is not yet noticeable, as the integration grid does not extend significantly beyond the cutoff radius. The parallel scalability of our implemented SMPBE solver depends thereby entirely on the scaling of the computational bottleneck in form of the multipole summation. Since `FHI-aims` uses atom-centered integration grids that are designed for optimal parallel scalability, the multipole summations can be very efficiently parallelized, cf. Fig. (10) in ref. [1].

As the MERM scheme performs the numerical integration to solve the SPE on the `FHI-aims` internal integration grids, it is subject to the same truncation and integration grid parameters already present in any regular `FHI-aims` DFT calculation. In detail, these are the `radial_multiplier` defining the radial integration grid density, the maximum angular momentum in the multipole expansion $l_{\mathrm{max,at}}$, cf. Eq. (3.80), and the radii $r_{\mathrm{onset,at}}$ and
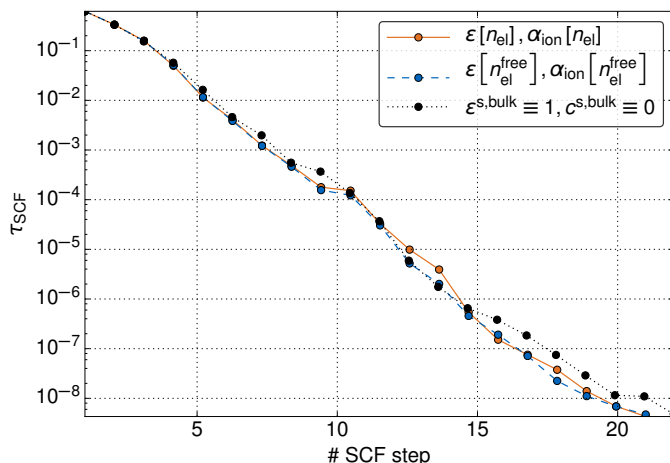
Figure 3.7.: Illustration of the SCF convergence for the SMPB-DFT scheme in `FHI-aims` (default *tight* settings) using a nitrobenzene molecule dissolved in water containing a 1 M 1:1 electrolyte as example. Compared is the integrated root mean square change of n_{el}, τ_{SCF}, as a function of SCF steps for the molecule in vacuum (black dotted line) and in the electrolyte (orange solid line). Additionally shown (blue dashed line) is the convergence when the superposition of free atom densities n_{el}^{free} is used in the evaluation of the dielectric and ion exclusion function for the solvated case, cf. Section 3.2.2. Reproduced with permission from ref. [86]. © 2016 American Chemical Society.
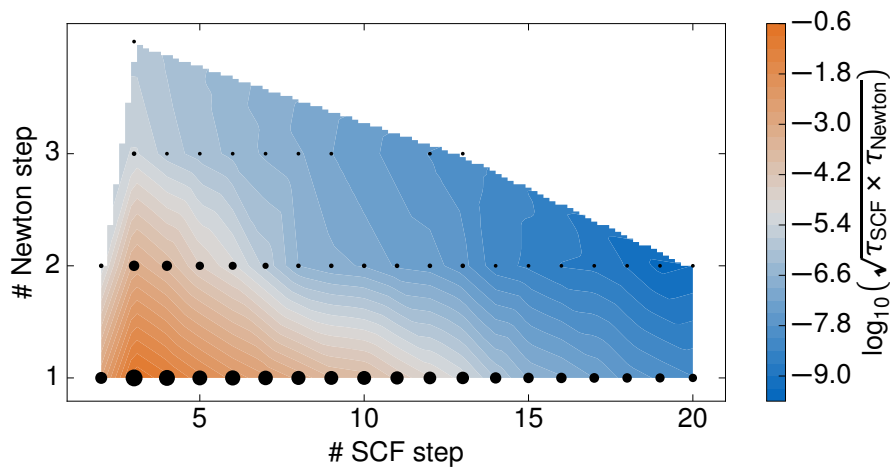
Figure 3.8.: Convergence of electron density and electrostatic potential during a SMPB-DFT calculation of nitrobenzene dissolved in water containing a 1 M 1:1 electrolyte (shown for all SCF steps > 1, "tight" settings). The contour lines show the weighted root mean square change in n_{el} and v at each SCF and Newton step. The dot size represents the number of relaxation steps needed to solve the SPE until self-consistence at each Newton step (the first initialization cycle was not considered). All SMPB-DFT parameters are as for Fig. 3.7. Reproduced with permission from ref. [86]. © 2016 American Chemical Society.

$r_{cut,at}$ defined by the confinement potential $v_{cut,at}$. Convergence of ΔG_{sol} and $\Delta\Delta G_{ion}$ for the molecular test set is obtained at the meV-level for the default *tight* production settings for these values as listed in Tab. 3.1 with $l_{max,at}$ replacing the multipole truncation parameter

$l_{\text{hartree,at}}$. As a consequence, this eliminates the need to introduce separate truncation and integration grid parameters for the MERM. As further detailed in Appendix A.7, equivalent findings are obtained for the convergence of ΔG_{sol} and $\Delta\Delta G_{\text{ion}}$ with the NAO basis, i.e. also here meV-level convergence is obtained at the predefined default settings.

In practice, SMPB-DFT solvation free energy calculations can thus be performed at the recommended *tight* production settings of `FHI-aims`.[1] Further increase of the truncation and integration grid parameters allows to also converge a quantity like the ionic charge distribution $n_{\text{ion}}^{\text{SMPB}}$, which is highly sensitive to small changes in the outer electrostatic potential. In order to evaluate the performance of the Newton-MERM scheme to resolve such functions, we compare results with the adaptive FEM program package `KARDOS`[145] in which we implemented both the SMPBE and LPBE.[146] FEMs are optimally suited for reference calculations due to the inherent hierarchical basis set providing a systematic way to increase the accuracy of the results. In order to solve the same PDEs in `KARDOS` as in `FHI-aims`, certain functions have to be transferred between both program packages. The vacuum δ-electron density δn_{el} as obtained by `FHI-aims` and used for the evaluation of ε and $\alpha_{\text{ion}}^{\pm}$ is written out on a regular grid and interpolated by a piecewise polynomial function represented as a tensor product of one-dimensional b-splines. To avoid numerical instabilities due to the singularities in the electrostatic potential, we use the same regularization as in `FHI-aims` of v with v^{free} and transfer the required free-atom potentials via the corresponding spline coefficients as defined in `FHI-aims`. In order to simplify the comparison we focus on linear molecules which additionally let us exploit the axial symmetry of the resulting PDEs to perform fast and highly accurate benchmark calculations. The resulting two-dimensional problem is solved on a domain of spatial dimensions 64×320 and by relaxing a corresponding time-depending problem to stationary state. The initial grid consists of 250 triangles and we require a spatial accuracy of 10^{-6} in δv. With these settings, the grid is adaptively refined 11 times, resulting in a mesh with roughly $100,000$ triangles and a minimal grid spacing of $\approx 10^{-2}$. We furthermore apply homogeneous Dirichlet boundary conditions $\delta v = 0$ at the edge of the domain.

To illustrate the comparison between `KARDOS` and `FHI-aims` , we first considered the ground-state charge distribution for the linear HCCH molecule in vacuum as obtained at the level of DFT with the PBE-GGA functional.[112] For this fixed n_{el}, the SMPBE was then solved in `FHI-aims` and in the equivalent external implementation of the SMPBE in `KARDOS` again for water containing a $1\,\text{M}$ 1:1 electrolyte and using the same SMPB parameters as before. Figure 3.9 compares the corresponding results for the ionic charge density $n_{\text{ion}}^{\text{SMPB}}$ obtained by both methods. The left panel shows the results from a highly accurate FEM benchmark calculation, while the upper right panel shows the results from `FHI-aims` calculation using $l_{\text{max,at}} = 6\ \forall$ at (default *tight* settings) and the lower right panel using $l_{\text{max,at}} = 8\ \forall$ at (*really tight* settings). As can be seen, qualitative agreement of the ion density is already achieved at `FHI-aims` production settings. The residual error in the electrostatic potential which we showed to be negligibly small on an energy scale (cf. Appendix A.7) is further reduced by increasing the order of the multipole expansion. Changing to a charged molecule, we even got excellent agreement for the difference of ionic charge densities $n_{\text{ion}}^{\text{SMPB}} - n_{\text{ion}}^{\text{LPB}}$, a quantity particularly challenging to resolve. A corresponding plot is shown in Fig. 3.10.
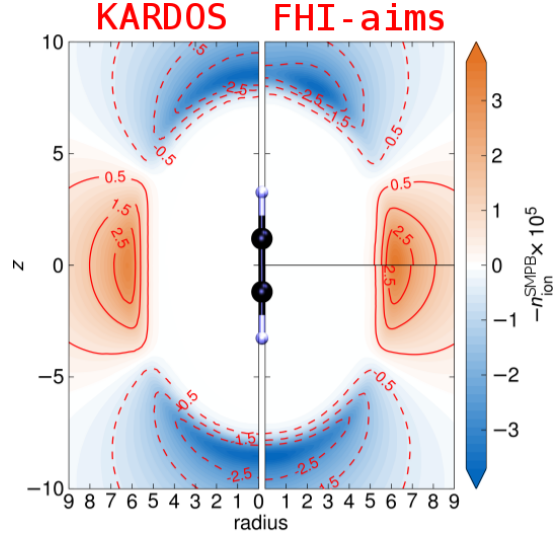
Figure 3.9.: Comparison of the ionic charge distribution $n_{\text{ion}}^{\text{SMPB}}$ as calculated for HCCH dissolved in water containing a 1 M 1:1 electrolyte (shown with intuitive sign convention), once with the adaptive finite-element program package `KARDOS` (left half) and with the implementation in `FHI-aims` (right half). The `FHI-aims` calculations were performed with the default numerical settings $l_{\text{max,at}} = 6 \, \forall$ at (upper panel) and with a higher accuracy of the multipole expansion $l_{\text{max,at}} = 8 \, \forall$ at (lower panel). Reproduced with permission from ref. [86]. © 2016 American Chemical Society.

3.4.4. Atomic Forces in the PB Scheme of `FHI-aims`

In order to extend the functionality of our SMPB-DFT scheme to dynamic simulations it is necessary to derive the corresponding atomic forces from the minimum free energy expression. To this end, we apply a similar strategy as in Section 3.3.6 leading to analogous expressions for HF, Pulay and multipole correction forces.

3.4.4.1. Hellmann-Feynman and Pulay Forces

Analogously to Section 3.3.6, we evaluate atomic forces also in the SMPB-DFT formalism from the total derivative of the minimum free energy expression, in this case $\Omega_{\circ}$ as given in Eq. (3.27)

$$\boldsymbol{F}_{\text{at}} = -\frac{\mathrm{d}\Omega_{\circ}}{\mathrm{d}\boldsymbol{R}_{\text{at}}} \quad . \tag{3.100}$$

Utilizing the Lagrangian in Eq. (3.15) in its unitary transformed form

$$\mathcal{L}[v, n_{\text{el}}] = \Omega_{\varepsilon, \alpha_{\text{ion}}^{\pm}}[v, n_{\text{el}}] + \sum_{l=1}^{N_{\text{states}}} \epsilon_l \left[\int \mathrm{d}\boldsymbol{r} \psi_l \psi_l^* - 1 \right] \quad , \tag{3.101}$$

we can express the minimum free energy in terms of this functional

$$\Omega_{\circ} = \min(\mathcal{L}[v, n_{\text{el}}]) = \mathcal{L}[v_{\circ}, n_{\text{el},\circ}] = \int \mathrm{d}\boldsymbol{r} \ell[v_{\circ}, n_{\text{el},\circ}] \quad , \tag{3.102}$$
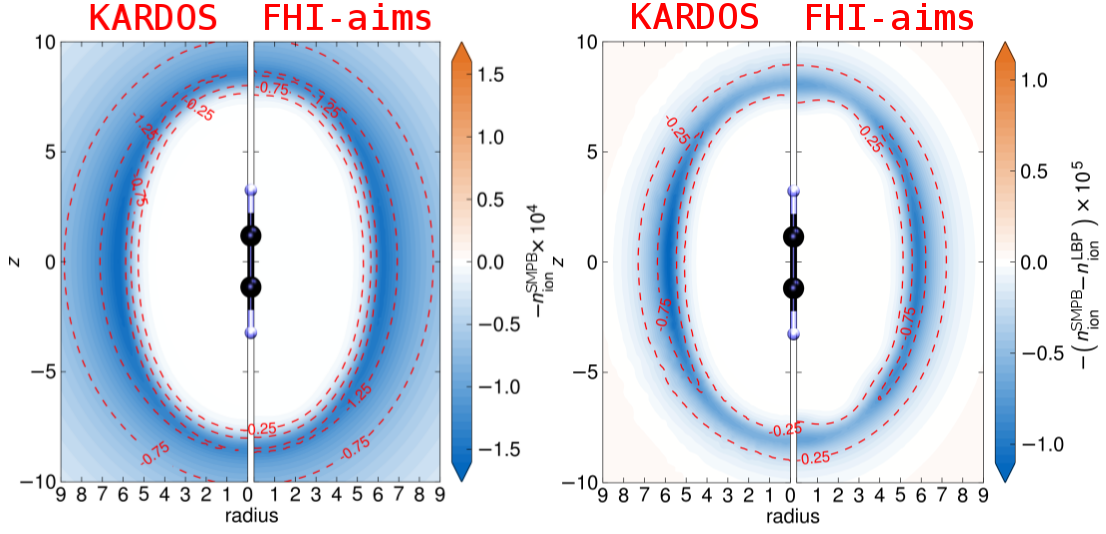
Figure 3.10.: Comparison of the ionic charge density $n_{\text{ion}}^{\text{SMPB}}$ (left) and difference of ionic charge densities $n_{\text{ion}}^{\text{SMPB}} - n_{\text{ion}}^{\text{LPB}}$ (right) as calculated for HCCH$^+$ dissolved in water containing a 1 M 1:1 electrolyte (shown with intuitive sign convention), once with the adaptive finite-element program package `KARDOS` (left half) and with the implementation in `FHI-aims` (right half). The `FHI-aims` calculations were performed with the default *tight* settings ($l_{\text{max,at}} = 6 \; \forall \, \text{at}$). Reproduced with permission from ref. [86]. © 2016 American Chemical Society.

with the Lagrangian energy functional density ℓ. Using the same procedure as in Section 3.3.6, we can express the atomic forces by an integral over functional derivatives of $\mathcal{L}$ with respect to $\psi_{l,\circ}$, n_{nuc} and $v_{\circ}$ which results analogously to Eq. (3.63) in the same expressions for HF and Pulay forces

$$\boldsymbol{F}_{\text{at}} = -\frac{\mathrm{d}\Omega_{\circ}}{\mathrm{d}\boldsymbol{R}_{\text{at}}} = \underbrace{-2 \sum_{l=1}^{N_{\text{states}}} \int \mathrm{d}\boldsymbol{r} \, \nabla_{\text{at}} \psi_{l,\circ} \left(\hat{h}_{\circ}^{\text{KS}} - \epsilon_{l,\circ} \right) \psi_{l,\circ}^{*}}_{\boldsymbol{F}_{\text{at}}^{\text{Pulay}}} \underbrace{- \int \mathrm{d}\boldsymbol{r} \left\{ v_{\circ} \nabla_{\text{at}} n_{\text{nuc}} \right\}}_{\boldsymbol{F}_{\text{at}}^{\text{HF}}} \quad , \quad (3.103)$$

69

In contrast to the vacuum case, the HF forces can, however, not be separated into electronic and nuclear contributions anymore. Instead, they have to be rewritten as

$$
\begin{aligned}
\boldsymbol{F}_{\mathrm{at}}^{\mathrm{HF}} &= -\int \mathrm{d}\boldsymbol{r}\left\{v_{\circ}\nabla_{\mathrm{at}}n_{\mathrm{nuc}}\right\} = \int \mathrm{d}\boldsymbol{r}\left\{v_{\circ}\nabla_{\mathrm{at}}\left(\sum_{\mathrm{at}'}Z_{\mathrm{at}'}\delta(\boldsymbol{r}_{\mathrm{at}'})\right)\right\} \\
&= \int \mathrm{d}\boldsymbol{r}\left\{v_{\circ}Z_{\mathrm{at}}\nabla_{\mathrm{at}}\delta(\boldsymbol{r}_{\mathrm{at}})\right\} \\
&= -\int \mathrm{d}\boldsymbol{r}\left\{v_{\circ}Z_{\mathrm{at}}\nabla\delta(\boldsymbol{r}_{\mathrm{at}})\right\} = \int \mathrm{d}\boldsymbol{r}\left\{\left(\sum_{\mathrm{at}'}\nabla v_{\mathrm{at}',\circ}(\boldsymbol{r}_{\mathrm{at}'})\right)Z_{\mathrm{at}}\delta(\boldsymbol{r}_{\mathrm{at}})\right\} \\
&= -\int \mathrm{d}\boldsymbol{r}\left\{\left(\sum_{\mathrm{at}'}\nabla_{\mathrm{at}'}v_{\mathrm{at}',\circ}(\boldsymbol{r}_{\mathrm{at}'})\right)Z_{\mathrm{at}}\delta(\boldsymbol{r}_{\mathrm{at}})\right\} \\
&= -Z_{\mathrm{at}}\sum_{\mathrm{at}'}\nabla_{\mathrm{at}'}v_{\mathrm{at}',\circ}(\boldsymbol{R}_{\mathrm{at}}-\boldsymbol{R}_{\mathrm{at}'}) = Z_{\mathrm{at}}\sum_{\mathrm{at}'}\nabla_{\mathrm{at}}v_{\mathrm{at}',\circ}(\boldsymbol{R}_{\mathrm{at}}-\boldsymbol{R}_{\mathrm{at}'}) \\
&\rightarrow Z_{\mathrm{at}}\left[\left(\nabla_{\mathrm{at}}v_{\mathrm{es,at}}^{\mathrm{free}}+\nabla_{\mathrm{at}}\delta v_{\mathrm{at},\circ}\right)\Big|_{\boldsymbol{r}=\boldsymbol{R}_{\mathrm{at}}}+\sum_{\mathrm{at}'\neq\mathrm{at}}\nabla_{\mathrm{at}}v_{\mathrm{at}',\circ}(\boldsymbol{R}_{\mathrm{at}}-\boldsymbol{R}_{\mathrm{at}'})\right] \quad, \quad (3.104)
\end{aligned}
$$

where we removed the nuclear charge interaction with their own potential gradient in the last step. We thereby made use of the fact that both v as δv can be decomposed into their atomic contributions (cf. Eq. (3.80)).

Evaluating the Pulay force terms is in principle straightforward, if we apply the modified KS operator that was derived in Section 3.2.3. In contrast to energy calculations, the evaluation of forces does, however, now imply the need for the explicit evaluation of the Hessian matrix due to the xc correlation term E^{xc} (in the case of a GGA xc-functional[1]) and the term $\Omega_{\varepsilon}^{\mathrm{non-mf}}$ both depending on the gradient of the electron density. While in static DFT calculations, this can be avoided by moving the gradient onto the basis functions as shown in Eq. (3.23). The gradient of the basis functions is in this case already present.

Considering the $\Omega_{\varepsilon}^{\mathrm{non-mf}}$-part of the KS Hamiltonian given in Eq. (3.19) the resulting contribution to the Pulay force is given by:

$$
\begin{aligned}
\boldsymbol{F}_{\mathrm{at}}^{\mathrm{Pulay},\Omega^{\mathrm{non-mf}}} = {}&-2\sum_{l=1}^{N_{\mathrm{states}}}\int \mathrm{d}\boldsymbol{r}\nabla_{\mathrm{at}}\psi_{l,\circ}\left(\left\{(\alpha+\gamma)\frac{\partial\vartheta_{\circ}}{\partial n_{\mathrm{el},\circ}}+\beta\frac{\partial s_{\circ}}{\partial n_{\mathrm{el},\circ}}\right\}-\epsilon_{l,\circ}\right)\psi_{l,\circ}^{*} \\
&-2\sum_{l=1}^{N_{\mathrm{states}}}\int \mathrm{d}\boldsymbol{r}\nabla_{\mathrm{at}}\psi_{l,\circ}\left\{\beta\nabla\cdot\frac{\partial s_{\circ}}{\partial\nabla n_{\mathrm{el},\circ}}\right\}\psi_{l,\circ}^{*} \quad. \quad (3.105)
\end{aligned}
$$

The second part can then be rewritten by moving the ∇-operator onto the basis functions (neglecting the surface integrals):

$$
\begin{aligned}
\boldsymbol{F}_{\mathrm{at}}^{\mathrm{Pulay},\Omega^{\mathrm{non-mf}}} = {}&-2\sum_{l=1}^{N_{\mathrm{states}}}\int \mathrm{d}\boldsymbol{r}\nabla_{\mathrm{at}}\psi_{l,\circ}\left(\left\{(\alpha+\gamma)\frac{\partial\vartheta_{\circ}}{\partial n_{\mathrm{el},\circ}}+\beta\frac{\partial s_{\circ}}{\partial n_{\mathrm{el},\circ}}\right\}-\epsilon_{l,\circ}\right)\psi_{l,\circ}^{*} \\
&+2\int \mathrm{d}\boldsymbol{r}\beta\frac{\partial s_{\circ}}{\partial\nabla n_{\mathrm{el},\circ}}\sum_{l=1}^{N_{\mathrm{states}}}\left(\left[\nabla_{\mathrm{at}}\nabla\psi_{l,\circ}\right]\psi_{l,\circ}+(\nabla_{\mathrm{at}}\psi_{l,\circ})(\nabla\psi_{l,\circ})\right)\right\} \quad.
\end{aligned}
$$
$$(3.106)$$

The resulting expression now contains the above mentioned second derivatives of the single-electron wave-functions $\psi_{l,\circ}$ requiring the explicit evaluation of the Hessian matrix.

3.4.4.2. Multipole Correction Force

Analogously to Section 3.3.6.2 we can also in the SMPB case derive modified force terms that take into account the multipole correction of the total energy as presented in Section 3.4.2. We start by writing down the multipole corrected minimum SMPB free energy as the minimum of the corresponding Lagrangian functional. After introducing a new function $q_{n_{\mathrm{el},\circ}}^{\mathrm{mp}} = n_{\mathrm{sol},\circ} - q_{\mathrm{iter},\circ}^{\mathrm{res}}$, this is given by:

$$
\begin{aligned}
\tilde{\Omega}_{\circ} &= \min(\mathcal{L}[v, n_{\mathrm{el}}]) = \mathcal{L}[v_{\circ}, n_{\mathrm{el},\circ}] \\
&= T^{\mathrm{S}}[n_{\mathrm{el},\circ}] + E^{\mathrm{xc}}[n_{\mathrm{el},\circ}] + \tilde{\Omega}_{\varepsilon,\alpha_{\mathrm{ion}}^{\pm}}^{\mathrm{mf}}[n_{\mathrm{el},\circ}, n_{\mathrm{nuc}}, q_{n_{\mathrm{el},\circ}}^{\mathrm{mp}}, v_{\circ}^{\mathrm{mp}}] \\
&\quad + \Omega_{\varepsilon}^{\mathrm{non-mf}}[n_{\mathrm{el},\circ}] + \sum_{l=1}^{N_{\mathrm{states}}} \epsilon_{l,\circ}\left[\int \mathrm{d}\boldsymbol{r}\,\psi_{l,\circ}\psi_{l,\circ}^{*} - 1\right] \quad,
\end{aligned}
\tag{3.107}
$$

with

$$
\tilde{\Omega}_{\varepsilon,\alpha_{\mathrm{ion}}^{\pm}}^{\mathrm{mf}} = \int \mathrm{d}\boldsymbol{r}\,n_{\mathrm{sol},\circ}v_{\circ}^{\mathrm{mp}} - \frac{1}{2}\int \mathrm{d}\boldsymbol{r}\,q_{n_{\mathrm{el},\circ}}^{\mathrm{mp}}v_{\circ}^{\mathrm{mp}} + \Omega_{\alpha_{\mathrm{ion}}^{\pm}}^{\mathrm{ion}}[n_{\mathrm{el},\circ}, v_{\circ}^{\mathrm{mp}}] \quad.
\tag{3.108}
$$

In order to calculate the corresponding atomic forces, we again rely on the formulation in terms of functional derivatives, here with respect to $\{n_{\mathrm{el},\circ}(\{\psi_l\}), n_{\mathrm{nuc}}, q_{n_{\mathrm{el},\circ}}^{\mathrm{mp}}, v_{\circ}^{\mathrm{mp}}\}$:

$$
\boldsymbol{F}_{\mathrm{at}} = -\frac{\mathrm{d}}{\mathrm{d}\boldsymbol{R}_{\mathrm{at}}}\tilde{\Omega}_{\circ} = -2\sum_{l=1}^{N_{\mathrm{states}}}\int \mathrm{d}\boldsymbol{r}\bigg\{\underbrace{\frac{\delta\mathcal{L}}{\delta\psi_{l,\circ}}}_{(\hat{h}_{\circ}^{\mathrm{KS}}-\epsilon_{l,\circ})\psi_{l,\circ}^{*}}\nabla_{\mathrm{at}}\psi_{l,\circ}\bigg\} - \underbrace{\int \mathrm{d}\boldsymbol{r}\bigg\{\underbrace{\frac{\delta\mathcal{L}}{\delta n_{\mathrm{nuc}}}}_{v_{\circ}^{\mathrm{mp}}}\nabla_{\mathrm{at}}n_{\mathrm{nuc}}\bigg\}}_{\boldsymbol{F}_{\mathrm{at}}^{\mathrm{HF}}}
$$

$$
\underbrace{-\int \mathrm{d}\boldsymbol{r}\bigg\{\underbrace{\frac{\delta\mathcal{L}}{\delta q_{n_{\mathrm{el},\circ}}^{\mathrm{mp}}}}_{-\frac{1}{2}v_{\circ}^{\mathrm{mp}}}\nabla_{\mathrm{at}}q_{n_{\mathrm{el},\circ}}^{\mathrm{mp}} - \underbrace{\frac{\delta\mathcal{L}}{\delta v_{\circ}^{\mathrm{mp}}}}_{n_{\mathrm{sol},\circ}-\frac{1}{2}q_{n_{\mathrm{el},\circ}}^{\mathrm{mp}}}\nabla_{\mathrm{at}}v_{\circ}^{\mathrm{mp}}\bigg\}}_{\boldsymbol{F}_{\mathrm{at}}^{\mathrm{mp}}} \quad.
\tag{3.109}
$$

The first and second terms represent as before the HF and Pulay force contributions, respectively. In contrast to the vacuum case, we now have to evaluate both terms with the multipole approximated potential $v_{\circ}^{\mathrm{mp}}$, not only the Pulay force. The remaining derivatives with respect to the multipole expanded properties constitute again the multipole correction force $\boldsymbol{F}_{\mathrm{at}}^{\mathrm{mp}}$. We thereby ignored the dependence of the ionic part of the free energy on the multipole potential, i.e. we assumed $\frac{\partial\Omega_{\alpha_{\mathrm{ion}}^{\pm}}^{\mathrm{ion}}}{\partial v_{\circ}^{\mathrm{mp}}} \approx 0$. As discussed in detail in Appendix A.3, A.5 and A.6, we expect that the presence of the ions does not critically influence the multipole convergence of energies and atomic forces. We, however, stress that such an approximation

has to be tested thoroughly in the future and an implementation of the missing terms should be generally straightforward. Following this argumentation, we then get for $\boldsymbol{F}_{\mathrm{at}}^{\mathrm{mp}}$:

$$
\begin{aligned}
\boldsymbol{F}_{\mathrm{at}}^{\mathrm{mp}} &= \int \mathrm{d}\boldsymbol{r} \left\{ \frac{1}{2} \left(v_{\mathrm{o}}^{\mathrm{mp}} \nabla_{\mathrm{at}} q_{n_{\mathrm{el}},\mathrm{o}}^{\mathrm{mp}} + q_{n_{\mathrm{el}},\mathrm{o}}^{\mathrm{mp}} \nabla_{\mathrm{at}} v_{\mathrm{o}}^{\mathrm{mp}} \right) - n_{\mathrm{sol},\mathrm{o}} \nabla_{\mathrm{at}} v_{\mathrm{o}}^{\mathrm{mp}} \right\} \\
&\approx -q_{\mathrm{iter},\mathrm{o}}^{\mathrm{res}} \nabla_{\mathrm{at}} v_{\mathrm{o}} \quad ,
\end{aligned}
\tag{3.110}
$$

where the last line follows from the recasting presented in Appendix A.6. The multipole correction force thus adopts an analogous functional form to the vacuum-expression in `FHI-aims`, given in Eq. (3.69). As discussed in detail in Appendix A.6, Eq. (3.110) is exactly valid only for the vacuum case and approximately for the solvent case. We have proven this for some molecular test systems by performing multipole order convergence tests and comparing to numerical forces obtained from a finite difference scheme discretizing the ∇_{at}-operator.[147] For finite ionic strengths, the non-linearity of the SMPB leads to a much more complex result for the multipole correction force. Since we, however, as mentioned above, assume ions to induce only a negligible effect on the multipole convergence of the atomic forces (cf. argumentation in Appendix A.3), Eq. (3.110) will most probably also hold in these cases. We leave it here to future studies to evaluate the validity of this statement by performing profound convergence studies and comparing to FDM calculations.

Parametrization*†

<div style="text-align: right; font-size: 4em;">4</div>

Continuum solvation methods are effective approaches which integrate out the electrolyte's degrees of freedom and thereby avoid an explicit modeling of the liquid phase. As a consequence, their capabilities and reliability stand and fall with the parametrization of the coarse-grained interactions. Our SMPB-DFT scheme builds on a total of four parameters defining the solute-solvent interactions: $\{n_{\min}, n_{\max}\}$ describing the solvation cavity and dielectric function transition and $\{(\alpha + \gamma), \beta\}$, governing the non-mean-field free energy contributions. In the following, the electron density iso-values $\{n_{\min}, n_{\max}\}$ will be referenced to in atomic units. In accordance with literature we use cgs units for $(\alpha + \gamma)$(dyn/cm) and SI units for β(GPa).[5] Solute-ion interactions on the other hand depend on the choice of the ionic parameters $\{a, d_{\alpha_{\mathrm{ion}}}^{\pm}, \xi_{\alpha_{\mathrm{ion}}}^{\pm}\}$ describing the finite ion size and the thickness and smoothness of the Stern layer, respectively, whereby a will be given in Å and the Stern layer parameters are unitless.

Aspiring to derive a transferable parameter set that holds for a wide range of systems and conditions, we suggest to separately determine and optimize the prior non-ionic parameter group through solvation calculations for ion-free solvents. Such an approach will be particularly suitable for weakly charged or neutral solutes, but may also fail if the solvent structure and dielectric permittivity are largely influenced by the ionic charges. The latter leads for example to the well-known *dielectric decrement* effect which describes a reduction of the dielectric permittiviy in regions of high ion concentrations.[149–152] In this thesis we focus on the simpler case where solute interactions with both ions and solvent molecules are expected to decouple. Furthermore, although our method is in principle not limited to a specific solvent, we restrict our studies to water for which the wide availability of experimental reference data enables the construction of training sets which can be used for the derivation of transferable parameters. Corresponding solvation model parameters have already been obtained with the so called SCCS scheme,[5] to which our SMPB-DFT scheme reduces in the case of zero ionic strengths. In these studies, parameters applicable to both neutral[5] and charged[6] molecular solutes have been determined, yielding reasonably accurate agreement (neutral molecules: mean absolute error (MAE)$\approx$50 meV, cations: MAE$\approx$100 meV, anions: MAE$\approx$240 meV) with experimental hydration energies. In this

---

chapter, we therefore adopt these parameters and use the results as a quality check for the numerical accuracy of our implementation.

While there have been many studies on parametrization strategies for ion-free implicit solvation models,[18] only little is known about ion-specific PB parameters defining e.g. the Stern layer or the ion size.[60,63,78] Moreover, even though PB methods have been applied extensively in chemistry,[48] in particular in (electro-)catalysis,[49–51] electrochemistry,[52–54] electrokinetics[55,56] and biology,[36,37,45,47,57–63] it is still often not even clear which of the two mentioned modifications is essential for an accurate modeling of ion-specific effects. This ambiguity eventually led to the pragmatic combination of both strands into SMPB models.[23,24,60,72,78] This prevailing knowledge gap stands in contrast to the fact that ion-specific parameters often sensitively affect the outcome of PB-based solvation calculations,[60,63,78] highlighting the need to more extended studies.

In this chapter, we therefore start with a basic assessment of the SMPB ionic parameter space by simulating different solutes with varying ionic parameters and comparing to experimental reference data. In particular, we consider properties related to the ion effect on the solvation energy $\Delta\Delta G_{\mathrm{ion}}$ as e.g. mean activity[7] or Setschenow coefficients[8] which have been experimentally widely studied and can be easily extracted from SMPB-DFT calculations. From this first analysis, we then find that the ionic parameter space can be condensed into a single relevant parameter $d_{\alpha_{\mathrm{ion}}}$. In order to determine this parameter for a particular salt solution, we utilize again Setschenow coefficients which are available for sufficiently large databases of various neutral solutes. As a result, we arrive at transferable parameters for a wide range of monovalent salt solutions whereby the optimized parameters satisfy physically realistic trends with hydration number[9,121] of the respective ions.

Finally, we refer the reader also to the respective publications [86] and [148] from which large parts have been included in this chapter.

4.1. Solvation Model

In the ion-free case, our developed SMPB-DFT model reduces formally to the implicit solvation model (SCCS scheme) as introduced by the work of Andreussi *et al.*[5] While the SCCS scheme uses Fourier transforms instead of multipole expansions to solve the appearing Green's function integral (cf. Section 3.4.1.2 and Eqs. (49)-(51) in ref. [5]), the parametrization protocol as presented in Section 3.2.2 is equivalent. This allows us to adopt the already available parameters for water as a solvent. In order to optimize these parameters for the case of neutral solutes, Andreussi *et al.* fitted to the experimental hydration free energies $\Delta G_{\mathrm{sol}}^{\mathrm{exp}}$ of the 240-molecule test set of Shivakumar *et al.*[144] to obtain the "fitg03+β" parameter set: $n_{\mathrm{min}} = 0.0001$, $n_{\mathrm{max}} = 0.005$, $\alpha + \gamma = 50\,\mathrm{dyn/cm}$, $\beta = -0.35\,\mathrm{GPa}$ (using $\varepsilon^{\mathrm{s,bulk}} = 78.36$). Similarly, they arrived at optimized parameter sets for charged solutes, i.e. the "fit cations" ($n_{\mathrm{min}} = 0.0002$, $n_{\mathrm{max}} = 0.0035$, $\alpha + \gamma = 5\,\mathrm{dyn/cm}$, $\beta = 0.125\,\mathrm{GPa}$) and the "fit anions" ($n_{\mathrm{min}} = 0.0024$, $n_{\mathrm{max}} = 0.0155$, $\alpha + \gamma = 0$, $\beta = 0.450\,\mathrm{GPa}$) parameter sets. In Fig. 4.1 we compare the solvation free energies of the neutral molecule test set, calculated with our implementation and the "fitg03+β" parameters of Andreussi *et al.*[5] to their respective results. Specifically, we show the deviation with respect to the experimental reference. For a maximum comparability we
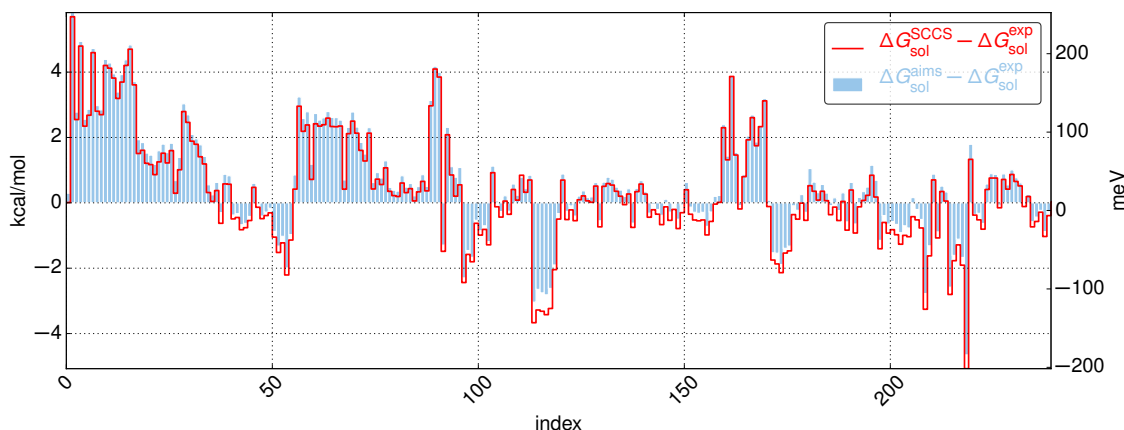
Figure 4.1.: Deviations of calculated room-temperature solvation free energies $\Delta G_{\mathrm{sol}}(c^{\mathrm{s,bulk}} = 0)$ from experimental values for the Shivakumar test set of 240 neutral molecules.[144] Compared are published results from the SCCS solver of Andreussi *et al.*[5] with our implementation in `FHI-aims` (*tight* settings), both using the optimized "fitg03+β" parameter set. The MAE of the present implementation with respect to experiment is 53 meV, the MAE with respect to the SCCS solver is 9.3 meV. Reproduced with permission from ref. [86]. © 2016 American Chemical Society.

employ the reference geometries provided by Andreussi *et al.* and the same DFT PBE-GGA functional.[112] The agreement between both solvers is excellent with an MAE of 9.3 meV over the whole test set. A large part of this already small difference can be traced back to the different basis sets employed in the two DFT program packages. These in turn affect the position of the solvation cavity via the density cutoffs. Using e.g. a Gaussian aug-cc-pVDZ basis in the `FHI-aims` implementation indeed reduces the MAE to an insignificant 6.5 meV (cf. Fig. 4.2).

Note, that we performed all calculations in this section using a non-self-consistent evaluation of the $\Omega_{\varepsilon}^{\mathrm{non-mf}}$ term, i.e. we assumed that $\frac{\delta \Omega_{\varepsilon}^{\mathrm{non-mf}}}{\delta n_{\mathrm{el}}} \approx 0$ which cancels the respective term in the modified KS-Hamiltonian in Eq. (3.24). We found this approximation to be valid for the case of neutral solutes as the non-mean-field contributions exert only negligible influence on the electron density, justifying the computationally efficient treatment of this contribution as a post-correction. In contrast to other authors who neglect these contributions outright,[130,153] we expect this approach in general to capture the majority of non-electrostatic effects. Such an approach can in general also avoid problems related to a numerically instable representation of corresponding derivatives (cf. Section 3.2.3) on the integration grid as observed by other authors before.[154] In the case of molecular systems, we did, however, not observe such numerical instabilities. Starting from Section 4.2.4, where we additionally account for finite ionic strengths, we therefore switch to a fully-self-consistent calculation of non-electrostatic contributions which avoids any possible inaccuracies stemming from an approximate post-corrective treatment.
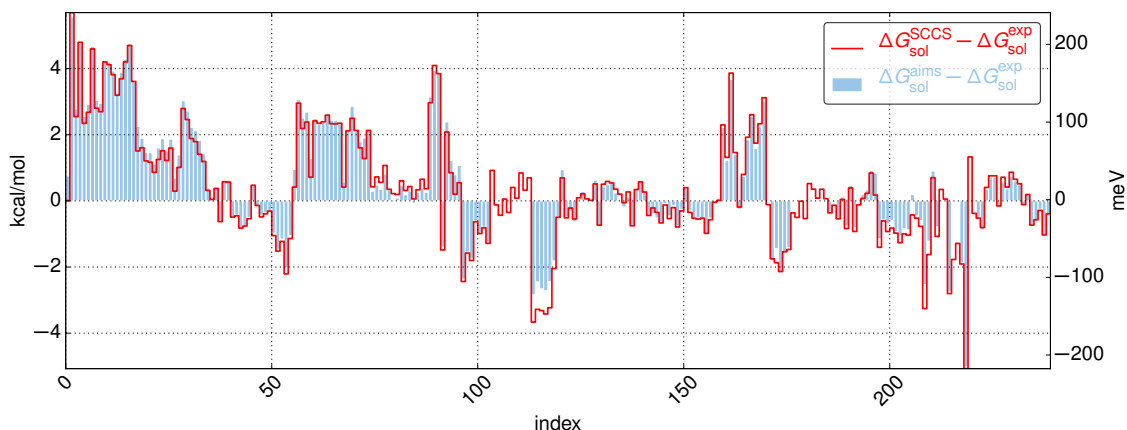
Figure 4.2.: Deviations of calculated solvation free energies $\Delta G_{\rm sol}(c^{\rm s,bulk} = 0)$ from experimental values for the Shivakumar test set of 240 neutral molecules. [144] Compared are published results from the SCCS solver of Andreussi *et al.* [5] with our implementation in `FHI-aims` using an aug-cc-pVDZ Gaussian basis set. Both solvers use the optimized "fitg03+β" parameter set. Reproduced with permission from ref. [86]. © 2016 American Chemical Society.

4.2. PB Ionic Charge Model

The true potential of the SMPB approach unfolds in the application to electrolyte solutions, where it accounts for effects of a finite ionic strength on top of the pure solvation effects. For this, five further ion-specific parameters need to be specified, $\{a, d^{\pm}_{\alpha_{\rm ion}}, \xi^{\pm}_{\alpha_{\rm ion}}\}$, describing the finite ion size, thickness and shape of the Stern layer, respectively. Notwithstanding the sensitivity of ionic effects on the choice of these parameters, [60,63,78] it is to date not clear which of these are most crucial for the outcome of PB simulations and there exists no general parametrization protocol that would provide them for a wide range of systems and conditions. This section, therefore, focuses first on a basic study and assessment of the ionic parameter space following a discussion and development of a coherent and transferable parametrization strategy. Our focus will thereby entirely be on aqueous monovalent salt electrolytes, due to the both wider availability of reference data and the current limitations of the here developed SMPB ion model. Extending the scope to higher-valent ions would e.g. also give rise to stronger ion correlation effects [73] which are beyond the reach of the mean-field scheme.

4.2.1. Stern Layer and Finite Ion Size

As already mentioned in the introduction, one of the main hurdles to determining the ionic parameters is a lack of knowledge about the physical interactions dominating the experimentally observed ion effects. In Fig. 4.3 we show all such interactions as accounted for on the level of SMPB theory at the example of a neutral solute embedded into an aqueous salt solution. In ionic mean-field models, stabilization of the solute occurs exclusively by electrostatic interactions of the solute with the mean-field of the ions, which are expected to be important in particular in the case of charged or highly polar solutes. Repulsive solute-ion interactions on the other hand lead to the creation of an ion-free Stern layer which

consists of a solvation layer around the solute and the more rigid part of the hydration shell of the ions.[121] Finally, hydrated ion-ion repulsions close to the solvation cavity can again destabilize the solute in solution. In general, an overall reduction of the solute's solvation energy at high salt concentrations is often denoted as *salting-out* effect.[109]
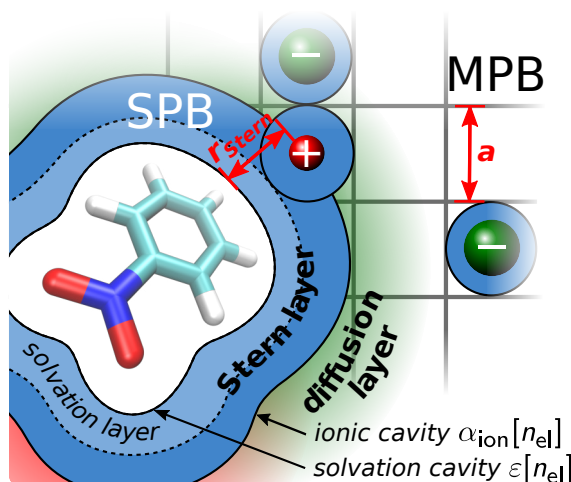

Figure 4.3.: Schematic representation of an electrolytic environment around a molecular solute, illustrating two prominent modifications of standard PB theory: A solvent Stern layer of thickness r_{Stern} separates the solute from the diffusive ions in the SPB approach, while MPB theory accounts for more or less rigid solvation shells around the ions by describing them with a finite size a. As apparent from the drawing, the Stern layer can receive contributions from both the solute's solvation layer and the solvation shells around the ions leading to correlation between the corresponding model parameters. Reproduced from ref. [148], with the permission of AIP Publishing.

In most realistic systems the existence of a Stern layer is undisputed[52,122,123,155,156] apart from a few specific cases, such as for instance highly charged solutes in contact with ions of low complexing ability.[157] Empirically, such a layer can be observed as a shift of the solute-ion radial distribution functions (RDFs) further outward than the solute-solvent RDF, cf. Fig. 4.3. While finite ion sizes as included in the MPB model can also prevent over-crowding of ions by the introduction of steric ion-ion repulsions, only the explicit inclusion of solute-ion interaction potentials can provide this observed different offset of the solute-ion RDF. This is illustrated in Fig. 4.4 where we calculated the ionic concentrations in an aqueous solution around a potassium cation by using the SMPB-DFT scheme and different choices of the parameters a and $d_{\alpha_{\text{ion}}}^{\pm} = d_{\alpha_{\text{ion}}}$. While sometimes disputed,[62,72] the inclusion of a volume-based (MPB) ion exclusion does therefore not suppress the need for a distance-based (SPB) ion exclusion (Stern layer correction), since both modifications address different physical short-comings of PB theory (cf. Fig. 4.4).[63] Similarly, there are indications that inclusion of solvated ion-ion interactions through MPB does give additional improvement that can not be reached by a Stern layer alone, in particular for large ions or close to high electrostatic potentials due to high local ion densities.[62,63,72,156] While this generally motivates the use of the combined SMPB model, it is also clear that both corrections, MPB and SPB, are partly correlated, cf. Fig. 4.3. Parameter optimization disregarding one or the other correction may therefore lead to

physically unrealistic parameters,[60,78] while simultaneous unconstrained optimization may lead to overfitted models with little transferability (*vide infra*).
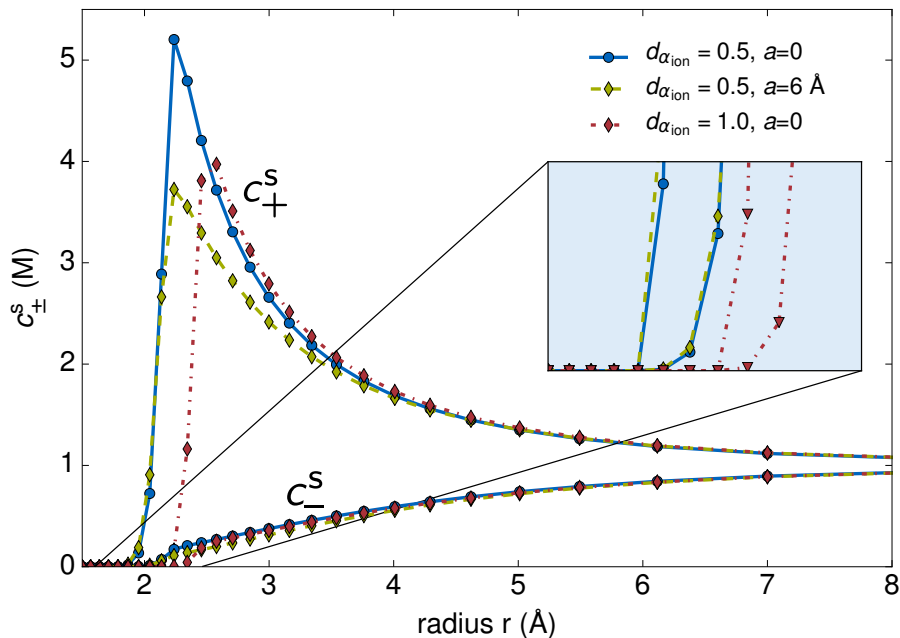

Figure 4.4.: Ionic charge concentrations $c_{\pm}^{s}(r)$ around a potassium cation as obtained from a SMPB-DFT calculation. Different choices have been made for the Stern layer thickness $d_{\alpha_{\mathrm{ion}}}^{\pm} = d_{\alpha_{\mathrm{ion}}} = \{0.5, 1.0\}$ and the ion size parameter $a = 0.6\,\text{Å}(\xi_{\alpha_{\mathrm{ion}}}^{\pm} = 1.0)$. As seen from the picture, the ionic size parameter a merely reduces the charge density, but does not change the onset of the ionic charge distribution, while the Stern layer thickness parameter alters both. The inset shows a zoom into the onset region to clarify this statement. Other parameters are: *tight* settings, $T = 300\,\text{K}$, $c^{\mathrm{s,bulk}} = 1\,\text{M}$, $\{(\alpha + \gamma), \beta, n_{\mathrm{min}}, n_{\mathrm{max}}\}$ from the "fit cations" parameter set[158] (cf. Section 4.1).

Considering their related physical origin, the ion size parameter a and the Stern layer thickness r_{Stern} should depend on ionic properties like hydrated radii or hydration numbers of the ions.[9,121] For the size parameter a exclusive correlations with hydrated ion sizes have a reasonable legitimation,[78] since it represents the size of the singly-occupied lattice cells and thus correlates with the strength of the solvated ion-ion repulsions. In contrast, the Stern layer thickness is an effective parameter that results from the interactions of multiple different species such as attractive[59,159–163] and repulsive solute-ion, solute-solvent, or ion-ion interactions. It will therefore also depend strongly on the properties of the solute. This makes it unlikely that parametrization strategies for r_{Stern} that exclusively draw on solute-independent ion sizes[63,72,84,85,157,160] will lead to the targeted degree of transferability. More general procedures that also consider an explicit dependence on the solute have hitherto only met limited success.[78,164,165] Transferable models of the Stern layer that can utilize the same parameters for a wide range of chemically most diverse solutes are lacking so far.[157] In the SMPB-DFT approach, this problem can efficiently be addressed by modeling the Stern layer thickness as a function of both ionic properties and the solute's electron density. With a single choice of the parameters $d_{\alpha_{\mathrm{ion}}}^{\pm}$ and $\xi_{\alpha_{\mathrm{ion}}}^{\pm}$ for a

particular salt solution, r_{Stern} will then automatically adapt to the size of the solute as measured by the extent of the electron density.

4.2.2. Experimental Reference Properties

The determination of transferable SMPB parameters requires accurate experimental data covering a diverse range of solute molecules, salts and ionic strengths. Among experimentally accessible observables, properties related to solvation free energy changes with ionic strengths $\Delta\Delta G_{\text{ion}}(c^{\text{s,bulk}})$ are hereby particularly appealing due to their availability for a great number of solutes and salts. In the case of charged, electrolytic solutes like simple monovalent salts, these are often tabulated in literature in terms of mean molar activity coefficients[7]

$$\ln(\gamma^{\text{mean}}) = \frac{1}{2}\bigg(\ln(\gamma_-) + \ln(\gamma_+)\bigg) \quad , \tag{4.1}$$

where an average is taken over anionic and cationic contributions. The activity coefficients of anions, γ_-, and cations, γ_+, can be expressed as

$$\frac{1}{\beta}\ln(\gamma_\pm(c^{\text{s,bulk}})) = \mu_\pm(c^{\text{s,bulk}}) - \mu_\pm(c^{\text{s,bulk}} = 0) = \Delta\Delta G_{\text{ion}}^\pm \quad . \tag{4.2}$$

Here, $\mu_\pm(c^{\text{s,bulk}})$ and $\mu_\pm(c^{\text{s,bulk}} = 0)$ are the chemical potentials of cation/anion in an electrolyte of salt concentration $c^{\text{s,bulk}}$ and pure solvent, respectively. Since these chemical potentials represent the free energy change $\frac{\partial\Omega_\circ}{\partial n_\pm}$ of the electrolyte or pure solvent system induced by changes in solute charge density n_{sol}, respectively, the difference of these chemical potentials is just the already introduced ion effect on the solvation free energies $\Delta\Delta G_{\text{ion}}^\pm$. Mean activity coefficients as defined above are optimally suited for the investigation of ion effects, since they are highly sensitive to the respective salt solution[110,166–168] and are tabulated accurately for a wide range of experimental conditions.[169,170] Unfortunately, however, mean activity coefficients are commonly only available for small charged solutes (e.g. alkali halides) embedded into an aqueous solutions containing a certain concentration of the solute itself. The construction of a training set and the derivation of transferable parameters, however, requires knowledge of ion effects for various different solutes embedded into the same salt solution. In this respect it is better to consider neutral molecules as solutes for which the ion effect on the solvation energy can be for most salts up to 2-5 M molarities[109,171–174] written as

$$\Delta\Delta G_{\text{ion}} = k_{\text{s}}\frac{1}{\beta\log_{10}(\text{e})}c^{\text{s,bulk}} \qquad \text{(linear)} \quad . \tag{4.3}$$

k_{s} is the so-called Setschenow coefficient, a property of the solute and salt of choice.[8,109] For most systems, k_{s} is positive indicating a reduction of the solubility of the dissolved molecules, i.e. the already mentioned *salting-out* effect. Setschenow coefficients are tabulated for many different salt solutions and most importantly various solutes making them highly useful in actual parametrization schemes.

4.2.3. The Case of Charged Solutes

Charged solutes strongly attract ions and the resulting high degree of ionic screening leads generally to strong solubility changes. In some cases such effects can be accurately modeled by mean-field theories like our SMPB-scheme, but often also correlated interactions contribute substantially to the solvation energy. Furthermore, charged solutes and ions compete to align solvent molecules in their solvation shells.[152] Such mutual effects induce a stronger coupling of solvation and ion effects rendering a simple adoption of ion-free solvation models as discussed in Section 4.1 and a separate determination of ionic parameters at least doubtful. Moreover, experimental data for the ionic strength-dependent solubility of charged molecular solutes is rare and limited to more complex properties like acid dissociation constants[26] which are often difficult to model on the level of continuum methods already in the ion-free case.[175] These facts render it nearly impossible to construct appropriate training sets which could be used to verify advanced PB methods and arrive at transferable parametrizations. Notwithstanding this both theoretically and experimentally challenging task, the often strong ion effects arising in these systems make them still most interesting to study also from the viewpoint of PB theory. For the above discussed reasons, we focus in this section on a simple test system, the KCl aqueous solution for which experimental data is accurately accessible in terms of the mean activity coefficient. Furthermore, we expect the chemical simplicity of such a system expressed among others by the low ionic charge to render a mean-field PB treatment of the ions a particularly valuable approximation. While considering only a single system does not offer a path to a transferable parametrization, the studies will be helpful to understand the influence of the ionic SMPB-parameters on changes of experimentally measurable properties with ionic strengths.

We start by evaluating the mean activity coefficients γ^{mean} of KCl aqueous solutions from two separate SMPB-DFT calculations for an electrolyzed K^+ and a Cl^- ion, and the respective two ion-free solvent calculations performed by the LPB-DFT solver. Figure 4.5 depicts the corresponding results obtained with a solvent parameter set $\{(\alpha + \gamma), \beta, n_{\min}, n_{\max}\}$ which was optimized for cationic and anionic solutes. This set differs remarkably from the neutral solute parameter set especially for cationic solutes.[158] Finite ion sizes were considered by choosing parameters $a > 0$ and we used a small value for the thickness of the Stern layer of $d_{\alpha_{\text{ion}}}^{\pm} = d_{\alpha_{\text{ion}}} = 0.5$. Fig. 4.5 further depicts the experimental reference data (where we used $m^{\text{s,bulk}} \approx c^{\text{s,bulk}}$ for aqueous solutions at room temperature, where $m^{\text{s,bulk}}$ is the molality of the solution) up to ion concentrations close to the limit of saturated solutions ($m^{\text{s,bulk}} = 4.803 \, \text{mol/g}$),[170] as well as the analytic DH limiting law

$$\ln(\gamma^{\text{mean}}(c^{\text{s,bulk}})) = -\frac{\beta z^2 \kappa}{2\epsilon^{\text{s,bulk}}} = -1.166 M^{-1/2}\sqrt{c^{\text{s,bulk}}} \quad . \tag{4.4}$$

It is obtained within LPB theory for the purely electrostatic interaction of a point-like charge embedded in a homogeneous dielectric medium with point-like ions of concentration $c_{\pm}^{\text{s,bulk}}$. Quite clearly, the deviation of the experimental data from the DH limit cannot be accounted for solely on the basis of finite size ions. Only large values of $a = 6 \, \text{Å}$ yield a significant deviation of the calculated activity coefficient away from the linear DH dependence, but do then not produce a curvature that matches the experimental data. Furthermore, such large

ion sizes also lack a physical legitimation as seen by comparing to experimentally measured average hydrated ion sizes: From size exclusion chromatography measurements, K^+ and Cl^- ions were found to have dynamic hydration radii of $\approx 2\,\text{Å}$[121] which are significantly lower than the value of the ionic size parameter $a = 6\,\text{Å}$ for which strong derivations from the activity coefficient curve are observed.
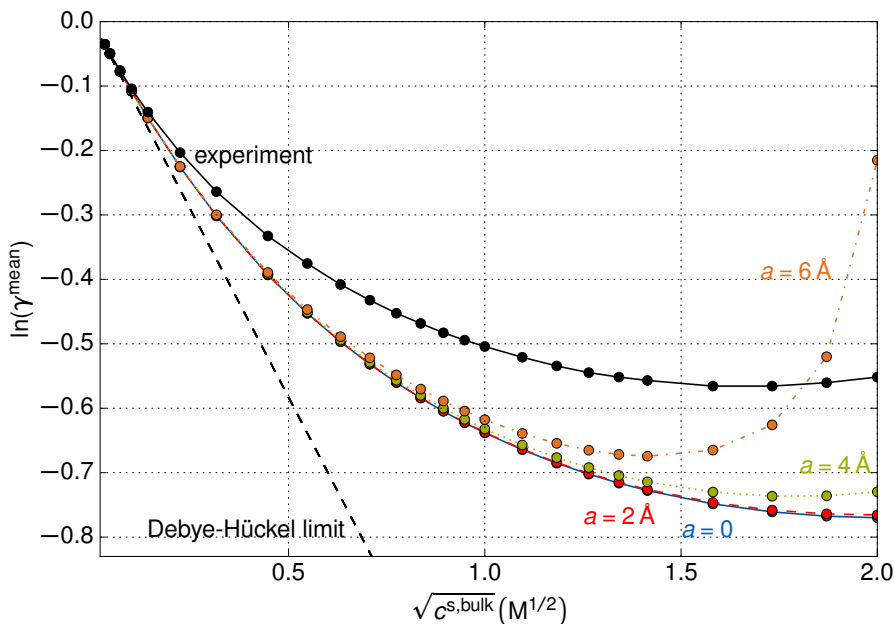

Figure 4.5.: Mean molar activity coefficient γ^{mean} at room temperature as a function of the square root of the ionic bulk concentration $c^{\mathrm{s,bulk}}$ of a KCl aqueous solution. The solid black line indicates the experimental curve, [170] while the dashed black straight line represents the limit of the DH limiting law. Compared are calculated activity coefficients using a range of a values to account for finite size ions. Other parameters are: *tight* settings, $\{(\alpha + \gamma), \beta, n_{\mathrm{min}}, n_{\mathrm{max}}\}$ from the "fit cations" and "fit anions" parameter sets, [158] $d_{\alpha_{\mathrm{ion}}} = 0.5$, $\xi_{\alpha_{\mathrm{ion}}} = 1.0$. Reproduced with permission from ref. [86]. © 2016 American Chemical Society.

This highlights the necessity to consider an additional Stern layer correction in the PB model. Figure 4.6 correspondingly explores the effect of the Stern layer defining parameters $d_{\alpha_{\mathrm{ion}}}$ and $\xi_{\alpha_{\mathrm{ion}}}$, which for the present KCl system are chosen to be identical for the anionic and cationic case. Since we found the results to be rather insensitive to the exact value of a, as had also been reported by Harris *et al.*,[78] the results shown in Fig. 4.6 are obtained for a physically reasonable $a = 2\,\text{Å}$. The calculated activity coefficients vary sensitively with the chosen $(d_{\alpha_{\mathrm{ion}}}, \xi_{\alpha_{\mathrm{ion}}})$-pair, indicating that a good account of the experimental variation with ion concentration can be achieved within this two-dimensional parameter space. The light green curve in Fig. 4.6 demonstrates this for optimized parameter values $d_{\alpha_{\mathrm{ion}}} = 1.54$ and $\xi_{\alpha_{\mathrm{ion}}} = 0.137$ as resulting from a simple Nelder-Mead [176] fit to the experimental reference data. For these parameter values the SMPB-DFT approach achieves a decent description over a wide range of ionic concentrations, even without any further fine-tuning of the other SMPB parameters. For these optimized ionic parameters, the calculated ionic charge density profile $n_{\mathrm{ion}}^{\mathrm{SMPB}}$ around the central ion shows a good coincidence of the Stern
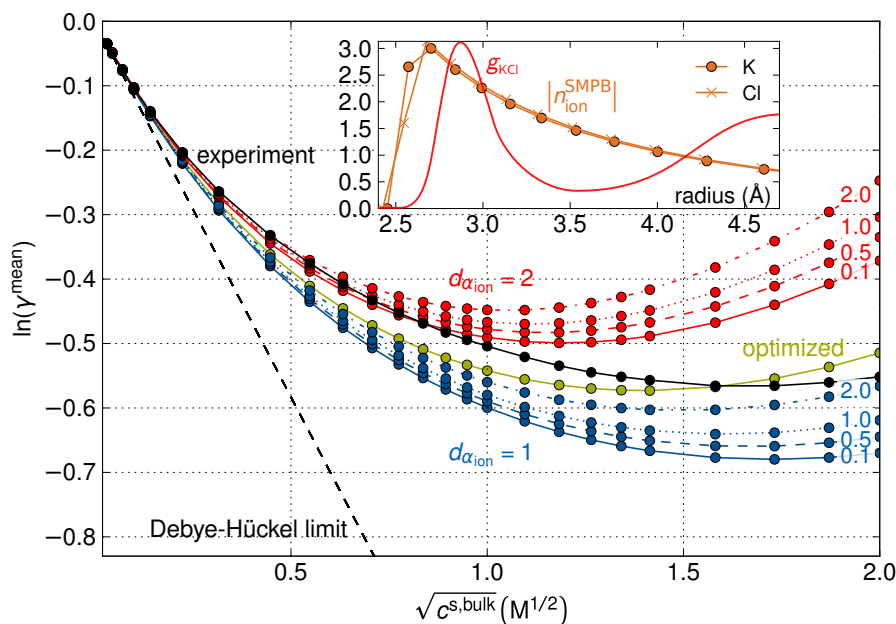
Figure 4.6.: Same as Fig. 4.5, but this time exploring the effect of different choices of the ionic parameters $d_{\alpha_{\mathrm{ion}}}$ and $\xi_{\alpha_{\mathrm{ion}}}$ describing the Stern layer correction. The four upper red curves explore different $\xi_{\alpha_{\mathrm{ion}}}$ values for $d_{\alpha_{\mathrm{ion}}} = 2$, the lower blue curves the same for $d_{\alpha_{\mathrm{ion}}} = 1$. The middle light green curve is the result of an optimum fit to the experimental data achieved for $d_{\alpha_{\mathrm{ion}}} = 1.54$ and $\xi_{\alpha_{\mathrm{ion}}} = 0.137$. The inset compares the absolute value of the ionic charge density $n_{\mathrm{ion}}^{\mathrm{MPB}}$ obtained for the latter parameter values with a typical radial distribution function g_{KCl} obtained from explicit FF-MD simulations for this system. [167] Other parameters as in Fig. 4.5 with $a = 2\,\text{Å}$. Reproduced with permission from ref. [86]. © 2016 American Chemical Society.

layer onset with the location of the first solvation shell as derived from explicit solvation molecular dynamics simulations by Lenart *et al.*, [167] cf. inset in Fig. 4.6.

The good agreement between the modeled ionic charge density and the radial distribution function gives additional physical legitimation to the introduction of an ion-free Stern layer. This finding motivated us to also evaluate mean activity coefficients for other alkali halide salts whereby we indeed could find a correlation between the Stern layer thicknesses and mean ionic distances as available in literature. [177,178] The inclusion of a Stern layer in PB models therefore allows to capture the dominating ion-specific effects underlying experimentally measured activity coefficients. Hydrated ion-ion interactions as induced by the finite ion size a, on the other hand, are expected to be only relevant at high ionic strengths. [78]

4.2.4. The Case of Neutral Solutes

Neutral solutes commonly exhibit weaker interactions with ions in the solution than charged solutes due to the reduced electrostatic attractions. Observable ion effects are therefore rather influenced by non-electrostatic interactions as the solute-ion repulsions leading to the creation of Stern layers with a thickness depending on both solute and salt.

The theoretical treatment is thereby simplified by the fact that the solvation effects often completely decouple from the ion effects. The study of ionic phenomena is therefore in general not limited by the accuracy of the solvation model. Moreover, due to the fact that we focus in this thesis on monovalent salt solutions, parametrization protocols can make use of the linear Setschenow regime given in Eq. (4.3) commonly holding up to concentrations as high as 2-5 M with the corresponding Setschenow coefficients being widely available for various molecular solutes. [109,171–174]

We start this section by first describing the databases of experimentally measured Setschenow coefficients which we constructed for various monovalent salts and molecular solutes. Analogously to the case of charged solutes, we then assess a meaningful ionic parameter space and fit the remaining relevant Stern layer thickness parameter to the Setschenow coefficient database of NaCl solutions. Finally, we apply a similar strategy to other monovalent salt solutions. Despite the scarcity of the thereby utilized experimental reference data, we show that the observed trends are physically reasonable and can be condensed into a simple linear scaling with the experimentally determined average number of strongly bound water molecules around the ions, the hydration number. As such, this relation can even be used to derive SMPB parameters for salts not explicitly covered in this work.

4.2.4.1. Database of Setschenow coefficients

Over the years different collections of molecular Setschenow coefficients in aqueous NaCl solutions have been put forward. [174,179–182] They often contain data from early experimental measurements though, which are likely more strongly affected by experimental uncertainties. Setschenow coefficients obtained from fitting entirely to experimental measurements at low ion concentrations are for instance by now known to be prone to large systematic errors which can easily yield uncertaincies up to 0.04 l/mol. [174,181] Likewise, k_s for strongly polar molecules obtained from solubility measurements are masked by solute-solute self-interaction energy changes. [109] From initially about 150 experimentally measured molecular Setschenow coefficients found in literature [109,123,174,179–182] we have therefore selected a database with 95 entries (database I [109,123,180–182]), listed in Tab. A.1 in Appendix A.8. Our selection was based not only on gaining the highest apparent experimental accuracy, but also to arrive at a balanced and broad range of different organic functionalities and physical properties (cf. dipole, polarity and isotropic static dipole polarizability distributions in Fig. 4.7) in the database. This database was exclusively used in the fitting of the SMPB parameters described below. In addition we collected a second validation database (database I$_{val}$ [182]) containing 33 Setschenow coefficients of mainly apolar aromatic molecules, cf. Tab. A.2 in Appendix A.8 and Fig. 4.7, which we used to test the transferability of the determined parameters.

Unfortunately, experimental Setschenow coefficients for salts other than NaCl are very scarce. This does generally not allow to discard data for balanced sets of different organic functionalities. Nevertheless applying similar quality criteria as for NaCl we collect another database II for various alkali halides as well as NaNO$_3$ and NH$_4$Cl salt solutions that in total contains 195 entries. [109,172,180,183–199]). The individual number of molecular reference
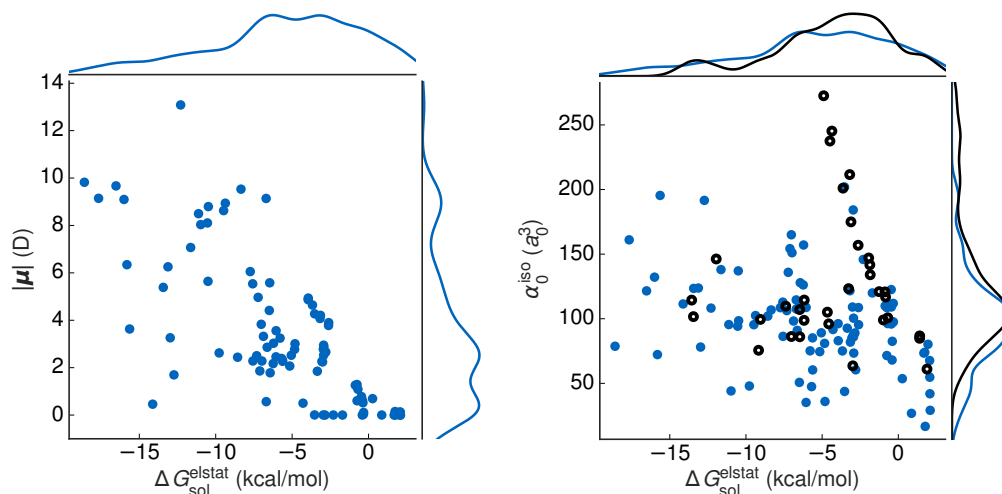
Figure 4.7.: Left panel: Distributions of absolute dipole moments and hydration energies for the molecules in database I visualized via a Gaussian kernel density estimation using a bandwidth of $0.25 \times$ sd, where sd is the standard deviation of the respective sample. Right panel: Distribution of isotropic, static dipole polarizabilities and hydration energies over the databases I and I$_{\text{val}}$. Respective 1D density plots are depicted on top respectively to the right of the corresponding 2D distribution plots. All properties were calculated with `FHI-aims`,[1] the polarizabilities with DFPT,[100] and the hydration energies with the SMPB solver (cf. Section 4.1). Reproduced from ref. [148], with the permission of AIP Publishing.

values for each salt is listed in Tab. 4.2 below, while the whole database is explicitly listed in Tab. A.3 in Appendix A.8.

All `FHI-aims` calculations on molecules from these databases were carried out using *tight* accuracy settings. Solute molecule geometries were first relaxed in vacuum until residual forces fell below 0.23 kcal/(mol/Å). These geometries were then taken as starting point for a subsequent optimization in implicit water using the newly implemented force functionality of the SMPB solver in `FHI-aims`. Test calculations showed only negligible further geometry changes when reoptimizing these relaxed geometries at finite ionic strength. The experimental Setschenow coefficients in the databases were measured at room temperature. For consistency, we therefore also employed $T = 298.14$ K as ionic temperature in the SMPB model. However, we note that for many neutral solutes k_{s} does not show a strong temperature dependence, typically a few percent for variations of ± 20 K.[200,201]

4.2.4.2. Assessment of SMPB Parameter Space

In its full generality, the SMPB model contains five ionic parameters $\{a, d_{\alpha_{\text{ion}}}^+, d_{\alpha_{\text{ion}}}^-, \xi_{\alpha_{\text{ion}}}^+, \xi_{\alpha_{\text{ion}}}^-\}$ that need to be optimized. This already assumes a single ion size a for both cations and anions, and extensions would have to be implemented for the application to salts with very different anion and cation sizes.[60] As discussed above, correlations between these ionic parameters are to be expected. An unconstrained optimization by simultaneously fitting all parameters to experimental Setschenow coefficients is therefore likely to get

trapped in local minima and lead to overfitted models of low predictive quality. In the following we thus first concentrate on NaCl solutions, for which we can draw on a large experimental database to first meaningfully assess the ionic parameter space.

As already mentioned above, ion effects on the stability of neutral solutes are mainly non-electrostatic in nature. This allows us to derive an approximate analytical expression for $\Delta\Delta G_{\text{ion}}$ which is much cheaper to evaluate than the performance of a fully self-consistent SMPB-DFT calculation. The realization that neutral molecular solutes do not exhibit strong electrostatic fields and therefore lead to only weak ionic accumulation, suggests to approximate the electron density of the solute n_{el} and the electrostatic potential v as unaffected by a finite ionic strength. Starting from the general minimal SMPB free energy expression, Eq. (3.27), this leads to the following approximate expression for the solvation free energy change

$$\Delta\Delta G_{\text{ion}} = \Omega_\circ(c^s) - \Omega_\circ(n_{\text{sol}} = 0, c^s) - \Omega_\circ(c^s = 0) + \Omega_\circ(n_{\text{sol}} = 0, c^s = 0)$$

$$\approx \int \mathrm{d}\boldsymbol{r} \left\{ \underbrace{-\frac{1}{\beta a^3} \ln\left(1 + \frac{1}{2}\frac{\phi_0}{1-\phi_0}\left(\alpha_{\text{ion}}^+ e^{-\beta zv} + \alpha_{\text{ion}}^- e^{\beta zv}\right)\right)}_{\Omega_\circ(c^s) - \Omega_\circ(c^s=0)} \right.$$

$$\left. + \underbrace{\frac{1}{\beta a^3} \ln\left(\frac{1}{1-\phi_0}\right)}_{\Omega_\circ(n_{\text{sol}}=0,c^s=0) - \Omega_\circ(n_{\text{sol}}=0,c^s)} \right\}$$

$$= -\frac{1}{\beta a^3}\int \mathrm{d}\boldsymbol{r} \ln\left(1 + \phi_0\left[\frac{1}{2}\left(\alpha_{\text{ion}}^+ e^{-\beta zv} + \alpha_{\text{ion}}^- e^{\beta zv}\right) - 1\right]\right) \quad . \tag{4.5}$$

Taylor expanding the exponential function to 0th order allows to further simplify Eq. (4.5) to

$$k_{\text{s}} \approx -\frac{\log_{10}(e)}{c^{\text{s,bulk}} a^3}\int \mathrm{d}\boldsymbol{r} \ln\left(1 + \phi_0\left(\frac{\alpha_{\text{ion}}^+ + \alpha_{\text{ion}}^-}{2} - 1\right)\right) \quad , \tag{4.6}$$

where the expression is given here directly in terms of the Setschenow coefficient as defined by Eq. (4.3).

This derived equation reveals that in the general case of $a \neq 0$ the Setschenow coefficient can not be constant, but varies with the ionic concentration. Only the limit $a \to 0$ allows to recover a linear Setschenow regime as observed experimentally. Taking this limit and using $\lim_{x \to 0}\frac{1}{x}\ln(1+bx) = b$ we get

$$k_{\text{s}}(a \to 0) \approx \log_{10}(e)\,(V_{\text{ion,cav}}^+ + V_{\text{ion,cav}}^-) \quad , \tag{4.7}$$

where $V_{\text{ion,cav}}^\pm = \int \mathrm{d}\boldsymbol{r}(1 - \alpha_{\text{ion}}^\pm)$ are the volumes of the ionic cavities as determined by the DFT electron density of the solute in ion-free implicit water and the chosen Stern layer parameters. In the case of identical ion exclusion functions for cations and anions, we arrive at

$$k_{\text{s}}(a \to 0) \approx 2\log_{10}(e)V_{\text{ion,cav}} \quad . \tag{4.8}$$

In the limit $a \to 0$, the Setschenow coefficient is thus uniquely given by the ionic cavity volume. This is consistent with the known correlation of Setschenow coefficients with the

solute molecular volume. [180–182] It also agrees with the current understanding that the dominant contribution for the *salting-out* effect of neutral molecules is a change of the cohesive energy of the aqueous solution by the presence of the ions and the concomitant higher ionic cavity creation costs. [123]
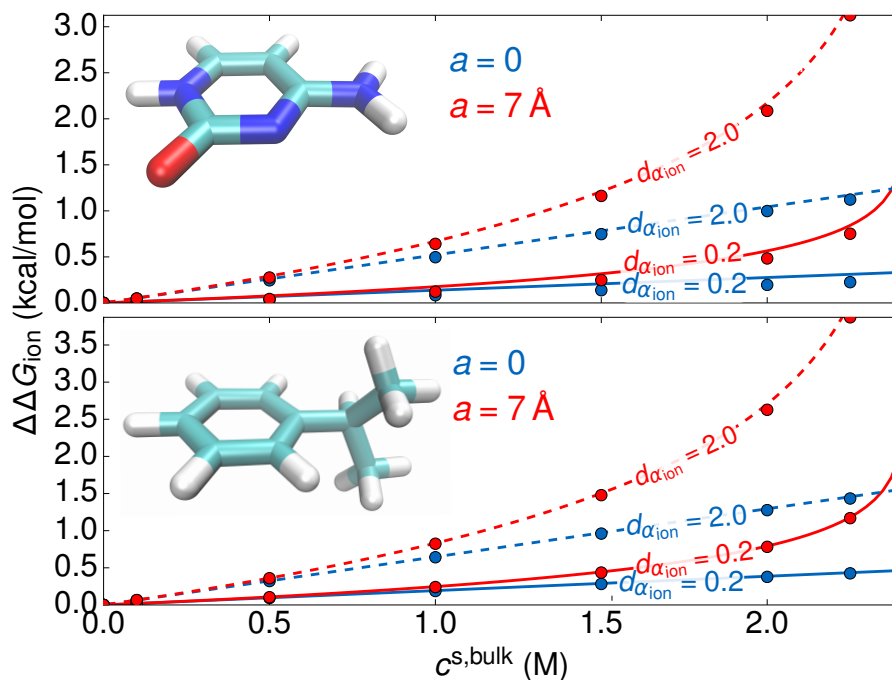

Figure 4.8.: Calculated $\Delta\Delta G_{\mathrm{ion}}$ as a function of ionic bulk concentration $c^{\mathrm{s,bulk}}$ for the highly polar molecule cytosine (upper panel) and the apolar molecule isopropylbenzene (lower panel). Compared are the results from full SMPB-DFT calculations (filled circles) with the analytical expressions for the Setschenow coefficient of Eq. (4.6) (red lines) and Eq. (4.8) (blue lines). Shown are results for two different ionic sizes a (red vs. blue data) and Stern layer thicknesses $d_{\alpha_{\mathrm{ion}}}^{\pm} = d_{\alpha_{\mathrm{ion}}}$ (dashed vs. solid lines). The Stern layer smoothness parameter is fixed to $\xi_{\alpha_{\mathrm{ion}}}^{\pm} = 0.5$. In the case $a = 7\,\text{Å}$, the ionic bulk concentration $c^{\mathrm{s,bulk}} = 2.42\,\mathrm{M}$ represents the upper bound for the physically realistic region in which the lattice occupation of the MPB model by ions $\phi_0 < 1$. Reproduced from ref. [148], with the permission of AIP Publishing.

In Fig. 4.8 we compare the approximate expressions for the Setschenow coefficient with numerical results obtained from full SMPB-DFT calculations for both a highly polar (cytosine) and an apolar (isopropylbenzene) molecule. Deferring the analysis of different ionic cavity volumes to below, this comparison considers the same Stern layer parameter $d_{\alpha_{\mathrm{ion}}}$ and fixed smoothness parameters $\xi_{\alpha_{\mathrm{ion}}}^{\pm} = 0.5$ for both cations and anions. For two very different sets of values of $d_{\alpha_{\mathrm{ion}}}$ and the ionic size parameter a, excellent agreement is achieved across a wide range of ionic concentrations. Only for the highly polar cytosine and thin Stern layers minor deviations can be discerned at the highest ionic concentrations shown. In this regime, ions accumulate significantly in regions of higher electrostatic potential and the approximations behind the approximate analytical expressions start to break down.

Having validated the approximate analytical expressions, we can now proceed to analyze the SMPB parameter space. For the class of neutral molecules, use of any finite ion size parameter a will intrinsically lead to deviations from the linear Setschenow regime, in particular at higher ionic concentrations. The actual value of the Setschenow coefficient is instead primarily governed through the choice of the Stern layer thickness, $d_{\alpha_{\mathrm{ion}}}^{\pm}$ and the smoothness of the ionic transition, $\xi_{\alpha_{\mathrm{ion}}}^{\pm}$, as these are the central parameters determining the ionic cavity volumes for a given solute. As apparent from Fig. 4.8, the choice of a larger ion size parameter can in principle also lead to an increasing slope of $\Delta\Delta G_{\mathrm{ion}}$ in a pseudo-linear regime at lower ionic concentrations and could therefore also be used to effectively fit experimental values for $\Delta\Delta G_{\mathrm{ion}}$ at a particular concentration. This highlights the correlations in the SMPB parameter space discussed earlier. On the basis of the obtained analytical understanding, we expect a low transferability of corresponding $a \neq 0$ parameter sets. Instead, we set $a = 0$ – and thus discard the effect of size modification on the PBE – for the targeted class of neutral solutes at low to medium ion concentrations. Our analytical treatment of $\Delta\Delta G_{\mathrm{ion}}$, Eq. (4.8), shows that such MPB-like modifications with finite a are only useful to describe deviations from the Setschenow law at high ion concentrations or in regions of high local ion concentrations as expected e.g. for large ion sizes or charged solutes.

To further analyze the role of the remaining four ionic parameters, we compute the Setschenow coefficients for the whole database I with the approximate Eq. (4.7) for varying choices of $d_{\alpha_{\mathrm{ion}}}^{\pm}$ and $\xi_{\alpha_{\mathrm{ion}}}^{\pm}$. These calculations are done for an ionic bulk concentration of $c^{\mathrm{s,bulk}} = 1\mathrm{M}$, at which the Setschenow law is known to hold for most monovalent salt solutions. Evaluating the root mean square error (RMSE) of the thus estimated Setschenow coefficients for each set of SMPB parameter values with respect to the experimental data clearly demonstrates the expected effect of the total ionic cavity volume as the central feature governing the accuracy of the fit. Parameter combinations that effectively lead to the same total volume ($V_{\mathrm{ion,cav}}^{+} + V_{\mathrm{ion,cav}}^{-}$) generally achieve the same RMSE. As exemplified by Fig. 4.9, a larger cationic volume through choice of a larger cationic Stern layer thickness $d_{\alpha_{\mathrm{ion}}}^{+}$ can for instance be compensated by a smaller anionic volume through choice of a smaller Stern layer thickness $d_{\alpha_{\mathrm{ion}}}^{-}$ to yield the same RMSE fit. For the given functional form of the transition function for the ionic cavity, Eq. (3.11), changes of the smoothness parameters $\xi_{\alpha_{\mathrm{ion}}}^{\pm}$ lead to (albeit small) variations of the enclosed volume. Correspondingly, we also obtain a weak sensitivity of the RMSE to the choice of this parameter, where effective increases of the volume through $\xi_{\alpha_{\mathrm{ion}}}^{\pm}$ can again be compensated by reductions of the Stern layer thickness (cf. Fig. 4.10).

Given these correlations, unconstrained fitting of all four parameters is clearly not advisable. For the targeted alkali-halide electrolytes and their roughly similar cationic and anionic sizes we instead employ identical Stern layer thicknesses $d_{\alpha_{\mathrm{ion}}}^{\pm} = d_{\alpha_{\mathrm{ion}}}$ and shapes $\xi_{\alpha_{\mathrm{ion}}}^{\pm} = \xi_{\alpha_{\mathrm{ion}}}$ for both ion types. Since the Stern layer shape has a similar but weaker impact on the total ionic cavity volume than the thickness parameter, we simply fix it to a value $\xi_{\alpha_{\mathrm{ion}}} = 0.5$ that yields a reasonable agreement with the MD data shown in Fig. 4.11 below. In total, this thus leaves only the Stern layer thickness as meaningful SMPB parameter to be optimized by fitting to the experimental database.
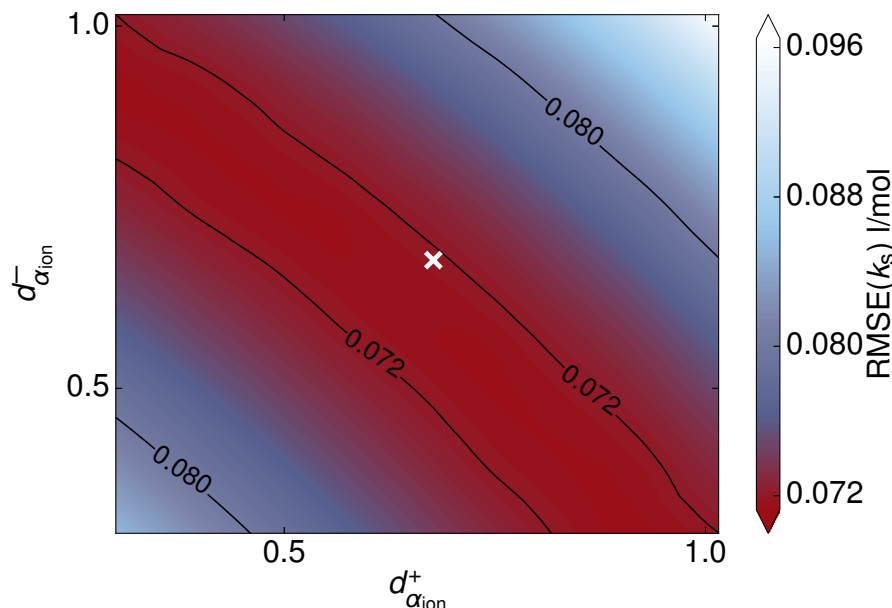
Figure 4.9.: RMSE for the NaCl training set (database I) between calculated (through Eq. (4.7)) and measured Setschenow coefficients as obtained for different choices of Stern layer parameters $d^+_{\alpha_{\text{ion}}}$ and $d^-_{\alpha_{\text{ion}}}$ ($a = 0$, $\xi^\pm_{\alpha_{\text{ion}}} = 0.5$). The optimum RMSE of the full SMPB-DFT approach, achieved for $d^\pm_{\alpha_{\text{ion}}} = d_{\alpha_{\text{ion}}} = 0.68$ is indicated by a white cross. Reproduced from ref. [148], with the permission of AIP Publishing.

4.2.4.3. Optimized SMPB Model: Strengths and Limitations

Under the constraint of equal Stern layer thicknesses for cations and anions, an optimum RMSE of 0.068 l/mol to the experimental Setschenow coefficients of database I is achieved for $d_{\alpha_{\text{ion}}} = 0.68$, cf. Fig. 4.9. At a bulk ion concentration of 1 M, this corresponds to an excellent prediction of the solvation free energy change on average to within ~ 0.1 kcal/mol. A good transferability of the thus determined SMPB parameter set is thereby indicated by essentially the same RMSE for the validation database I_{val} (cf. Tab. 4.1). We attribute this predictive power to successfully capturing the correct physics of the ion-specific effects with the established SMPB ion distribution model. This is for instance indicated by comparison to the explicit solute-solvent and solute-ion RDFs obtained from all-atom MD simulations for naphthalene in NaCl solutions by Li *et al.*[123] As shown in Fig. 4.11 the onset of the solute solvation shell and the outward Stern layer shift of the ion distribution as modeled by the n_{el} and α_{ion} functions of the optimized SMPB model agree almost exactly. Note that we found this onset to also be independent of the specific dielectric function parametrization (cf. Fig. 4.12) as expected from the validity of Eqs. (4.7) and (4.8), additionally supporting the generality of the drawn conclusions about the role of the SMPB parameters.

Interestingly, the RMSE achieved with the effective one-parameter SMPB model is only slightly worse than the one achieved with state-of-the-art multi-parameter data regression models, cf. Tab. 4.1. The main contribution to this RMSE in the training (I) and validation (I_{val}) databases thereby arises from a small number of highly functionalized and polar
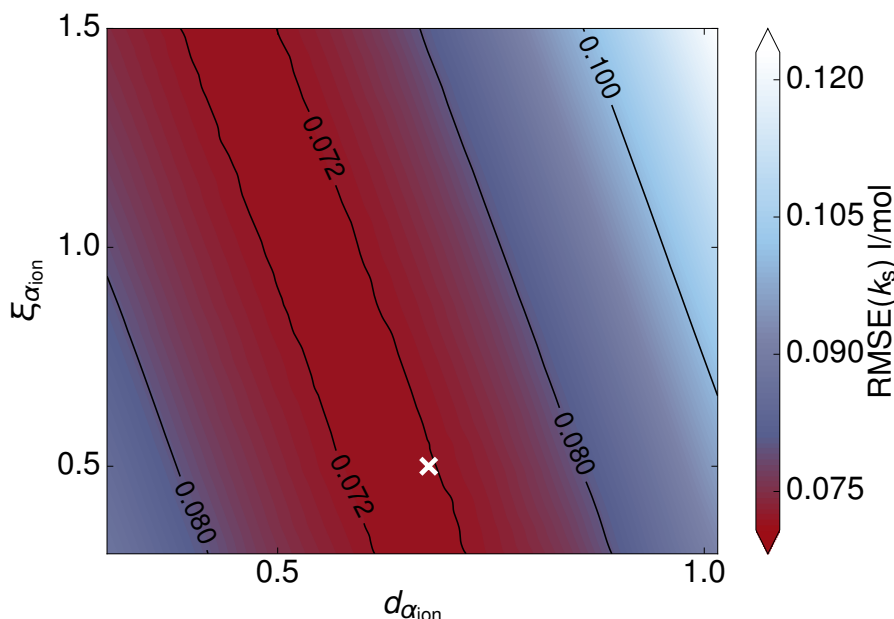
Figure 4.10.: RMSE for the NaCl training set (database I) between calculated (through Eq. (4.8)) and measured Setschenow coefficients as obtained for different choices of Stern layer parameters $d_{\alpha_{ion}} = d^{\pm}_{\alpha_{ion}}$ and $\xi_{\alpha_{ion}} = \xi^{\pm}_{\alpha_{ion}}$ ($a = 0$). The optimum RMSE of the full SMPB-DFT approach, achieved for $d^{\pm}_{\alpha_{ion}} = 0.68$ and $\xi^{\pm}_{\alpha_{ion}} = 0.5$, is indicated by a white cross. Reproduced from ref. [148], with the permission of AIP Publishing.

descriptor/ method	#pa– rams	training		validation	
		size	RMSE	size	RMSE
SMPB	1	95	0.068	33	0.064
pp-LFER [181]	5	43	0.030	91	0.047
QSPR [202]	4	71	0.030	30	0.043
QSPR (SVM) [203]	4	51	0.019	50	0.029
connect. inx [204]	3	71	0.041	30	0.038
TIP3P/TI [123]	-	-	-	43	0.084
SEA [123]	-	-	-	43	0.050

Table 4.1.: Comparison of the achieved accuracy of the present optimized SMPB model in reproducing experimental Setschenow coefficient databases against models from the literature. This comprises both physically motivated models (TIP3P/TI, [123] semi-explicit assembly (SEA) [123]) and descriptor-based approaches (all others [181,182,202–204]). Stated is the number of parameters involved in the model (#params), the sizes of the training and validation set and the achieved RMSE (in l/mol) in both sets. Other acronyms: Polyparameter linear free energy relationship (pp-LFER), quantitative structure-property relationship (QSPR), connectivity index (connect. inx), thermodynamic integration (TI). Reproduced from ref. [148], with the permission of AIP Publishing.

molecules, for which the SMPB model strongly overestimates the Setschenow coefficients. These outliers are illustrated in Fig. 4.13. A similar overestimation for polar molecules has also been reported for regression-model studies, [181] which points towards experimental
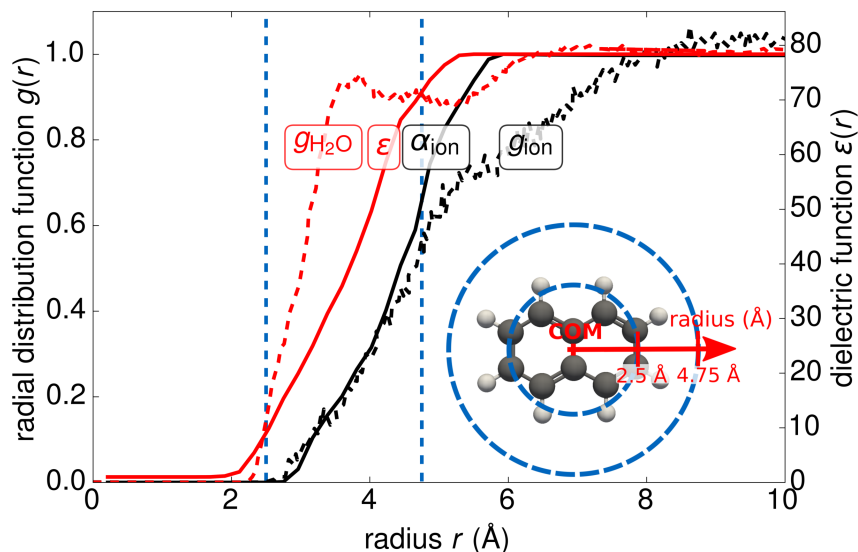
Figure 4.11.: Comparison of the solvation environment around the COM of naphthalene in a 2.18 M
NaCl solution. Shown are the spherically-averaged RDFs of the oxygen atoms in the water solvent
(g_{H_2O}, dashed red line) and of the sum of both ion types (g_{ion}, dashed black line) as reported by Li *et al.*
from all-atom molecular dynamics simulations,[123] as well as the corresponding spherically-averaged
dielectric function $\varepsilon(r)$ (solid red line) and ion exclusion function $\alpha_{ion}(r)$ (solid black line) as obtained
with the optimized SMPB model. Both the onset of the solute solvation shell and the radial Stern layer
shift of the ionic distribution are well reproduced. To better grasp the involved scales, two dotted
vertical lines illustrate the radial distance to the molecule COM as shown in the top view in the inset.
Reproduced from ref. [148], with the permission of AIP Publishing.

uncertainties or an incorrect account of experimental conditions in the models as reason
for the discrepancies. An important aspect here could be the actual protonation state of the
solute in the measurements, as reference values for k_s are often obtained by averaging over
solubility measurements at different pH values.[205] Since stabilizing electrostatic solute-
ion interactions drastically increase for charged molecules, deviations in the protonation
state can have a large impact on the determined Setschenow coefficient. In this respect,
it is intriguing to realize that amino acids are a prominent group among the outliers in
Fig. 4.13. Close to their isoelectric point amino acids adopt a zwitterionic form, rather than
the neutral geometry which we considered in the calculations by default. Recalculating
the SMPB Setschenow coefficients for four such amino acids in the zwitterionic geometry
indeed leads to much reduced k_s values in much better agreement with the experimental
reference data, cf. Fig. 4.13.

While this underscores the importance of accurate experimental reference data obtained
in carefully adjusted physical conditions, it is nevertheless clear that the SMPB model
generally performs worse with increasing polarity of the solute. In fact, when taking the
solvation free energy $\Delta G_{sol}(c^{s,bulk} = 0)$ as a measure for this polarity, a good correlation can
actually be obtained with the signed error in the Setschenow coefficient ($k_s^{SMPB-DFT} - k_s^{exp}$)
(cf. Fig. 4.14). This indicates that the SMPB model fails to capture interactions which are
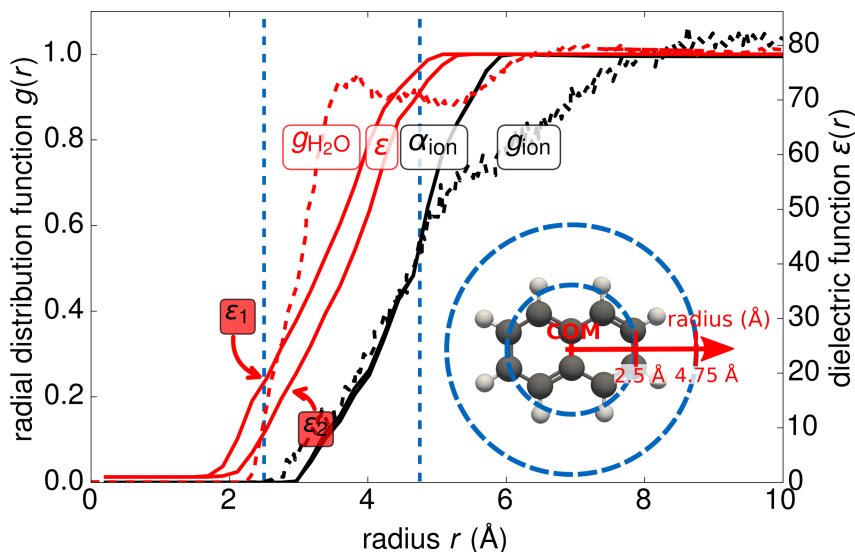
Figure 4.12.: Comparison of the solvation environment around the COM of naphthalene in a 2.18 M NaCl solution. Shown are the spherically-averaged RDFs of the oxygen atoms in the water solvent (g_{H_2O}, dashed red line) and of the sum of both ion types (g_{ion}, dashed black line) as reported by Li *et al.* from all-atom molecular dynamics simulations,[123] as well as the corresponding spherically-averaged dielectric functions $\varepsilon(r)$ (solid red lines) and ion exclusion functions $\alpha_{ion}(r)$ (solid black lines) as obtained with the optimized SMPB model. To better grasp the involved scales, two dotted vertical lines illustrate the radial distance to the molecule COM as shown in the top view in the inset. Two different dielectric function parametrizations have been used, ε_1 ($n_{min} = 0.0001$, $n_{max} = 0.005$) and ε_2 ($n_{min} = 0.0004$, $n_{max} = 0.007$) to test the influence of the solvation model definition on the calculated ion effect. $d_{\alpha_{ion}}$ was then for both solvation models optimized in order to perfectly reproduce the experimental Setschenow coefficient of naphthalene. As seen from the figure, both optimizations predict the same ionic distributions. Reproduced from ref. [148], with the permission of AIP Publishing.

particularly strong for highly polar molecules. This could comprise ion complexation, a reduction of the dielectric permittivity by strong ion-polar group interactions (dielectric decrement[149–152]), or solute-ion dispersive interactions, all of which would increase the attractive solute-ion interactions and therewith yield lower k_s values than the ones presently calculated.

More insight can be obtained by considering the vacuum isotropic and static dipole polarizability as obtained from the trace of the diagonalized polarizability tensor $\alpha_0^{iso} = \text{tr}(\boldsymbol{\alpha}_0)/3$ calculated with density-functional perturbation theory in `FHI-aims`.[100] As put forward by Ninham, Parsons and Boström, solute-ion dipole dispersion interactions which scale with the solute's polarizability are suspected to play an important role in the explanation of ion-specific effects.[59,159–163] While, however, the polarizability correlates well with the modeled Setschenow coefficients $k_s^{SMPB-DFT}$, we found experimental values to be largely independent of it (cf. Fig. 4.14). At first sight, the introduction of such artificial correlation could indicate that the electron density representation of the solute volume employed in the present SMPB model might not be optimal to introduce volume corre-
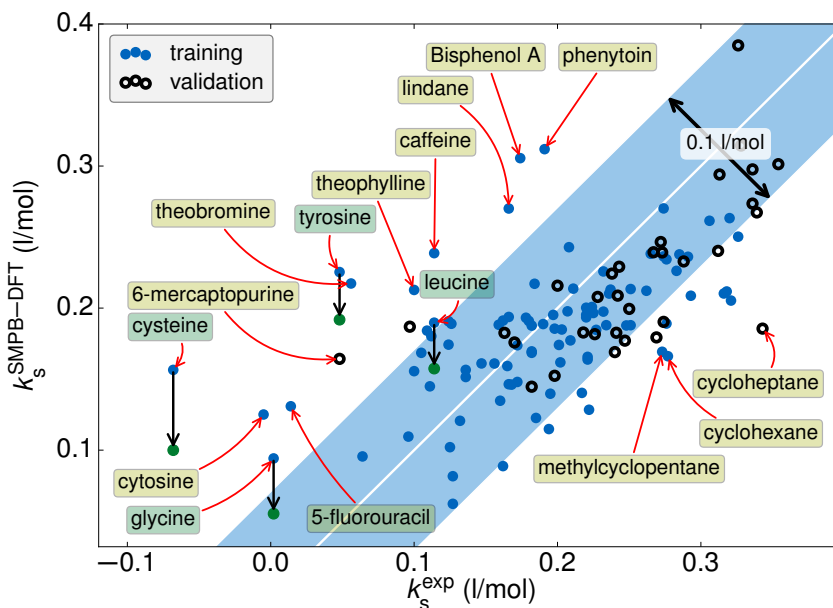
Figure 4.13.: Comparison of Setschenow coefficients obtained by the optimized SMPB model with the experimental references from the training database I (filled circles) and the validation database I_{val} (empty circles). The light blue region around the correlation line marks an error within $0.05\,l/mol$. The largest outliers are explicitly labeled with the solute name. Amino acid solutes are marked by darker label color. The black arrows visualize the shift of the calculated Setschenow coefficients for four amino acids when considering a zwitterion molecular structure, see text. Reproduced from ref. [148], with the permission of AIP Publishing.

lations in the Setschenow coefficient, at least not throughout the whole database I. The good transferability of our SMPB model, however, renders it more plausible that the found correlation would eventually be compensated by the inclusion of other, so far neglected physical interactions discussed above. Among all possible such interactions, we do not expect solute-ion dispersion interactions to play a major role, as indicated by the missing correlation of the experimental data with the dipole polarizabilities. However, in the end, this can only be decided through the development of more advanced PB methods in order to gain more insight into the complex physics of solute-ion interactions.

4.2.4.4. Parameter Sets for other Monovalent Salt Solutions

In principle, the SMPB parametrization strategy developed for NaCl solutions can straightforwardly be extended to other monovalent salt solutions. For each salt, an optimized Stern layer thickness is determined by fitting to the experimental Setschenow coefficients of this salt contained in database II. Table 4.2 summarizes the thus optimized $d_{\alpha_{ion}}^{opt}$ values. The RMSEs also reported in Tab. 4.2 and the correlation plot in Fig. 4.15 generally indicate a similar capability and limitations to reproduce the experimental reference data as found for NaCl before. Somewhat higher RMSEs are only obtained for the iodides. We attribute this to strongly attractive solute-ion interactions beyond the reach of the SMPB model. For
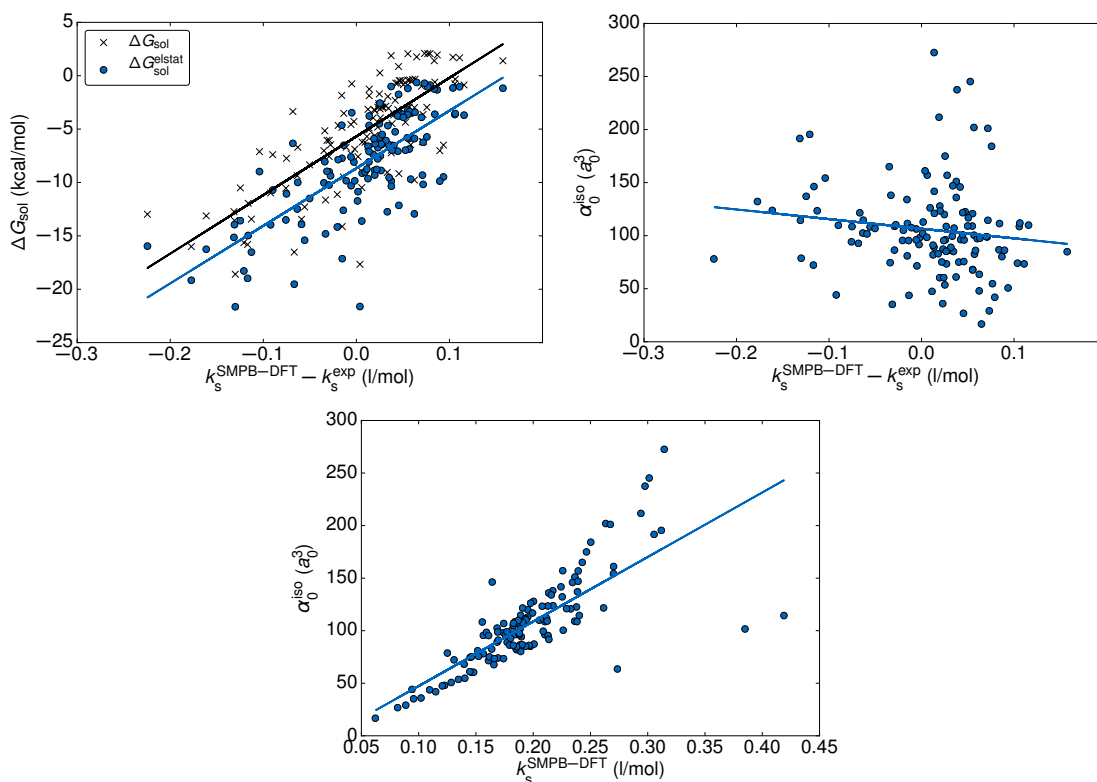
Figure 4.14.: Correlations of molecular descriptors evaluated with `FHI-aims` with the signed error in the prediction of Setschenow coefficients (top panels) and the SMPB predicted Setchenow coefficients (bottom panel). The following correlation coefficients were obtained: top left: $R^2 = 0.58$, top right: $R^2 = 0.02$, bottom: $R^2 = 0.60$ by using the SMPB parameters $\xi_{\alpha_{ion}} = 0.5$, $a = 0$, $d_{\alpha_{ion}} = 0.677$. Hydration energies and static, isotropic dipole polarizabilities α_0^{iso} (with DFPT[100]) were calculated for all molecules from the databases I and database I_{val}. In the top left panel separately to hydration energy ΔG_{sol} (black crosses) are shown the electrostatic solvation energies ΔG_{sol}^{elstat} as filled blue circles ($R^2 = 0.56$). Reproduced from ref. [148], with the permission of AIP Publishing.

corresponding molecules like lindane or γ-butyrolactone these forces would even result in an overall *salting-in* effect, i.e. negative experimental Setschenow coefficients, which the current SMPB model is unable to reproduce.

Unfortunately, the transferability of the thus optimized Stern layer parameters for the other salts is also not as clear as it was the case for the NaCl solution. The corresponding experimental data sets are generally smaller than database I, for some salts like LiBr, NaF, NaI or KF even considerably smaller, cf. Tab. 4.2. It is thus not possible to ensure a balanced and broad range of different organic functionalities in the data set, as was done in database I for NaCl. Every reliable empirical Setschenow coefficient is needed for the training; no validation databases can be spared. To nevertheless arrive at some form of independent validation we recall the physical picture behind different Stern layer parameters for the different salts in the SMPB model. As apparent from Fig. 4.3, corresponding variations would be attributed to different sizes of the hydrated salt ions. As such, one would expect

salt	size	$d_{\alpha_{\text{ion}}}^{\text{opt}}$	RMSE
LiCl	30	0.46	0.047
LiBr	8	0.27	0.021
NaF	7	1.51	0.026
NaCl	95	0.68	0.068
NaBr	21	0.34	0.064
NaI	6	0.07*	0.127*
KF	9	1.34	0.080
KCl	48	0.48	0.063
KBr	29	0.09*	0.071*
KI	14	0.09*	0.136*
NH_4Cl	11	0.13	0.047
$NaNO_3$	12	0.08*	0.076*

Table 4.2.: Optimized Stern layer parameters $d_{\alpha_{\text{ion}}}^{\text{opt}}$ for monovalent salt solutions. Listed is for each salt the size of the employed training set of experimental Setschenow coefficients, as well as the achieved RMSE (in l/mol) over the training set. Detailed lists of the various training sets (database II) are provided in Tab. A.3 in Appendix A.8. Data marked with an asterisk could not be completely converged, as the implemented SMPB solver exhibits numerical instabilities at $d_{\alpha_{\text{ion}}} \lesssim 0.09$. Reproduced from ref. [148], with the permission of AIP Publishing.

the optimized Stern layer thicknesses for the different salts to roughly scale with empirical hydrated ion sizes.

Static observables like mean ion-water nuclear distances[206,207] provide only an inappropriate representation of the Stern layer thickness though, as they do not include information about the bonding strength of the hydration shells. Consistent with this expectation we indeed do not find a correlation of the Stern layer parameters with such quantities reported in literature. A more helpful set of descriptors are instead dynamic hydration sizes which resemble the average sizes of hydrated ions as they propagate through the solution.[121] These sizes are directly related to the number of strongly bound water molecules (*hydration numbers*) which can be obtained by different experimental techniques.[208] Figure 4.16 shows that the optimized Stern layer parameters indeed correlate well with such hydration numbers as obtained from bulk electrolyte compressibility measurements at the infinite dilution limit.[9] We thereby averaged the available empirical cation and anion hydration numbers[9] to be consistent with the SMPB model using identical Stern layer thicknesses for both ion types. This correlation is another good indicator for the transferability of the Stern layer parameters given in Tab. 4.2. Note that the Stern layer parameters with the largest deviations from the regression line were also those obtained with the smallest training set sizes, while NaCl values – obtained from a converged training set – is found directly on top of the line.

The reported correlation reveals that ion-specific effects on neutral molecular systems can indeed be explained by varying Stern layer thicknesses, which by themselves are determined by the hydration state of the ions. Moreover, the relation between the optimized Stern layer parameters and the hydration numbers can serve as a predictor for the parameters of
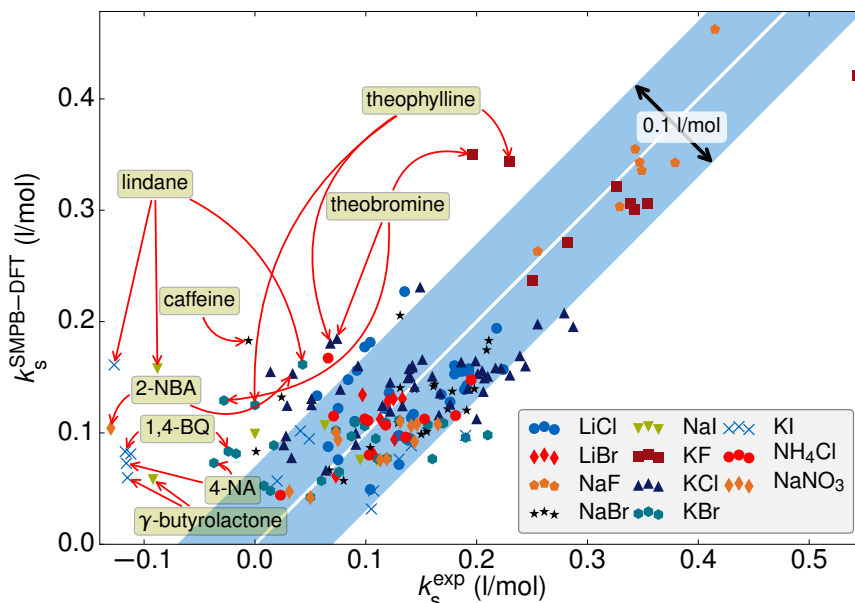
Figure 4.15.: Correlation of SMPB-DFT calculated Setschenow coefficients with the experimental references of database II. For each salt, the optimized Stern layer thickness parameter $d_{\alpha_{ion}}^{opt}$ from Tab. 4.2 is used. The light blue region around the correlation line marks an error within $0.05\,l/mol$. Some of the points with largest deviations have been exemplarily labeled using the following abbreviations: 1,4-BQ = 1,4-benzoquinone, 4-NA = 4-nitroaniline, 2-NBA = 2-nitrobenzaldehyde. Reproduced from ref. [148], with the permission of AIP Publishing.

other monovalent salts for which little or no experimental Setschenow data is available. Using the obtained regression expression

$$d_{\alpha_{ion}}^{opt} \;=\; 0.52\,\text{h.n.} - 0.85 \quad , \tag{4.9}$$

with h.n. the hydration number – to derive the Stern layer thickness parameter, we expect that salt effects can be predicted to a good degree of accuracy for most molecules and monovalent salts. Overall we thus arrive at a rather optimistic perspective on the obtained optimized SMPB models, which suggests their applicability in production first-principles electrolytic solvation calculations. Notwithstanding, more reliable reference Setschenow coefficients from experiment would clearly be desirable to fully validate the parameter transferability.
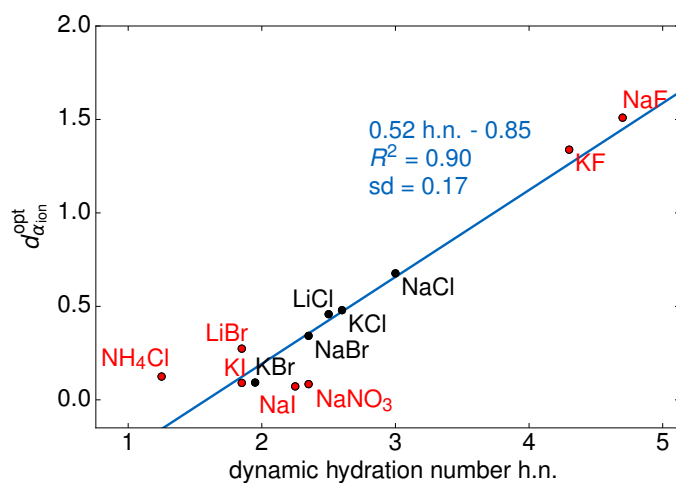
Figure 4.16.: Correlation of the optimized Stern layer thicknesses $d_{\alpha_{\text{ion}}}^{\text{opt}}$ for different monovalent salts, cf. Tab. 4.2, with the hydration numbers h.n. as obtained from bulk electrolyte compressibility data and reported by Marcus.[9] The linear regression showed a low sd = 0.17 and a high coefficient of determination $R^2 = 0.90$. The Stern layer parameters marked in red were obtained with training sets containing less than 20 molecules. Reproduced from ref. [148], with the permission of AIP Publishing.

Summary and Outlook

<div style="text-align: right; font-size: 3em;">5</div>

In the last few years, new developments in the computational modeling of solvent effects have enabled studies of various chemical systems in liquid environments.[23,24,60,62,209] Among the most prominently applied simulation methods are continuum embedding approaches which model solutes on an accurate *first-principles* level and coarse-grain the environmental liquid down to a mere dielectric medium. Notwithstanding the conceptual simplicity of such approaches, efficient parametrization schemes have been developed yielding predictive and computationally efficient methodologies.[5,18]

In this thesis, we combined a recently developed implicit solvation model[5] with an account for finite ionic strengths via a modified variant of the PB theory, the SMPB theory. In the past, similar PB methods have been integrated into different force field and DFT program packages[23,24,58,60,63,79–85] whereby the often present regular and rectangular mesh structures supported the use of FDM schemes for the solution of the non-linear PBE. All-electron DFT program packages like `FHI-aims`,[1] however, utilize non-rectangular integration grids to optimally resolve the Coulomb singularity, rendering the direct usage of common grid- or function-space-based approaches computationally inefficient. On the other hand, in particular `FHI-aims` does not only provide an explicit description of core electrons, but also offers a highly parallelizable infrastructure equipped with advanced computational techniques[96–101] which facilitate the accurate modeling of a wide range of different chemical systems.[12,102–108] These arguments finally motivated the present work in which we developed a novel function-space-based solution scheme for the SMPBE and established an efficient integration into the infrastructure of `FHI-aims`.

Non-linear PDEs like the SMPBE require sufficiently robust numerical solution schemes. In this thesis, we utilize the Newton method to transform the SMPBE into a simpler linearized PDE which can then be solved by a simple relaxation scheme. To that end we rewrote the linearized PDE as an analytically invertible screened Poisson equation and performed successive Green's function integrations until self-consistency of the electrostatic potential was reached. The arising two-center integrals can be efficiently solved with the help of the already present multi-center multipole expansion infrastructure in `FHI-aims`. In summary, such a Newton-MERM scheme was shown in this thesis to provide an efficient, fast converging and highly parallelizable alternative to grid-based approaches thereby being particularly suited for the integration into all-electron DFT program packages.

A central problem in the application of effective models like the SMPB implicit solvation scheme to realistic systems is the parametrization of the coarse-grained interactions. For

the case of the solute-solvent interactions, we adopted the parametrization of Andreussi *et al.* for water as a solvent which was shown to give accurate hydration energies for a wide range of molecular solutes.[5] Solute-ion interactions and the respective SMPB-parameters have, on the other hand, so far only rarely been studied.[60,63,78] In this thesis we presented a first systematic assessment of the SMPB ionic parameter space comprising the parameters $d_{\alpha_{ion}}^{\pm}$ and $\xi_{\alpha_{ion}}^{\pm}$ describing the Stern layer thickness and shape in terms of the solute's electron density, respectively, as well as the ion size parameter a. We thereby compared to experimentally measured Setschenow coefficients which in the case of neutral solutes scale linearly with the ion effect on the solvation energy up to ionic molarities as high as 2-5 M.[109,171–174] By studying these coefficients in NaCl aqueous solutions, we observed that finite ion sizes $a > 0$ lead to deviations from the expected linear Setschenow regime. On the other hand, finite ion size effects were found to be important in agreement with calculations on charged solutes, in the case of high ionic charge densities. Eventually, we could reduce the ionic parameter space to a single relevant parameter describing the Stern layer thickness $d_{\alpha_{ion}}$. Optimizing this remaining free variable for various monovalent salt solutions, we ended up with Stern layer thickness parameters which showed a strong correlation with the ionic hydration numbers obtained from experimental bulk electrolyte compressibility data. This relation can in principle also be used to predict ion effects for any other monovalent salt solution for which experimental data is scarce. This finding gives a physical reasoning for the electron density-based Stern-layer model and was further supported by the fact that ionic charge radial distribution functions as obtained by the optimized SMPB-DFT method showed a similar onset as those obtained from molecular dynamics simulations.

The comparison with experimental data, which led to the derivation of transferable parametrizations for both solute-solvent as solute-ion interactions motivates the development of more sophisticated approaches. Future developments could e.g. focus on an improved description of so far rarely studied non-mean-field solute-solvent interactions or consider so far unaccounted effects like ionic correlations[73] or the reduction of the dielectric permittivity by the presence of ions (*dielectric decrement*).[150,151] Ultimately, parametrization strategies as introduced in this thesis can then again be invoked to re-optimize such complex models. In terms of the solvation model, it will further be interesting to derive so far missing parametrizations for non-aqueous solutions, a project we are currently working on. Regarding applications, it will moreover be desirable to also improve upon the algorithmic side of the implementation and to speed up the convergence of the MERM e.g. by using more advanced mixing techniques or gradient-based optimization schemes.

Notwithstanding the mentioned possibilities to methodologically and technically improve on the SMPB-DFT scheme in `FHI-aims`, the so far achieved efficient parametrization strategies already enable its application in typical molecular cluster calculations. Of particular interest are e.g. *first-principles* studies on biological systems which are a central issue in `FHI-aims` conducted computer simulations.[105–108] The here developed SMPB-DFT scheme enables for the first time to perform such calculations in electrolytic media which has been shown to be critical for a wide range of biochemical processes.[25] Finally, a future implementation of periodic boundary conditions will also enable the application of

the SMPB-DFT scheme for the modeling of extended systems like solid-liquid interfaces as present e.g. in electrochemical systems.

List of Acronyms

BO   Born-Oppenheimer
BOA   Born-Oppenheimer approximation
COM   center of mass
CPU   central processing unit
DFPT   density functional perturbation theory
DFT   density functional theory
DH   Debye-Hückel
DNA   deoxyribonucleic acid
FDM   finite difference method
FEM   finite element method
FF   force field
GC   Gouy-Chapman
GGA   generalized gradient approximation
GPE   generalized Poisson equation
HEG   homogeneous electron gas
KS   Kohn-Sham
LDA   local density approximation
LPB   linearized PB
LPBE   LPB equation
MAE   mean absolute error
MBD   many-body dispersion
MD   molecular dynamics
MERM   multipole expansion relaxation method
MM   molecular mechanics
MP2   Møller-Plesset perturbation theory of 2nd order
MPB   finite size modified PB
NAO   numerically tabulated atom-centered orbitals
PB   Poisson-Boltzmann
PBE   PB equation
PBE-GGA   Perdew-Burke-Ernzerhof-generalized gradient approximation
PDE   partial differential equation
PES   potential energy surface
PMF   potential of mean force
QM   quantum mechanics
RDF   radial distribution function
RMSE   root mean square error
RPA   random phase approximation
SCCS   self-consistent continuum solvation method
SCF   self-consistent field
sd   standard deviation

SE   Schrödinger equation
SI   supplementary information
SMPB   finite size and Stern layer modified PB
SMPBE SMPB equation
SPB   Stern layer modified PB
SPE   screened Poisson equation
HF   Hellmann-Feynman
TD-SE   time-dependent Schrödinger equation
xc   exchange-correlation

Bibliography

[1]   V. Blum, R. Gehrke, F. Hanke, P. Havu, V. Havu, X. Ren, K. Reuter, M. Scheffler, *Comput. Phys. Commun.* **2009**, *180*, 2175–2196, DOI: 10.1016/j.cpc.2009.06.022.

[2]   M. Holst, F. Sajed, *J. Comput. Chem.* **1993**, *14*, 105–113, DOI: 10.1002/jcc.540140114.

[3]   M. J. Holst, F. Saied, *J. Comput. Chem.* **1995**, *16*, 337–364, DOI: 10.1002/jcc.540160308.

[4]   C. M. Cortis, R. A. Friesner, *J. Comput. Chem.* **1997**, *18*, 1591–1608, DOI: 10.1002/(SICI)1096-987X(199710)18:13<1591::AID-JCC3>3.0.CO;2-M.

[5]   O. Andreussi, I. Dabo, N. Marzari, *J. Chem. Phys.* **2012**, *136*, 064102, DOI: 10.1063/1.3676407.

[6]   I. Dabo, E. Cancès, Y. L. Li, N. Marzari, Towards First-principles Electrochemistry, **2008**, arXiv:0901.0096, arXiv.org ePrint archive, `http://arxiv.org/abs/0901.0096` [latest access: 2016/06/02].

[7]   R. A. Robinson, R. H. Stokes, *Electrolyte Solutions*, 2 ed., Butterworths Publications Limited, New York, **1959**, p. 28.

[8]   I. Sechenow, *Ann. Chim. Phys.* **1892**, *25*, 226.

[9]   Y. Marcus, *Ions in solution and their solvation*, Wiley, New Jersey, USA, **2015**, pp. 145–146, DOI: 10.1002/9781118892336.

[10]   H. Lin, D. G. Truhlar, *Theor. Chem. Acc.* **2007**, *117*, 185, DOI: 10.1007/s00214-006-0143-z.

[11]   H. M. Senn, W. Thiel, *Angew. Chem. Int. Ed.* **2009**, *48*, 1198–1229, DOI: 10.1002/anie.200802019.

[12]   T. Stecher, K. Reuter, H. Oberhofer, *Phys. Rev. Lett.* **2016**, *117*, 276001, DOI: 10.1103/PhysRevLett.117.276001.

[13]   M. Born, *Z. physik. Chem.* **1920**, *1*, 45–48.

[14]   J. L. Fattebert, F. Gygi, *J. Comput. Chem.* **2002**, *23*, 662–666, DOI: 10.1002/jcc.10069.

[15]   J. L. Fattebert, F. Gygi, *Int. J. Quant. Chem.* **2003**, *93*, 139–147, DOI: 10.1002/qua.10548.

[16]   D. A. Scherlis, J. L. Fattebert, F. Gygi, M. Cococcioni, N. Marzari, *J. Chem. Phys.* **2006**, *124*, 074103, DOI: 10.1063/1.2168456.

[17]   C. P. Kelly, C. J. Cramer, D. G. Truhlar, *J. Chem. Theory Comput.* **2005**, *1*, 1133–1152, DOI: 10.1021/ct050164b.

[18]   J. Tomasi, B. Mennucci, R. Cammi, *Chem. Rev.* **2005**, *105*, 2999–3093, DOI: 10.1021/cr9904009.

[19]   C. J. J. Cramer, D. G. Truhlar, *Chem. Rev.* **1999**, *99*, 2161–2200, DOI: 10.1021/cr960149m.

[20]   J. Srinivasan, T. E. Cheatham, P. Cieplak, P. A. Kollman, D. A. Case, *J. Am. Chem. Soc.* **1998**, *120*, 9401–9409, DOI: 10.1021/ja981844+.

[21]   D. Bashford, D. A. Case, *Annu. Rev. Phys. Chem.* **2000**, *51*, 129–152, DOI: 10.1146/annurev.physchem.51.1.129.

[22]   J. Chen, C. L. Brooks, J. Khandogin, *Curr. Opin. Struct. Biol.* **2008**, *18*, 140–148, DOI: 10.1016/j.sbi.2008.01.003.

[23]   R. Jinnouchi, A. B. Anderson, *Phys. Rev. B* **2008**, *77*, 245417, DOI: 10.1103/PhysRevB.77.245417.

[24]   Y.-H. Fang, G.-F. Wei, Z.-P. Liu, *Cat. Today* **2013**, *202*, 98–104, DOI: 10.1016/j.cattod.2012.04.055.

[25]   Y. Zhang, P. S. Cremer, *Curr. Opin. Chem. Biol.* **2006**, *10*, 658–663, DOI: 10.1016/j.cbpa.2006.09.020.

[26]   C. Bretti, O. Giuffrè, G. Lando, S. Sammartano, *Springerplus* **2016**, *5*, 1–21, DOI: 10.1186/s40064-016-2568-8.

[27]   A. H. Crevenna, N. Naredi-Rainer, D. C. Lamb, R. Wedlich-Söldner, J. Dzubiella, *Biophys. J.* **2012**, *102*, 907–915, DOI: 10.1016/j.bpj.2012.01.035.

[28] F. Hofmeister, *Arch. Exp. Pathol. Pharmocol.* **1888**, *24*, 247–260.

[29] Schematische Struktur einer DNA-Helix und Verteilung von Wassermolekülen [online]. `https://www.mbi-berlin.de/highlights/archive/2015/highlights_de.html` [latest access: 2017/01/04].

[30] A Simulation Cell Showing the Catalytic Surfaces, Ions and Solvent [online]. `http://web.stanford.edu/group/markland/research.html` [latest access: 2017/01/04].

[31] Molecular Dynamics Simulation of Sodium Chloride in Water [online]. `https://www.youtube.com/watch?v=3B6MWs8Omt0` [latest access: 2017/01/05].

[32] Gouy, G., *J. de Physique* **1910**, *9*, 457–468.

[33] G. Gouy, *Ann. Phys.(Paris)* **1917**, *7*, 129–184.

[34] D. Chapman, *Philos. Mag.* **1913**, *25*, 475–481, DOI: 10.1080/14786440408634187.

[35] P. Debye, E. Hückel, *Phys. Z.* **1923**, *24*, 185–206.

[36] S. W. W. Chen, B. Honig, *J. Phys. Chem. B* **1997**, *101*, 9113–9118, DOI: 10.1021/jp971521k.

[37] P. Weetman, S. Goldman, C. G. Gray, *J. Phys. Chem. B* **1997**, *101*, 6073–6078, DOI: 10.1021/jp971162t.

[38] F. Fogolari, A. Brigo, H. Molinari, *J. Mol. Recognit.* **2002**, *15*, 377–392, DOI: 10.1002/jmr.577.

[39] R. J. Hunter, *Foundations of Colloid Science*, Oxford University Press, Oxford, **2001**, pp. 304–402.

[40] J. Lipfert, V. B. Chu, Y. Bai, D. Herschlag, S. Doniach, *J. Appl. Crystallogr.* **2007**, *40*, s229–s234.

[41] E. J. W. Verwey, J. T. G. Overbeek, *Theory of the Stability of Lyophobic Colloids*, Elsevier, Amsterdam, **1948**.

[42] S. Alexander, P. M. Chaikin, P. Grant, G. J. Morales, P. Pincus, D. Hone, *J. Chem. Phys.* **1984**, *80*, 5776–5781, DOI: 10.1063/1.446600.

[43] J. L. Barrat, J. F. Joanny, *Adv. Chem. Phys.* **1996**, *94*, 1–66, DOI: 10.1002/9780470141533.ch1.

[44] J. Lyklema, *Fundamentals of Interface and Colloid Science,Volume II: Solid-Liquid Interfaces*, Academic Press, San Diego, **1995**, pp. 3.2–4.11.

[45] D. Harries, S. May, W. M. Gelbart, A. Ben-Shaul, *Biophys. J.* **1998**, *75*, 159–173, DOI: 10.1016/S0006-3495(98)77503-4.

[46] I. Borukhov, D. Andelman, H. Orland, *Macromolecules* **1998**, *31*, 1665–1671, DOI: 10.1021/ma9707300.

[47] D. Andelman, in *Structure and Dynamics of Membranes: From Cells to Vesicles*, vol. 1 of *Handbook of Biological Physics*, (Edited by R. Lipowsky, E. Sackmann), North-Holland, Chapt. 12, **1995**, DOI: 10.1016/S1383-8121(06)80005-9.

[48] B. Honig, A. Nicholls, *Science* **1995**, *268*, 1144–1149, DOI: 10.1126/science.7761829.

[49] Y.-H. Fang, Z.-P. Liu, *J. Am. Chem. Soc.* **2010**, *132*, 18214–18222, DOI: 10.1021/ja1069272.

[50] H.-F. Wang, Z.-P. Liu, *J. Phys. Chem. C* **2009**, *113*, 17502–17508, DOI: 10.1021/jp9059888.

[51] R. Jinnouchi, K. Kodama, T. Hatanaka, Y. Morimoto, *Phys. Chem. Chem. Phys.* **2011**, *13*, 21070–21083, DOI: 10.1039/c1cp21349k.

[52] D. Boda, W. R. Fawcett, D. Henderson, S. Sokołowski, *J. Chem. Phys.* **2002**, *116*, 7170–7176, DOI: 10.1063/1.1464826.

[53] K. Bohinc, A. Shrestha, M. Brumen, S. May, *Phys. Rev. E* **2012**, *85*, 031130, DOI: 10.1103/PhysRevE.85.031130.

[54] Y. X. Yu, J. Z. Wu, G. H. Gao, *J. Chem. Phys.* **2004**, *120*, 7223–7233, DOI: 10.1063/1.1676121.

[55] J. Cervera, P. Ramirez, J. A. Manzanares, S. Mafe, *Microfluid Nanofluid* **2010**, *9*, 41–53, DOI: 10.1007/s10404-009-0518-2.

[56] M. S. Kilic, M. Z. Bazant, A. Ajdari, *Phys. Rev. E* **2007**, *75*, 021503, DOI: 10.1103/PhysRevE.75.021503.

[57] D. Antypov, M. C. Barbosa, C. Holm, *Phys. Rev. E* **2005**, *71*, 061106, DOI: 10.1103/PhysRevE.71.061106.

[58] N. A. Baker, D. Sept, S. Joseph, M. J. Holst, J. A. McCammon, *P. Natl. Acad. Sci. USA* **2001**, *98*, 10037–10041, DOI: 10.1073/pnas.181342398.

[59] M. Boström, F. W. Tavares, D. Bratko, B. W. Ninham, *J. Phys. Chem. B* **2005**, *109*, 24489–24494, DOI: 10.1021/jp0551869.

[60] V. B. Chu, Y. Bai, J. Lipfert, D. Herschlag, S. Doniach, *Biophys. J.* **2007**, *93*, 3202–3209, DOI: 10.1529/biophysj.106.099168.

[61] M. O. Fenley, R. C. Harris, B. Jayaram, A. H. Boschitsch, *Biophys. J.* **2010**, *99*, 879–886, DOI: 10.1016/j.bpj.2010.04.066.

[62] S. Kirmizialtin, A. R. Silalahi, R. Elber, M. O. Fenley, *Biophys. J.* **2012**, *102*, 829–838, DOI: 10.1016/j.bpj.2011.12.055.

[63] N. Wang, S. Zhou, P. M. Kekenes-Huskey, B. Li, J. A. McCammon, *J. Phys. Chem. B* **2014**, *118*, 14827–14832, DOI: 10.1021/jp511702w.

[64] I. Borukhov, D. Andelman, H. Orland, *Electrochim. Acta* **2000**, *46*, 221–229, DOI: 10.1016/S0013-4686(00)00576-4.

[65] I. Borukhov, D. Andelman, H. Orland, *Phys. Rev. Lett.* **1997**, *79*, 435–438, DOI: 10.1103/PhysRevLett.79.435.

[66] A. H. Boschitsch, P. V. Danilov, *J. Comput. Chem.* **2012**, *33*, 1152–1164, DOI: 10.1002/jcc.22946.

[67] J. H. Chaudhry, S. D. Bond, L. N. Olson, *J. Sci. Comput.* **2011**, *47*, 347–364, DOI: 10.1007/s10915-010-9441-7.

[68] V. Kralj-Iglic, A. Iglic, *J. Phys. II* **1996**, *6*, 477–491, DOI: 10.1051/jp2:1996193.

[69] S. Zhou, Z. Wang, B. Li, *Phys. Rev. E* **2011**, *84*, 021901, DOI: 10.1103/PhysRevE.84.021901.

[70] A. Abrashkin, D. Andelman, H. Orland, *Phys. Rev. Lett.* **2007**, *99*, 077801, DOI: 10.1103/PhysRevLett.99.077801.

[71] G. Tresset, *Phys. Rev. E* **2008**, *78*, 061506, DOI: 10.1103/PhysRevE.78.061506.

[72] A. R. Silalahi, A. H. Boschitsch, R. C. Harris, M. O. Fenley, *J. Chem. Theory Comput.* **2010**, *6*, 3631–3639, DOI: 10.1021/ct1002785.

[73] R. R. Netz, H. Orland, *Euro. Phys. J. E* **2000**, *1*, 203–214, DOI: 10.1007/s101890050023.

[74] O. Stern, *Z. Elektrochem. Angew. P.* **1924**, *30*, 508–516.

[75] D. B. Lukatsky, S. A. Safran, *Phys. Rev. E* **1999**, *60*, 5848–5857, DOI: 10.1103/PhysRevE.60.5848.

[76] M. J. Stevens, M. O. Robbins, *Europhys. Lett.* **1990**, *12*, 81–86, DOI: 10.1209/0295-5075/12/1/015.

[77] R. R. Netz, H. Orland, *Europhys. Lett.* **1999**, *45*, 726–732, DOI: 10.1209/epl/i1999-00228-6.

[78] R. C. Harris, A. H. Boschitsch, M. O. Fenley, *J. Chem. Phys.* **2014**, *140*, 075102, DOI: 10.1063/1.4864460.

[79] G. Fisicaro, L. Genovese, O. Andreussi, N. Marzari, S. Goedecker, *J. Chem. Phys.* **2016**, *144*, 014103, DOI: 10.1063/1.4939125.

[80] K. Mathew, R. G. Hennig, Implicit self-consistent description of electrolyte in plane-wave density-functional theory, **2016**, arXiv:1601.03346, arXiv.org ePrint archive, `http://arxiv.org/abs/1601.03346` [latest access: 2016/12/19].

[81] K. Letchworth-Weaver, T. A. Arias, *Phys. Rev. B* **2012**, *86*, 075140, DOI: 10.1103/PhysRevB.86.075140.

[82] D. J. Tannor, B. Marten, R. Murphy, R. A. Friesner, D. Sitkoff, A. Nicholls, M. Ringnalda, W. A. Goddard, B. Honig, *J. Am. Chem. Soc.* **1994**, *116*, 11875–11882, DOI: 10.1021/ja00105a030.

[83] M. Otani, O. Sugino, *Phys. Rev. B* **2006**, *73*, 115407, DOI: 10.1103/PhysRevB.73.115407.

[84] K. Chin, K. A. Sharp, B. Honig, A. M. Pyle, *Nat. Struct. Mol. Biol.* **1999**, *6*, 1055–1061, DOI: 10.1038/14940.

[85] M. K. Gilson, K. A. Sharp, B. H. Honig, *J. Comput. Chem.* **1988**, *9*, 327–335, DOI: 10.1002/jcc.540090407.

[86] S. Ringe, H. Oberhofer, C. Hille, S. Matera, K. Reuter, *J. Chem. Theory Comput.* **2016**, *12*, 4052–4066, DOI: 10.1021/acs.jctc.6b00435.

[87] G. Kresse, J. Hafner, *Phys. Rev. B* **1993**, *47*, 558, DOI: 10.1016/0022-3093(95)00355-X.

Bibliography

[88] G. Kresse, J. Hafner, *Phys. Rev. B* **1994**, *49*, 14251, DOI: 10.1103/PhysRevB.49.14251.

[89] G. Kresse, J. Furthmüller, *Comput. Mater. Sci.* **1996**, *6*, 15–50, DOI: 10.1016/0927-0256(96)00008-0.

[90] G. Kresse, J. Furthmüller, *Phys. Rev. B* **1996**, *54*, 11169, DOI: 10.1103/PhysRevB.54.11169.

[91] S. J. Clark, M. D. Segall, C. J. Pickard, P. J. Hasnip, M. I. Probert, K. Refson, M. C. Payne, *Z. Kristallogr. Cryst. Mater.* **2005**, *220*, 567–570, DOI: 10.1524/zkri.220.5.567.65075.

[92] D. Vanderbilt, *Phys. Rev. B* **1990**, *41*, 7892, DOI: 10.1103/PhysRevB.41.7892.

[93] G. Kresse, J. Hafner, *Journal of Physics: Condensed Matter* **1994**, *6*, 8245, DOI: 10.1088/0953-8984/6/40/015.

[94] P. E. Blöchl, *Phys. Rev. B* **1994**, *50*, 17953, DOI: 10.1103/PhysRevB.50.17953.

[95] G. Kresse, D. Joubert, *Phys. Rev. B* **1999**, *59*, 1758, DOI: 10.1103/PhysRevB.59.1758.

[96] X. Ren, P. Rinke, V. Blum, J. Wieferink, A. Tkatchenko, A. Sanfilippo, K. Reuter, M. Scheffler, *New J. Phys.* **2012**, *14*, 053020, DOI: 10.1088/1367-2630/14/5/053020.

[97] A. Tkatchenko, R. A. DiStasio Jr, R. Car, M. Scheffler, *Phys. Rev. Lett.* **2012**, *108*, 236402, DOI: 10.1103/PhysRevLett.108.236402.

[98] A. Tkatchenko, A. Ambrosetti, R. A. DiStasio Jr, *J. Chem. Phys.* **2013**, *138*, 074106, DOI: 10.1063/1.4789814.

[99] A. Tkatchenko, M. Scheffler, *Phys. Rev. Lett.* **2009**, *102*, 073005, DOI: 10.1103/PhysRevLett.102.073005.

[100] H. Shang, C. Carbogno, P. Rinke, M. Scheffler, *Comput. Phys. Commun.* **2017**, *215*, 26–46, DOI: 10.1016/j.cpc.2017.02.001.

[101] D. Berger, A. J. Logsdail, H. Oberhofer, M. R. Farrow, C. R. A. Catlow, P. Sherwood, A. A. Sokol, V. Blum, K. Reuter, *J. Chem. Phys.* **2014**, *141*, 024105, DOI: 10.1063/1.4885816.

[102] N. A. Richter, S. Sicolo, S. V. Levchenko, J. Sauer, M. Scheffler, *Phys. Rev. Lett.* **2013**, *111*, 045502, DOI: 10.1103/PhysRevLett.111.045502.

[103] D. Berger, H. Oberhofer, K. Reuter, *Phys. Rev. B* **2015**, *92*, 075308, DOI: 10.1103/PhysRevB.92.075308.

[104] V. W.-h. Lau, I. Moudrakovski, T. Botari, S. Weinberger, M. B. Mesch, V. Duppel, J. Senker, V. Blum, B. V. Lotsch, *Nat. Commun.* **2016**, *7*, DOI: 10.1038/ncomms12165.

[105] A. Tkatchenko, M. Rossi, V. Blum, J. Ireta, M. Scheffler, *Phys. Rev. Lett.* **2011**, *106*, 118102, DOI: 10.1103/PhysRevLett.106.118102.

[106] S. Chutia, M. Rossi, V. Blum, *J. Phys. Chem. B* **2012**, *116*, 14788–14804, DOI: 10.1021/jp3098268.

[107] C. Baldauf, K. Pagel, S. Warnke, G. von Helden, B. Koksch, V. Blum, M. Scheffler, *Chem. Eur. J.* **2013**, *19*, 11224–11234, DOI: 10.1002/chem.201204554.

[108] A. Supady, V. Blum, C. Baldauf, *J. Chem. Inf. Model.* **2015**, *55*, 2338–2348, DOI: 10.1021/acs.jcim.5b00243.

[109] F. Long, W. McDevit, *Chem. Rev.* **1952**, *51*, 119–169, DOI: 10.1021/cr60158a004.

[110] R. I. Slavchov, *J. Chem. Phys.* **2014**, *140*, 164510, DOI: 10.1063/1.4871661.

[111] A. A. Barba, M. d'Amore, in *Microwave Materials Characterization*, (Edited by S. Costanzo), Intech, **2012**, DOI: 10.5772/51098.

[112] J. P. Perdew, K. Burke, M. Ernzerhof, *Phys. Rev. Lett.* **1996**, *77*, 3865–3868, DOI: 10.1103/PhysRevLett.77.3865.

[113] M. Ernzerhof, G. E. Scuseria, *J. Chem. Phys.* **1999**, *110*, 5029–5036, DOI: 10.1063/1.478401.

[114] G. I. Csonka, J. P. Perdew, A. Ruzsinszky, P. H. Philipsen, S. Lebègue, J. Paier, O. A. Vydrov, J. G. Ángyán, *Phys. Rev. B* **2009**, *79*, 155107, DOI: 10.1103/PhysRevB.79.155107.

[115] P. Janthon, S. Luo, S. M. Kozlov, F. Vines, J. Limtrakul, D. G. Truhlar, F. Illas, *J. Chem. Th. Comput* **2014**, *10*, 3832–3839, DOI: 10.1021/ct500532v.

[116] H. v. Helmholtz, *Ann. d. Phys* **1853**, *165*, 211–233.

[117] J. N. Israelachvili, *Intermolecular and surface forces*, 3 ed., Academic press, **2011**, pp. 291–340.

[118] F. Fogolari, P. Zuccato, G. Esposito, P. Viglino, *Biophys. J.* **1999**, *76*, 1–16, DOI: 10.1016/S0006-3495(99)77173-0.

[119] M. S. Kilic, M. Z. Bazant, A. Ajdari, *Phys. Rev. B* **2007**, *75*, 021502, DOI: 10.1103/PhysRevE.75.021502.

[120] G. J. Bartlett, C. T. Porter, N. Borkakoti, J. M. Thornton, *J. Mol. Biol.* **2002**, *324*, 105–121, DOI: 10.1016/S0022-2836(02)01036-7.

[121] M. Y. Kiriukhin, K. D. Collins, *Biophys. Chem.* **2002**, *99*, 155–168, DOI: 10.1016/S0301-4622(02)00153-9.

[122] M. A. Brown, A. Goel, Z. Abbas, *Angew. Chem. Int. Ed.* **2016**, *55*, 3790–3794, DOI: 10.1002/anie.201512025.

[123] L. Li, C. J. Fennell, K. A. Dill, *J. Chem. Phys.* **2014**, *141*, 22D518, DOI: 10.1063/1.4900890.

[124] T. Brandes, Statistische Mechanik, **2015**, lecture Notes, TU Berlin, WS 2014/2015.

[125] A. Zee, *Quantum Field Theory in a Nutshell*, Princeton University Press, **2003**, pp. 14–15.

[126] H. Kleinert, *Particles and Quantum Fields*, World Scientific, Singapore, Chapt. 14, **2015**, pp. 930–931.

[127] A. Zee, *Quantum Field Theory in a Nutshell*, Princeton University Press, **2003**, p. 16.

[128] K. Reuter, C. Stampf, M. Scheffler, in *Handbook of Materials Modeling*, (Edited by S. Yip), Springer, Chapt. 1, **2005**, DOI: 10.1007/978-1-4020-3286-8_10.

[129] S. Gekle, R. R. Netz, *J. Chem. Phys.* **2012**, *137*, 104704, DOI: 10.1063/1.4749380.

[130] S. N. Steinmann, P. Sautet, *J. Phys. Chem. C* **2016**, *120*, 5619–5623, DOI: 10.1021/acs.jpcc.6b01938.

[131] R. E. Stratmann, G. E. Scuseria, M. J. Frisch, *Chem. Phys. Lett.* **1996**, *257*, 213–223, DOI: 10.1016/0009-2614(96)00600-8.

[132] B. I. Dunlap, J. W. D. Connolly, J. R. Sabin, *J. Chem. Phys.* **1979**, *71*, 3396–3402, DOI: 10.1063/1.438728.

[133] P. Deuflhard, in *Newton Methods for Nonlinear Problems*, (Edited by R. Bank, R. Graham, J. Stoer, R. Varga, H. Yserentant), Springer, pp. 7–41, DOI: 10.1007/978-3-642-23899-4.

[134] P. J. Hasnip, M. I. J. Probert, Auxiliary density functionals: a new class of methods for efficient, stable density functional theory calculations, **2015**, arXiv:1503.01420, arXiv.org ePrint archive, `http://arxiv.org/abs/1503.01420` [latest access: 2016/06/02].

[135] Y. Shiihara, O. Kuwazuru, N. Yoshikawa, *Model. Simul. Mater. Sc.* **2008**, *16*, 035004, DOI: 10.1088/0965-0393/16/3/035004.

[136] G. P. Kerker, *Phys. Rev. B* **1981**, *23*, 3082–3084, DOI: 10.1103/PhysRevB.23.3082.

[137] G. Watson, *A treatise on the theory of Bessel functions*, 2 ed., Cambridge University Press, **1966**, p. 366.

[138] A. H. Boschitsch, M. O. Fenley, W. K. Olson, *J. Comput. Phys.* **1999**, *151*, 212–241, DOI: 10.1006/jcph.1998.6176.

[139] J. G. Ángyán, I. Gerber, M. Marsman, *J. Phys. A* **2006**, *39*, 8613, DOI: 10.1088/0305-4470/39/27/005.

[140] J. McKinley, P. Schmidt, Taylor-Laplace Expansions of the Yukawa and Related Potential Energy Functions., *Techn. Ber.*, DTIC Document, **1981**.

[141] F. Olver, A. Olde Daalhuis, D. Lozier, B. Schneider, R. Boisvert, C. Clark, B. Miller, B. Saunders, eds. , NIST Digital Library of Mathematical Functions, Release 1.0.14 of 2016-12-21. `http://dlmf.nist.gov/`.

[142] M. Abramowitz, I. A. Stegun, *Handbook of Mathematical Functions*, Applied Mathematics Series, National Bureau of Standards, New York, **1964**, pp. 374–378.

[143] M. Abramowitz, I. A. Stegun, *Handbook of Mathematical Functions*, Applied Mathematics Series, National Bureau of Standards, New York, **1964**, p. 896.

[144] D. Shivakumar, J. Williams, Y. Wu, W. Damm, J. Shelley, W. Sherman, *J. Chem. Theory Comput.* **2010**, *6*, 1509–1519, DOI: 10.1021/ct900587b.

[145] J. Lang, *Adaptive multilevel solution of nonlinear parabolic PDE systems: theory, algorithm, and applications*, vol. 16, Springer Science & Business Media, **2013**.

[146] C. Hille, *Adaptive finite element approximation of the linearized Poisson-Boltzmann equation for implicit solvent models*, Master's Thesis, TU Munich, **2014**.

[147] C. J. Muschielok, *Towards Dynamic Modeling of Poisson-Boltzmann Electrolytes*, Master's Thesis, TU Munich, **2016**.

[148] S. Ringe, H. Oberhofer, K. Reuter, *J. Chem. Phys.* **2017**, *146*, 134103, DOI: 10.1063/1.4978850.

[149] A. Levy, D. Andelman, H. Orland, *Phys. Rev. Lett.* **2012**, *108*, 227801, DOI: 10.1103/PhysRevLett.108.227801.

[150] H. Li, B. Lu, *J. Chem. Phys.* **2014**, *141*, 024115, DOI: 10.1063/1.4887342.

[151] Y. Nakayama, D. Andelman, *J. Chem. Phys.* **2015**, *142*, 044706, DOI: 10.1063/1.4906319.

[152] N. Gavish, K. Promislow, *Phys. Rev. E* **2016**, *94*, 012611, DOI: 10.1103/PhysRevE.94.012611.

[153] N. Lespes, J. S. B. Filhol, *J. Chem. Theory Comput.* **2015**, *11*, 3375–3382, DOI: 10.1021/acs.jctc.5b00170.

[154] S. N. Steinmann, P. Sautet, C. Michel, *Phys. Chem. Chem. Phys.* **2016**, *18*, 31850–31861, DOI: 10.1039/C6CP04094B.

[155] B. Jayaram, S. Swaminathan, D. Beveridge, K. Sharp, B. Honig, *Macromolecules* **1990**, *23*, 3156–3165, DOI: 10.1021/ma00214a021.

[156] D. J. Bonthuis, R. R. Netz, *J. Phys. Chem. B* **2013**, *117*, 11397–11413, DOI: 10.1021/jp402482q.

[157] V. L. Shapovalov, G. Brezesinski, *J. Phys. Chem. B* **2006**, *110*, 10032–10040, DOI: 10.1021/jp056801b.

[158] C. Dupont, O. Andreussi, N. Marzari, *J. Chem. Phys.* **2013**, *139*, 214110, DOI: 10.1063/1.4832475.

[159] B. W. Ninham, T. T. Duignan, D. F. Parsons, *Curr. Opin. Colloid. In.* **2011**, *16*, 612–617, DOI: 10.1016/j.cocis.2011.04.006.

[160] D. F. Parsons, B. W. Ninham, *Colloid Surface A* **2011**, *383*, 2–9, DOI: 10.1016/j.colsurfa.2010.12.025.

[161] D. F. Parsons, M. Boström, P. L. Nostro, B. W. Ninham, *Phys. Chem. Chem. Phys.* **2011**, *13*, 12352–12367, DOI: 10.1039/C1CP20538B.

[162] M. Boström, D. R. M. Williams, B. W. Ninham, *Langmuir* **2001**, *17*, 4475–4478, DOI: 10.1021/la0102298.

[163] M. Boström, D. Williams, B. W. Ninham, *Biophys. J.* **2003**, *85*, 686–694, DOI: 10.1016/S0006-3495(03)74512-3.

[164] X. Pang, H.-X. Zhou, *Commun. Comput. Phys.* **2013**, *13*, 1–12, DOI: 10.4208/cicp.270711.140911s.

[165] F. Dong, M. Vijayakumar, H.-X. Zhou, *Biophys. J.* **2003**, *85*, 49–60, DOI: 10.1016/S0006-3495(03)74453-1.

[166] M. Valisko, D. Boda, *J. Chem. Phys.* **2014**, *140*, 234508, DOI: 10.1063/1.4883742.

[167] P. J. Lenart, A. Jusufi, A. Z. Panagiotopoulos, *J. Chem. Phys.* **2007**, *126*, 044509, DOI: 10.1063/1.2431169.

[168] Z. Mester, A. Z. Panagiotopoulos, *J. Chem. Phys.* **2015**, *142*, 044507, DOI: 10.1063/1.4906320.

[169] R. A. Robinson, R. H. Stokes, *Electrolyte Solutions*, 2 ed., Butterworths Publications Limited, New York, **1959**, pp. 476–509.

[170] W. J. Hamer, Y. C. Wu, *J. Phys. Chem. Ref. Data* **1972**, *1*, 1047–1099, DOI: 10.1063/1.3253108.

[171] D. F. Keeley, M. A. Hoffpauir, J. R. Meriwether, *J. Chem. Eng. Data* **1988**, *33*, 87–89, DOI: 10.1021/je00052a006.

[172] P. Pérez-Tejeda, A. Maestre, M. Balón, J. Hidalgo, M. A. Muñoz, M. Sánchez, *J. Chem. Soc. Farad. T. 1* **1987**, *83*, 1029–1039, DOI: 10.1039/F19878301029.

[173] E. M. Waxman, J. Elm, T. Kurtén, K. V. Mikkelsen, P. J. Ziemann, R. Volkamer, *Environ. Sci. Technol.* **2015**, *49*, 11500–11508, DOI: 10.1021/acs.est.5b02782.

[174] A. Burant, G. V. Lowry, A. K. Karamalidis, *Chemosphere* **2016**, *144*, 2247–2256, DOI: 10.1016/j.chemosphere.2015.10.115.

[175] J. Ho, *Austr. J. Chem.* **2014**, *67*, 1441–1460, DOI: 10.1071/CH14040.

[176] J. A. Nelder, R. Mead, *Comput. J.* **1965**, *7*, 308–313, DOI: 10.1093/comjnl/7.4.308.

[177] A. C. Ribeiro, M. A. Esteso, V. M. Lobo, H. D. Burrows, A. M. Amado, A. M. A. da Costa, A. J. Sobral, E. F. Azevedo, M. A. Ribeiro, *J. Mol. Liq.* **2006**, *128*, 134–139, DOI: 10.1016/j.molliq.2005.12.004.

[178] A. C. Ribeiro, V. M. Lobo, H. D. Burrows, A. J. Valente, A. J. Sobral, A. M. Amado, C. I. Santos, M. A. Esteso, *J. Mol. Liq.* **2009**, *146*, 69–73, DOI: 10.1016/j.molliq.2009.02.006.

[179] P. Debye, I. MacAulay, *Physik. Z.* **1925**, *131*, 22–29.

[180] W.-H. Xie, W.-Y. Shiu, D. Mackay, *Mar. Environ. Res.* **1997**, *44*, 429–444, DOI: 10.1016/S0141-1136(97)00017-2.

[181] S. Endo, A. Pfennigsdorff, K.-U. Goss, *Environ. Sci. Technol.* **2012**, *46*, 1496–1503, DOI: 10.1021/es203183z.

[182] N. Ni, S. H. Yalkowsky, *Int. J. Pharm.* **2003**, *254*, 167–172, DOI: 10.1016/S0378-5173(03)00008-5.

[183] W. Xie, H. Ji, W. Li, *Acta Physico-Chimica Sinica* **1985**, *1*, 304–307, DOI: 10.3866/PKU.WHXB19850402.

[184] M. A. Paul, *J. Am. Chem. Soc.* **1952**, *74*, 5274–5277, DOI: 10.1021/ja01141a011.

[185] H. Kruyt, C. Robinson, *Proc. Acad. Sci. Amsterdam* **1926**, *29*, 1244.

[186] R. L. Bergen, F. A. Long, *J. Phys. Chem.* **1956**, *60*, 1131–1135, DOI: 10.1021/j150542a024.

[187] A. Osol, M. Kilpatrick, *J. Am. Chem. Soc.* **1933**, *55*, 4430–4444.

[188] J. N. Sugden, *J. Chem. Soc.* **1926**, *129*, 174–196.

[189] W. Herz, S. E., *Z. physik. Chem.* **1927**, *128*, 399.

[190] P. Groß, K. Schwarz, *Monatsh. Chem. Verw. Tl.* **1930**, *55*, 287–306.

[191] W. L. Masterton, T. P. Lee, *Environ. Sci. Technol.* **1972**, *6*, 919–921, DOI: 10.1021/es60069a011.

[192] A. Al-Maaieh, D. R. Flanagan, *J. Pharm. Sci.* **2002**, *91*, 1000–1008, DOI: 10.1002/jps.10046.

[193] F. I. El-Dossoki, *J. Chem.* **2016**, *2016*, 1–8, DOI: 10.1155/2016/7234320.

[194] M. Randall, C. F. Failey, *Chem. Rev.* **1927**, *4*, 285–290.

[195] M. Randall, C. F. Failey, *Chem. Rev.* **1927**, *4*, 271–284.

[196] M. Randall, C. F. Failey, *Chem. Rev.* **1927**, *4*, 291–318.

[197] A. G. Leiga, J. N. Sarmousakis, *J. Phys. Chem.* **1966**, *70*, 3544–3549, DOI: 10.1021/j100883a031.

[198] J. C. Philip, A. Bramley, *J. Chem. Soc. T.* **1915**, *107*, 377–387.

[199] T. Morrison, F. Billett, *J. Chem. Soc.* **1952**, 3819–3822, DOI: 10.1039/JR9520003819.

[200] W. E. May, S. P. Wasik, D. H. Freeman, *Anal. Chem.* **1978**, *50*, 997–1000, DOI: 10.1021/ac50029a042.

[201] G. Gold, S. Rodriguez, *Can. J. Chemistry* **1989**, *67*, 822–826, DOI: 10.1139/v89-127.

[202] Q. Xu, L. Fan, J. Xu, *Maced. J. Chem. Chem. En.* **2016**, *35*, 53–62, DOI: 10.20450/mjcce.2016.848.

[203] X. Yu, R. Yu, *Ind. Eng. Chem. Res.* **2013**, *52*, 11182–11188, DOI: 10.1021/ie400001u.

[204] Y. Li, Q. Hu, C. Zhong, *Ind. Eng. Chem. Res.* **2004**, *43*, 4465–4468, DOI: 10.1021/ie049811s.

[205] R. Carta, G. Tola, *J. Chem. Eng. Data* **1996**, *41*, 414–417, DOI: 10.1021/je9501853.

[206] H. Ohtaki, *Monatsh. Chem.* **2001**, *132*, 1237–1268, DOI: 10.1007/s007060170016.

[207] Y. Marcus, *Chem. Rev.* **1988**, *88*, 1475–1498, DOI: 10.1021/cr00090a003.

[208] Y. Marcus, *Ions in solution and their solvation*, Wiley, New Jersey, USA, **2015**, pp. 141–146.

[209] S. N. Steinmann, C. Michel, R. Schwiedernoch, P. Sautet, *Phys. Chem. Chem. Phys.* **2015**, *17*, 13949–13963, DOI: 10.1039/C5CP00946D.

Acknowledgements

At this point, I would like to thank all the people that supported me on the way to this thesis. This is first of all my doctoral advisor Karsten Reuter who provided me with a thrilling and challenging project in a perfect working environment, realized various visits of international conferences and meetings with other scientists and supported me at any time. A special thanks goes to my direct supervisor Harald Oberhofer who was always a reliable and great support in all kinds of questions and accompanied my whole way through this thesis. In particular when it comes to mathematical issues I am furthermore highly indebted to Sebastian Matera with whom I enjoyed the intense scientific discussions and who was also a steady support in particular in the method development part of this thesis.

A thanks goes to my students Christoph Hille and Christoph Muschielok who left decisive footprints on the presented work and to Volker Blum who was always highly supportive in answering all kinds of `FHI-aims` related questions. Furthermore, I want to particularly thank also my office mates Zhen Yao and Juan Manuel Lorenzi for making the office time as comfortable and enjoying as it can be and in particular Juan for being a good friend at any time. Thanks also again to him and Harald for taking their time to carefully proof-read this thesis.

Thanks go to the whole group of Karsten Reuter which whom I share many great experiences and in particular the IT-team around Christoph Scheurer for the huge effort they are spending to keep our computer infrastructure running as stable as it is. Furthermore, I appreciate the help of Nicola Marzari and Oliviero Andreussi who supported me with the database of molecular hydration energies.

Finally, the biggest thanks of all goes to my wife Jinyoung Ringe who always supported me through all difficult times and to my family to which I could steadily rely on with all sorts of problems.

Appendix
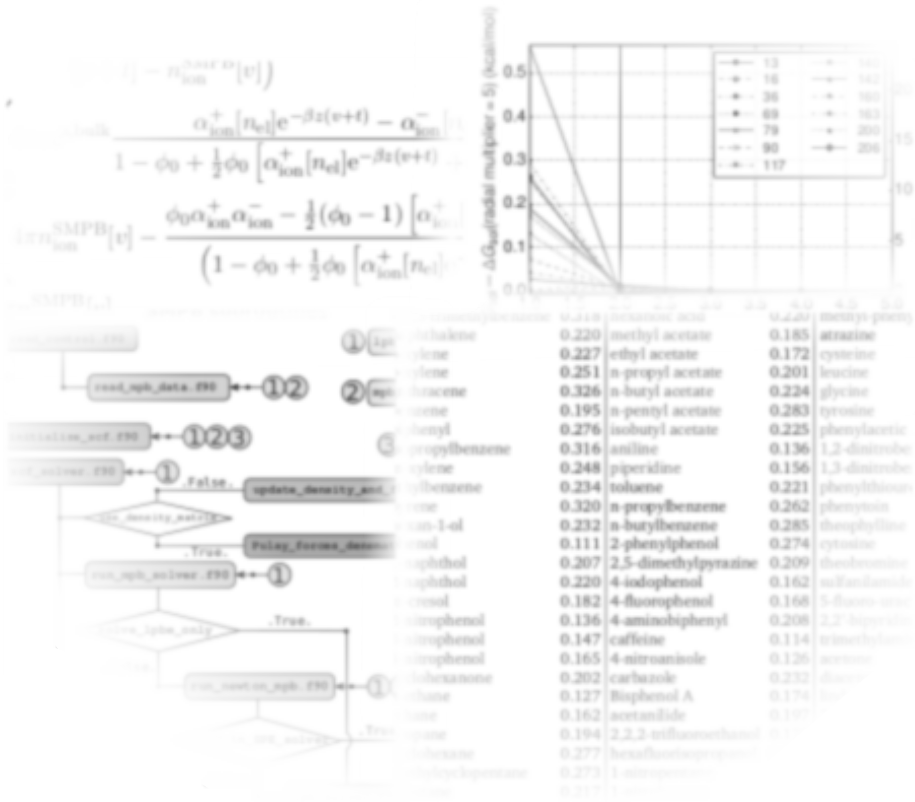
A

Supplementary Material

A.1. KS Hamiltonian for Modified Debye-Hückel Theory

The derivative of the LPB ionic charge density with respect to electron density is given by

$$\frac{\partial n_{\text{ion}}^{\text{LPB}}}{\partial n_{\text{el}}} = \frac{\partial \bar{\kappa}_0^2}{\partial n_{\text{el}}} + \frac{\partial \left(\bar{\kappa}^2 v\right)}{\partial n_{\text{el}}} \quad , \tag{A.1}$$

with

$$\frac{\partial \bar{\kappa}_0^2}{\partial n_{\text{el}}} = zc^{\text{s,bulk}} \left\{ \frac{\frac{\partial \alpha_{\text{ion}}^+[n_{\text{el}}]}{\partial n_{\text{el}}} \left(1 - \phi_0 + \phi_0 \alpha_{\text{ion}}^-[n_{\text{el}}]\right) - \frac{\partial \alpha_{\text{ion}}^-[n_{\text{el}}]}{\partial n_{\text{el}}} \left(1 - \phi_0 + \phi_0 \alpha_{\text{ion}}^+[n_{\text{el}}]\right)}{\left(1 - \phi_0 + \frac{1}{2}\phi_0 \left[\alpha_{\text{ion}}^+[n_{\text{el}}] + \alpha_{\text{ion}}^-[n_{\text{el}}]\right]\right)^2} \right\} \tag{A.2}$$

and

$$\frac{\partial \left(\bar{\kappa}^2 v\right)}{\partial n_{\text{el}}} = -\frac{\kappa^2 \varepsilon^{\text{s,bulk}} v}{4\pi} \frac{1}{\left(1 - \phi_0 + \frac{1}{2}\phi_0 \left[\alpha_{\text{ion}}^+[n_{\text{el}}] + \alpha_{\text{ion}}^-[n_{\text{el}}]\right]\right)^3}$$

$$\times \left\{ \left(\phi_0 \frac{\partial \alpha_{\text{ion}}^+[n_{\text{el}}]}{\partial n_{\text{el}}} \alpha_{\text{ion}}^-[n_{\text{el}}] + \phi_0 \frac{\partial \alpha_{\text{ion}}^-[n_{\text{el}}]}{\partial n_{\text{el}}} \alpha_{\text{ion}}^+[n_{\text{el}}] \right. \right.$$

$$\left. - \frac{1}{2}(\phi_0 - 1) \left[\frac{\partial \alpha_{\text{ion}}^+[n_{\text{el}}]}{\partial n_{\text{el}}} + \frac{\partial \alpha_{\text{ion}}^-[n_{\text{el}}]}{\partial n_{\text{el}}} \right] \right) \left(1 - \phi_0 + \frac{1}{2}\phi_0 \left[\alpha_{\text{ion}}^+[n_{\text{el}}] + \alpha_{\text{ion}}^-[n_{\text{el}}] \right] \right)$$

$$- \frac{1}{2}\phi_0 \left[\frac{\partial \alpha_{\text{ion}}^+[n_{\text{el}}]}{\partial n_{\text{el}}} + \frac{\partial \alpha_{\text{ion}}^-[n_{\text{el}}]}{\partial n_{\text{el}}} \right]$$

$$\left. \times \left(\phi_0 \alpha_{\text{ion}}^+[n_{\text{el}}] \alpha_{\text{ion}}^-[n_{\text{el}}] - \frac{1}{2}(\phi_0 - 1) \left[\alpha_{\text{ion}}^+[n_{\text{el}}] + \alpha_{\text{ion}}^-[n_{\text{el}}] \right] \right) \right\} \quad . \tag{A.3}$$

A.2. Laplace Expansion

A.2.1. Taylor Expansion of the Green's Function

We start by introducing the angle γ between two vectors $\boldsymbol{r}_{\text{at}}$ and $\boldsymbol{r}'_{\text{at}}$ which enables us to rewrite the atom-centered Green's function G_0 as:

$$G_0(|\boldsymbol{r}_{\text{at}} - \boldsymbol{r}'_{\text{at}}|) = \frac{1}{4\pi|\boldsymbol{r}_{\text{at}} - \boldsymbol{r}'_{\text{at}}|} = \frac{1}{4\pi\sqrt{r_{\text{at}}^2 + r'^2_{\text{at}} - 2r_{\text{at}}r'_{\text{at}}\cos(\gamma)}}$$

$$= \begin{cases} \frac{1}{4\pi r_{\text{at}}} \frac{1}{\sqrt{1+h^2-2h\cos(\gamma)}} & \text{case I} \\ \frac{1}{4\pi r'_{\text{at}}} \frac{1}{\sqrt{1+h'^2-2h'\cos(\gamma)}} & \text{case II} \end{cases}, \tag{A.4}$$

with $h = \frac{r'_{\text{at}}}{r_{\text{at}}}$ and $h' = \frac{r_{\text{at}}}{r'_{\text{at}}}$. We can expand the second factor in the case I in a Taylor series around $h = 0$:

$$\frac{1}{\sqrt{1+h^2-2h\cos(\gamma)}} = 1 + h\cos(\gamma) + \frac{1}{2}h^2(3\cos^2(\gamma) - 1) + \dots$$

$$= \sum_{l=0}^{\infty} h^l P_l(\cos(\gamma)) \quad, \tag{A.5}$$

where we introduced the Legendre polynomials P_l. The expanded function is therefore a generating function for the Legendre polynomials with the arising sum converging fast with l if $h \approx 0$ ($r_{\text{at}} \gg r'_{\text{at}}$). Analogously, we can in the case II expand the function around $h' = 0$ with fast convergence for $h' \approx 0$ ($r'_{\text{at}} \gg r_{\text{at}}$). Utilizing the spherical harmonics addition theorem

$$P_l(\cos(\gamma)) = \frac{4\pi}{2l+1} \sum_{m=-l}^{l} Y_{lm}(\Omega_{\text{at}})Y^*_{lm}(\Omega'_{\text{at}}) \quad, \tag{A.6}$$

we then arrive at the spherical harmonics expansion of the Green's function as given in Eq. (3.49).

A.2.2. Physical Interpretation

According to Eq. (3.50), each atom-centered multipole component of δv is given as

$$\delta v_{\text{at},lm}(r_{\text{at}})Y_{lm}(\Omega_{\text{at}}) = 4\pi \int d\boldsymbol{r}'_{\text{at}} \delta n_{\text{el},\text{at},lm}(r'_{\text{at}})Y_{lm}(\Omega'_{\text{at}})G_0(|\boldsymbol{r}_{\text{at}} - \boldsymbol{r}'_{\text{at}}|) \quad. \tag{A.7}$$

Expansion of G_0 around $h = 0$ according to case I therefore corresponds to a situation where the observation point (at which $\delta v_{\text{at},lm}$ is evaluated) is much farer from the atom center then the partitioned charged density at that atom $\delta n_{\text{el},\text{at},lm}$ which is why this case is often called the *far-field* case. Analogously, the case II can be considered as the *near-field* case.

A.2.3. Radial Integral Splitting

The calculation of the atom-centered multipole components of δv according to Eq. (A.7) requires a 1-d integration over all possible distances to the respective atom center. We know that for $r'_{\mathrm{at}} < r_{\mathrm{at}}$ the Taylor expansion according to case I will be rather accurate while for $r'_{\mathrm{at}} > r_{\mathrm{at}}$ the case II expansion should be more reliable. We make use of this fact by splitting the radial integral into two integrals representing the two expansion limits as performed in Eq. (3.50).

A.3. Multipole Correction to the Hartree Energy

We start by writing down the Hartree energy and recast the expression:

$$
\begin{aligned}
E_{\mathrm{es}} &= \frac{1}{2}\int \mathrm{d}\boldsymbol{r}\, n_{\mathrm{el},\circ} v_{\mathrm{es},\circ} = \int \mathrm{d}\boldsymbol{r}\, n_{\mathrm{el},\circ} v_{\mathrm{es},\circ}^{\mathrm{mp}} - \frac{1}{2}\int \mathrm{d}\boldsymbol{r}\, n_{\mathrm{el},\circ} v_{\mathrm{es},\circ}^{\mathrm{mp}} + \frac{1}{2}\int \mathrm{d}\boldsymbol{r}\, n_{\mathrm{el},\circ} v_{\mathrm{es},\circ}^{\mathrm{res}}\\
&= \int \mathrm{d}\boldsymbol{r}\, n_{\mathrm{el},\circ} v_{\mathrm{es},\circ}^{\mathrm{mp}} - \frac{1}{2}\int \mathrm{d}\boldsymbol{r}\, n_{\mathrm{el},\circ}^{\mathrm{mp}} v_{\mathrm{es},\circ}^{\mathrm{mp}} - \frac{1}{2}\int \mathrm{d}\boldsymbol{r}\, n_{\mathrm{el},\circ}^{\mathrm{res}} v_{\mathrm{es},\circ}^{\mathrm{mp}} + \frac{1}{2}\int \mathrm{d}\boldsymbol{r}\, n_{\mathrm{el},\circ} v_{\mathrm{es},\circ}^{\mathrm{res}}\\
&= \int \mathrm{d}\boldsymbol{r}\, n_{\mathrm{el},\circ} v_{\mathrm{es},\circ}^{\mathrm{mp}} - \frac{1}{2}\int \mathrm{d}\boldsymbol{r}\, n_{\mathrm{el},\circ}^{\mathrm{mp}} v_{\mathrm{es},\circ}^{\mathrm{mp}} + \frac{1}{2}\int \mathrm{d}\boldsymbol{r}\, n_{\mathrm{el},\circ}^{\mathrm{res}} v_{\mathrm{es},\circ}^{\mathrm{res}}\\
&\quad + \underbrace{\frac{1}{2}\int \mathrm{d}\boldsymbol{r}\, \left[n_{\mathrm{el},\circ}^{\mathrm{mp}} v_{\mathrm{es},\circ}^{\mathrm{res}} - n_{\mathrm{el},\circ}^{\mathrm{res}} v_{\mathrm{es},\circ}^{\mathrm{mp}} \right]}_{=0} \quad .
\end{aligned}
\tag{A.8}
$$

The last term vanishes, since $n_{\mathrm{el},\circ}$ and $v_{\mathrm{es},\circ}$ are related by the Green's function G_0:

$$
\int \mathrm{d}\boldsymbol{r}\, n_{\mathrm{el},\circ}^{\mathrm{mp}} v_{\mathrm{es},\circ}^{\mathrm{res}} = 4\pi \int \mathrm{d}\boldsymbol{r}\,\mathrm{d}\boldsymbol{r}'\, n_{\mathrm{el},\circ}^{\mathrm{mp}}(\boldsymbol{r}) n_{\mathrm{el},\circ}^{\mathrm{res}}(\boldsymbol{r}') G_0(|\boldsymbol{r}-\boldsymbol{r}'|) = \int \mathrm{d}\boldsymbol{r}\, n_{\mathrm{el},\circ}^{\mathrm{res}} v_{\mathrm{es},\circ}^{\mathrm{mp}}
\tag{A.9}
$$

A.4. Derivation of the Newton Method*

The derivation of the function-space variant of the Newton method as presented here was adapted from the one presented in the supplementary information (SI) of the respective ref. [86]. We start by introducing the regularized free atom electrostatic potential, $v = v^{\mathrm{free}} + \delta v$, into Eq. (3.70)

$$
\begin{aligned}
\mathcal{F}[v] &= \nabla \cdot \left[\varepsilon \nabla v^{\mathrm{free}} \right] + \nabla \cdot [\varepsilon \nabla \delta v] + 4\pi \left(n_{\mathrm{sol}} + n_{\mathrm{ion}}^{\mathrm{SMPB}}[v] \right)\\
&= 4\pi \left(n_{\mathrm{el}} - \varepsilon n_{\mathrm{el}}^{\mathrm{free}} \right) + (\nabla \varepsilon) \cdot (\nabla v^{\mathrm{free}}) + \nabla \cdot [\varepsilon \nabla \delta v] + 4\pi n_{\mathrm{ion}}^{\mathrm{SMPB}}[v]\\
&= 0 \quad ,
\end{aligned}
\tag{A.10}
$$

with $\Delta v^{\mathrm{free}} = -4\pi n_{\mathrm{el}}^{\mathrm{free}} - 4\pi n_{\mathrm{nuc}}$. For improved legibility we do not explicitly write down the dependencies on n_{el} in this section. To find the root of this equation with respect to δv we then employ a Newton scheme, which necessitates the calculation of the first derivative

---

of the functional $\mathcal{F}[v]$. Such a function space derivative $\mathcal{F}'[v]$, generally known as the Fréchet derivative, is defined through the following relation

$$\lim_{t \to 0} \frac{||\mathcal{F}[v+t] - \mathcal{F}[v] - \hat{D}\mathcal{F}[v]t||}{||t||} = 0 \quad , \tag{A.11}$$

where $\hat{D}$ is a bounded linear operator $\hat{D}\mathcal{F}[v] : X \to Y$. If there exists such an operator $\hat{D}$ which fulfills this equation, then the Fréchet derivative of $\mathcal{F}[v]$ is given by

$$\mathcal{F}'[v] = \hat{D}\mathcal{F}[v] \quad . \tag{A.12}$$

To show the existence of $\hat{D}$ and obtain $\mathcal{F}'[v]$, we first calculate the difference

$$\mathcal{F}[v+t] - \mathcal{F}[v] = \nabla \cdot [\varepsilon \nabla t] + 4\pi \left(n_{\text{ion}}^{\text{SMPB}}[v+t] - n_{\text{ion}}^{\text{SMPB}}[v] \right) \quad , \tag{A.13}$$

where the last term can be expanded in a Taylor series around $t = 0$:

$$4\pi \left(n_{\text{ion}}^{\text{SMPB}}[v+t] - n_{\text{ion}}^{\text{SMPB}}[v] \right)$$

$$= \left(4\pi z c^{\text{s,bulk}} \frac{\alpha_{\text{ion}}^{+}[n_{\text{el}}]e^{-\beta z(v+t)} - \alpha_{\text{ion}}^{-}[n_{\text{el}}]e^{\beta z(v+t)}}{1 - \phi_0 + \frac{1}{2}\phi_0 \left[\alpha_{\text{ion}}^{+}[n_{\text{el}}]e^{-\beta z(v+t)} + \alpha_{\text{ion}}^{-}[n_{\text{el}}]e^{\beta z(v+t)} \right]} \right) - 4\pi n_{\text{ion}}^{\text{SMPB}}[v]$$

$$= \left(4\pi n_{\text{ion}}^{\text{SMPB}}[v] - \frac{\phi_0 \alpha_{\text{ion}}^{+}\alpha_{\text{ion}}^{-} - \frac{1}{2}(\phi_0 - 1)\left[\alpha_{\text{ion}}^{+}[n_{\text{el}}]e^{-\beta zv} + \alpha_{\text{ion}}^{-}[n_{\text{el}}]e^{\beta zv} \right]}{\left(1 - \phi_0 + \frac{1}{2}\phi_0 \left[\alpha_{\text{ion}}^{+}[n_{\text{el}}]e^{-\beta zv} + \alpha_{\text{ion}}^{-}[n_{\text{el}}]e^{\beta zv} \right] \right)^2} \varepsilon^{\text{s,bulk}} \kappa^2 \cdot t + \mathcal{O}(t^2) \right)$$

$$- 4\pi n_{\text{ion}}^{\text{SMPB}}[v]$$

$$= -\frac{\phi_0 \alpha_{\text{ion}}^{+}\alpha_{\text{ion}}^{-} - \frac{1}{2}(\phi_0 - 1)\left[\alpha_{\text{ion}}^{+}[n_{\text{el}}]e^{-\beta zv} + \alpha_{\text{ion}}^{-}[n_{\text{el}}]e^{\beta zv} \right]}{\left(1 - \phi_0 + \frac{1}{2}\phi_0 \left[\alpha_{\text{ion}}^{+}[n_{\text{el}}]e^{-\beta zv} + \alpha_{\text{ion}}^{-}[n_{\text{el}}]e^{\beta zv} \right] \right)^2} \varepsilon^{\text{s,bulk}} \kappa^2 \cdot t + \mathcal{O}(t^2)$$

$$= -h^2[v]t + \mathcal{O}(t^2) \quad . \tag{A.14}$$

Putting it all together we get

$$\mathcal{F}[v+t] - \mathcal{F}[v] = \nabla \cdot [\varepsilon \nabla t] - h^2[v]t + \mathcal{O}(t^2) = \hat{L}'[v]t + \mathcal{O}(t^2) \quad , \tag{A.15}$$

with the linear operator

$$\hat{L}'[v] = \nabla \cdot [\varepsilon \nabla] - h^2[v] \quad . \tag{A.16}$$

This implies existence of the Fréchet derivative

$$\mathcal{F}'[v] = \hat{D}\mathcal{F}[v] = \hat{L}'[v] \quad , \tag{A.17}$$

if higher-order terms vanish

$$\lim_{t \to 0} \frac{||\mathcal{O}(t^2)||}{||t||} = 0 \quad . \tag{A.18}$$

In our case this condition is indeed fulfilled, since the numerator converges faster to zero than the denominator. Consequently, Eq. (A.17) is valid and we have found the Fréchet derivative. Inserting these results for $\mathcal{F}'$ and $\mathcal{F}$ into Eq. (3.71) finally yields Eq. (3.72) of the main text.

A.5. Multipole Correction to the Electrostatic Energy in the PB Case
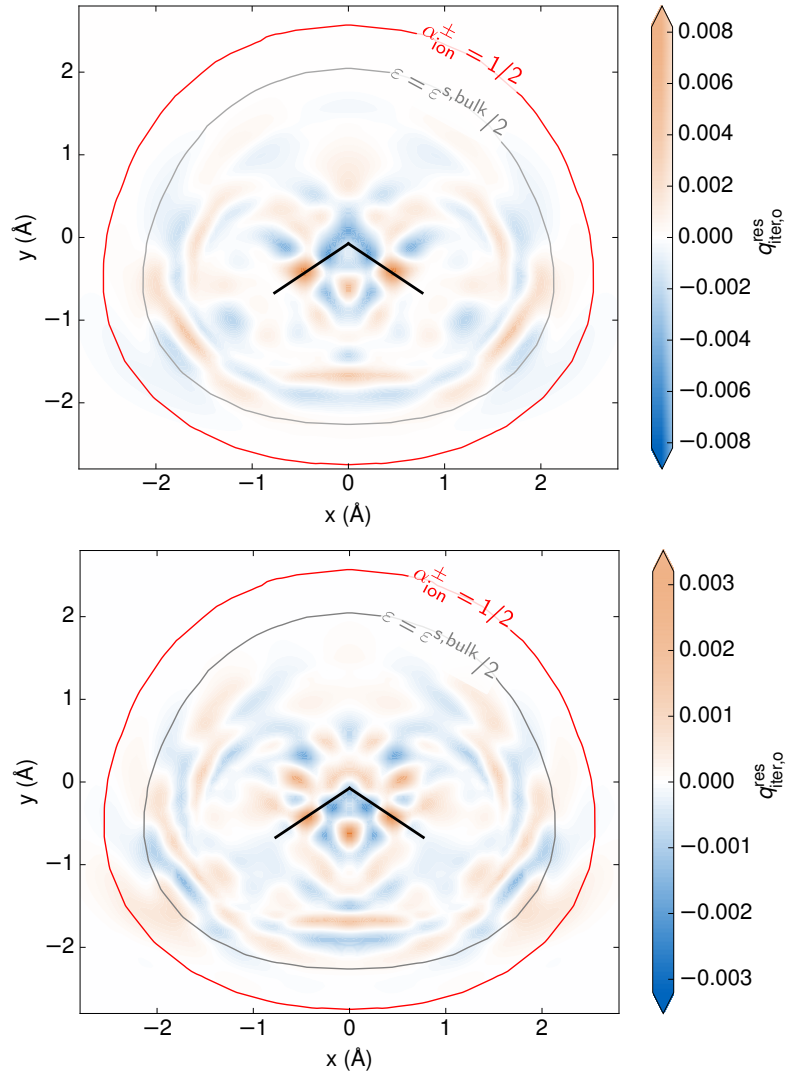
Figure A.1.: $q_{\mathrm{iter,o}}^{\mathrm{res}}$ in the bonding plane of an H_2O molecule embedded into a model SMPB aqueous electrolyte ($\varepsilon^{\mathrm{s,bulk}} = 78.36$, $n_{\min} = 0.0001$, $n_{\max} = 0.005$, $d_{\alpha_{\mathrm{ion}}} = 0.5$, $\xi_{\alpha_{\mathrm{ion}}} = 1.0$, $a = 5\,\text{Å}$, $T = 300\,\text{K}$) calculated with $l_{\max,\mathrm{at}} = 4\ \forall$ at (left panel) and $l_{\max,\mathrm{at}} = 6\ \forall$ at (right panel). Additionally shown are contour lines at the transition regions of dielectric function (gray) and ion exclusion function (red) and the water molecule bonds (solid black lines).

We proceed analogously to Appendix A.3, but now rewrite the electrostatic energy of the solute instead of the Hartree energy:

$$
\begin{aligned}
\frac{1}{2}\int d\boldsymbol{r}\, n_{\mathrm{sol,\circ}}v_\circ &= \int d\boldsymbol{r}\, n_{\mathrm{sol,\circ}}v_\circ^{\mathrm{mp}} - \frac{1}{2}\int d\boldsymbol{r}\, n_{\mathrm{sol,\circ}}v_\circ^{\mathrm{mp}} + \frac{1}{2}\int d\boldsymbol{r}\, n_{\mathrm{sol,\circ}}v_\circ^{\mathrm{res}} \\
&= \int d\boldsymbol{r}\, n_{\mathrm{sol,\circ}}v_\circ^{\mathrm{mp}} - \frac{1}{2}\int d\boldsymbol{r}\left(n_{\mathrm{sol,\circ}} - q_{\mathrm{iter,\circ}}^{\mathrm{res}}\right)v_\circ^{\mathrm{mp}} - \frac{1}{2}\int d\boldsymbol{r}\, q_{\mathrm{iter,\circ}}^{\mathrm{res}}v_\circ^{\mathrm{mp}} \\
&\quad + \frac{1}{2}\int d\boldsymbol{r}\, n_{\mathrm{sol,\circ}}v_\circ^{\mathrm{res}} \\
&= \int d\boldsymbol{r}\, n_{\mathrm{sol,\circ}}v_\circ^{\mathrm{mp}} - \frac{1}{2}\int d\boldsymbol{r}\left(n_{\mathrm{sol,\circ}} - q_{\mathrm{iter,\circ}}^{\mathrm{res}}\right)v_\circ^{\mathrm{mp}} + \frac{1}{2}\int d\boldsymbol{r}\, q_{\mathrm{iter,\circ}}^{\mathrm{res}}v_\circ^{\mathrm{res}} \\
&\quad + \underbrace{\frac{1}{2}\int d\boldsymbol{r}\left[\left(n_{\mathrm{sol,\circ}} - q_{\mathrm{iter,\circ}}^{\mathrm{res}}\right)v_\circ^{\mathrm{res}} - q_{\mathrm{iter,\circ}}^{\mathrm{res}}v_\circ^{\mathrm{mp}}\right]}_{\approx 0} \quad .
\end{aligned}
\tag{A.19}
$$

Note, that the last term is in general non-zero in contrast to the vacuum case. An exact evaluation is, however, not possible, since the multipole error in the electrostatic potential $v_\circ^{\mathrm{res}}$ is usually unknown. In order to analyze this term, we rewrite it using the Green's function G_1:

$$
\begin{aligned}
&\frac{1}{2}\int d\boldsymbol{r}\left[\left(n_{\mathrm{sol,\circ}} - q_{\mathrm{iter,\circ}}^{\mathrm{res}}\right)v_\circ^{\mathrm{res}} - q_{\mathrm{iter,\circ}}^{\mathrm{res}}v_\circ^{\mathrm{mp}}\right] \\
&= \frac{4\pi}{2}\int d\boldsymbol{r}d\boldsymbol{r}'\left(n_{\mathrm{sol,\circ}}(\boldsymbol{r}) - \cancel{q_{\mathrm{iter,\circ}}^{\mathrm{res}}(\boldsymbol{r})}\right)q_{\mathrm{iter,\circ}}^{\mathrm{res}}(\boldsymbol{r}')G_1(|\boldsymbol{r}-\boldsymbol{r}'|) - \frac{1}{2}\int d\boldsymbol{r}\, q_{\mathrm{iter,\circ}}^{\mathrm{res}}v_\circ \\
&\quad + \frac{4\pi}{2}\int d\boldsymbol{r}d\boldsymbol{r}'\cancel{q_{\mathrm{iter,\circ}}^{\mathrm{res}}(\boldsymbol{r})q_{\mathrm{iter,\circ}}^{\mathrm{res}}(\boldsymbol{r}')G_1(|\boldsymbol{r}-\boldsymbol{r}'|)} \\
&= \frac{1}{2}\int d\boldsymbol{r}\, q_{\mathrm{iter,\circ}}^{\mathrm{res}}(\boldsymbol{r})\left[4\pi\int d\boldsymbol{r}'\, n_{\mathrm{sol,\circ}}(\boldsymbol{r}')G_1(|\boldsymbol{r}-\boldsymbol{r}'|) - v_\circ\right] \quad .
\end{aligned}
\tag{A.20}
$$

From this reformulation we can conclude, that the last term in Eq. (A.19) vanishes only if

$$
v_\circ \approx 4\pi\int d\boldsymbol{r}'\, n_{\mathrm{sol,\circ}}(\boldsymbol{r}')G_1(|\boldsymbol{r}-\boldsymbol{r}'|) \quad ,\text{where } q_{\mathrm{iter,\circ}}^{\mathrm{res}} \neq 0 \quad .
\tag{A.21}
$$

This equation will be exactly fulfilled in the vacuum case, where $\varepsilon = 1$ and $\kappa = 0$. In the presence of solvent and ions, $v_\circ$ is instead defined as solution of the non-linear SMPBE

$$
\nabla\left[\varepsilon[n_{\mathrm{el}}]\nabla v_\circ\right] = -4\pi n_{\mathrm{sol,\circ}} - 4\pi n_{\mathrm{ion,\circ}}^{\mathrm{SMPB}}[v_\circ, n_{\mathrm{el,\circ}}] \quad ,
\tag{A.22}
$$

for which no analytic Green's function like G_1 is available. Since, however, $q_{\mathrm{iter,\circ}}$ is confined to the region inside the solvation cavity (cf. Section 3.4.1.2), the same is also true for the multipole error $q_{\mathrm{iter,\circ}}^{\mathrm{res}}$ (cf. Fig. A.1). Inside the solvation cavity where $q_{\mathrm{iter,\circ}}^{\mathrm{res}} \neq 0$, the SMPBE becomes for $\kappa = 0$ the Poisson equation in vacuum

$$
\Delta v_\circ = -4\pi n_{\mathrm{sol,\circ}}
\tag{A.23}
$$

since $\varepsilon = 1$. For zero ionic strengths Eq. (A.21) thus approximately holds and the last term in Eq. (A.19) vanishes. For finite ionic strengths ($\kappa \neq 0$), Eq. (A.21) is generally not valid, since the corresponding PDE to G_1, the SPE

$$
\left(\Delta - \kappa^2\right)v_\circ = -4\pi n_{\mathrm{sol,\circ}}
\tag{A.24}
$$

does not represent the limit of the SMPBE inside the solvation cavity. When performing multipole order convergence tests of free energy differences (cf. Appendix A.7), we, however, find the last term of Eq. (A.19) to be still negligible for all considered test systems even for finite ionic strengths. A possible explanation might be that charges at the outside of the solvation cavity only lead to a nearly constant shift of the electrostatic potential inside the solvation cavity where multipole errors are largest. Such an offset does not require higher orders in the multipole expansion of $v_\circ$. We therefore expect the presence of ions to induce in general only a small multipole truncation error on the total energy, but leave a detailed testing also for other, possibly charged solutes to future studies.

A.6. Multipole Correction to the Forces in the PB Case

We start with the expression for the multipole correction force as given in the main text:

$$
\begin{aligned}
\boldsymbol{F}_{\mathrm{at}}^{\mathrm{mp}} &= \int \mathrm{d}\boldsymbol{r} \left\{ \frac{1}{2} \left(v_\circ^{\mathrm{mp}} \nabla_{\mathrm{at}} q_{n_{\mathrm{el}},\circ}^{\mathrm{mp}} + q_{n_{\mathrm{el}},\circ}^{\mathrm{mp}} \nabla_{\mathrm{at}} v_\circ^{\mathrm{mp}} \right) - n_{\mathrm{sol},\circ} \nabla_{\mathrm{at}} v_\circ^{\mathrm{mp}} \right\} \\
&= -\frac{1}{2} \int \mathrm{d}\boldsymbol{r} \left\{ n_{\mathrm{sol},\circ} \nabla_{\mathrm{at}} v_\circ^{\mathrm{mp}} - v_\circ^{\mathrm{mp}} \nabla_{\mathrm{at}} n_{\mathrm{sol},\circ} + q_{\mathrm{iter},\circ}^{\mathrm{res}} \nabla_{\mathrm{at}} v_\circ^{\mathrm{mp}} + v_\circ^{\mathrm{mp}} \nabla_{\mathrm{at}} q_{\mathrm{iter},\circ}^{\mathrm{res}} \right\} \quad,
\end{aligned}
$$
(A.25)

where the second line follows from the definition of $q_{n_{\mathrm{el}},\circ}^{\mathrm{mp}}$. We now replace $v_\circ^{\mathrm{mp}}$ with $v_\circ - v_\circ^{\mathrm{res}}$:

$$
\begin{aligned}
\boldsymbol{F}_{\mathrm{at}}^{\mathrm{mp}} = -\frac{1}{2} \int \mathrm{d}\boldsymbol{r} \Big\{ &[n_{\mathrm{sol},\circ} \nabla_{\mathrm{at}} v_\circ - v_\circ \nabla_{\mathrm{at}} n_{\mathrm{sol},\circ}] - [n_{\mathrm{sol},\circ} \nabla_{\mathrm{at}} v_\circ^{\mathrm{res}} - v_\circ^{\mathrm{res}} \nabla_{\mathrm{at}} n_{\mathrm{sol},\circ}] \\
&+ \left[q_{\mathrm{iter},\circ}^{\mathrm{res}} \nabla_{\mathrm{at}} v_\circ + v_\circ \nabla_{\mathrm{at}} q_{\mathrm{iter},\circ}^{\mathrm{res}} \right] + \left[q_{\mathrm{iter},\circ}^{\mathrm{res}} \nabla_{\mathrm{at}} v_\circ^{\mathrm{res}} + v_\circ^{\mathrm{res}} \nabla_{\mathrm{at}} q_{\mathrm{iter},\circ}^{\mathrm{res}} \right] \Big\} \quad.
\end{aligned}
$$
(A.26)

We consider now first the ion-free case ($\kappa = 0$) for which a Green's function exists for the inversion of the GPE (cf. Eq. (2.55)), hence:

$$
v_\circ = 4\pi \int \mathrm{d}\boldsymbol{r}' n_{\mathrm{sol},\circ}(\boldsymbol{r}') G(\boldsymbol{r},\boldsymbol{r}') \quad.
$$
(A.27)

Using this equation, the first term in Eq. (A.26) vanishes and the multipole correction force becomes:

$$
\begin{aligned}
\boldsymbol{F}_{\mathrm{at}}^{\mathrm{mp}} = \frac{1}{2} \int \mathrm{d}\boldsymbol{r} \left\{ [n_{\mathrm{sol},\circ} \nabla_{\mathrm{at}} v_\circ^{\mathrm{res}} - v_\circ^{\mathrm{res}} \nabla_{\mathrm{at}} n_{\mathrm{sol},\circ}] - \left[q_{\mathrm{iter},\circ}^{\mathrm{res}} \nabla_{\mathrm{at}} v_\circ + v_\circ \nabla_{\mathrm{at}} q_{\mathrm{iter},\circ}^{\mathrm{res}} \right] \right\} \\
+ \int \mathrm{d}\boldsymbol{r} q_{\mathrm{iter},\circ}^{\mathrm{res}} \nabla_{\mathrm{at}} v_\circ^{\mathrm{res}} \quad,
\end{aligned}
$$
(A.28)

where we used the Green's function G_0 ($= G_1$ for $\kappa = 0$) to shorten the last two terms. As already mentioned in the previous section and in the main text, $q_{\mathrm{iter},\circ}$ is confined to the region of the solvation cavity. Inside the solvation cavity, the vacuum Poisson equation holds and we can thus write

$$
v_\circ = 4\pi \int \mathrm{d}\boldsymbol{r}' n_{\mathrm{sol},\circ}(\boldsymbol{r}') G_0(|\boldsymbol{r} - \boldsymbol{r}'|) \quad,
$$
(A.29)

which leads to

$$\boldsymbol{F}_{\text{at}}^{\text{mp}} = \frac{1}{2} \int \mathrm{d}\boldsymbol{r} \Bigg\{ \left[n_{\text{sol,o}} \nabla_{\text{at}} v_{\text{o}}^{\text{res}} - v_{\text{o}}^{\text{res}} \nabla_{\text{at}} n_{\text{sol,o}} \right]$$
$$- \int \mathrm{d}\boldsymbol{r}' G_0(|\boldsymbol{r} - \boldsymbol{r}'|) \left[q_{\text{iter,o}}^{\text{res}}(\boldsymbol{r}) \nabla_{\text{at}} n_{\text{sol,o}}(\boldsymbol{r}') + n_{\text{sol,o}}(\boldsymbol{r}') q_{\text{iter,o}}^{\text{res}}(\boldsymbol{r}) \right] \Bigg\}$$
$$+ \int \mathrm{d}\boldsymbol{r} \, q_{\text{iter,o}}^{\text{res}} \nabla_{\text{at}} v_{\text{o}}^{\text{res}} \quad . \tag{A.30}$$

Considering now that still for $\kappa = 0$

$$v_{\text{o}}^{\text{res}} = 4\pi \int \mathrm{d}\boldsymbol{r}' q_{\text{iter,o}}^{\text{res}}(\boldsymbol{r}') G_0(|\boldsymbol{r} - \boldsymbol{r}'|) \quad , \tag{A.31}$$

we then get

$$\boldsymbol{F}_{\text{at}}^{\text{mp}} = \frac{1}{2} \int \mathrm{d}\boldsymbol{r}\mathrm{d}\boldsymbol{r}' G_0(|\boldsymbol{r} - \boldsymbol{r}'|) \Bigg\{ \left[\cancel{n_{\text{sol,o}}(\boldsymbol{r}) \nabla_{\text{at}} q_{\text{iter,o}}^{\text{res}}(\boldsymbol{r}')} - q_{\text{iter,o}}^{\text{res}}(\boldsymbol{r}') \nabla_{\text{at}} n_{\text{sol,o}}(\boldsymbol{r}) \right]$$
$$- \left[q_{\text{iter,o}}^{\text{res}}(\boldsymbol{r}) \nabla_{\text{at}} n_{\text{sol,o}}(\boldsymbol{r}') + \cancel{n_{\text{sol,o}}(\boldsymbol{r}') \nabla_{\text{at}} q_{\text{iter,o}}^{\text{res}}(\boldsymbol{r})} \right] \Bigg\} + \int \mathrm{d}\boldsymbol{r} \, q_{\text{iter,o}}^{\text{res}} \nabla_{\text{at}} v_{\text{o}}^{\text{res}}$$
$$= - \int \mathrm{d}\boldsymbol{r} \, q_{\text{iter,o}}^{\text{res}} \nabla_{\text{at}} v_{\text{o}} + \int \mathrm{d}\boldsymbol{r} \, q_{\text{iter,o}}^{\text{res}} \nabla_{\text{at}} v_{\text{o}}^{\text{res}} \quad , \tag{A.32}$$

where we in the last step again used the confinement of q_{iter}. The second term in the last line converges quadratically with the multipole error and can be neglected at standard `FHI-aims` settings. We proved this and the accuracy of the resulting multipole correction force expression

$$\boldsymbol{F}_{\text{at}}^{\text{mp}} = -q_{\text{iter,o}}^{\text{res}} \nabla_{\text{at}} v_{\text{o}} \tag{A.33}$$

by comparing to FDM calculations in which we discretized the ∇_{at}-operator to derive numerical forces.[147] By evaluating forces on the methanol-O atom, we found a maximum angular momentum of $l_{\text{max,at}} = 4$ to be already sufficient to reproduce the numerical forces.

The derivation presented above is strongly valid only for the ion-free case where $\kappa = 0$. Nevertheless, as already discussed in the previous section, we expect ions to induce only a small multipole error on the total energy and therefore also the corresponding forces. We leave it here to future studies to perform an extensive testing of the validity of Eq. (A.33) for the cases of finite ionic strengths.

A.7. Numerical Convergence of Energies[†]

All numerical convergence tests here and in the main text have been performed with the test set of 13 organic molecules listed in Tab. 3.2. The following figures detail the convergence behavior as a function of the major numerical integration grid and truncation

---

[†] Reproduced in part with permission from ref. [86]. © 2016 American Chemical Society.

parameters of `FHI-aims`, as well as of the NAO basis set size (cf. Section 3.3.1 and 3.3.3). By default all calculations have been performed with *tight* settings, at $T = 300\,\text{K}$ and with the following SMPB parameters: The parameters from the "fitg03+β" fit from Andreussi *et al.*,[5] $a = 5\,\text{Å}$, $z = 1$, $d_{\alpha_{\text{ion}}} = d^{\pm}_{\alpha_{\text{ion}}} = 0.5$, $\xi_{\alpha_{\text{ion}}} = \xi^{\pm}_{\alpha_{\text{ion}}} = 1$. Each figure displays for each molecule the variation of the deviation of the calculated solvation free energy ΔG_{sol} at $c^{\text{s,bulk}} = 1\,\text{M}$ and the variation of the deviation of the calculated ion effect on the solvation free energy $\Delta\Delta G_{\text{ion}}$ when selectively increasing one particular parameter. The zero reference for this deviation of ΔG_{sol} and $\Delta\Delta G_{\text{ion}}$ is each time the value obtained with the largest parameter value shown. The conclusion to draw from all performed tests is that the standard `FHI-aims` production settings, i.e. *tight* settings with $l_{\text{max,at}} = 6$, `radial_multiplier = 2` and $r_{\text{cut,at}} = 4\,\text{Å}$ yields well-converged results in the meV to sub-meV region. Thus, the SMPB-DFT solver does not necessitate any higher accuracy settings than standard semi-local DFT.
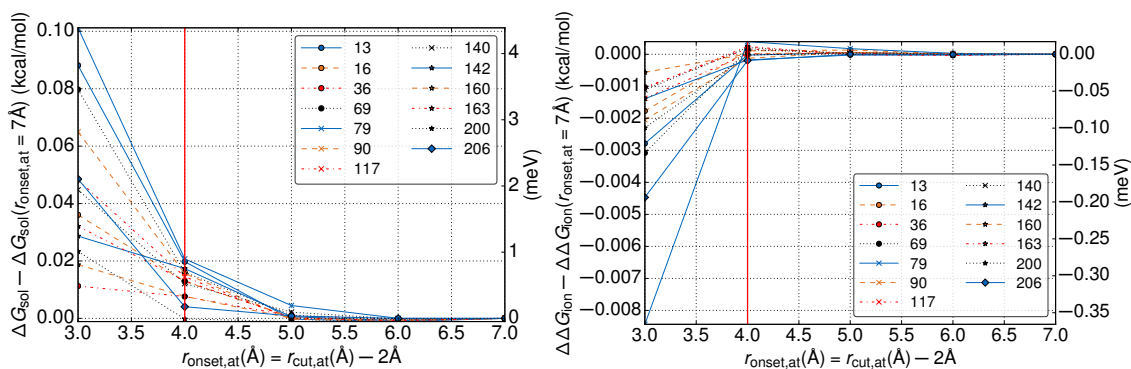
Figure A.2.: Convergence of deviation of ΔG_{sol} (left) and $\Delta\Delta G_{\text{ion}}$ (right) with $r_{\text{onset,at}}$. The red vertical line indicates the standard `FHI-aims` production settings. Reproduced with permission from ref. [86]. © 2016 American Chemical Society.
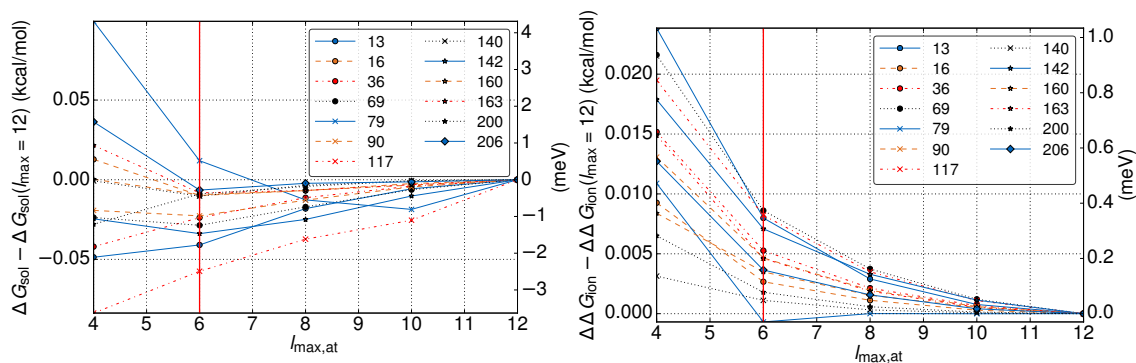
Figure A.3.: Convergence of deviation of ΔG_{sol} (left) and $\Delta\Delta G_{\text{ion}}$ (right) with $l_{\text{max,at}}$ chosen here equal for all atoms. The red vertical line indicates the standard `FHI-aims` production settings. Reproduced with permission from ref. [86]. © 2016 American Chemical Society.
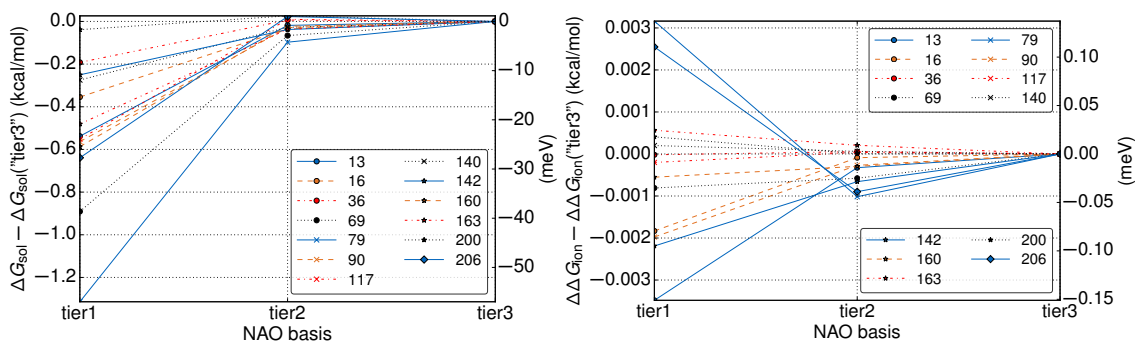
Figure A.4.: Convergence of deviation of ΔG_{sol} (left) and $\Delta\Delta G_{\text{ion}}$ (right) with NAO basis. Reproduced with permission from ref. [86]. © 2016 American Chemical Society.
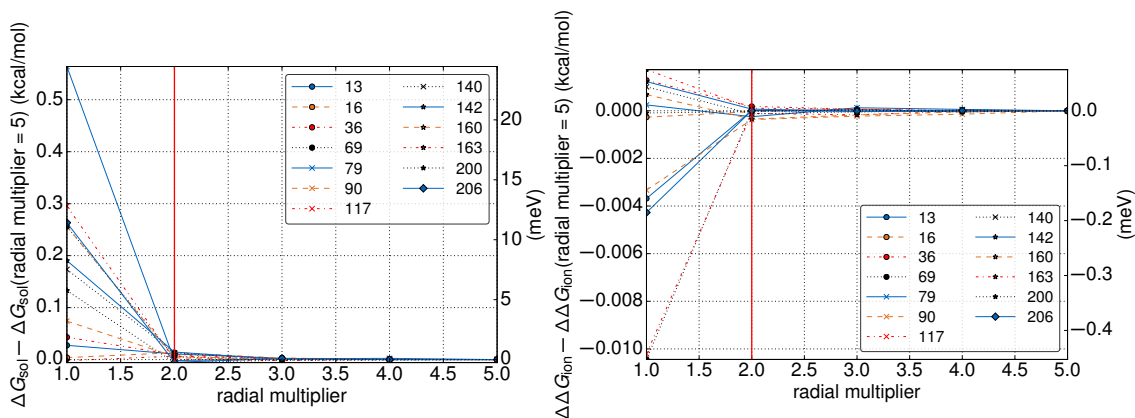
Figure A.5.: Convergence of deviation of ΔG_{sol} (left) and $\Delta\Delta G_{\text{ion}}$ (right) with radial integration grid density. The red vertical line indicates the standard `FHI-aims` production settings. Reproduced with permission from ref. [86]. © 2016 American Chemical Society.
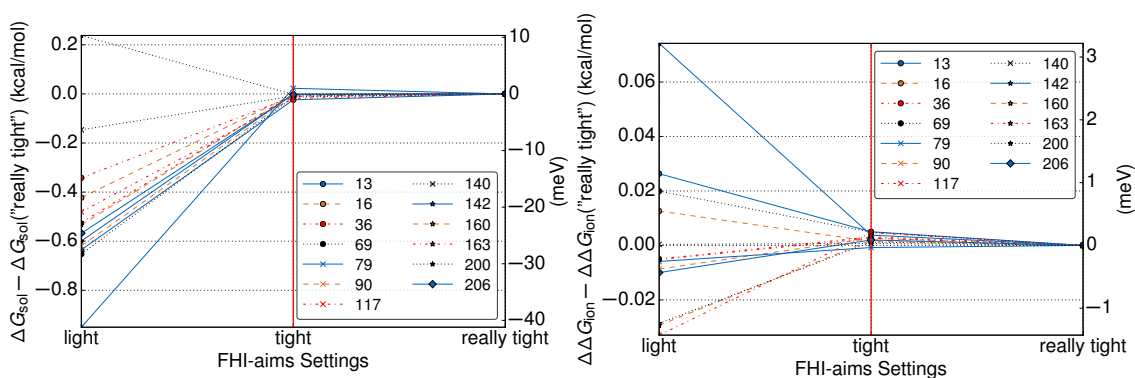
Figure A.6.: Convergence of deviation of ΔG_{sol} (left) and $\Delta\Delta G_{\text{ion}}$ (right) with `FHI-aims` settings. The red vertical line indicates the standard `FHI-aims` production settings. Reproduced with permission from ref. [86]. © 2016 American Chemical Society.

A.8. Databases of Setschenow Coefficients[‡]

molecule	k_s	molecule	k_s	molecule	k_s
1,2,3-trimethylbenzene	0.321	propanoic acid	0.132	4-ethyl-3-hexanol	0.291
1,2,4-trimethylbenzene	0.293	butanoic acid	0.166	2-butoxyethanol	0.211
1,3,5-trimethylbenzene	0.318	hexanoic acid	0.220	methyl-phenyl sulfoxide	0.166
naphthalene	0.220	methyl acetate	0.185	atrazine	0.274
o-xylene	0.227	ethyl acetate	0.172	cysteine	-0.068
p-xylene	0.251	n-propyl acetate	0.201	leucine	0.114
anthracene	0.326	n-butyl acetate	0.224	glycine	0.002
benzene	0.195	n-pentyl acetate	0.283	tyrosine	0.048
biphenyl	0.276	isobutyl acetate	0.225	phenylacetic acid	0.190
isopropylbenzene	0.316	aniline	0.136	1,2-dinitrobenzene	0.124
m-xylene	0.248	piperidine	0.156	1,3-dinitrobenzene	0.109
ethylbenzene	0.234	toluene	0.221	phenylthiourea	0.184
pyrene	0.320	n-propylbenzene	0.262	phenytoin	0.191
hexan-1-ol	0.232	n-butylbenzene	0.285	theophylline	0.100
phenol	0.111	2-phenylphenol	0.274	cytosine	-0.005
1-naphthol	0.207	2,5-dimethylpyrazine	0.209	theobromine	0.056
2-naphthol	0.220	4-iodophenol	0.162	sulfanilamide	0.124
m-cresol	0.182	4-fluorophenol	0.168	5-fluoro-uracil	0.014
2-nitrophenol	0.136	4-aminobiphenyl	0.208	2,2'-bipyridine	0.251
3-nitrophenol	0.147	caffeine	0.114	trimethylamine	0.160
4-nitrophenol	0.165	4-nitroanisole	0.126	acetone	0.096
cyclohexanone	0.202	carbazole	0.232	diacetone alcohol	0.159
methane	0.127	Bisphenol A	0.174	lindane	0.166
ethane	0.162	acetanilide	0.197	2-phthalic acid	0.178
propane	0.194	2,2,2-trifluoroethanol	0.125	benzoic acid	0.182
cyclohexane	0.277	hexafluorisopropanol	0.222	2-chlorobenzoic acid	0.182
methylcyclopentane	0.273	1-nitropentane	0.203	3-chlorobenzoic acid	0.180
n-butane	0.217	1-nitrohexane	0.236	salicylic acid	0.172
n-hexane	0.276	2-hexanone	0.198	benzylamine	0.112
n-pentane	0.221	2-nonanone	0.306	4-nitroaniline	0.100
ethene	0.127	heptanal	0.237	3-nitroaniline	0.105
acetic acid	0.064	octanal	0.265		

Table A.1.: Database I (NaCl training set) of Setschenow coefficients k_s (l/mol)[§] for various organic molecules in NaCl aqueous solution at $T = 298.14$ K. The data was collected from Li *et al.*,[123] Endo *et al.*,,[181] Ni *et al.*[182] and other sources.[109,180,185–187,191] Reproduced from ref. [148], with the permission of AIP Publishing.

[§]Some of the Setschenow coefficients have originally been measured in inverse molality rather than molarity units and have not been directly converted by the respective experimental groups. In water as a solvent this does, however, only change the values of the coefficients very slightly, usually below the accuracy in which they can be accurately measured. Also, the experimental temperature sometimes varies slightly from room temperature ($\pm 5K$). The same is valid also for the other databases.

molecule	k_s	molecule	k_s	molecule	k_s
1,2,4-trichlorobenzene	0.250	chlorobenzene	0.198	1,4-dichlorobenzene	0.240
1,2-benzanthracene	0.354	chrysene	0.336	1,4-dinitrobenzene	0.097
1-ethylanthracene	0.313	cycloheptane	0.343	p-nitrotoluene	0.163
1-ethylnaphthalene	0.273	cyclopentane	0.182	p-toluidine	0.170
1-methylnaphthalene	0.200	fluoranthene	0.339	phenanthrene	0.272
2,4,6-trichlorophenol	0.228	fluorene	0.267	progesterone	0.288
2,4-dichlorophenol	0.218	heptanoic acid	0.242	s-butyl acetate	0.241
2-methylanthracene	0.336	hexyl acetate	0.312	s-butylbenzene	0.288
6-mercaptopurine	0.048	1,3-dichlorobenzene	0.226	t-butyl acetate	0.269
acenaphthene	0.238	methylcyclohexane	0.274	t-butylbenzene	0.243
benzo[a]pyrene	0.328	1,2-dichlorobenzene	0.247	testosterone	0.326

Table A.2.: Database $\mathbf{I_{val}}$ (NaCl validation set) of Setschenow coefficients k_s (l/mol) for various organic molecules in NaCl aqueous solution at $T = 298.14$ K. This database comprises all Setschenow coefficients from Ni *et al.* [182] which were not already included in database I. Reproduced from ref. [148], with the permission of AIP Publishing.

molecule	LiCl	KCl	KBr	LiBr	NaF	NaBr	NaI	KF	KI	NaNO$_3$	NH$_4$Cl
2-chlorobenzoic acid [180]	0.193	0.139	0.099	-	-	-	-	-	-	-	-
benzene [109,180,184]	0.141	0.166	0.119	0.126	0.255	0.155	0.095	0.250	-	0.119	0.103
4-nitroaniline [185]	0.118	0.051	-0.037	-	-	-	-	-	-0.116	-	-
1,4-benzoquinone [185]	0.075	0.029	-0.024	-	-	-	-	-	-0.117	-	-
propanoic acid [183]	0.130	0.091	0.076	0.107	-	0.104	-	-	-	-	-
theophylline [172]	0.099	0.068	0.000	-	-	-	-	0.230	-	-	-
4-nitrophenol [185]	0.176	0.051	-0.017	-	-	-	-	-	-0.112	-	-
diacetone alcohol [109]	0.092	0.142	0.118	-	-	0.131	0.063	-	-	-	-
phenol [109,186]	0.143	0.122	0.111	-	-	0.155	-	-	-	0.113	-
salicylic acid [187]	0.191	0.122	0.087	-	-	-	-	-	-	-	-
2-phthalic acid [109]	0.224	0.093	0.073	-	-	-	-	-	0.041	0.073	0.118
3-nitroaniline [185]	0.121	0.077	0.017	-	-	-	-	-	0.141	-	-
acetic acid [188]	0.075	0.033	0.014	0.073	-	0.067	-	-	-	0.031	-
naphthalene [180,184]	0.180	0.186	0.130	0.097	0.343	0.162	-	0.326	-	0.131	0.071
acetone [109,189,190]	0.066	0.091	0.060	-	-	-	-	-	0.020	-	-
toluene [180]	0.168	0.206	0.138	0.113	0.329	0.191	-	0.282	-	0.144	0.136
theobromine [172]	0.104	0.074	-0.028	-	-	-	-	0.196	-	-	-
lindane [191]	0.135	0.149	0.043	-	0.415	0.131	-0.088	0.544	-0.127	-	0.066
benzoic acid [109]	0.189	0.144	0.109	-	-	-	-	-	0.049	0.075	-
trimethylamine [109]	0.090	0.200	0.160	-	-	0.150	0.110	-	0.130	-	-
o-xylene [180]	0.180	0.205	0.156	0.120	0.349	0.178	-	0.342	-	0.141	0.102
m-xylene [180]	0.185	0.222	0.170	0.125	0.379	0.144	-	0.354	-	0.165	0.153
p-xylene [180]	0.187	0.217	0.168	0.133	0.347	0.198	-	0.339	-	0.146	0.099
3-chlorobenzoic acid [180]	0.193	0.142	0.090	-	-	-	-	-	-	-	-
biphenyl [184]	0.218	0.255	-	-	-	0.209	-	-	-	-	-
1,2,4-trichlorobenzene [180]	-	0.239	-	-	-	-	-	-	-	-	-
3-methylbenzoic acid [180]	-	0.160	0.140	-	-	-	-	-	0.130	-	-
chlorobenzene [180]	-	0.176	-	-	-	0.129	-	-	-	-	-
n-hexane [180]	-	0.244	-	-	-	0.161	-	-	-	-	0.181
2-methylbenzoic acid [180]	-	0.230	0.210	-	-	-	-	-	0.190	-	-
piperidine [186]	0.056	0.167	-	-	-	-	-	-	-	-	-
caffeine [192]	-	-	-	-	-	-0.0058	-	-	-	-	-
1,3-dichlorobenzene [180]	-	0.201	-	-	-	-	-	-	-	-	-
γ-butyrolactone [109]	-	0.028	-	-	-	0.001	-0.092	-	-0.115	-	-
1-naphthol [193]	-	0.199	-	-	-	-	-	-	-	-	-
2-nitrobenzaldehyde [194]	-	0.034	-	-	-	-	-	-	-	-0.130	-
phenanthrene [180]	-	0.279	-	-	-	0.211	-	-	-	-	0.195
1,4-dichlorobenzene [180]	-	0.192	-	-	-	0.174	-	-	-	-	-
4-chlorobenzoic acid [180]	-	0.138	-	-	-	-	-	-	-	-	-
naphthalene-1,5-diol [193]	-	0.151	-	-	-	-	-	-	-	-	-
1,3-dinitrobenzene [197]	-	0.014	-	-	-	-	-	-	-	-	-
benzylamine [186]	0.084	0.140	-	-	-	0.024	0.000	-	-	-	-
ethyl acetate [198]	0.117	0.133	-	-	-	-	-	-	-	-	-
4-amino-3-hydroxy-1-naphtha–lenesulphonic acid [193]	-	0.287	-	-	-	-	-	-	-	-	-
1,2-dichlorobenzene [180]	-	0.207	-	-	-	-	-	-	-	-	-
ethene [195]	-	0.064	0.050	-	-	0.080	-	-	-	0.050	0.023
chloroacetic acid [196]	-	0.026	0.008	-	-	-	-	-	-	-	-
ethane [199]	0.130	-	-	-	-	-	-	-	0.107	-	-
4-methylbenzoic acid [180]	-	0.200	0.190	-	-	-	-	-	-	-	-
aniline [186]	-	0.115	-	-	-	-	-	-	-	-	-
methane [199]	0.104	-	-	-	-	-	-	-	0.105	-	-

Table A.3.: Database II of Setschenow coefficients k_s (l/mol) for various organic molecules in different salt solutions at $T = 298.14$ K. The table explicitly excludes solubility data for highly polar molecules which is expected to be masked by solute-solute self-interaction effects.[109] Reproduced from ref. [148], with the permission of AIP Publishing.

B

Computer Code Infrastructure

The SMPB-DFT infrastructure in `FHI-aims` is invoked by using the key tag `solvent_mpb` in the `FHI-aims` input file `control.in`. All additional user options (subtags) are provided in Tab. B.1 including a short explanation.

Fig. B.1 shows all implemented subroutines and modules comprising the SMPB infrastructure in `FHI-aims` as created within this thesis and Tab. B.2 lists them again with a short description. All subtags given in Tab. B.1 are read in by the subroutine `read_mpb_data.f90` which inherits all variables and functions from the modules `lpb_solver_utilities.f90` and `mpb_solver_utilities.f90`. `initialize_scf.f90` initializes all variables needed for the SMPB-DFT calculation. During each SCF step first the electron density is updated from the single-electron wave-functions (`update_density_and_forces_p2.f90` or `update_density_and_forces_densmat.f90` if the density matrix should be used to update the electron density), `run_mpb_solver.f90` is called as a wrapper to the SMPBE or LPBE solver, `sum_up_whole_potential_p1.f90` is invoked to use the just obtained electrostatic potential v to evaluate the KS-Hamiltonian and energy contributions such as double counting correction or nuclei-nuclei interaction energy, `integrate_hamiltonian_matrix_p2.f90` solves KS-eigenvalue problem and finally the total energy is calculated and outputted by the routine `get_total_energy.f90`.

	tag	explanation
solvent	`dielec_func kind` $\varepsilon^{\mathrm{s,bulk}}$ `par1 par2`	Define the dielectric function. `kind=0` selects a function as suggested by Fattebert *et al.* [14] using the parameters `par1`=β and `par2`=n_0, `kind=1` takes the standard function of Andreussi *et al.* (`par1`=$n_{\min}$, `par2`=$n_{\max}$) as used in this thesis (default). [5]
	`set_nonelstat_params` $(\alpha + \gamma)$ (dyn/cm) β (GPa)	Set the parameters defining the $\Omega_\varepsilon^{\mathrm{non-mf}}$ term. Default: $(\alpha + \gamma) = 50\,\mathrm{dyn/cm}$ and $\beta = -0.35\,\mathrm{GPa}$.
	`dynamic_cavity_off`	If set, ε is parameterized in the beginning by the usage of $n_{\mathrm{el}}^{\mathrm{free}}$ and then fixed during the SCF cycle. Default: not set.

ions	`ions_temp` T (K)	Set temperature in SMPB lattice model. Default: $T = 300\,\mathrm{K}$.
	`ions_conc` $c^{\mathrm{s,bulk}}$ (M)	Set ionic bulk concentration. Default: $c^{\mathrm{s,bulk}} = 1\,\mathrm{M}$
	`ions_charge` z	Set ionic charge. Default: $z = 1$
	`ions_size` a (Å)	Set ionic size given as the side length of a lattice cell. Default: $a = 5\,\text{Å}$
	`ions_kind` kind	Use either sharp step function for the ionic exclusion functions $\alpha_{\mathrm{ion}}^{\pm}$ (`kind=0`) or the default smooth function as used in this thesis (`kind=1`).
	`ions_mod_alpha` $d_{\alpha_{\mathrm{ion}}}^{+}$ $\xi_{\alpha_{\mathrm{ion}}}^{+}$	Set parameters for cationic ion exclusion function $\alpha_{\mathrm{ion}}^{+}$. Default: $d_{\alpha_{\mathrm{ion}}}^{+} = 0.5$, $\xi_{\alpha_{\mathrm{ion}}}^{+} = 1.0$. Within the more common sign convention of negatively charged electrons, these are the parameters for the anions!
	`ions_mod_alpha_anion` $d_{\alpha_{\mathrm{ion}}}^{-}$ $\xi_{\alpha_{\mathrm{ion}}}^{-}$	Set parameters for anionic ion exclusion function $\alpha_{\mathrm{ion}}^{-}$. Default: $d_{\alpha_{\mathrm{ion}}}^{-} = d_{\alpha_{\mathrm{ion}}}^{+}$, $\xi_{\alpha_{\mathrm{ion}}}^{-} = \xi_{\alpha_{\mathrm{ion}}}^{+}$. Within the more common sign convention of negatively charged electrons, these are the parameters for the cations!
	`dynamic_ions_off`	If set, the exclusion functions $\alpha_{\mathrm{ion}}^{\pm}$ are evaluated from $n_{\mathrm{el}}^{\mathrm{free}}$ and then fixed during the SCF cycle. Default: not set.
SPE	`SPE_lmax` l_{max}	Set maximum limiting value for all $l_{\mathrm{max,at}}$. Default: $\max\limits_{\mathrm{at}}\left(l_{\mathrm{hartree,at}}\right)$. The atom-specific maximum angular momenta are given by $l_{\mathrm{max,at}} = \min\left(l_{\mathrm{max}}, l_{\mathrm{hartree,at}}\right)$.
	`SPE_cut_and_lmax_ff` $r_{\mathrm{cut,at}}^{\mathrm{mp}}$ $l_{\mathrm{max}}^{\mathrm{ff}}$	$r_{\mathrm{cut,at}}^{\mathrm{mp}}$: value of r_{at} at which far field is turned on, default: `multipole_radius_free`$+2.0\,\text{Å}$ where `multipole_radius_free` is the radius of the innermost radial grid shell at which $n_{\mathrm{el,at}}^{\mathrm{free}}$ is still zero. $l_{\mathrm{max}}^{\mathrm{ff}}$: maximum angular momentum in the far field, default: l_{max}
MERM	`delta_rho_in_merm`	Setting this keyword, evaluates the change of the source term $4\pi q[v_n] - \hat{L}_1[v_n]\delta v_{n+1}$ during the MERM iteration and solves the SPE for this change rather than the full source density.
	`MERM_in_SPE_solver` T/F	Perform the MERM iterations inside the `SPE_solver.f90` routine without updating δv_{n+1} on the full integration grid at each step, but only at the points where we actually need it to form the source term (cf. Section 3.4.1.2 and Tab. B.2). Default: `.True.`
	`SPE_conv` τ_{MERM} η	MERM convergence parameters. Defaults: $\tau_{\mathrm{MERM}} = 10^{-10}$, $\eta = 0.5$

others		
	`nonsc_Gnonmf`	Setting this keyword, calculates the free energy term $\Omega_\varepsilon^{\mathrm{non-mf}}$ as a post-correction to be added after the SCF cycle, no corresponding correction term is added to $\hat{h}^{\mathrm{KS}}$. Default: not set.
	`not_converge_rho_mpb`	Setting this keyword, runs a vacuum calculation first and then subsequently solves the SMPBE once with the vacuum electron density and then outputs all energetics. Default: not set.
	`solve_lpbe_only T/F`	Solve the LPBE Eqs. (2.52) and (3.30) instead of the SMPBE and use corresponding energetics from modified Debye-Hückel theory (cf. Section 3.2.6). Default: `.False.`.

Table B.1.: All currently available user options (subtags) for the implemented SMPB-DFT method. If not indicated elsewise the input values are in atomic units.
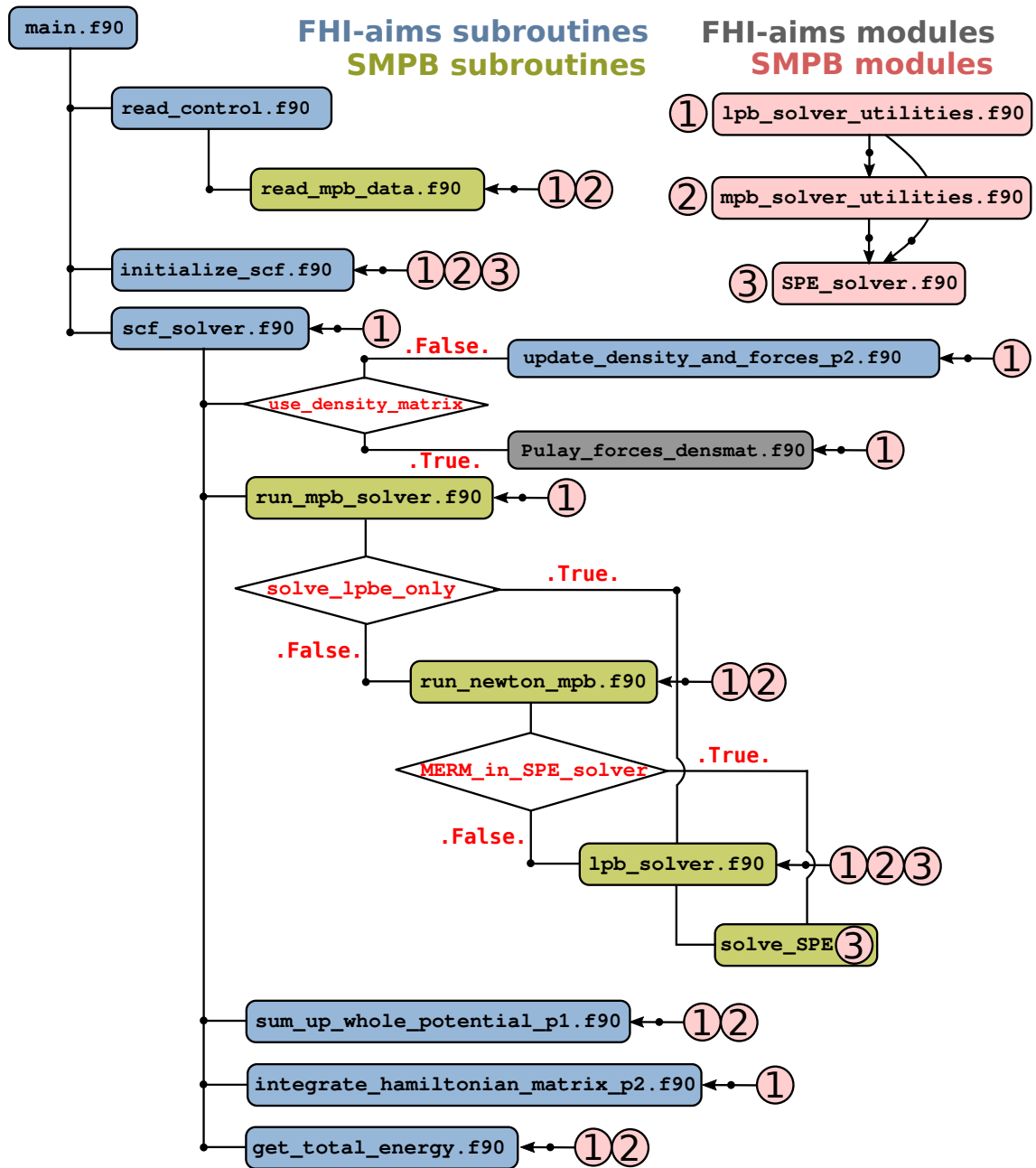
Figure B.1.: Scheme which visualizes the integration of the SMPB-DFT scheme into the code structure of `FHI-aims`. Blue and gray boxes denote `FHI-aims` routines and modules which have been partly modified. Subroutines that have been newly created within the scope of this thesis are shown as green boxes (cf. also Tab. B.2), while the new modules are highlighted with a red background color. All routines that all used within a particular file are connected to it to the right by a line with a filled circle. Arrows indicate the inheritance of variables and functions from modules. Finally, the subroutine `solve_SPE` is part of the module `SPE_solver.f90` indicated by the module number inset.

file	content
`read_mpb_data.f90`	The subroutine `read_mpb_data` is called from the `FHI-aims` routine `read_control.f90` which reads the `FHI-aims` input file `control.in`. `read_mpb_data` reads the SMPB-specific part of the `control.in` file, i.e. all parameters listed in Tab. B.1.
`run_newton_mpb.f90`	The subroutine `run_newton_mpb` performs the iterations of the Newton solver. For that purpose, it repeatedly evaluates the functions $-4\pi\varepsilon q[v_n]$ and $h^2[v_n]$ which define the LPBE-like PDE Eq. (3.72) which is solved by the called routine `lpb_solver.f90` until convergence of the Newton method.
`lpb_solver.f90`	The subroutine `lpb_solver` solves any LPBE-type of PDEs. This can be either Eq. (3.72) when coupling the routine to the Newton solver or directly the LPBE Eqs. (2.52) and (3.30) as resulting from modified Debye-Hückel theory. If `MERM_in_SPE_solver=F`, the MERM iterations are performed within this routine and the arising SPE is solved by the subroutine `solve_SPE` from the module `SPE_solver.f90`. In the case of `MERM_in_SPE_solver=T` the iterations are outsourced to the routine `solve_SPE` with the linear mixing applied directly on the source term multipole components (cf. Section 3.4.1.2).
`SPE_solver.f90`	This module contains all subroutines and functions necessary for the solution of SPE-like equations as e.g. Eq. (3.75). The module is a modified version of the `FHI-aims` module `precondition.f90` which contains the Kerker preconditioner used for increasing the convergence of the SCF cycle.[136] In the case of `MERM_in_SPE_solver=T` the routine `solve_SPE` solves instead a LPBE-like equation (cf. Section 3.4.1.2).
`run_mpb_solver.f90`	Wrapper routine calling either `solve_SPE`, `run_newton_mpb` or `lpb_solver` depending if the vacuum Poisson equation in `FHI-aims` should be replaced by the SPE (`solve_lpbwith_constant_dielec=T`, experimental), SMPBE (default) or LPBE (`solve_lpbe_only=T`), respectively.
`lpb_solver_utilities.f90`	This module contains all basic routines and functions needed in the SMPB-DFT framework as e.g. routines evaluating the dielectric and ion exclusion function and their gradients, KS-Hamiltonian correction terms or terms related to the atomic forces. Moreover, it includes all routines needed by the LPB-solver which calculate e.g. the source term $-4\pi q[v_n] + \hat{L}_1[v_n]\delta v_{n+1}$ or the MERM convergence criterium τ_{MERM}.
`mpb_solver_utilities.f90`	This module contains all SMPB specific routines and functions needed for the Newton method evaluating e.g. the $h^2[v_n]$-function, the ionic charge density $n_{\mathrm{ion}}^{\mathrm{SMPB}}$ or SMPB free energy contributions.

Table B.2.: Short description of all Fortran files of the SMPB implementation in `FHI-aims` that were created within this thesis.